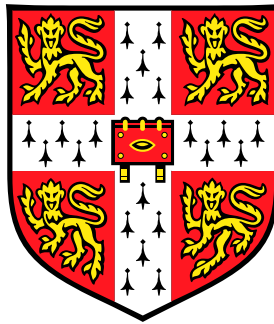


THEORETICAL AND EXPERIMENTAL
SECONDARY ELECTRON SPIN
POLARISATION STUDIES
AND 3D THEORY OF FIELD EMISSION
FOR NANOSCALE EMITTERS



Sabrina Marion Masur
Wolfson College

This thesis is submitted for the degree of
Doctor of Philosophy
at the University of Cambridge

April 2021

Declaration

This thesis is the result of my own work and includes nothing which is the outcome of work done in collaboration except as declared in the Preface and specified in the text. It is not substantially the same as any that I have submitted, nor is it being concurrently submitted for a degree or diploma or other qualification at the University of Cambridge or any other University or similar institution except as declared in the Preface and specified in the text. I further state that no substantial part of my thesis has already been submitted, nor is it being concurrently submitted for any such degree, diploma or other qualification at the University of Cambridge or any other University or similar institution except as declared in the Preface and specified in the text. It does not exceed the prescribed word limit for the Degree Committee of the Faculty of Physics.

Sabrina Marion Masur

March 2021

Abstract

Spin-polarised electron beams are an invaluable probe of spin-dependent phenomena in fields of atomic and molecular physics, magnetism and biophysics. For this purpose, this work explores both theoretical and experimental aspects of field emission properties of point-like nano-scale emission sources with special emphasis on their spin-polarising ability.

Firstly, the development of a novel multi-scale field emission simulation procedure is introduced and its capability to successfully combine classically calculated boundary conditions with quantum mechanical density functional theory (DFT) simulations are demonstrated. This technique is then applied to two emission tips based on a capped (5,5) carbon nanotube and a small tungsten-pyramid. In so doing, this thesis demonstrates how this novel simulation method can provide insights into material properties, such as the spatial distribution of charge density, the physical distribution and energies of individual orbitals for different applied fields and the changes in total potential energy with varying fields. Secondly, to investigate the interactions between spin-polarised electron beams with ferromagnetic materials experimental work on several magnetic heterostructures was conducted using a spin-polarised low-energy electron microscope. The analysis of the energy- and spin-dependent energy loss and newly-developed secondary electron yield experiments gave insights into inelastic scattering mechanisms. Measuring the energy-dependent reflectivity in conjunction with DFT simulation further gives indications about the material's spin-dependent electronic band structure a few electronvolts above the Fermi level. Furthermore, this work includes the design, fabrication, and integration of specialised experimental equipment into a pre-existing ultra-high vacuum system to analyse nano-sized field emitters. As these emitters are based on ultra-thin magnetic Fe and Fe₃O₄ nano-disks, theoretical studies using micromagnetic simulations were performed to analyse their magnetic behaviour. Based on the resulting phase diagrams suitable dimensions that enable the fabrication of robust spin-polarised field emitter systems, which have a stable in-plane magnetisation and long Néel relaxation times, were found.

In loving memory of my Grandfather Peter.

Acknowledgement

First and foremost, I would like to express my gratitude to Dr. Chris Edgcombe and Dr. Adrian Ionescu who both have provided me with unlimited guidance, encouragement, and mentorship throughout my doctoral degree. Their guidance has helped me tremendously to advance as a researcher and has extended beyond academics. Both have helped bring me to where I am today personally and professionally. Moreover, I would like to thank Professor Crispin Barnes for the invaluable resources provided and for his help in administrative matters.

In addition, I would like to thank my other collaborators and co-authors, Dr Edward Linscott and Dr. Gabriel Constantinescu to whom I am indebted for their work implementing the boundary-matching method into the ONETEP code and to Dr. Peter Newton for all his time, support and technical expertise. I am also grateful to Dr. Yasushi Yamauchi and Dr. Masahiko Suzuki at the National Institute of Material Science in Japan for all their help and expertise during my experiments there.

Further thanks goes to all my friends at home, in the TFM group, in Wolfson College and in the SIMDALEE project, who made these past years unforgettable.

I feel privileged and humbled to study at Cambridge, and I am grateful to the Marie Curie Association (European Union's Seventh Framework Programme FP7/2007–2013/ under REA grant agreement no. 606988) and Thermo Fisher Scientific for funding an extension to my research.

Finally, I am incredibly grateful to my family and friends for their encouragement throughout my life. Most of all, enormous thanks to my loving parents Martina and Waldemar, my brother Marco and my grandmother Martha for their continuous support and for inspiring me to pursue my dreams.

Preface

Part of Chapter 4 has been published as:

C. J. Edgcombe, S. M. Masur, E. B. Linscott, J. A. J. Whaley-Baldwin, C. H. W. Barnes,
“Analysis of a capped carbon nanotube by linear-scaling density-functional theory”,
Ultramicroscopy 198, 26 (2019)

and

S. Masur, E. Linscott, and C. Edgcombe,
“Modelling a capped carbon nanotube by linear-scaling density-functional theory”,
Journal of Electron Spectroscopy and Related Phenomena 141, 146896 (2020).

This chapter is the outcome of work done in collaboration with my co-authors. Specifically, the implementation of the boundary matching method into the ONETEP DFT code that made the simulation model possible was done by Dr. E. Linscott and Dr. G. Constantinescu. All the simulated results of the chapter were run, analysed and interpreted by myself, in consultation with Dr. C. Edgcombe. The geometry optimisation discussed in Section 4.2 was aided by molecular mechanics simulation conducted by D. H. Phillips.

Part of Chapter 5 will be published as:

S. M. Masur, P. J. Newton, A. Ionescu, M. Suzuki, Y. Yamauchi, D. Fujita and
C. H. W. Barnes

“Spin-polarised secondary electron emission spectroscopy on ultra-thin Fe/Ag(001)”,
(in preparation)

That chapter is the outcome of work done in collaboration with the National Institute of Material Science in Tsukuba, Japan. In particular, the experiments using a spin-polarised electron microscope have been carried out by Dr. M. Suzuki. The analysis and interpretation of the data was done by myself in consultation with my co-authors.

Table of Contents

Declaration	i
Abstract	iii
Acknowledgement	vii
Preface	ix
Table of Contents	xi
List of Figures	xv
1 Introduction	1
2 Theoretical Background	9
2.1 Density functional theory	10
2.1.1 The many-body problem	10
2.1.2 Kohn-Sham concept	11
2.1.3 Exchange and correlation functionals	13
2.1.4 ONETEP - $\mathcal{O}(N)$ Electronic Total Energy Package	14
2.2 Fundamentals of micromagnetism	16
2.2.1 Exchange energy	18
2.2.2 Demagnetisation energy	19
2.2.3 Magnetic anisotropy energy	21
2.3 Materials	23
2.3.1 Carbon nanotubes	23
2.3.2 Magnetic thin films and nanostructures	28
3 Computational and experimental methods	31
3.1 Computational multi-scale method	32
3.1.1 Multi-scale atomistic-continuum model	32

3.2	(5,5) CNT model and computational setup	35
3.2.1	(5,5) CNT geometry	35
3.2.2	Simulation parameters and convergence test	37
3.2.3	Semi-classical continuum model	40
3.2.4	Multi-scale model and boundary condition matching	42
3.3	Experimental methods	45
3.3.1	Molecular beam epitaxy	45
3.3.2	Auger electron spectroscopy	46
3.3.3	Low-energy electron diffraction	47
3.3.4	Spin-polarised low-energy electron microscopy	49
3.3.5	Mott polarimeter	56
4	Ab-initio study of field emission properties	59
4.1	Characterisation of a capped (5,5) CNT	60
4.1.1	Fermi level and metallic radius	60
4.1.2	Electron charge density	63
4.1.3	Electron charge density with applied field	67
4.1.4	Local density of states	68
4.1.5	Energy levels	71
4.1.6	Molecular orbitals	72
4.1.7	Binding energy	74
4.1.8	Potential barrier with applied field	75
4.1.9	Work function	79
4.2	Initial analysis of a W pyramid	81
4.2.1	Geometry optimisation	81
4.2.2	Multi-scale model with applied field	85
4.2.3	Local density of states	89
4.2.4	Charge density with and without applied field	91
4.2.5	Molecular orbitals	93
4.2.6	Electric potential	95
4.3	Conclusion	97
5	Spin-polarised secondary electron emission spectroscopy	99
5.1	SPLEEM investigation of ultra-thin Fe films on Ag(001)	100
5.1.1	Sample preparation of Fe/Ag(001)	100
5.1.2	Onset of the magnetic domain structure and orientation	102
5.1.3	Spin-dependent energy loss spectra	105
5.1.4	Reflectivity scans and band structure probing	112

5.1.5	ESSEY-SPLEEM mode	115
5.2	SPLEEM investigation of ultra-thin Fe/W (110)	119
5.2.1	Sample preparation of Fe/W (110)	119
5.2.2	Onset of magnetic domain structure and orientation	120
5.2.3	Spin-dependent energy loss spectra	123
5.2.4	Reflectivity scans and band structure probing	126
5.2.5	ESSEY-SPLEEM mode	127
5.3	SPLEEM investigation of Ag/Fe/W (110)	129
5.3.1	Sample preparation of Ag/Fe/W (110) and magnetic orientation	129
5.3.2	Spin-dependent energy loss spectra	130
5.3.3	Reflectivity scans and band structure probing	134
5.3.4	ESSEY-SPLEEM mode	135
5.4	Conclusion	138
6	Experimental setup for spin-polarised field emission experiments	141
6.1	UHV-MBE chamber with attached Mott polarimeter	142
6.1.1	Pumping chamber	143
6.1.2	Experimental chamber	145
6.1.3	Refurbishment and improvements	146
6.2	Novel sample holder for field emission experiments	152
6.2.1	Field emission holder design	153
6.3	Conclusion	159
7	Theoretical investigation of potential spin-polarised FESs	161
7.1	Preliminary design considerations for spin-polarised FEs	162
7.2	Micromagnetic simulations	165
7.2.1	Simulation parameters	165
7.2.2	Magnetisation direction and single-domain state	167
7.2.3	Thermal stability and demagnetisation tensor	177
7.2.4	Current stability	180
7.3	Conclusion	181
8	Summary and further work	183
8.1	Summary	183
8.2	Further work	185
	List of Acronyms	189
	Bibliography	191

List of Figures

1.1	Comparison of the beam divergence from a blunt and a sharp field emission tip.	2
1.2	Depiction of different types of spin-polarised electron beams.	4
1.3	Schematic of the nano-sized spin-polarised field emission source proposed in this work.	6
2.1	Flowchart of ONETEP's self-consistent algorithm to calculate the ground state of the system.	15
2.2	Schematic of the idealised band structure of a) a strong and b) a weak itinerant ferromagnet.	18
2.3	Schematic showing how the creation of domains can reduce the external demagnetisation field	20
2.4	a) Angular dependence of the energy surface for cubic MCA; b) Magnetisation direction for different nano-sized structures.	22
2.5	Visualisation of the sp^2 -hybridisation for benzene.	24
2.6	a) Schematic of the creation of a SWCNT; b) Graphene sheet with the primitive lattice vectors and the chiral indices.	25
2.7	Visualisation of a) a closed and b) an open (5,5) CN; c-e) Examples of CNT fragments for different chiral indices.	27
2.8	a) Magnetic thin film with coordinate system; b) Representation of a magnetic vortex state.	29
2.9	Schematic plot of coercivity versus sample size.	30
3.1	Hierarchy of multi-scale modelling techniques.	32
3.2	Schematic of the different stages of the multi-scale modelling process.	34
3.3	Model of the CNT's conducting Fermi isosurface.	36
3.4	DFT simulation model of the (5,5) CNT in the simulation cell.	37

3.5	Convergence of the kinetic cut-off energy for a (5,5) CNT. The inset shows the correlation between the cut-off energy and the grid-spacing and the number of cells.	39
3.6	NGWF radius convergence of the (5,5) CNT using the LDA functional and $E_{\text{cut}} = 1000 \text{ eV}$	40
3.7	a) Adaptive mesh distribution and b) electrostatic equipotentials of the full CNT model and a zoom of the DFT box.	41
3.8	Section containing the CNT axis, showing the matching between the micro and macro model.	43
3.9	Morphology of different epitaxial growth modes.	46
3.10	Schematic of the Auger electron process.	47
3.11	a) Diagram of Bragg diffraction; b) Schematic of a LEED syetm.	48
3.12	Schematics of a SPLEEM setup.	50
3.13	a) Schematic of the interaction volume; b) Interaction volume for different primary beam energies.	51
3.14	Energy dependence of the a) exchange potential and the b) spin-dependent inelastic mean free path.	53
3.15	Typical SPEEL spectrum showing the elastic peak, the SE electron peak and the systems energy resolution.	55
3.16	a) Mott scattrng potential; b)Simplified schematic of the retarding potential Mott polarimeter.	58
4.1	Display of the different contributions to the overall potentials: Hartree, XC and pseudopotential along the CNT axis.	61
4.2	Comparison between the one-dimensional potential found by DFT, the Poisson solver and a classical calculation.	62
4.3	Different electron density isosurfaces of a (5,5) CNT for zero applied field.	64
4.4	Relation between the charge density and the electrostatic potential without an applied field.	65
4.5	Mulliken charge population of the capped (5,5) CNT.	66
4.6	a) 3D and b) 2D representation of the change in electron density on application of an external field.	67
4.7	Comparision between the LDoS at the tip and the tube region.	68
4.8	LDoS of a long CNT.	69
4.9	Local density of states for four values of applied field.	70
4.10	Change in orbital energies with applied field.	71
4.11	HOMO isosurface for the (5,5) CNT in different electic fields.	73

4.12	Electron charge densities of the HOMO and LUMO with and without an applied field.	74
4.13	Changes in the binding energy of the (5,5) CNT with changing applied field.	75
4.14	2D and 3D representation of the potential energy of a CNT.	76
4.15	Potential energy for eight values of applied electric field.	77
4.16	Comparison of a) the potential barrier width, b) the potential barrier height and c) the position of the metallic surface between DFT simulations and classical calculations.	78
4.17	Comparison of the simulated potential energy along the CNT axis using an LDA, GGA and without a XC functional.	80
4.18	a) 2D image of the four-sided W pyramid showing its dimension and crystallographic directions. b) Schematic of the periodic “Coulomb cut-off” boundary condition.	82
4.19	Optimisation process of the W-pyramid’s atomic positions.	84
4.20	Plot of the atomic model of the W pyramid, where the colours indicate the atomic forces acting on the individual atom.	85
4.21	Schematic of the FlexPDE model for the W-pyramid simulations.	86
4.22	a) Adaptive mesh distribution and b) electrostatic equipotentials of the W pyramid.	87
4.23	Section through the W-pyramid axis, showing the matching between the macro- and nano-model.	88
4.24	LDoS of a W-pyramid.	90
4.25	Different electron density isosurfaces of a W pyramid for zero applied field.	91
4.26	Representation of the change in electron density on application of an external field.	92
4.27	HOMO isosurface for the W-pyramid.	93
4.28	Electron charge densities of the HOMO and LUMO at zero applied field.	94
4.29	Comparison of the emission pattern between experiment and theory for a four-faced W-pyramid.	94
4.30	Potential energy for the W-pyramid along the z -axis with and without applied field.	95
4.31	Enlarged view of the potential energy for the W-pyramid along the z -axis with and without applied field.	96
5.1	Low-energy electron diffraction pattern of a) Ag (001) and b) Fe/Ag (001).	101

5.2	In situ observation of the thickness-dependent changes in in-plane spin-asymmetry during Fe growth on Ag (001).	103
5.3	SPLEEM images of the magnetisation of Fe/Ag (001) for different beam alignments.	104
5.4	Comparison of SPEEL spectra of Ag (001) and 5 ML Fe/Ag (001). . .	107
5.5	SPEEL spectra of 8 ML Fe/Ag (001) for three different beam energies.	109
5.6	Spin-resolved DoS for Fe and schematic of Stoner excitations.	110
5.7	Enlarged view of the secondary electron peaks with indicated maximum SE peaks.	112
5.8	Reflectivity scan for Fe/Ag (001) and simulated band structure of Fe and Ag.	114
5.9	ESSAY spectrum of Fe/Ag (001).	116
5.10	a) Calculated SE electron yield versus primary beam energy; b) Comparison of the secondary electron yield for Fe.	118
5.11	Low-energy electron diffraction pattern of a) W (110) and b) Fe/W (110).	120
5.12	In situ observation of the thickness-dependent changes in spin-asymmetry during Fe growth on W (110).	121
5.13	SPLEEM images of the magnetisation of Fe/W (110) for different beam alignments.	122
5.14	SPEEL spectra of 5 ML Fe/W (110) for three different beam energies.	124
5.15	Reflectivity scan for Fe/W (110) and simulated band structure of Fe and W.	127
5.16	ESSAY spectrum of Fe/W (110).	128
5.17	a) Total electron yield and SE electron yield; b) Measured MCP voltage.	129
5.18	a) LEED pattern of Ag(1 monolayer (ML))/Fe(5 ML)/W (110); b) SPLEEM images of the magnetisation for different beam alignments.	130
5.19	SPEEL spectra of Ag(1 ML)/Fe(5 ML)/W (110) for three different beam energies.	131
5.20	Comparison of the SPEEL spectra of Fe/Ag (001), Fe/W (110) and Ag/Fe/W (110).	133
5.21	Reflectivity scan for Ag/Fe/W (110) and simulated band structure of Ag, Fe and W.	135
5.22	ESSAY spectrum of Ag/Fe/W (110).	136
5.23	a) Total electron yield and SE electron yield; b) Measured MCP voltage.	136
5.24	Comparison of the ESSAY spectrum and the SPEELS spectra of Ag/Fe/W (110).	137
6.1	Complete Mott/MBE UHV chamber after the refurbishment.	142

6.2	Schematic of the vacuum and gas handling system.	144
6.3	Picture of the current triple-axis manipulator.	146
6.4	Picture of the new stabilising mounts and the new UHV chamber body.	147
6.5	Picture of a) one of the new height-adjustable stand and b) the new cooling shroud and the pump's safety frame.	149
6.6	Picture of the extended sample manipulator.	151
6.7	Schematic of the measurement setup using the FE-holder and a Mott polarimeter.	152
6.8	CAD model of the "top-hat" anode and the two aperture designs. . .	154
6.9	Comsol simulations of detectable electron count versus applied voltage.	155
6.10	CAD model of the sample holder base.	156
6.11	Comsol simulations of detectable electron count with and without a suppressor electrode.	157
6.12	COMSOL simulations without and b) with a suppressor electrode. . .	158
6.13	Finished CAD design of the new FE-holder assembly.	159
6.14	Final FE-holder assembly.	160
7.1	First design idea for a point-like spin-polarised field emission tip. . . .	162
7.2	Second design idea for a point-like spin-polarised field emission tip. .	164
7.3	m_z versus L for a single-crystalline and amorphous Fe nano-disk for $d = 9$ nm.	168
7.4	$ \vec{m} $ versus L for a single-crystalline Fe nano-disks, with a $d = 28$ nm. .	169
7.5	Phase diagram for a) single-crystalline and b) amorphous Fe nano-disks.	171
7.6	Difference in m_z components between the single-crystalline and amorphous Fe simulations models.	172
7.7	Oop-component of the magnetisation versus thickness of single-crystalline and amorphous magnetite models.	173
7.8	Plot of the curl of the magnetisation indicating spin-canting.	174
7.9	Phase diagram for a) single-crystalline and b) amorphous magnetite simulation models.	176
7.10	a) Diagram of the magnitude of the demagnetisation energy for three different circular nano disks.	178
7.11	Dimensional-dependency of the threshold temperature for the onset of superparamagnetism in a) Fe and b) Fe_3O_4 nano-disks.	179
7.12	a) SEM image of an ion milled AFM tip. b) Image of gold coated GaAs micropillars fabricated via reactive ion etching.	181

In the middle of difficulty lies
opportunity.

ALBERT EINSTEIN

1 | Introduction

Even though field emission (FE) can certainly count as one of the oldest methods in surface science dating back to the 18th century [1], it still represents one of the key mechanisms driving modern science and enables the development of novel devices and technologies. Due to a wide range of applications, such as electron emission-based imaging techniques [2,3], electron beam lithography [4,5], ultra-fast electronics [6,7], novel electronic displays [8–10] and being driven by the capabilities of nanotechnology, the field is experiencing a renaissance.

Generally, W tips are widely used as field emission sources (FESs) in standard electron beam-based experimental techniques, such as scanning electron microscopy (SEM), low-energy electron microscopy (LEEM) or electron energy loss spectroscopy (EELS), which consist of single electrochemically etched tungsten (W) needles with tip radii ranging from about 50 nm to a few hundred nanometres depending on the exact fabrication process [11–13]. These tips usually exhibit a high emission efficiency and brightness [14]. However, some disadvantages for such relatively blunt FESs are for instance high turn-on electric fields and a high electron beam divergence [15]. A tip with a radius between 50 nm to 100 nm, for example, exhibits beam opening angles in the order of 35° to 50° as seen in Figure 1.1 a [16]. Thus, the control of such broad beams necessitates large and technically complex collimation optics that focus the beam and reduce the focal spot size enough to achieve a spatial resolution of only a few nanometres.

One option to overcome these disadvantages would be to use FE sources with apex radii, R , in the range of a few nanometres or even single-atom tips. Such emitters have been found to significantly enhance the FE performance as they not only exhibit higher brightness, lower turn-on electric fields and enhanced emission stability [17,18] but also produce spatially coherent beams from a small emission area, creating an almost point-like field emitter. It was, for example, found that the angular beam divergence from the normal direction for ultra-sharp W emitter tips was as small as 0.5° (Figure 1.1 b) [19]. Theoretical calculations for atomically sharp FESs even predict them to exhibit self-focusing properties which would remove the

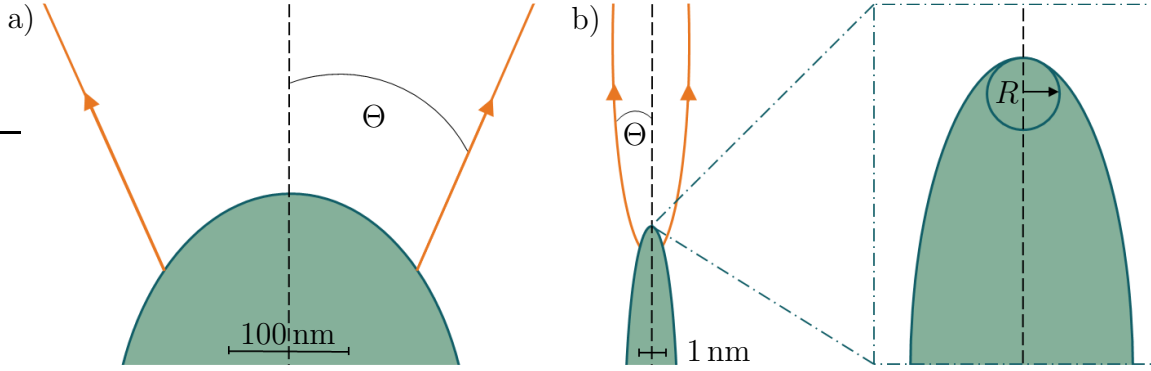


Figure 1.1: a) Field emission from a blunt metal tip with $R > 100$ nm exhibiting a beam divergence of $\Theta = 35^\circ - 50^\circ$. b) Field emission from a nanotip with an apex radius $R < 10$ nm exhibiting a beam divergence of typically $\Theta = 0.5^\circ - 4^\circ$.

need for extensive collimation optics to achieve high spatial resolution [20, 21].

Another recently developed field emission source is based on LaB_6 nanowires [22, 23]. These wires have a thickness of 50 nm to 80 nm, which is still higher than the apex size desired in this work. However, these emitters have a low work function compared to W and emit at a high current density while displaying no current decay. Furthermore, they are inert and are thus promising candidates for new point-like field emission sources. Motivated by these enhanced FE properties, many experimental investigations of novel point-like FESs have been published throughout the 21st century [22–27].

Another consequence of this novel FE behaviour is, that these FESs can no longer be described by the classical one-dimensional model of a planar field emitter as applied in the Fowler-Nordheim (FN) theory [28, 29]. Instead, more complex calculation methods and models are necessary to describe and predict an emitter's field emission properties. Thus, much effort has been put into creating more accurate three-dimensional descriptions accounting for the actual emitter geometry and confined dimensionality [30–32] using, *inter alia*, first-principles calculations [33, 34]. These calculations have been applied to further types of emitters such as carbon nanotubes (CNTs) and others. One such simulation approach will be introduced in this dissertation, which aims to help with understanding the behaviour at an atomic-scale of nano-sized FESs, such as CNTs.

This material is chosen as carbon-based allotropes such as CNTs, nano-wires or graphene [35, 36] have been found to offer an especially improved FE performance compared to classical materials such as W due to their high aspect ratio [37] and unique properties [38]. CNTs in particular exhibit a narrow energy spectrum of the emitted electrons, a high brightness, a low turn-on field and a very high stability of the emitted current [39, 40], making them ideal field emission cathodes. Thus, a lot

of research has been done on, *e.g.* CNT-based field emitter arrays [41, 42].

A further step in the development of electron beam-based experimental techniques is to utilise the electron spin. Examples of this technique are spin-polarised LEEM (SPLEEM) and spin-polarised EELS (SPEELS), which use a spin-polarised field emission source (SP-FES) to gain additional information about a material’s magnetic properties such as the spin-dependent band structure [43–45], the magnetic domain structure [46–49] or magnetisation dynamics [44, 50]. Thus, another goal of this dissertation is the investigation of potential SP-FESs to be used in such experimental techniques.

An electron source is said to be spin-polarised if the electron spins are oriented along some preferred direction. Here one generally has to distinguish between two cases, in which the component of the electron’s spin is either aligned parallel to the quantisation axis (“spin-up”) or antiparallel (“spin-down”) [51, 52]. In the context of an ensemble of electrons such as an electron beam, one has to further investigate the averaged spin orientation. An electron beam is, for example, called “unpolarised” when the electrons’ spin directions are randomly oriented such that the number of spin-up electrons along any specific axis is equal to the number of spin-down electrons as seen in Figure 1.2 a. However, in the case of a SP-FES, the electrons have a dominant direction along one axis and thus create an imbalance in the number of spin-up versus spin-down electrons. The definition of the polarisation P , along a polarisation axis, is given as

$$P = \frac{N_{\uparrow} - N_{\downarrow}}{N_{\uparrow} + N_{\downarrow}}, \quad (1.1)$$

with N_{\uparrow} and N_{\downarrow} giving the number of electrons with a spin orientation parallel and antiparallel to the quantisation axis, respectively [52]. For a fully polarised beam, as seen in Figure 1.2 b, P equals 1, whereas a partially polarised beam results in $0 < P < 1$ (Figure 1.2 c). For most experiments it is desirable to achieve a high spin polarisation, hence multiple concepts on how to generate spin-polarised (SP) beams have been developed over the years. One approach, for example, would be to magnetically manipulate an unpolarised electron beam and to align its electron spins. However, this option can be dismissed as the required magnetic fields to manipulate the energy-dependent Lorentz force would be extremely high, rendering this option infeasible. Another approach is to manipulate the emission process directly to achieve a SP beam. One such current state-of-the-art SP source, which is based on photoemission from a solid by irradiating the emitter with polarised light, is a gallium arsenide (GaAs) based cathode. In particular, GaAs-GaAsP strained superlattice emitters can exhibit polarisation of up to 95% [53–55]. These emitters however have the disadvantage of having large emission areas thus acting

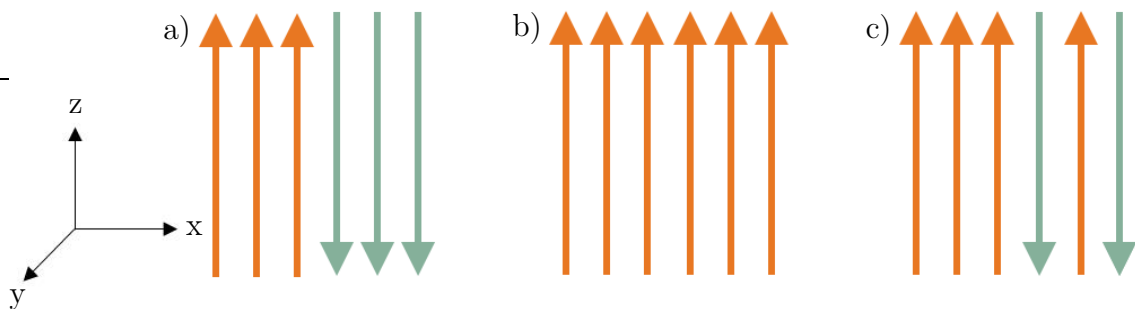


Figure 1.2: A simplified schematic of a) an unpolarised electron beam, b) a fully polarised electron beam and c) a partially polarised electron beam with z being the quantisation axis. The arrows indicate the electrons’ spin direction along the z -axis with orange being “up” and green being “down”.

more like bulk materials than needle-like emitters. One approach to overcome this disadvantage was to use pyramidal-shaped GaAs emitters which have tip areas of about 25 nm [56]. These tips, even though they achieved a high brightness and a polarisation of 20%–38%, have the disadvantage that the extracted current is limited to less than 20 nA due to tip melting. Moreover, GaAs-type photocathodes are difficult to implement in existing instruments such as electron microscopes, because the photocathode requires a laser optical system and an additional chamber for Cs-O activation to lower the emitters work function. Furthermore, such alkali-based FES have the additional disadvantages of needing to periodically replace the activation layer material, and their extreme sensitivity to poor vacuum conditions [57].

Another option, which is of interest for this thesis, is to utilise field emission from a material with inherent spin polarisation such as a magnetic solid [58–60]. As field emission in a metal is expected to mainly stem from a narrow energy range around the Fermi level, E_F , where ferromagnets (FMs) exhibit a spin-dependent density of states, the emitted electrons are assumed to be spin-polarised. This effect was found in field emission from single-crystal tips of the 3d ferromagnets (Fe, Co, and Ni) [61], thin films of the 3d and rare earth elements on W tips [62–65] and W tips coated with europium-based compounds [66–68].

Here one of the highest values for P was achieved for EuS-coated W tips which have been found to have a polarisation of as much as 90% below 21 K [66]. However, this value dropped drastically when the temperature was increased [67]. Thus this promising material suffers from some great disadvantages, such as the temperature limitation due to its low Curie temperature of only $T_C = 16.5$ K, high extraction voltages, large tip radii of about 100 nm [69] and high vacuum conditions, preventing it from being a practical candidate for a SP-FES. Hence, this dissertation will

concentrate on the investigation of ferromagnetic $3d$ metals for the development of novel SP-FESs.

These materials have several advantages, like high Curie temperatures, low resistivity and good thermal stability. Experiments on spontaneously or remanently magnetised Fe- and Co-coated W tips demonstrated polarised emission of 10% - 48% for Co/W (111), 20% - 35% for Co/W (001), 10% - 35% for Fe/W (111), 20% - 35% for Fe/W (001) and about 41% for Fe/W (110) tips in the absence of a magnetic field [62–65]. Other publications reported polarisation of up to 80% (47%) for Fe-coated (Co-coated) W tips with radii larger than 100 nm depending on the fabrication procedure [60]. Another benefit of these materials is the option to selectively control the direction of magnetisation to lie either in-plane or out-of-plane by adjusting the dimensions of the FM, utilising its shape anisotropy.

Thus, to build highly efficient SP-FESs it is imperative to combine the spin-polarising properties of the $3d$ metals with the improved FE efficiency of sharp, high aspect ratio emission tips. Here one has to be careful as studies on Fe-coated W nano-emitters with only a few hundred atoms at the tip have demonstrated a superparamagnetic response of the tip at room temperature [70]. These magnetic fluctuations produce unwanted spontaneous fluctuations of the spin polarisation direction, rendering them useless as SP-FESs. However, this effect can be suppressed by adjusting the film thickness [62]. It has also been found that it is possible to avoid unwanted oxidation of the FM by using graphene as an inert passivation layer [71], which could combine the theoretical simulations presented here with the experimental work of this thesis. Overall, all these positive attributes make tips based on ferromagnetic thin film promising candidates for the fabrication of viable point-like SP-FESs.

Motivation

The main motivation of this thesis is to investigate the possibility of fabricating spin-polarised point-like field emission sources based on the emission from ferromagnetic materials and their potential use for experiential investigations of magnetic samples. A schematic of the concept is depicted in Figure 1.3.

For this, both experimental and theoretical studies should be carried out to provide a detailed insight into the influence of the emitter’s material and geometry on its field emission properties and spin polarisation, and to investigate the interactions of such a spin-polarised electron beam with ferromagnetic materials. To achieve this the following tasks had to be performed:

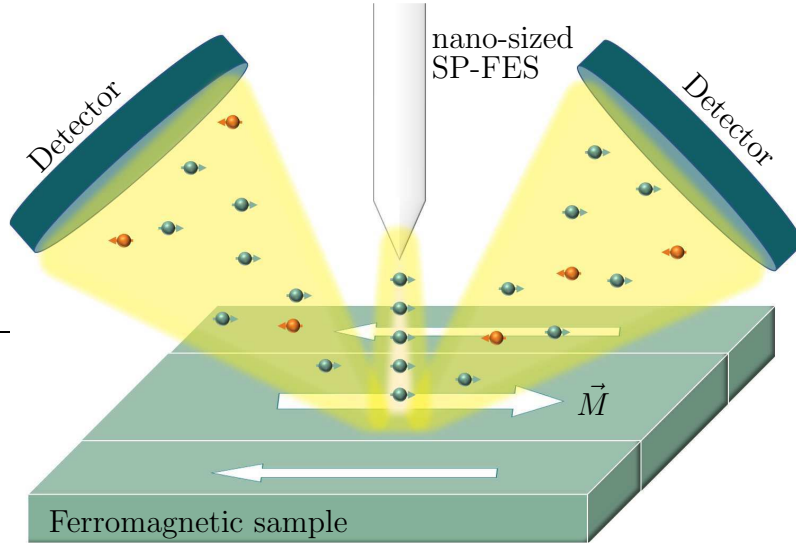


Figure 1.3: Schematic of the proposed nano-sized SP-FES, which could be used to analyse magnetic materials without the need for collimation optics.

1. The establishment of a computational model that simulates field emission properties from structures of arbitrary dimensionality, geometry, and material to resolve discrepancies between classical FE theory and experimental results. Unlike the FN theory, this novel atomistic-continuum model framework should incorporate first principles calculations into semi-classical finite element models to adopt a multidimensional simulation approach and develop a coherent treatment that models realistic emitter geometries. Using a first-principles approach, such as density functional theory (DFT), allows the description of certain behaviours with more accuracy than classical calculations.
2. The investigation of interactions between spin-polarised electron beams with ferromagnetic and non-magnetic samples. For this purpose, extensive studies of the energy- and spin-dependent reflectivity, energy losses and changes in secondary electron yield should be conducted employing spin-polarised low-energy electron microscopy (SPLEEM) measurement. These should give an overarching understanding of the underlying physics of spin-dependent scattering processes.
3. The design and fabrication of specialised equipment to characterise and test potential SP-FESs. For this, the maintenance, repair and modification of pre-existing vacuum equipment and a Mott polarimeter were required. Furthermore, a specialised sample holder for field emission experiments should be designed which enables the analysis of various FESs.

4. The initial investigation of a design concept and a fabrication process for potential SP-FESs. These nano-sized tips should be based on the combination of a well established, dependable electron emitter with a thin magnetic film acting as a spin-polarising layer. Special significance should be given to the investigation on how the FM's dimensions and crystallinity influence the emitter's magnetisation direction.

Combining the information of the experimentally analysed ferromagnetic thin films with the emitter design and the first-principles modelling described here will not only give an improved picture of an emitter's field emission properties but will also guide future experiments to improve the performance of SP-FESs.

Overview

The structure of this thesis is given in the following:

Chapter 2: This chapter reviews the relevant background concepts related to both the experimental as well as the computational work presented in this thesis. First, the classical field emission theory developed by Fowler and Nordheim is introduced, highlighting its shortcomings with regards to nano-meter sized emitters. Next, the DFT method, which is essential for the computational model developed in this work, will be briefly explained. Following this, the basics of ferromagnetism are introduced with special emphasis on the different contributions to the total magnetic energy. Lastly, the materials used in this work are briefly discussed.

Chapter 3: In this chapter, the methodology used during this thesis will be discussed which includes both the theoretical and experimental part. The theoretical part outlines the computational methodology for the multi-scale atomistic-continuum model developed here, which combines DFT with semi-classical boundary conditions. This procedure will be explained in detail using a (5,5) CNT model. The second part mainly relates to the experimental techniques, starting from a short description of the procedure for sample growth, then discussing conventional structural and chemical analysis techniques and finishing with a detailed description of the here-used magnetic characterisation methods and newly developed energy-selective secondary electron yield (ESSEY) technique.

Chapter 4: This part of the thesis aims to outline the capabilities and feasibility of the novel atomistic-continuum simulation method, which is based on

first-principles density functional theory in combination with semi-classical boundary conditions. This new method is then used to study previously unknown properties of emission sources, such as their behaviour in an externally applied electric field, the shape of the metallic surface as well as the potential barrier, their work function or the deformation of the atomic orbitals.

Chapter 5: This chapter investigates the energy- and spin-dependent interactions and scattering processes between a spin-polarised electron beam and magnetic materials. For this, three different systems of Fe/Ag (001), Fe/W (110), and Ag/Fe/W (110) are introduced and characterised using a SPLEEM. Furthermore, energy- and spin-dependent reflectivity scans, energy loss spectra for different primary beam energies, and energy-selective secondary electron yield measurements were conducted. To further aid the interpretation of the results, DFT simulations of the materials' electronic band structures were performed.

Chapter 6: This chapter is dedicated to the description of the ultra-high vacuum (UHV) chamber with attached Mott polarimeter and all steps taken to refurbish the system. Furthermore, a novel sample holder for field emission experiments inside the pre-existing system is introduced. The design and optimisation of the individual components are based on COMSOL simulations and will be presented in detail. This versatile sample holder allows to characterise FE properties from emitters of varying shape and material.

Chapter 7: This chapter describes the initial considerations for the fabrication of a novel spin-polarised field emission source. The proposed concept is based on the fusion of a well-established and dependable emitter material with a thin ferromagnetic film, which acts as a spin filter. Special emphasis is put on optimising the magnetic thin film's dimensions to assure properties such as an in-plane magnetisation, a single-domain structure, a small emission area and a uniform magnetisation direction. Thus, micromagnetic simulations on single- and polycrystalline Fe and Fe_3O_4 structures are presented in detail.

Chapter 8: The last chapter will give a brief summary of the obtained results and a final conclusion. In addition, suggestions on how to extend the present theoretical and experimental work are made.

2 | Theoretical Background

This chapter will review the major theories relevant to the experiments and simulations discussed in this dissertation. First, the basics of classical field emission theory are presented with special emphasis on the shortcomings of the traditionally-used Fowler-Nordheim theory for nano-sized emitters. This discussion will highlight the necessity for more elaborate and detailed simulation models like the one presented in Chapter 3. The theoretical basis of this simulation model will be introduced in the second section, which discusses DFT. The third section briefly reviews the origin of ferromagnetism and magnetism-related phenomena. In particular the magnetic anisotropy and the spin-splitting of the electronic band structure in magnetic materials are of importance as they build the foundation for the later shown experimental results and the design of the SP-FES presented here. The last section introduces the two materials which are significant to this work, namely carbon nanotubes and magnetic thin films. The former will be important for the FES simulations presented in Chapter 4, as their dimensions are a good representation of point-like emitters. The latter concerns not only the analysis of the spin-polarisation of secondary electron emission in Chapter 5 but also builds the basis of the proposed SP-FES design in Chapter 7.

2.1 Density functional theory

The density functional theory described in this section builds the basis for the atomistic-continuum model detailed in Chapter 3.1.

2.1.1 The many-body problem

A fully quantum mechanical treatment of a nanoscale system requires solving the many-body Schrödinger equation

$$\hat{H}\Psi = E\Psi, \quad (2.1)$$

where \hat{H} is the system's Hamiltonian, E is the energy eigenvalue and Ψ is the wave function. In quantum mechanics the many-body Hamiltonian fully describes the system's state and thus includes all relevant interactions. It can be expressed by

$$\hat{H} = \hat{E}_{\text{kin,e}} + \hat{E}_{\text{kin,n}} + \hat{V}_{\text{ee}} + \hat{V}_{\text{nn}} + \hat{V}_{\text{en}}, \quad (2.2)$$

with the terms being, respectively, the electronic and nuclear kinetic energy, the Coulomb repulsion between electrons and between nuclei, and the Coulomb attraction of electron and nuclei. The individual terms are defined as followed:

$$\hat{E}_{\text{kin,e}} = -\frac{\hbar^2}{2m_e} \sum_{i=1}^{N_e} \nabla_i^2,$$

$$\hat{E}_{\text{kin,n}} = -\frac{\hbar^2}{2} \sum_{I=1}^{N_n} \frac{\nabla_I^2}{M_I},$$

$$\hat{V}_{\text{ee}} = \frac{1}{2} \frac{e^2}{4\pi\epsilon_0} \sum_{i,j,i \neq j}^{N_e} \frac{1}{|r_i - r_j|},$$

$$\hat{V}_{\text{nn}} = \frac{1}{2} \frac{e^2}{4\pi\epsilon_0} \sum_{I,J,I \neq J}^{N_n} \frac{Z_I Z_J}{|R_I - R_J|},$$

$$\hat{V}_{\text{en}} = -\frac{e^2}{4\pi\epsilon_0} \sum_{i,I}^{N_e, N_n} \frac{Z_I}{|r_i - R_I|}.$$

Here, ϵ_0 is the vacuum permittivity^a, M_I is the rest mass of the nuclei, ∇^2 is the Laplacian of the wave function, and Ze is the charge of the nuclei (where Z is the atomic number)^b.

Even with today's advances in computer performance, solving Eq. (2.1) with the many-body Hamiltonian (Eq. (2.2)) is still a very challenging problem and only possible for very simple systems. Thus, one has to make some reasonable assumptions to simplify the problem. Since the rest mass of a proton is around 1800 times larger than the rest mass of an electron ($m_p \approx 1836m_e$) it is common to assume that compared to the time scale of nuclear motion, electrons will relax rapidly to their ground-state configuration. This means that electron and nuclear motion can be regarded as independent of each other and one can separate both wave functions. This concept is known as the Born-Oppenheimer approximation (BO) [72]

$$\Psi = \Psi_e \cdot \Psi_n . \quad (2.3)$$

With this separation one can now concentrate on solving the many-body Schrödinger equation for the electrons only. Furthermore, as the nuclei react very slowly to displacement they can be approximated as fixed in their positions, creating an external potential (V_{ext}) in which the electrons move. Thus, the Hamiltonian in Eq. (2.2) can be simplified to

$$\hat{H} = \hat{E}_{\text{kin,e}} + \hat{V}_{\text{ee}} + \hat{V}_{\text{ext}} . \quad (2.4)$$

However, even with all these simplifications, the problem remains vastly complex with realistic systems consisting of several thousands of electrons each with three degrees of freedom. With the full wave function $\Psi(r_1, \dots, r_N)$ being $3N$ -dimensional ($\mathcal{O}(N^3)$) the computational costs are just too high, which indicates that one needs a simpler approach.

2.1.2 Kohn-Sham concept

One such approach is the so-called density functional theory (DFT). This theory is based on the concept that one does not have to consider each electron in the system as an individual particle with three degrees of freedom which are all interacting with

^aVacuum permittivity: $\epsilon_0 = 8.854\,187 \times 10^{-12} \text{ F m}^{-1}$.

^bElectrons are denoted by lower case indices (i, j) and nuclei by upper case (I, J).

each other, but one can consider them as an electron density

$$n(r) = 2 \sum_{i=1}^{N_{\text{occ}}} |\Psi(r)|^2. \quad (2.5)$$

This way, the system has only three degrees of freedom no matter how many electrons the system has, making it much simpler to calculate. The theory is that $n(r)$ contains the same information as the wave function Ψ and that the ground-state can be calculated by just using the electron density instead of wave functions for each electron. Furthermore, it was proven that the electron density that minimises the total energy of the system is the exact ground-state electron density $n_0(r)$.

These two theorems were developed by Hohenberg and Kohn in 1964 as a fundamental concept [73] and the mathematical procedure was later developed by Kohn and Sham in which they further simplified the problem by assuming that $n_0(r)$ for a system of interacting electrons, is equal to $n_0(r)$ of non-interacting electrons in an external potential \hat{V}_{ext} [74]. Their total energy of a system can be expressed by

$$E^{\text{KS}}[n(r)] = \hat{E}_{\text{kin,e}}[n(r)] + \int \hat{V}_{\text{ext}}(r)n(r) dr + E_{\text{H}}[n(r)] + E_{\text{XC}}[n(r)], \quad (2.6)$$

where $E_{\text{H}}[n(r)]$ is the Hartree term

$$E_{\text{H}}[n(r)] = \frac{1}{2}e^2 \int d^3r \int d^3r' \frac{n(r)n(r')}{|r - r'|}, \quad (2.7)$$

which includes the electron-electron interactions and $E_{\text{XC}}[n(r)]$ is the exchange-correlation energy. After minimizing the above energy functional and variation of the ground-state energy, one can derive the Kohn-Sham (KS) equation for the ground-state of a system as

$$H^{\text{KS}}\Psi_i(r) = E\Psi_i(r), \quad (2.8)$$

with

$$H^{\text{KS}} = \frac{\hbar^2}{2m_e}\nabla^2 + \hat{V}_{\text{eff}}(r), \quad (2.9)$$

$$\hat{V}_{\text{eff}}(r) = \hat{V}_{\text{ext}}(r) + \hat{V}_{\text{H}}(r) + \hat{V}_{\text{XC}}(r). \quad (2.10)$$

Here, the \hat{V}_{H} is the Hartree potential and \hat{V}_{XC} is the exchange-correlation potential, which includes all unknown terms caused by exchange and correlation effects. The exact form of \hat{V}_{XC} is unknown and must be approximated. The two potentials are

defined as

$$\hat{V}_{\text{H}}[n(r)] = e^2 \int d^3r' \frac{n(r')}{|r - r'|}, \quad (2.11)$$

$$\hat{V}_{\text{XC}}(r) = \frac{\delta E_{\text{XC}}[n(r)]}{\delta n(r)}. \quad (2.12)$$

One of the most common approaches of this KS-DFT is the plane-wave method due to its good balance between precision and efficiency. However, the computational cost for most plane-wave methods scale with the third power of the number of KS orbitals ($\mathcal{O}(N^3)$) which still limits the size of the system to some hundred atoms [75]. Furthermore, even though plane waves can well describe periodic structures such as bulk crystals, they struggle with non-homogeneous systems and large devoid regions.

To overcome those obstacles, one can use the so-called linear scaling DFT (see Section 2.1.4), in which doubling the number of atoms results in a computation time twice as large and which is well suited to simulate large heterogeneous structures.

2.1.3 Exchange and correlation functionals

The exchange and correlation (XC) functional includes all non-classical electron-electron interactions which are not included in the Hartree potential and thus, as briefly mentioned in Section 2.1.2, its exact functional form is unknown. Therefore one has to rely on approximate expressions, which has led to the development of an entire hierarchy of XC functionals. The different approaches can be classified as:

- the local density approximation (LDA):

This is probably the simplest approximation which states that E_{XC} can be obtained by assuming that the correlation is only dependent on the local electron density $n(r)$ and that the exchange energy per unit volume, ϵ_{XC} , is that of a homogeneous electron gas: $E_{\text{XC}}^{\text{LDA}} = \int n(r)\epsilon_{\text{XC}}[n(r)] dr$.

- the generalized gradient approximation (GGA):

This functional is more accurate than the simple LDA as it was developed to incorporate the spatial variations in the density by including the gradient of $n(r)$: $E_{\text{XC}}^{\text{GGA}} = \int n(r)\epsilon_{\text{XC}}[n(r), \nabla n(r)] dr$. In contrast to the LDA, there is no unique form for the GGA, and thus many variations are possible of which the most common parametrisation was developed by Perdew and Zunger [76].

- the meta-GGA:

This is an extension of GGA, which in addition to the inhomogeneity of the electron density includes a dependency on the Laplacian of density $\nabla^2 n(r)$ [77].

- the hybrid functionals:

This approach uses a “semi-local” XC term in combination with the exact Hartree-Fock exchange [78].

The choice of E_{XC} will ultimately depend on the model system and the desired accuracy of the calculation.

2.1.4 ONETEP - $\mathcal{O}(N)$ Electronic Total Energy Package

The problem of many DFT approaches, like plane-wave DFT, lies in the concept of the extended KS orbitals Ψ_i which are delocalised and spread over the whole system. To obtain a linearly scaling calculation with respect to the size of the system, one has to use a more localised basis. One such concept is to use a single-particle density matrix

$$\rho(r, r') = \sum_i f_i \Psi_i(r) \Psi_i(r'), \quad (2.13)$$

with f_i being the occupation number of orbital i .

By using the density matrix, instead of the electron density, one can take advantage of the so-called near-sightedness principle [79, 80], which states that the properties of the density matrix at a point r depend only on points r' in a localised region around r . It has been demonstrated that the matrix elements of $\rho(r, r')$ decay exponentially with distance from the atom at finite temperatures [81–84] with

$$\rho(r, r') \rightarrow 0 \quad \text{as} \quad |r - r'| \rightarrow \infty.$$

This means that one can neglect the non-zero elements of the density matrix which are below a certain threshold (density-kernel-cut-off r_K). This way the matrix is simple enough (sparse matrix) to scale linearly with the system size. However, the density matrix is still very complex to work with, thus a set of so-called support functions is introduced, which can be thought of as a localised basis around atom i to represent the KS orbitals Ψ_i . In comparison to other $\mathcal{O}(N)$ codes, Order-N Electronic Total Energy Package (ONETEP) uses spatially localised non-orthogonal generalised Wannier functions (NGWFs) [85, 86]. Implementing the new support functions and a density kernel $K^{\alpha\beta}$ in the density matrix, one can write the density

matrix in separable form given by

$$\rho(r, r') = \sum_{\alpha} \sum_{\beta} \phi_{\alpha}(r) K^{\alpha\beta} \phi_{\beta}(r'). \quad (2.14)$$

As the name suggests, these NGWFs ($\phi_{\alpha,\beta}$) are non-orthogonal, and forced to be confined within a spherical region of a fixed radius r_{α} . This confinement is achieved by expanding the NGWFs in terms of other underlying primitive basis functions, which are periodic sinc functions in the case of ONETEP^c. Imposing these spatial cut-offs on both the NGWFs and $K^{\alpha\beta}$ results in a density-matrix $\rho(r, r')$ which scales linearly with the size of the system, where the accuracy and complexity of

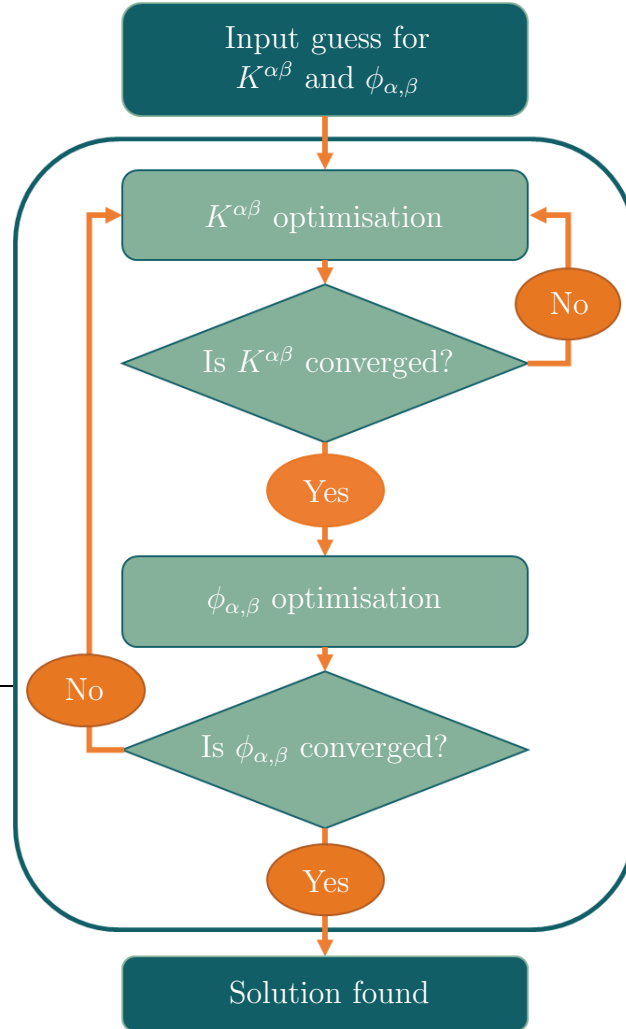


Figure 2.1: Flowchart of ONETEP’s self-consistent algorithm to calculate the ground-state of the system. After setting an initial guess, the density kernel $K^{\alpha\beta}$ and the NGWFs, $\phi_{\alpha,\beta}$, are optimised in tandem until overall convergence is reached.

^cMore information on the basis functions can be found in Ref. [85–87].

the simulation can be adjusted by controlling r_α and r_K . The optimisation of these two quantities is performed in tandem in a self-consistent manner^d, as illustrated in Figure 2.1.

This $\mathcal{O}(N)$ scaling code not only allows to simulate models with thousands of atoms but has the advantage of having highly localised basis functions, making it especially well suited for simulating non-periodic structures, such as large molecules, nanoparticles and CNTs. Thus, this DFT program was implemented in the multi-scale atomistic-continuum model in Chapter 3.1.

2.2 Fundamentals of micromagnetism

In the following, a short introduction to magnetism and its terminology is given. However, this section is not intended to be all-encompassing, thus for more detail, further reading is recommended [90–93].

In a simplified atomic orbital picture, magnetism is the result of the angular momentum of the electrons. Here one can distinguish between two contributions arising from the orbital motion of electrons (\vec{L}) and their fermionic nature which implies the existence of a half-integer spin (\vec{S}). Both angular momenta can be associated with a respective magnetic moment defined as

$$\vec{\mu}_L = -\mu_B \vec{L}, \quad (2.15)$$

$$\vec{\mu}_S = -2\mu_B \vec{S}, \quad (2.16)$$

with μ_B being the Bohr magneton. The atomic orbital magnetic moment, $\vec{\mu}_L$, and the atomic spin magnetic moment, $\vec{\mu}_S$, can be connected via spin-orbit coupling (SOC), which gives rise to the total magnetic moment, $\vec{\mu}_{\text{tot}}$, of an electron

$$\vec{\mu}_{\text{tot}} = \vec{\mu}_L + \vec{\mu}_S = -\mu_B(\vec{L} + 2\vec{S}). \quad (2.17)$$

In this model, only isolated atoms within an isotropic potential are considered, which following Hund’s rules have an unpaired electron. However, as most magnetic materials are in a solid state in which the atoms are located in an ordered atomic lattice, the situation gets more complex. The consequential overlap of the atom’s electron wave functions and subsequent Coulomb repulsion results in the so-called exchange interaction, which in turn leads to a long-range alignment of the magnetic moments in a material without the influence of an externally applied magnetic field.

^dInformation on the exact optimisation algorithm can be found in Ref. [75, 86, 88, 89].

As a magnetic solid consists of a large number of atoms, each with its own magnetic moment, one can define a macroscopic magnetisation \vec{M} as the sum of magnetic moments per unit volume.

Generally, there are three cases of collective magnetism: ferro-, ferri- or antiferromagnetism [92]. The first of which, in the form of itinerant ferromagnetism, is of particular interest for this work as the magnetic moment is carried by the strongly delocalised valence electrons near the Fermi level, making them well suited for the fabrication of SP-FESs.

According to Eq. (2.17), the measured magnetic moment in Fe, Co and Ni is expected to be an integer multiple of the Bohr magneton. However, measurements found μ_{tot} to be odd fractions of μ_B which cannot be explained by a successive orbital occupation as described by Hund’s rule. This discrepancy led to the development of the band theory for ferromagnetism which assumes that the bonding interaction between the $3d$ electrons causes a smearing of their energies into a band and that the exchange interaction forces a separation of the density of states for opposite spins (Stoner criterion).

Since both subbands are filled up to the Fermi level, this energy split leads to a population asymmetry between majority and minority spins and causes a finite spin polarisation of the d -band charge carriers near E_F , as can be seen in Figure 2.2. It is this effect of spin-dependent band splitting, which makes ferromagnetic materials suitable SP-FESs. The total magnetic moment is then given by the difference in the number of electrons, N , in the majority and minority bands, as defined by

$$m_{\text{tot}} = \mu_B(N^{\text{maj}} - N^{\text{min}}). \quad (2.18)$$

As can be seen in Figure 2.2 one can further distinguish between two cases depending on whether or not majority spins are present at E_F . If there are almost no majority spins, the magnetic moment is mainly due to the electrons in only one spin-band making them so-called “strong” ferromagnets (Figure 2.2 a). In contrast, materials with a substantial d -band contribution in both spin channels, such as Fe, are called “weak” ferromagnets (Figure 2.2 b). To utilise and tailor a material’s spin-polarising properties to work as an appropriate SP-FES, one has to consider the system’s total free energy, E_{tot} . This is important, as the magnetisation takes on an orientation that minimises E_{tot} , which itself can be expressed as the sum of four primary contributions

$$E_{\text{tot}} = E_{\text{ex}} + E_D + E_{\text{MCA}} + E_Z, \quad (2.19)$$

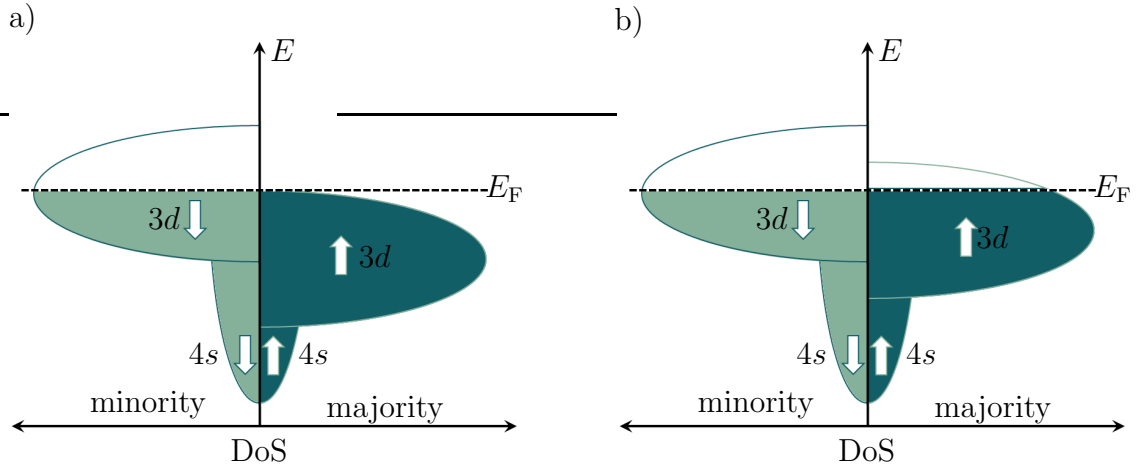


Figure 2.2: Schematic of the idealised band structure of the 4s and 3d bands for a) a strong and b) a weak itinerant ferromagnet, indicating the splitting of the 3d majority and minority spin-bands.

where E_{ex} is the exchange energy, E_{D} is the demagnetisation energy, E_{MCA} is the magneto-crystalline anisotropy energy, and E_{Z} is the Zeeman energy. Further energy terms can be added, if necessary, but they are irrelevant for further discussions in this thesis.

2.2.1 Exchange energy

As mentioned, the exchange interaction is the primary source of the macroscopically observed long-range magnetic order in ferromagnetic materials. It is a purely quantum mechanical effect as it is a direct consequence of the Coulomb interaction between electrons in conjunction with the Pauli exclusion principle, which results from overlapping atomic orbitals. Since these orbitals decay exponentially with distance, it itself is a short-ranged interaction [90]. The associated isotropic exchange energy, E_{ex} , between two neighbouring atoms, i and j , can be expressed as

$$E_{\text{ex}} = - \sum_{i \neq j} J_{ij} \vec{S}_i \cdot \vec{S}_j, \quad (2.20)$$

with \vec{S}_i and \vec{S}_j being the macrospins of the atoms and J_{ij} being the material-specific coupling constant, which results from the wave function overlap of the electrons [92]. The sign of J_{ij} determines the magnetic coupling between neighbouring spins. If $J_{ij} > 0$, the energy is minimised when the neighbouring spins are aligned parallel (ferromagnetic coupling), whereas $J_{ij} < 0$ describes an antiparallel alignment (antiferromagnetic coupling).

For macroscopic systems, a transition from discrete to continuous variables can be performed, replacing the summation by an integral. Hence, E_{ex} of a sample with volume, V , can be written as

$$E_{\text{ex}} = A_{\text{ex}} \int_V \left(\frac{\nabla \vec{M}}{M_s} \right) dV , \quad (2.21)$$

where the spin is replaced by the saturation magnetisation, M_s , which represents the average density of magnetic moments, and A_{ex} is the exchange stiffness constant between the spins [92]. Eq. (2.21) is particularly useful when computing the exchange energy in micromagnetic simulations (see Section 7.2).

2.2.2 Demagnetisation energy

If the size of the magnetic sample increases, the exchange interaction starts competing with an opposing effect: the dipolar interaction. This contribution of the system's free energy, also called demagnetising energy or stray field energy, represents the magnetic field generated by the magnetic body itself and it results from the discontinuous magnetisation distribution at the boundary of a finite structure at which $\nabla \vec{M} \neq 0$. These uncompensated surface dipoles lead to the creation of a stray field outside the sample which in turn creates a demagnetising field, H_D , inside the sample. This field is defined as

$$\vec{H}_D = -\overleftrightarrow{N} \cdot \vec{M}_s , \quad (2.22)$$

where \overleftrightarrow{N} is a demagnetising tensor. The associated demagnetising energy is given by

$$E_D = -\frac{\mu_0}{2} \int_V \vec{M} \cdot \vec{H}_D dV . \quad (2.23)$$

This energy is long-range in nature and is heavily influenced by the boundary conditions of the structure and thus is sometimes referred to as shape anisotropy energy for nano-scaled materials.

The analytical determination of E_D is generally only possible for some limited cases such as the homogeneously magnetised ellipsoid. However, one can estimate a thin film by an ellipsoid, where the half-axes x, y, z of the ellipsoid fulfil $x = y \mapsto \infty$

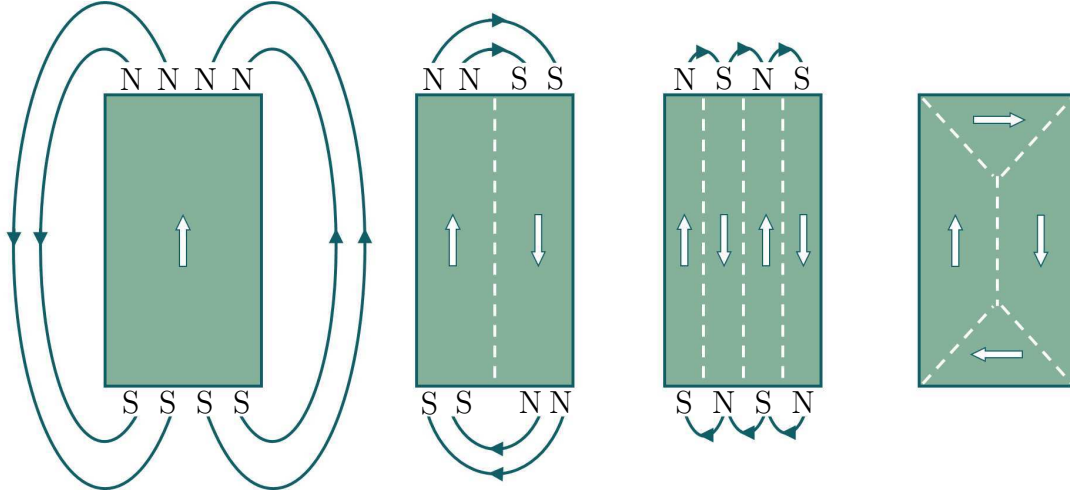


Figure 2.3: Changes in domain patterns in a ferromagnetic single-crystal, which result in a reduced demagnetisation energy from left to right.

and $z \ll x, y$. With this the demagnetising tensor becomes

$$\overleftarrow{N} = \begin{bmatrix} 0 & 0 & 0 \\ 0 & 0 & 0 \\ 0 & 0 & 1 \end{bmatrix}. \quad (2.24)$$

Thus, the demagnetising energy for a thin film is given by

$$E_D = \frac{\mu_0}{2} V \vec{M}_S^2 \cos^2 \theta, \quad (2.25)$$

where θ represents the angle between the film normal and the magnetisation \vec{M} . The difference of the demagnetising energies between these hard and easy axis directions of the magnetisation is given by the shape anisotropy $K_D = -(\mu_0/2)M_S^2$.

E_D increases with sample size and has its maximum value when a material is homogeneously magnetised (maximal stray field) when all spins are aligned parallel. Thus, unlike the exchange interaction, the demagnetising energy favours an antiparallel alignment of the magnetic moments. Hence, if this energy exceeds the exchange energy, the material will start to form multiple smaller domains to minimise the total stray field energy of the bulk material, as depicted in Figure 2.3.

Generally, the shape anisotropy lies along the elongated axis of the sample. This means that \vec{M} in a cubic element, as seen in Figure 2.4 a, points along the vertical direction, in a thin film it is generally found to lie in the plane of the film, while a nano-wire is magnetised along its long axis to avoid surface magnetic charge accumulation.

2.2.3 Magnetic anisotropy energy

In a system of spins such as the one described by Eq. (2.20), the magnetisation is considered to be isotropic. However, in real magnetic objects, the magnetisation tends to be aligned along a particular direction. This directional energy dependence of the magnetisation in the absence of an external magnetic field is called magnetic anisotropy. Here, the directions with the lowest energy are called “easy axes” and are the preferred directions for the spontaneous alignment of the magnetic moment, while the high energy directions are called “hard axes”. These preferred directions can, for example, be influenced by the sample’s shape, as discussed in the previous section, resulting in the shape anisotropy. Other contributions to the anisotropy are based on the crystalline axes of the material and the SOC, such as the magneto-crystalline volume and surface anisotropy, which will be discussed here in more detail. Other causes for magnetic anisotropy, such as lattice strain, interfaces or interdiffusion, will not be covered in the scope of this work.

Magneto-crystalline anisotropy

The magnetocrystalline anisotropy (MCA) arises from the coupling between \vec{S} and \vec{L} , typically referred to as SOC, in a crystal lattice [92]. Due to this SOC, different crystal structures have distinct preferential magnetisation directions depending on the crystal’s symmetry. Iron, for example, has a body-centred cubic (bcc) structure with the $\langle 100 \rangle$ directions being the three easy axes, while the $\langle 111 \rangle$ directions represent the hard axes [92].

For a cubic crystal, such as iron thin films used in this work, the anisotropy can be written as

$$E_{\text{MCA,V}} = K_{\text{C1}}(\alpha_x^2\alpha_y^2 + \alpha_y^2\alpha_z^2 + \alpha_z^2\alpha_x^2) + K_{\text{C2}}\alpha_x^2\alpha_y^2\alpha_z^2 + \dots, \quad (2.26)$$

where $\alpha_{x,y,z}^2$ are the direction cosines of the angle with respect to the cubic axes and K_{C1} and K_{C2} are the first- and second-order anisotropy coefficients [94]. These coefficients are often not reported separately, but as a sum $K_{\text{MCA,V}} = K_{\text{C1}} + K_{\text{C2}}$. Usually, higher-order terms can be neglected for most materials [92], though they can be extracted in specific cases such as for Fe/GaN (0001) [95]. A positive sign for K_{C} yields easy axes along the $\langle 100 \rangle$ directions, while a negative K_{C} has easy axes along $\langle 111 \rangle$ [93]. A representation of the energy surface of the cubic anisotropy energy with $K_{\text{C1}} > 0$ is shown in Figure 2.4 b.

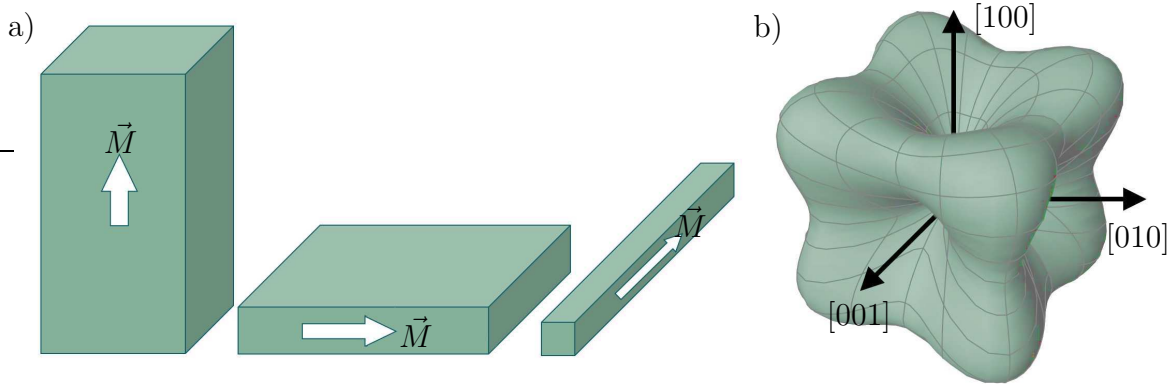


Figure 2.4: a) Shape anisotropy effects on the magnetisation direction for a cubic element, a thin film and an elongated needle. The magnetisation direction changes in the process as a result of minimising shape anisotropy energy and demagnetisation field. b) Angular dependence of the energy surface for cubic MCA with $K_{C1} > 0$.

Surface anisotropy

Surfaces and interfaces represent a strong break in the translational symmetry of the crystal lattice of a material. These boundaries can result in the localisation and band narrowing of the atomic orbitals at the surface atoms, which in turn leads to an increased density of states (DoS) at the Fermi level and an enhanced spin imbalance between majority and minority electron bands [94]. This effect, called surface anisotropy, results in uniaxial surface terms as a correction to the fourfold volume MCA anisotropy in Eq. (2.26), given as

$$E_{\text{MCA,S}} = K_{C1} \sin^2 \theta + K_{C2} \sin^4 \theta. \quad (2.27)$$

Comparing Eq. (2.25) with Eq. (2.27) shows, that the shape anisotropy (demagnetisation energy) and the surface anisotropy are competing effects, as the former favours in-plane magnetisation while the latter favours perpendicular magnetisation since they are proportional to $\cos^2 \theta$ and $\sin^2 \theta$, respectively. Thus, it can be seen, that at small thicknesses, the bulk contribution can be overwhelmed by the surface term so that in-plane magnetisation becomes energetically favourable.

Effective magnetic anisotropy

As can be seen, there are several contributions to the magnetic anisotropy of a material, which arise from its volume, surface and shape. These anisotropies can be summarised into an effective magnetic anisotropy K_{eff} . In thin films, the following

expression is obtained

$$K_{\text{eff}} = K_{\text{MCA,V}} - K_{\text{D}} + \frac{2K_{\text{MCA,S}}}{L}. \quad (2.28)$$

2.3 Materials

This section introduces the two materials used in this dissertation. First, carbon nanotubes will be discussed as they form the model-system for the first-principles simulations of nano-sized emitters presented later. Second, magnetic thin films will be shortly introduced as they were used for the SPLEEM measurements and also form the base for the proposed SP-FES design in Chapter 7.

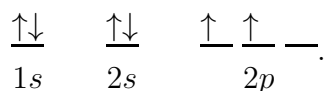
2.3.1 Carbon nanotubes

Carbon, in the form of diamond, graphite, amorphous-carbon and CNTs, has been investigated both theoretically and experimentally with regard to its FE properties, with all allotropes demonstrating desirable characteristics such as high current densities and low turn-on voltages [96]. In particular, CNTs with their unique quasi-one-dimensional structure have the advantage of very high aspect ratios of up to several million to one [37], which is unparalleled in nature. This feature, combined with their excellent electrical, mechanical and thermal properties [97–103] makes them ideal candidates for point-like field emission sources. To understand carbon’s exceptional properties, one first has to discuss its electronic structure and chemical bonds.

The Carbon-Carbon bond

Carbon is the fourth most abundant element in the universe and might be the most versatile with at least five known allotropes: graphene, diamond, graphite, CNTs and fullerenes. Interestingly, while all these materials are made of the same chemical element, each allotrope shows very different physical properties depending on its atomic structure. For example, while diamond is the hardest material on earth and transparent, graphite is soft and black in colour.

Carbon has the atomic number 6, and its ground-state electron configuration is $[\text{He}]2s^2 2p^2$ which can, following Hund’s rules, be written as:



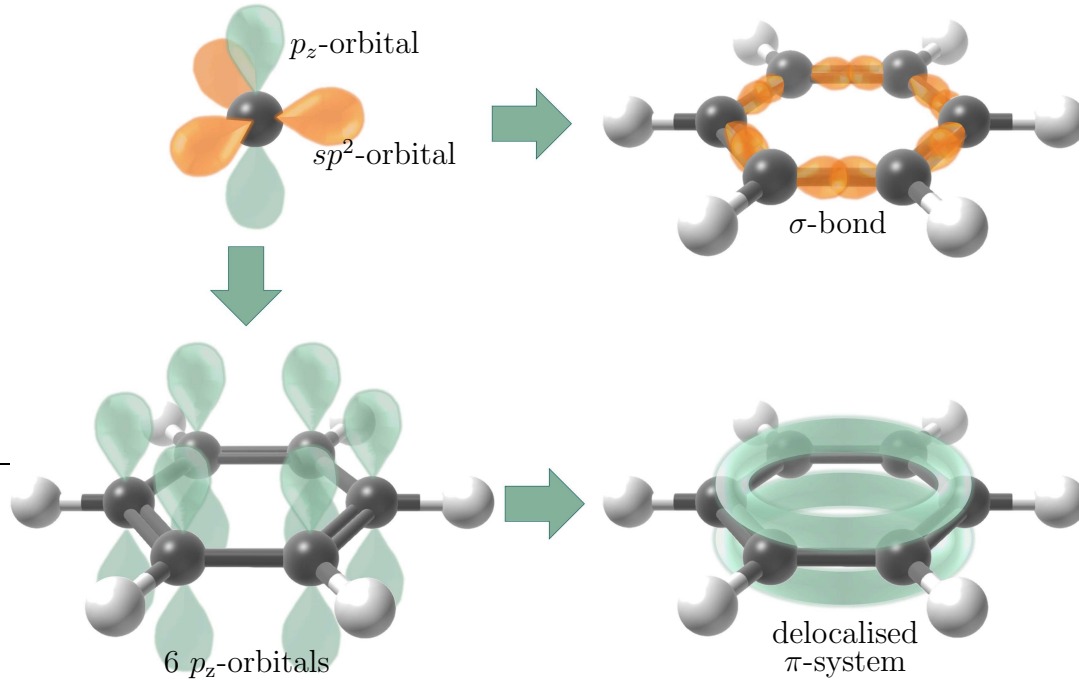
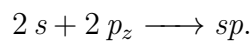
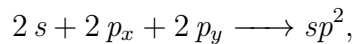
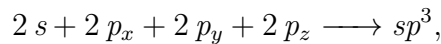


Figure 2.5: Visualisation of the sp^2 -hybridisation and the consequent π (blue) and σ (orange) orbitals for a benzene molecule.

Here, the two $1s$ electrons are called core electrons while the ones in the $2s$ and $2p$ orbitals are considered to be the 4 valence electrons. These atomic orbitals can overlap with the orbitals from neighbouring atoms forming covalent bonds, which usually result in three types of hybridisation:



It is due to this versatility that carbon-based allotropes have such a wide range of distinct properties. The sp^3 hybridisation, for example, is responsible for the formation of diamond, where the $2s$ and all three $2p$ orbitals form a set of four single bonds with neighbouring atoms, making the material exceptionally durable, which is a desirable property for a potential FES. However, FE experiments comparing the emission efficiency from diamond to CNTs showed that the latter is capable of achieving much higher emission current densities [104]. Thus, the simulations presented in Chapter 4 are mainly done for CNTs, which have a sp^2 hybridisation.

A visual representation of the sp^2 and $2p_z$ orbitals together with their hybridisations is shown in Figure 2.5. Here, the $2s$ orbital and two $2p$ orbitals form covalent

bonds with three adjacent atoms. These so-called σ -bonds are highly localised, resulting in a 2D structure with all atoms lying in-plane with an angle of 120° to each other (“honeycomb-structure”). This σ -bond is further responsible for the high mechanical in-plane strength of individual carbon layers, but it does not contribute to the material’s conductivity.

The high electrical conductivity is caused by the remaining fourth valence electron in the last $2p$ orbital. This orbital is oriented perpendicular to the plane and forms a delocalised electron cloud (π -bond) with the remaining $2p_z$ orbitals from the other C-atoms. Overlapping of such un-hybridised π -systems from different graphene layers with each other binds the layers via weak van der Waals forces and forms the basis for the formation of graphite.

General geometry

Generally, there are many different types of nanotubes to choose from when constructing an atomistic simulation model: multi-, double- and single-walled, open-ended, capped *etc.* The right choice of model will depend on which properties are investigated.

One of the simplest versions to model infinitely-long nanotubes is the single-walled open-ended CNT. This configuration is just a hollow cylinder rolled from of

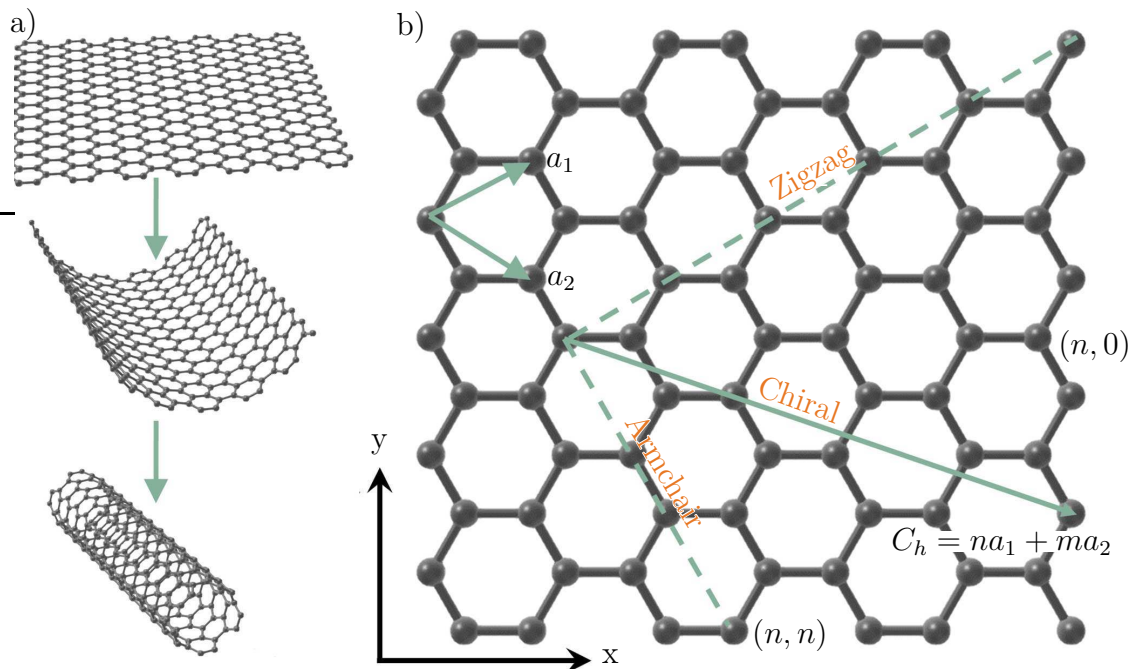


Figure 2.6: a) Schematic of the creation of a single-wall CNT by rolling a graphene sheet into a tube. b) Graphene sheet with the primitive lattice vectors a_1 and a_2 , the chiral indices (m, n) and the translational vector C_h .

a single sheet of graphene (Figure 2.6 a). This one-atomic-layer-thick tube has covalently bonded carbon atoms in a hexagonal grid (Figure 2.6 b) and can be described by using the primitive lattice vectors a_1 and a_2

$$a_1 = \left(\frac{3}{2}a_C, \frac{\sqrt{3}}{2}a_C \right), \quad a_2 = \left(\frac{3}{2}a_C, \frac{-\sqrt{3}}{2}a_C \right), \quad (2.29)$$

with $a_C = 1.42 \text{ \AA}$ being the length of the C-C bond [105]. Depending on how the graphene sheet is cut and rolled will further determine the CNT's chirality, which has a profound effect on its physical properties. One can define the chiral vector C_h in terms of the primitive lattice vectors as

$$C_h = na_1 + ma_2. \quad (2.30)$$

This equation shows that the chirality of the nanotube can be specified by two chiral indices, n and m . Here one can distinguish between three different types of nanotubes:

- if $m = 0$: Zigzag - metallic or semiconducting
- if $m = n$: Armchair - metallic
- if $0 < m, n$: Chiral - metallic or semiconducting

While armchair configurations are exclusively metallic, zigzag and chiral can be metallic or semiconducting with band gaps ranging from 0 eV to 1.5 eV [106, 107]. Since n and m can have any positive integer value, there is an infinite number of unique CNTs which all have slightly different physical properties.

Finite CNT model for first-principles simulations

To simulate a field emitter, the previously discussed open-ended CNTs are unusable as such infinite tubes lack a region from which the electrons will be emitted. Thus, to investigate a structure's FE properties, one has to use a finite, non-periodic structure. In such a model, one can distinguish between a "tip", a "tube" and an "end" region, which are defined by the direction of the applied electric field, as seen in Figure 2.7 a.

The CNT's tip region can be either "open" or "closed" as seen in Figure 2.7 a and b, respectively. In the case of a closed CNT the cap's precise geometry depends on the tube's diameter and chirality but is often modelled by half fullerenes. The simplest model, which is used in this dissertation, is the (5,5) CNT which has half of

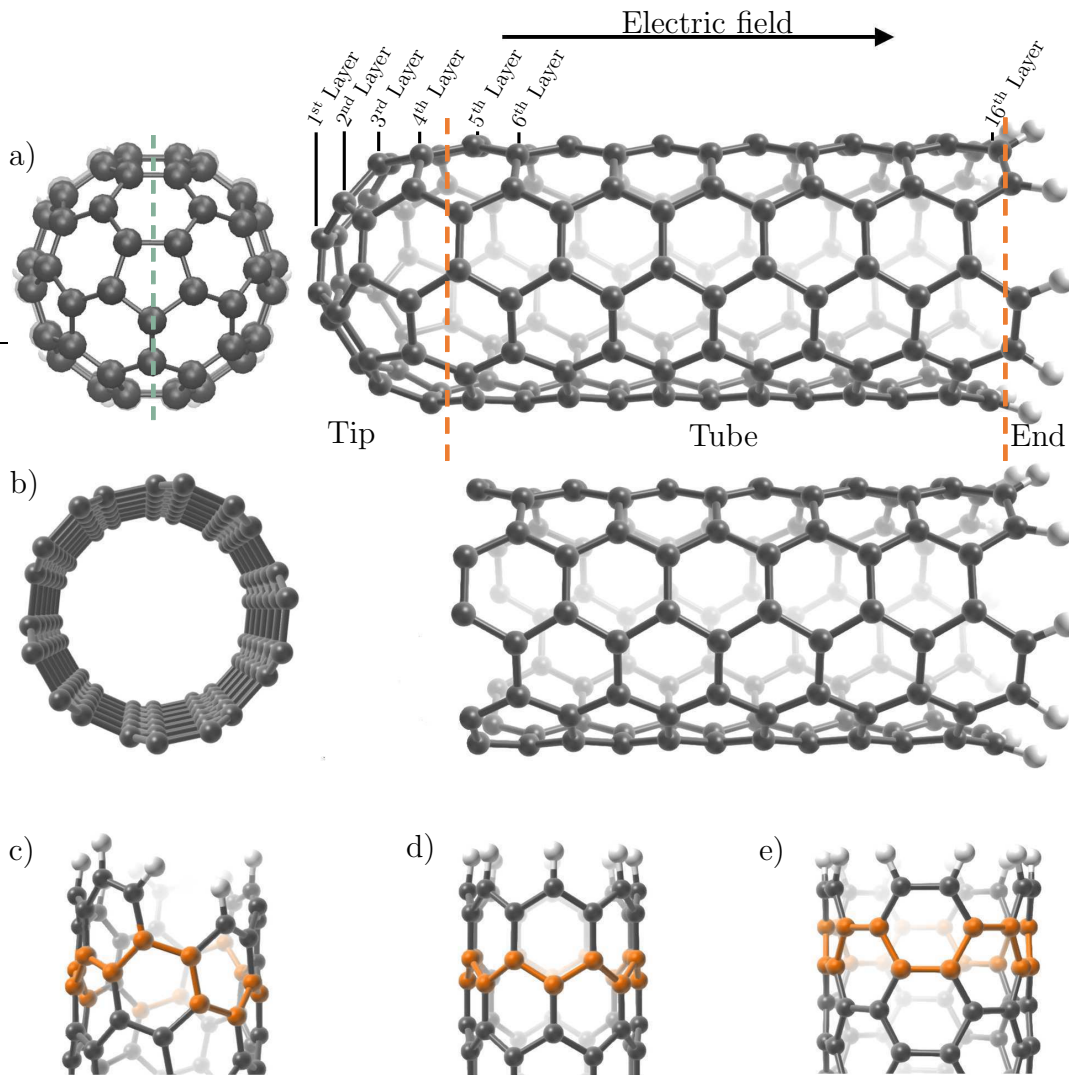


Figure 2.7: Visualisation of a) a closed (5,5) CNT and b) an open (5,5) CNT seen from the top and the side; Examples of CNT fragments and edges for different chiral indices n, m such as c) a (7,2) chiral edge, d) a (8,0) zigzag edge and e) a (5, 5) armchair edge. All fragments have simple H-terminated edges and the orange shaded carbon atoms highlight their chirality. All structures were visualised using the software Samson-connect [108].

a C60 fullerene as a cap. This type of CNT has the advantage of having a hemisphere at the tip and thus being the ideal system to compare to classical calculation using the “hemisphere-on-cylindrical-post” model. Moreover, this CNT’s tip is rotationally symmetric ending with a pentagon at the apex which simplifies the analysis of certain material properties, such as charge distributions at the tip.

The open CNT can also exhibit different edge form configurations depending on its chirality. While both armchair and zigzag CNTs have a consistent edge geometry independent of n or m , chiral CNTs will have varying edges depending on their chiral indices. Examples of such edge forms are shown in Figure 2.7 c-e.

To simulate a chemically and electrically neutral CNT it is important to terminate its edge atoms at the “end” to passivate the dangling bonds of the carbon atoms. Generally, there are different ways to terminate those atoms, with the most common ones being: single-hydrogen (H-termination), double-hydrogen (2H-termination) or hydroxyl groups (OH-termination). Depending on the simulation one has to decide which termination is the most suitable as it will affect the chemical and mechanical properties of these edge carbon atoms. Some examples for single-hydrogen terminated CNTs are shown in Figure 2.7 a - e.

The precise (5,5) CNT model used in the following chapters is shown in Figure 2.7 a. This model consists of 150 C atoms arranged in 16 layers of which 4 are classified as “tip-layers” and 12 as “tube-layers”. The individual layers will be counted starting with the tip layer as the first layer, going along the CNT axis with increasing integer number. The size of 16 layers was chosen as this length was sufficiently large to avoid influences of the hydrogen terminated end on the tip region of the CNT, while keeping the number of atoms in the model very low to increase simulation speed. In this model a simple H-termination of 10 H atoms at the bottom was used. The tip region consists of half a Buckminsterfullerene, which ends with a pentagon on its axis. If not otherwise stated, most cut-planes are taken along the CNT axis going through at least one of the atoms in the top layer pentagon (green line in Figure 2.7 a).

2.3.2 Magnetic thin films and nanostructures

A “thin film” is usually defined as a structure with one of its dimensions truncated compared to the other two dimensions. This constrained length scale, or thickness L , is typically of the order of nanometres, whereas the other two dimensions are of the order of millimetres or centimetres [109]. As a consequence of this reduction in dimensionality thin films can exhibit dramatic alteration of their properties compared to bulk materials, such as thickness-dependent para-ferromagnetic phase transitions, increased saturation magnetisations or altered Curie temperatures [94, 110, 111].

For the experiments presented in this work, special emphasis was placed on the investigation of how the sample’s dimensionality influences its magnetisation direction and domain structure. This was important, as the sample has to fulfil certain criteria to be a viable SP-FES. Amongst others, the FM thin films must have a stable in-plane magnetisation to create SP electrons that are detectable with the Mott polarimeter (see Section 3.3.5 for more information) and to be in a single-domain state to maximise the polarisation of the emitted secondary electrons.

In a large thin film, the shape anisotropy usually dominates and forces the mag-

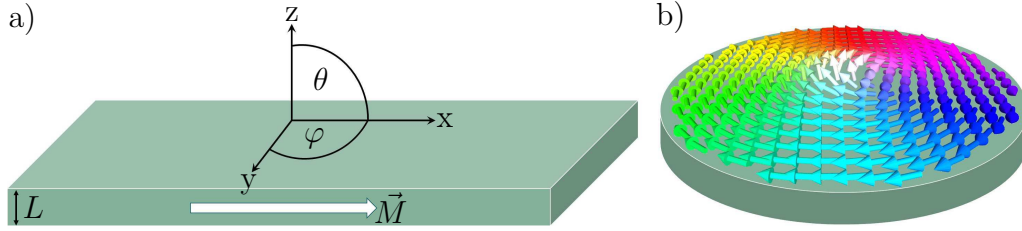


Figure 2.8: a) Magnetic thin film with in-plane magnetisation. The image shows the definition of the here-used coordinate system with θ being the polar angle and φ being the azimuthal angle. b) Representation of a magnetic vortex state in a circular magnetic disc. The spins are represented as arrows.

netisation to lie predominantly in-plane to minimise its demagnetisation energy, as seen in Figure 2.8 a. These films usually tend to form multi-domain states. However, during the later discussed fabrication process of the FES (Chapter 7) the thin film will be milled down to have a cylindrical or disk-like shape. In this case, not only the thickness but also the lateral dimensions are decreased to only a few nanometres. When decreasing all dimensions, the strength of the exchange energy (~ 0.1 eV/atom) becomes much larger than those of the magnetostatic energy (~ 0.1 meV/atom) and the magnetocrystalline anisotropy (~ 10 μ eV/atom) [94]. Thus, beyond a critical material-dependent size limit, the energy associated with the creation of Bloch domain walls is prohibitively high, meaning that despite the presence of edge charges all spins are pointing in one direction. This behaviour of uniform magnetisation is called a “single-domain state”.

One special case of the single-domain state, which can happen for disk-like structures such as the FES in Chapter 7, is the flux closure or vortex state. This configuration is characterised by a curling magnetisation, where the magnetic moments arrange themselves along the edge of the structure to reduce the magnetic stray field energy, as can be seen in Figure 2.8 b. Due to the high exchange interaction at the centre of the curl, the so-called vortex core, the magnetic moments there are perpendicular to the disk surface and pointing either upward or downward [110,112]. Such a state is unsuitable for the SP-FES as the emitted electrons would have a net in-plane polarisation of zero.

Another issue to consider for the fabrication of nano-sized field emitters is, that when the dimensions of the single-domain structure are even further reduced beyond a critical threshold size, they are no longer magnetically stable as thermal energy can easily overcome the energy barrier to induce domain switching. These structures are then superparamagnetic, rendering them unusable as SP-FESs [110].

The general behaviour of magnetic structures with decreasing dimensions is schematically depicted in Figure 2.9. This plot shows that larger structures form

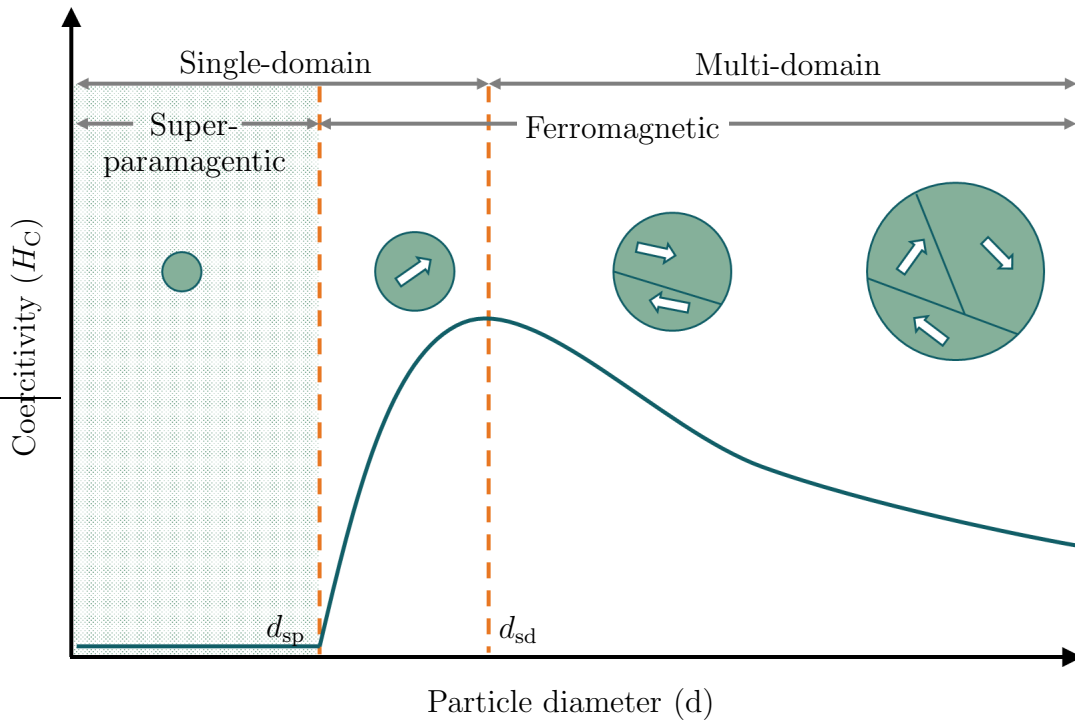


Figure 2.9: Size-dependent change in coercivity for magnetic particles showing the regions in which single-domain states and multi-domain states are formed.

complex multi-domain structures, which leads to a reduction in the magnetic remanence per unit volume compared to single-domain structures. The maximum value is reached at the conversion point from the multi- to the single-domain state. After this critical diameter, d_{sd} , all magnetic spins are pointing in the same direction and are stable against spontaneous domain switching. The transformation from ferromagnetic to superparamagnetic properties is reached at a diameter d_{sp} , after which the coercivity becomes zero [113]. For the later discussed SP-FES a thermally stable single-domain state is preferred, as it would result in the highest value of spin-polarised electron emission.

3 | Computational and experimental methods

This chapter discusses the computational and experimental methods used in this thesis. First, a brief introduction to multi-scale atomistic-continuum models will be presented, followed by a more detailed discussion of the initial computational setup and procedure for the multi-scale modelling of carbon nanotubes, which was developed in the course of this work. The second part concerns the experimental methods and provides a brief introduction on the sample growth as well as common structural and chemical analysis techniques. Furthermore, special focus is placed on the magnetic characterisation methods. In particular, the primarily used technique of spin-polarised low-energy electron microscopy is discussed in more detail, while Mott polarimetry, even though important to understand for the objective of the thesis, will only be introduced in a very rudimentary manner as the technique was not used to its full potential in the course of this work.

3.1 Computational multi-scale method

As the computational multi-scale atomistic-continuum model developed here can be applied to any type of material and geometry, the first section will give a general introduction on how to run a simulation. The second section will then give a more specific and detailed discussion of the individual steps and considerations for a CNT-based field emission source.

3.1.1 Multi-scale atomistic-continuum model

Multi-scale modelling is a technique that combines the application of modelling methods at two or more different length scales. These methods usually differ in their theoretical approach to a property calculation due to the change in scale. Generally, there are a few different simulation concepts to choose from, depending on the desired simulation scale. Figure 3.1 shows a commonly used schematic, displaying the hierarchy of different modelling techniques with regards to the spatial scale. Furthermore, one can make a distinction between two approaches, in which (a) the models are run separately and are later combined due to some sort of parametric coupling and (b) in which models are run at the same time over different spatial regions of a simulation. The concept presented here falls under category (a) and

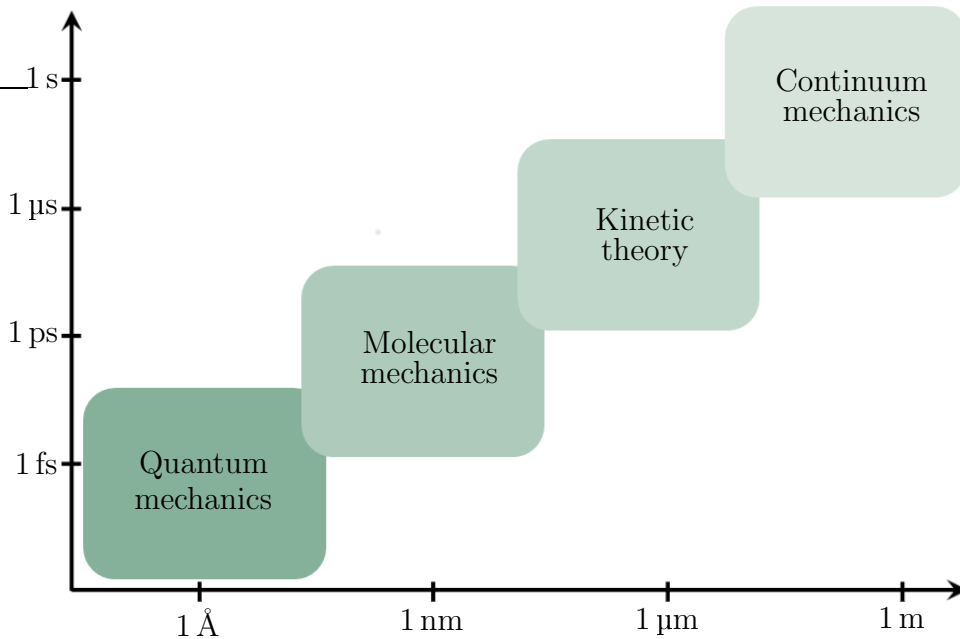


Figure 3.1: Hierarchy of multi-scale modelling techniques, showing the approximate range of temporal and spatial scales.

consists of two models: (1) a macro-model in which the medium is represented as a homogeneous continuum and (2) a nano-model in which the material’s atomistic structure is incorporated and analysed. The process can be divided into four steps:

1. A DFT simulation, without an applied field, is run to optimise the structure and to get the mesh over the boundary of the simulation cell.
2. A continuum model is designed using the previously found optimised emitter geometry and subsequently analysed to find the field distribution, the induced charge and the boundary condition for a confined volume.
3. The mesh of the DFT and the continuum model are matched to acquire the boundary conditions.
4. A second DFT simulation is carried out using the previously found induced electron charge and boundary conditions as initial conditions.

More specifically, the previously described ONETEP code (Chapter 2.1.4) is employed to optimise the geometry of a modelled field emitter tip on a nanoscale in the absence of an applied field. This gives the correct dimensions, such as radius and curvature of the structure, which will later be used to design the macroscopic model. For this, a limited volume (hereafter called “DFT box”) is defined, which contains a molecule, representing the emitter’s tip region (Figure 3.2 a). Afterwards, an initial simulation of the structure’s properties is run, which gives information on the generated mesh along the boundaries of the DFT box. For these simulations, Dirichlet boundary conditions (BC) are imposed on the DFT box to guarantee that the potential falls to zero at a certain distance from the molecule.

In a second step, a finite element method (FEM) was chosen as the numerical continuum mechanics-based approach to simulate the macro-model. More specifically, the software FlexPDETM (FlexPDE 7.02, PDE Solutions Inc., WA, [114]) was used, to model the different emitter shapes. Here, the classical emission system consisted of a planar capacitor model, meaning that it contains two parallel plates (cathode and anode) separated by a certain distance, with the emitting nano-structure approximated as a conducting rod standing perpendicular between the plates and in contact with the cathode plate (Figure 3.2 b). This rod’s apex is modelled to have the precise dimensions, found by the initial DFT geometry optimisation. To match the macro- and nano-model, a sub-region including the emitter’s tip region has to be defined, with the same dimension as the previously mentioned DFT box. Figure 3.2 c shows a general schematic of the model and how the macro- and nano-model need

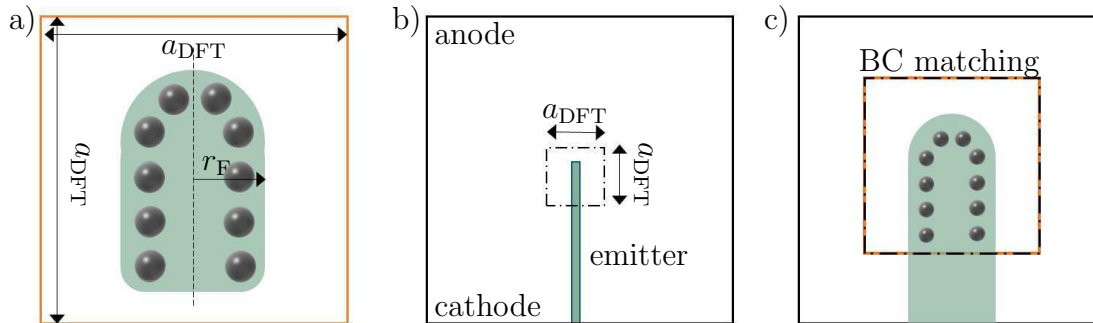


Figure 3.2: a) The DFT box containing the emission model on an atomic scale, which defines the metallic radius, r_{F} , for the classical model. b) The macroscopic model of the emitter, used to find the induced charges and the BC. c) The final simulation employs BC matching and combines the micro and macro-model

to overlap to match. Subsequently, the electrostatic potential between the capacitor plates and near the surface of the emitter was found by solving Poisson's equation

$$\nabla^2 V = \frac{-n(r)}{\epsilon}, \quad (3.1)$$

with $n(r)$ being the charge density and ϵ being the permittivity.

Further, one has to consider that by applying an external electric field additional charges are induced into the emitter, which accumulate at the apex. Thus, to incorporate this effect into the following DFT simulations as an initial condition, one has to calculate the induced charge inside the classical DFT box by using Gauss' theorem, *i.e.* one has to integrate the classical normal electric field over the surface of the box. Generally, one can adjust the value of the induced charge via the anode-cathode voltage.

A recent modification of the ONETEP code, done by Dr. E. B. Linscott, now permits the total number of excess electrons in the DFT box to be non-integral. This means that one is not constrained to studying external fields that induce precisely an integral additional charge in the DFT subsystem, making the simulations more flexible.

To solve any type of partial-differential equation, FlexPDE uses Galerkin finite element method to construct a triangular or tetrahedral mesh to discretise a two- or three-dimensional region, respectively. To achieve the required accuracy inside the DFT box, an adaptive mesh refinement procedure is used. Thus, in the third step, FlexPDE will report electrostatic potential field values for every mesh point on the surface of the classical DFT box. These values are then interpolated and matched to the cubic grid points of the ONETEP mesh and given as an initial condition to simulate the emission tip with applied field on an atomic-scale. Here

it is important to note, that, in contrast to the classical model of the emitter, the molecule representing the tip within the box is not connected to any electrode. Thus, to simulate the connection between the macroscopic emitter and the molecule, the potential of the area of intersection between the conducting rod and the DFT box was held at 0 V, while the other boundaries had Neumann BC. As can be seen in Figure 3.2 c, the cross-section of the rod used in the FlexPDE simulations is larger than the CNT molecule to match its “metallic radius^a”, r_F (Figure 3.2 a). This approximation will give the correct potential around the circumference of the rod at the radius of the Fermi level and over the rest of the DFT box (see Section 3.2.1).

Lastly, the ONETEP code is used again to simulate the emitter including the induced charges and the boundary potential given by the classical macroscopic model. The latter is a novel feature, which was initially implemented by Dr. G. Constantinescu and later refined by Dr. E. B. Linscott in the course of this dissertation. The result is a flexible multi-scale model in which one can perform calculations for any external field strength below the threshold for field emission in a reasonable time frame. The simulations can give many details about the field emitter, such as the changes in orbitals and barrier profile with different applied fields, the redistribution of the electron charge around the tip or it can shed light on the role of the exchange and correlation energy in producing the work function.

3.2 (5,5) CNT model and computational setup

This section presents a detailed description of the atomistic-continuum model simulations for a (5,5) CNT.

3.2.1 (5,5) CNT geometry

Before performing any type of DFT calculation one has to define the desired model and find the most suitable calculation parameters, such as model geometry, the kinetic cut-off energy and the optimal size of the NGWF radii in ONETEP. Thus, in the first step, the free academic version of the software package Virtual NanoLab 2016.3 [115] from QuantumATK [116] was used for the initial design of the carbon nanotubes. This software has the advantage of offering a “quick optimiser” to optimise the initial geometry of the molecule using a Brenner potential [117] to reduce the forces between the atoms to less than $0.05 \text{ eV}/\text{\AA}$. This initial optimisation only takes a few minutes and will reduce the computational time and cost for the

^aMore explanations in Section 3.2.1 and Section 4.1.1.

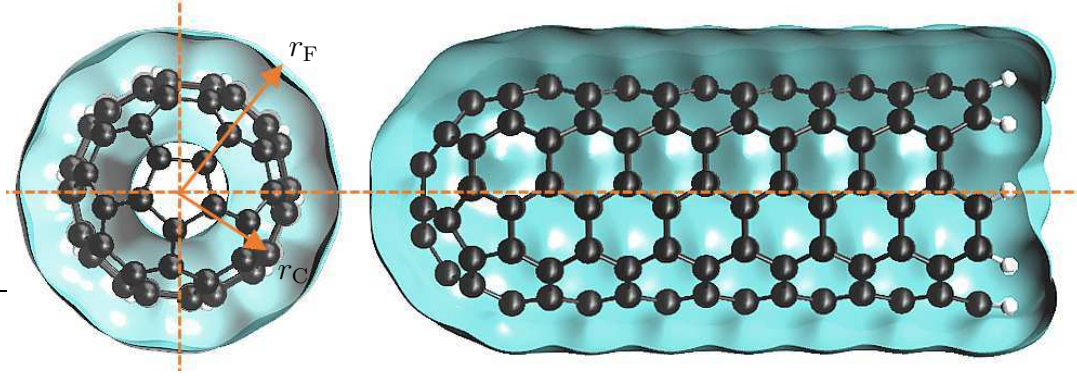


Figure 3.3: Front and side view of the (5,5) CNT model showing the Fermi isosurface, which represents the conducting surface of the structure used for the continuum model. The radii r_C and r_F indicate the distance from the CNT’s central axis to the carbon cores and the Fermi isosurface, respectively.

ONETEP optimisation significantly. As seen in Figure 3.3, the model consists of the cylindrical single-walled (5,5) CNT with one open and one closed end, as described in Section 2.3.1. After the “quick optimisation”, the model reached a maximum force component of $0.044 \text{ eV}/\text{\AA}$. The structure is then extracted and used as the initial geometry for the subsequent more precise ONETEP optimisation.

For the ONETEP simulations, one has to define a simulation cell (or DFT box) with a limited volume, in which the CNT is located, and over which the density functional calculation will be solved. For all further simulations (unless otherwise stated) a cubic simulation cell of $5 \text{ nm} \times 5 \text{ nm} \times 5 \text{ nm}$ is used. In this DFT box, the CNT axis must be parallel to the z -axis (as in Figure 3.4) and central in the box, and the CNT base must be close to the bottom surface of the simulation cell. This is important to assure the similarity between the macro- and nano-model, meaning that in the macro-model the conducting rod goes through the DFT box surface whereas the molecule does not. However, if the CNT is too close to the edge of the simulation cell, the NGWFs “leak” out of the box, which in turn would create errors. Therefore, the CNT was placed at $z = 6.5 \text{ \AA}$ which is approximately $12 a_0^b$, which matches the optimised NGWF radius for C (see Section 3.2.2).

The ONETEP geometry optimisation was then performed, using a cut-off energy of 1000 eV . The LDA in the form of the Perdew-Zunger parametrization [118] was chosen as the exchange-correlation functional and the projector augmented wave method (PAW) [119] was employed for the ion core potentials. The force tolerance was set to $0.001 E_h/a_0$ and the maximum energy tolerance was $1 \times 10^{-5} E_h^c$.

The optimised CNT had an average C–C bond length of 1.44 \AA for the top pen-

^bThe Bohr radius: $a_0 = 4\pi\epsilon_0\hbar^2/m_e e^2 = 5.291\,772\,1 \times 10^{-11} \text{ m}$.

^cThe Hartree energy: $E_h = 27.211\,386\,245 \text{ eV}$.

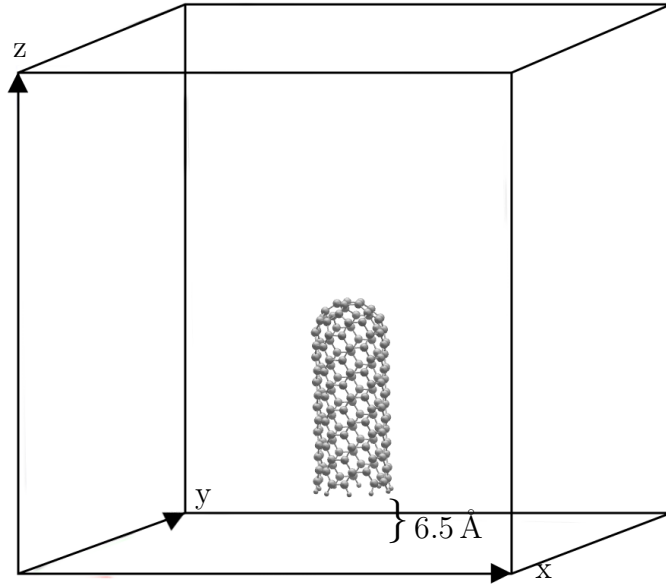


Figure 3.4: DFT simulation model of the (5,5) CNT showing its placement within the simulation cell.

tagon structure and 1.41 \AA along the tube. The total length of the CNT is 1.83 nm , measured from the hydrogen termination to the top pentagon ring and the radius r_C from the axis to the outermost carbon cores is 0.317 nm . However, it was found that the static radius r_C does not represent the correct “metallic surface” of a CNT inside an applied field, hence a more adequate definition to use for the macroscopic model has to be found. The general problem is, that most classical continuum models of a material’s surface neglect the atomic fine structure and consider it to be smooth. Thus, to combine the macro- and nano-model one has to consider where this “smooth” metal surface is defined for the DFT molecule. It was deduced, that the metal surface has to coincide with the potential isosurface value of the Fermi level (see Chapter 4.1.1 for a detailed discussion). This isosurface defines the distance up to which the delocalised electron cloud extends around the carbon ion cores. Figure 3.3 shows such an equipotential at $E_F = -4.43 \text{ eV}$ relative to the vacuum level, acquired by the geometry optimisation in zero field, which gives us the radius of the metallic conductor of $r_F = 0.47 \text{ nm}$. This value is then used to define the radius of the conduction rod in the macroscopic model.

3.2.2 Simulation parameters and convergence test

Using the previously simulated optimised geometry, multiple single point energy calculation were conducted to determine the optimal set of simulation parameters which permit a high accuracy, whilst keeping the computation time as low as pos-

sible.

As the structure being modelled is free-standing and non-periodic, all simulations had to be done using one of ONETEP’s open boundary condition algorithms. Thus, all results henceforth presented were obtained in real space using a multi-grid solver to determine the Hartree potential, the local pseudo-potential, and the core–core energy terms [86]. This method is especially suited for the later-implemented multi-scale-BC matching as the Hartree potential is calculated by solving the Poisson equation in real space with Dirichlet boundary conditions on all faces of the simulation cell.

Furthermore, as the system being simulated is metallic, ensemble density functional theory (EDFT) is used to simulate the conducting CNT [120]. This approach mimics a conducting system by allowing the KS states to have fractional occupancies, determined by the Fermi-Dirac distribution. This is done by introducing a finite temperature term, namely the Helmholtz free energy, to the Hamiltonian. This causes \hat{H} , after diagonalisation, to scale with the cube of the system size, thus increasing the simulation time. However, the computational cost is reduced significantly and kept to a minimum by using a minimal set of NGWFs^d. Unless otherwise stated, the simulations assumed a system temperature of 100 K (8.617 meV). For the exchange-correlation functional, the same LDA function was chosen as for the geometry optimisation, to be consistent between simulations.

The next step is to find the optimal simulation parameters for the cut-off energy and the NGWF radii to decrease the total energy and to find a trade-off between simulation accuracy and computational time.

Cutoff Energy

First, a series of simulations was conducted for the CNT to examine the impact of varying the cut-off energy on the model’s total energy. As can be seen in Figure 3.5, the total energy per atom follows a monotonic decrease when increasing the cut-off energy from 400 eV to 1300 eV. This asymptotic decrease slows down significantly for cut-off energies greater than 600 eV after which the energy gain is less than 2 meV/tom. A second detail to consider is that the cut-off energy specifies the kinetic energy of the maximum G-vector of the reciprocal-space grid, and thus influences the spacing of the real space grid. This correlation is especially important for the BC matching between the micro- and the nano-model. On the one hand, one wants a fine grid spacing to ensure good BC matching between the models, on the other hand, one wants to keep the number of grid points small as increasing them prolongs

^dMore information in Ref. [86].

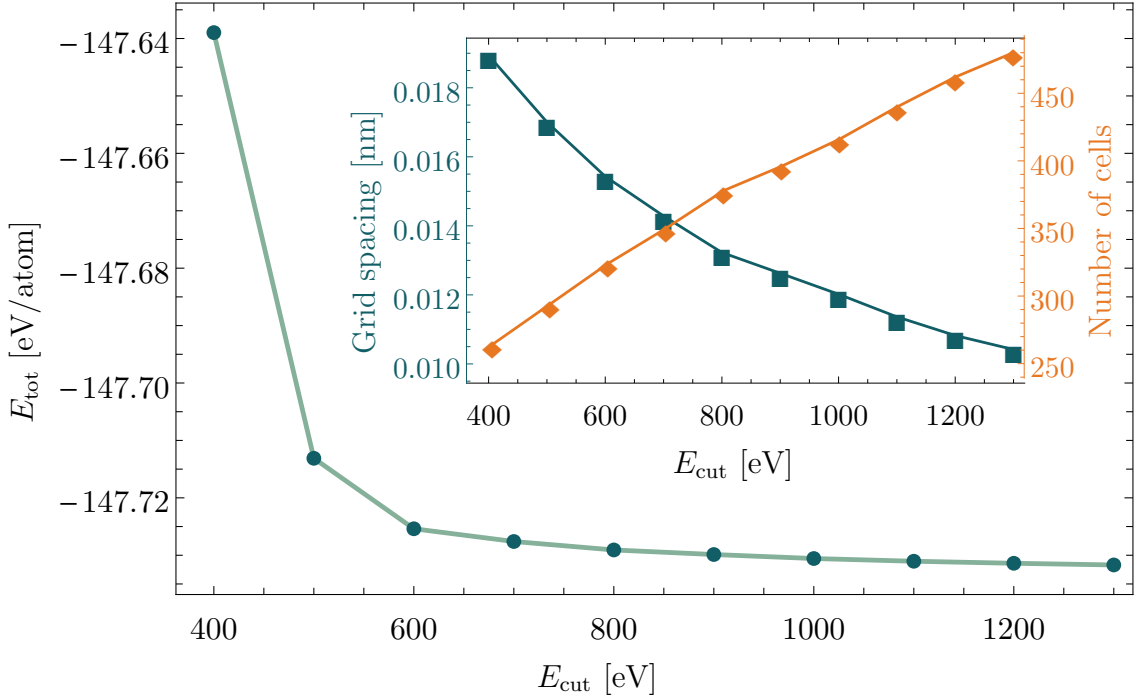


Figure 3.5: Convergence of the kinetic cut-off energy for a (5,5) CNT using the LDA functional. The inset shows the correlation between the cut-off energy and the grid spacing (■) or the number of cells (◆).

the computation time. The correlation between the number of grid points and the grid spacing can be seen in the inset of Figure 3.5.

All things considered, a cut-off energy of 1000 eV is chosen for all further simulations, as it results in a fine cubic mesh of $416 \times 416 \times 416$ gridpoints and a spacing of about 0.012 nm for the $5 \text{ nm} \times 5 \text{ nm} \times 5 \text{ nm}$ DFT box. This grid is sufficiently fine to allow a smooth boundary condition matching between the models, as can be seen in Section 3.2.4, while keeping the computational cost at a reasonable level.

NGWF radii

Another important parameter for ONETEP simulations, which determines the total energy of the system and thus the accuracy of the simulation, is the maximum radius of the NGWFs. As briefly mentioned before, this parameter determined how close the CNT can be placed to the simulation cell boundary. Therefore, the NGWF radii were varied from $7 a_0$ to $13 a_0$ for both C and H. As can be seen from Figure 3.6, the total energy decreases monotonically with increasing NGWF radius and is well converged at $12 a_0$. As always, one had to consider a trade-off between accuracy and computation time, as increasing the size of the NGWF spheres leads to a larger number of NGWF coefficients which need to be optimised simultaneously.

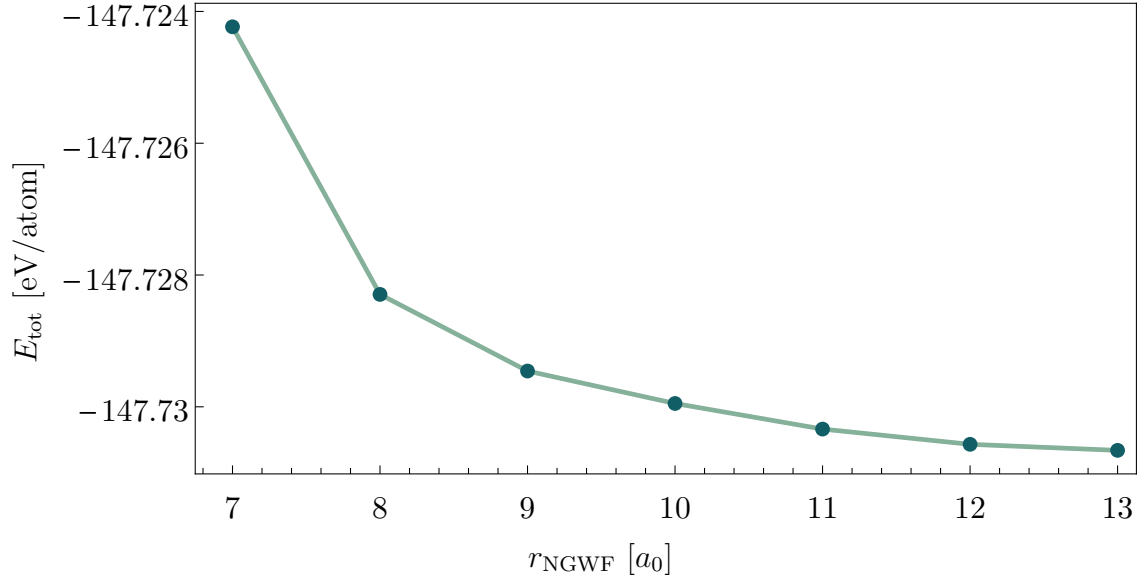


Figure 3.6: NGWF radius convergence of the (5,5) CNT using the LDA functional and $E_{\text{cut}} = 1000$ eV.

With regards to the number of NGWFs, ONETEP uses one NGWF to describe the s -orbitals and three for the p -orbitals resulting in a minimum number of NGWF of 4 for C ([He] $2s2; 2p2$) and 1 for H ($1s1$).

To summarise, all further calculations were conducted using a cut-off energy of 1000 eV and 4 NGWFs for C and 1 NGWFs for H, both with a radius of $12 a_0$. Moreover, the LDA was chosen as the exchange-correlation functional and the PAW method was employed for the ion core potentials.

3.2.3 Semi-classical continuum model

The classical 3D FlexPDETM model, as can be seen in Figure 3.7 a, consisted of two parallel, $100 \text{ nm} \times 100 \text{ nm}$ planes, which were separated by 100 nm . The voltage of the upper (anode) was varied depending on the simulation, while the cathode was always kept at 0 V . The simulated CNT emitter is represented by a conducting cylindrical rod, which is standing normal to and in the centre of the cathode plane with a total length of 50.3 nm . The rod was further modelled with a hemispherical end and with a diameter of 0.978 nm , chosen to approximate that of the Fermi equipotential. Furthermore, a $5 \text{ nm} \times 5 \text{ nm} \times 5 \text{ nm}$ DFT box is defined around the CNT apex region, matching the DFT simulation cell dimensions.

FlexPDE then solves the Poisson equation in three dimensions after discretising the region using a tetrahedral mesh. Figure 3.7 a displays the mesh of the full structure (left) and an enlargement (right) of the DFT box of a 2D cut-plane for

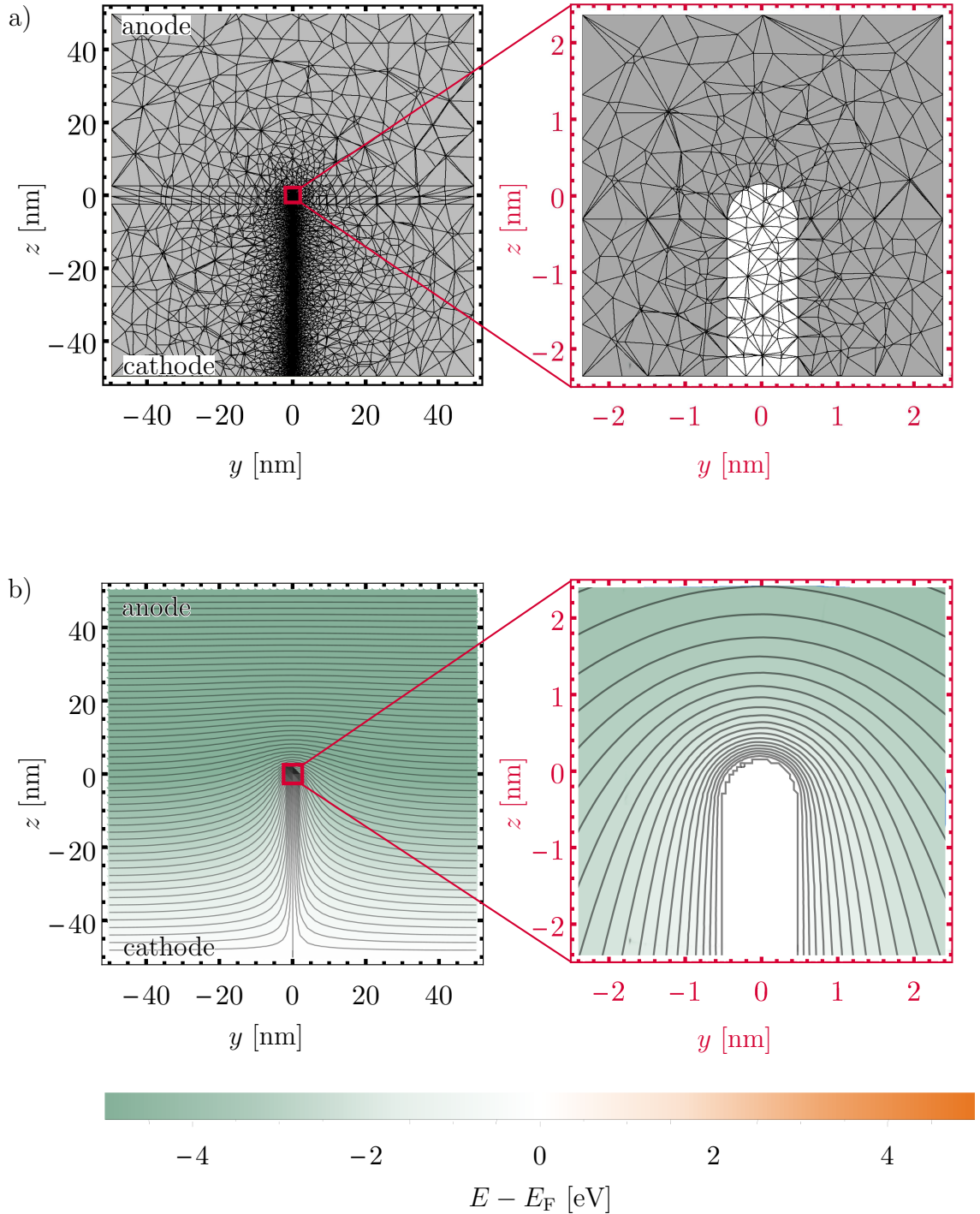


Figure 3.7: a) Section of the adaptive mesh distribution corresponding to an error limit of 1.1×10^{-5} for a conducting rod, representing the CNT, between a cathode and an anode at $z = \pm 50$ nm. The enlargement shows the finer mesh of the DFT box. b) The electrostatic potential isocontours at intervals of 0.2 V for an anode-cathode voltage of 10.8 V of the full emitter model and an enlargement of the emitter tip which corresponds to the DFT box volume.

a grid of 110637 elements and 19545 nodes (error limit of 1.1×10^{-5}) produced by FlexPDE. As can be seen, the mesh was adjusted to be finer and more precise inside the DFT box and around the CNT surface. The results for lower error limits were tested and showed qualitatively similar results but did take significantly more time.

The electrostatic potential and electric field intensity were calculated for every point inside the capacitor region and the resulting contours of the potential are displayed in Figure 3.7 b with the zoom into the DFT box indicated by the red square. The colour scale represents the electric potential in intervals of 0.2 V for an applied voltage of 5.4 V relative to the cathode, which corresponds to a background field in the absence of the nanotube of 0.054 V/nm. The distribution of the electrostatic potential on the surface of the DFT box and the induced charge within it are extracted and used as boundary conditions for the DFT calculation.

3.2.4 Multi-scale model and boundary condition matching

The last step of the multi-scale approach is to couple the atomistic simulation methods with the continuum model to achieve the desired balance between computational efficiency and accuracy. For this, another single-point calculation is run using the previously optimised geometry for zero field and the simulation parameters discussed in Section 3.2.2. Furthermore, the extracted BC acquired from the classical model are interpolated and mapped onto the DFT mesh and given as an external file to be used by ONETEP as boundary conditions. This was done by extending ONETEP's multi-grid solver code, used to simulate open-BC in real space, to use explicitly defined potential values for all grid points on the simulation cell surface as Dirichlet BC for the field solver. This way the calculated potential is forced to converge towards these set BC values creating a seamless transition between continuum and atomistic representations whilst ensuring a continuity of the electrostatic potential.

Figure 3.8 shows a longitudinal section containing the CNT axis, demonstrating the matching between the macro- and nano-model. For this, the DFT potential energy simulated for a background field of 0.054 V/nm and with one electron induced on the CNT by this field is superimposed on part of the classical potential, which is raised by the work function. This adjustment is necessary as the two simulations have different definitions of the zero potential. While the zero of potential for the DFT calculation is the vacuum level in zero field (see Section 4.1.9), FlexPDE defines it as the Fermi level of the cathode. Hence, the two simulations differ by the work function and can be matched by adjusting their potentials accordingly. The size and position of the DFT box is indicated by the red dashed frame. The solid white outline in the simulated potential indicates the Fermi equipotential and the

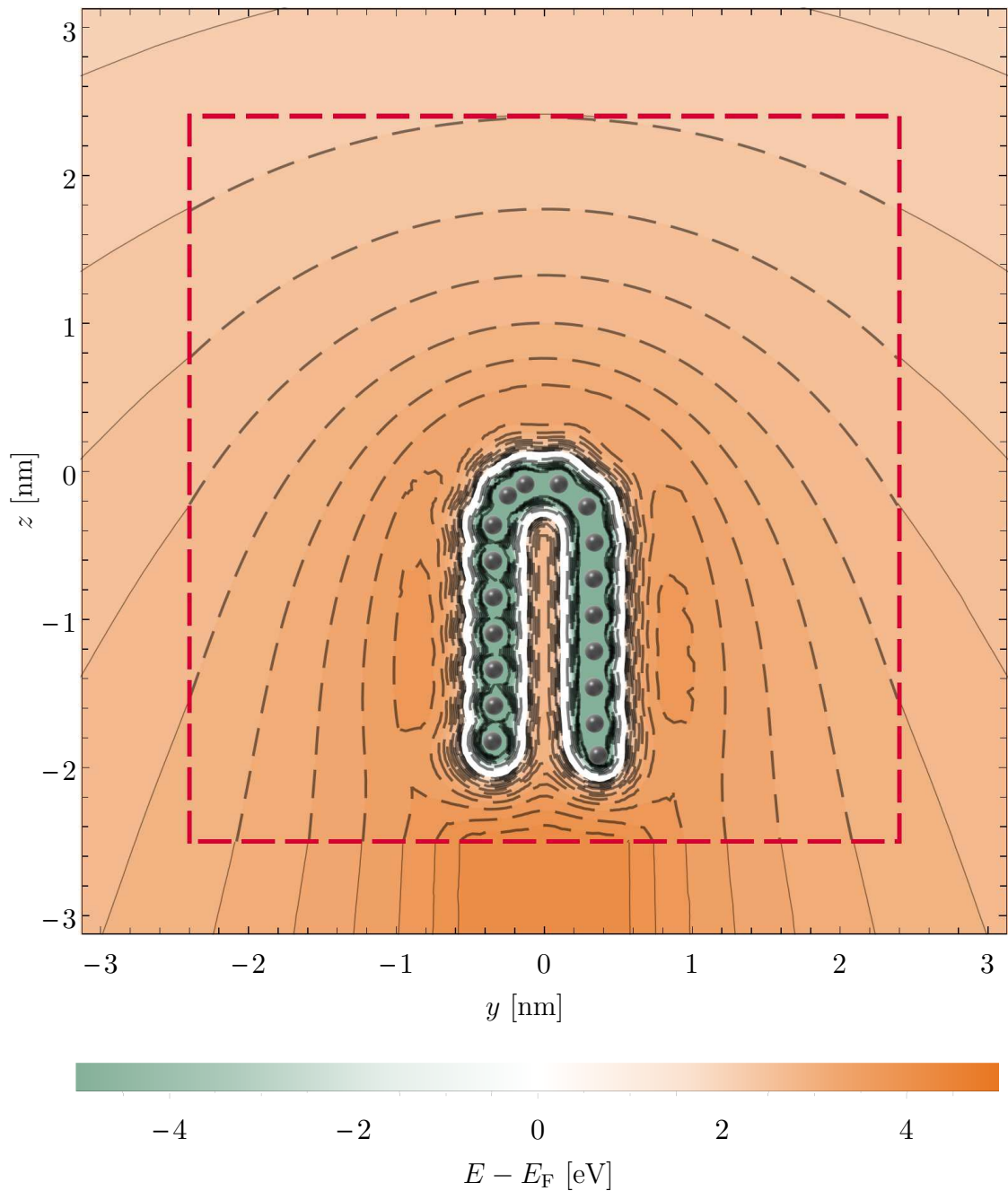


Figure 3.8: Section containing the CNT axis, showing the matching of the potential energy between the macro- and nano-model for a background field of 0.054 V/nm . The red dashed frame shows the size and position of the DFT box and thus indicates the boundary between the classical model raised by the work function (outside the box) and the superimposed DFT results (inside the box). The equipotentials (black lines) above and below E_F are at intervals of 0.2 eV and 1 eV , respectively. The solid white line around the CNT indicates the position of the Fermi equipotential. The atomic positions extracted from the DFT geometry optimisation are mapped in grey onto the tip region for visualisation.

dotted equipotential lines above and below E_F are at intervals of 0.2 eV and 1 eV, respectively. The agreement between the two models can be seen from the well-matched potential distributions at the interface.

As mentioned in Section 3.1.1, additional charges from the cathode will be induced into the emitter's tip when an external electric field is applied, where the exact number of charges is correlated to the field strength. As an electron is an elementary particle, the DFT code only allows for integer values of induced charges, which in turn means that only discrete applied field values could be used for the simulation. However, this would lead to an issue as depending on the model, high electric fields are needed to induce additional electron charges of $1e$, $2e$, $3e$, *etc.* At a certain field strength this would mean that the electrostatic potential would decrease below the Fermi level leading to field emission, a feature that is not yet implemented in the simulation model. Thus, the CNT model simulated in this work would have a maximum applicable field of 0.162 V/nm and three induced electrons while the next higher field for $4e$ would induce electron emission.

To analyse the shape and behaviour of the potential barrier close to the emission threshold, a new feature of the DFT code was implemented by Dr. E. B. Linscott, which allows for non-integer values of induced charges in the model. This means that one is no longer constrained to studying external fields that induce precisely an integral additional charge in the DFT subsystem. However, this will result in un-physical properties for some of the simulated attributes, such as the level of the highest occupied molecular orbital, the local density of states and the energy of individual orbitals, which will only be scientifically correct for integer electrons. Thus, within the scope of this work these values will always be given for integer values of the electron charge. Using non-integral values of induced electrons will however have no negative effect on the electrostatic potential, which is one of the most important properties to consider for field emission and can hence be used to analyse the potential barrier for a continuously varying field.

Although this method is currently restricted to equilibrium states, meaning that it is limited to applied fields below the emission threshold, the newly developed multi-scale method gives many details about an emitter's field emission properties. These include, for example, the changes in molecular orbitals and the barrier profile with different applied fields, the charge density redistribution on the apex and the role of E_{XC} in producing the work function, as will be discussed in Chapter 4.

3.3 Experimental methods

3.3.1 Molecular beam epitaxy

Epitaxy is the process of growing thin films that are crystallographically aligned with the underlying substrate. These thin films may be of the same (homoepitaxy) or different (heteroepitaxy) chemical composition and structure as the substrate. The exact form and orientation of this growth process are influenced by the crystalline orientation of the substrate material. Thus, by choosing a suitable substrate it is possible to control the crystallographic direction of the grown layers, induce strain or manipulate the epitaxial growth mode.

To increase the quality of the deposited film and to reduce defects, the substrate is usually heated, which provides the adsorbed atoms with enough energy to overcome the substrate surface's kinetic barrier and move to the most stable locations. However, too high annealing temperatures can also cause an unwanted intermixing of substrate atoms with atoms of the film, therefore the temperature must be controlled carefully.

The simplest way to guarantee unstrained high-quality epitaxial samples is to choose a suitable growing material that either has an identical or similar lattice constant compared to the substrate. Another option is to use materials, whose lattice constants are common multiples of each other. If neither of these conditions is met, lattice mismatch occurs which in turn causes strain in the film or causes defects at the interface. Depending on the interplay between lattice mismatch, chemical potentials and adsorption energies, the epitaxial growth process might result in three different growth modes as illustrated in Figure 3.9 [121]:

- Frank-Van der Merwe growth: This two-dimensional mode is also called layer-by-layer growth mode and is the ideal condition to obtain atomically smooth surfaces. Here adatoms attach themselves to the surface in a way that a complete layer of material is formed prior to the growth of subsequent layers.
- Volmer-Weber growth: In this growth model adatom-adatom interaction are the predominant forces, whereas the adatom-substrate interaction is comparably weak. This leads to the formation of three-dimensional islands instead of planar films.
- Stranski-Krastanov growth: This mode is also called layer-plus-island growth and is a combination of the two previous modes. Here the initial growth is governed by the two-dimensional layer-by-layer mode before transitioning to

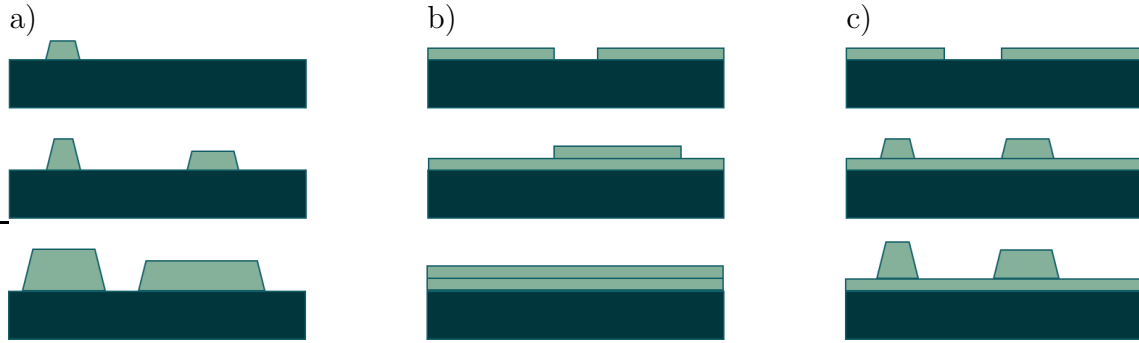


Figure 3.9: Schematic of different epitaxial growth modes showing the morphology of a) Volmer-Weber growth, b) Frank-van der Merwe growth and c) Stranski-Krastanov growth.

a three-dimensional island mode when reaching a critical layer thickness. The transitioning thickness is material dependent and is a function of properties such as surface energies and lattice parameters.

Even though there are various ways of obtaining an epitaxial film, all samples fabricated within this work were grown using molecular beam epitaxy (MBE) [122]. For this technique, a molecular beam of the target material impinges onto the surface of the substrate, forming crystalline films. The chemical composition and atomic layer thickness can be controlled by adjusting the sample temperature and the rate of the incoming flux. For this, MBE requires an ultra-high vacuum environment to ensure minimum contamination and a sufficiently long mean free path for the target atoms to reach the sample.

3.3.2 Auger electron spectroscopy

Auger electron spectroscopy (AES) is a surface characterisation technique, which provides qualitative and quantitative information about the chemical composition of the sample [123]. In the experiment, a focused electron beam with a kinetic energy from several eV up to 10 keV is directed onto the sample. This bombardment triggers the Auger process, which consists of several inter- and intrastate transitions of electrons in the ionised atoms. In other words, an electron or photon hits a core state electron (*e.g.* K shell), which results in the removal of that core electron and the generation of a hole. As this is an unstable state, the core-hole will be filled by an outer-shell electron (*e.g.* L_1 shell). This electron, when transitioning from the higher to the lower energy level, radiates an amount of energy equal to the difference in orbital energies. This energy can further couple to a second outer-shell electron (*e.g.* $L_{2,3}$ shell), which in turn can be emitted from the atom if the transferred energy is greater than the orbital binding energy, leaving the atom ionized. An overview

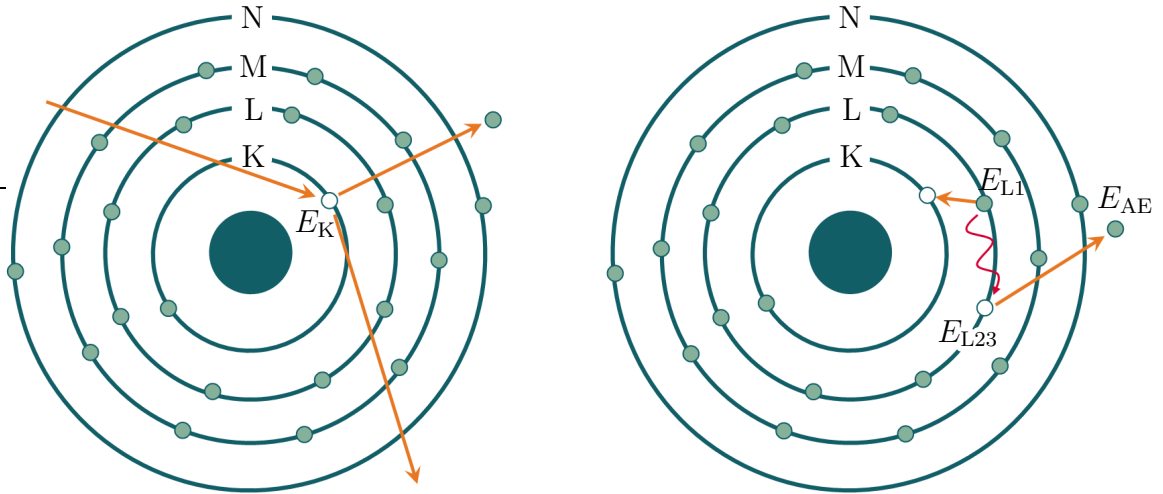


Figure 3.10: Schematic diagram of the Auger electron process in which the excited atom with an inner shell vacancy forms the initial state, an electron from a higher energy level fills this vacancy and the energy difference is released by emission of an Auger electron, whose energy is defined by the difference between the initial transition and the original energy level of the Auger electron before emission.

of the Auger process is shown in Figure 3.10. The emitted electron will have an element-specific kinetic energy of

$$E_{\text{AE}} = E_{\text{K}} - E_{\text{L1}} - E_{\text{L23}}. \quad (3.2)$$

These Auger electrons (AEs) are usually detected and analysed via hemispherical- or cylindrical-mirror energy analysers, which effectively act as a bandpass filter. This allows to scan through the energy range of detectable electrons giving a spectrum of the electron count in relation to their element-specific kinetic energy. As the mean free path of the impinging electron beam in the material is low in this energy range, AES is very surface sensitive.

3.3.3 Low-energy electron diffraction

Low-energy electron diffraction (LEED) is a very useful surface analysis technique in which an electron beam in the energy range between 20 eV to 500 eV is scattered by the surface atoms of the investigated sample [124]. The elastically backscattered electrons can form a diffraction pattern that is representative of the sample's crystal structure. As this technique only uses low-energy electrons for the diffraction, it exclusively shows the surface crystallography and does not provide information on the bulk structure.

The theoretical prediction of electron diffraction is based on the wave mechanics

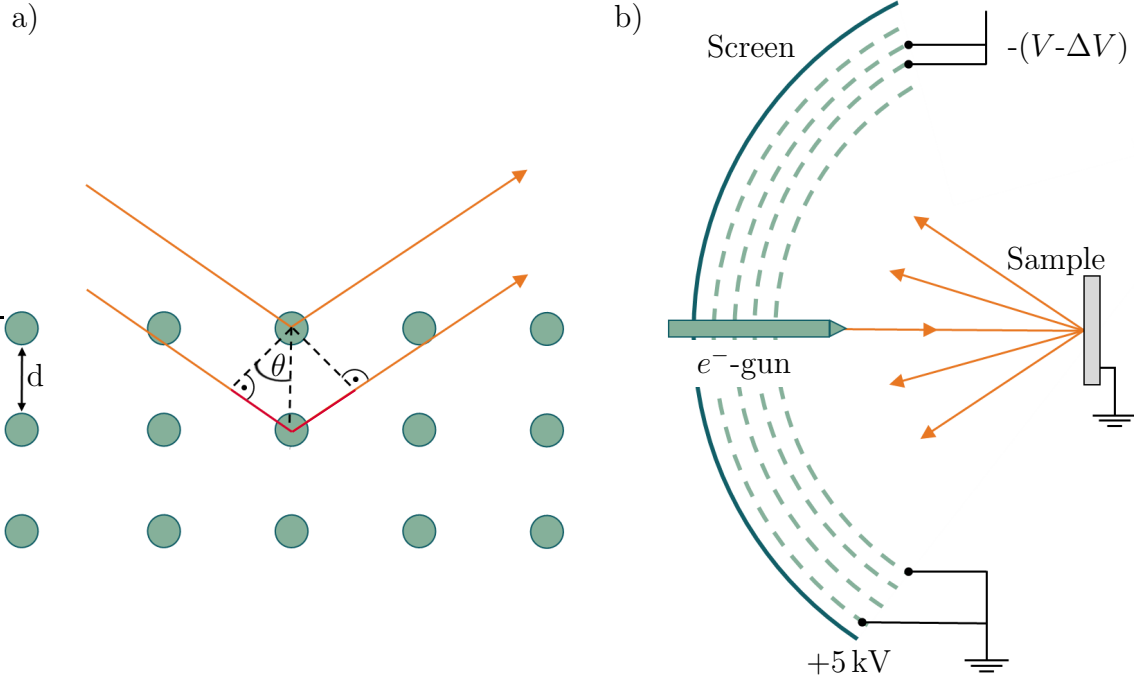


Figure 3.11: a) Diagram of Bragg diffraction in which, depending on the path difference (shown in red), constructive and destructive interference occurs. b) Schematic of a rear-view LEED apparatus.

proposed by de Broglie in 1924. He postulated that each particle has a corresponding wavelength given by

$$\lambda_{i,f} = \frac{h}{\sqrt{2m_e E}}. \quad (3.3)$$

Here, the index i represents the incident and f the scattered electrons. This equation shows that electrons with a sufficiently low energy have a wavelength in the order of the atomic distances in crystals. Thus, the atomic lattice can act as a periodic grid, resulting in electron scattering (schematic in Figure 3.11 a). This principle of electron diffraction from surfaces is based on Bragg's law of diffraction

$$n\lambda_{i,f} = 2d \sin \theta, \quad (3.4)$$

with a being the atomic spacing and θ describing the angle between the incident beam and the crystal surface. This relation shows that electrons impinging on the periodic sample surface at a specific angle would undergo constructive interference, leading to the observation of diffraction maxima.

In all the LEED systems used in this work, a beam of monochromatic electrons impinges onto the sample at an incident angle normal to the sample surface. The scattered electrons then pass through a retarding field analyser and are visualised on

a phosphor screen. The retarding field analyser is important as scattered electrons may have been elastically or inelastically scattered inside the sample, but only the former hold information on the sample surface. Therefore, the analyser, consisting of multiple grids, ensures that only elastically scattered electrons can pass through the grids while the inelastically scattered low-energy electrons are filtered out. This screen's hemispherical geometry allows to observe an undistorted projection of the reciprocal lattice. The resulting pattern gives important information about the sample's surface quality and the epitaxial growth mode (see Section 3.3.1). A schematic of a typical LEED setup is depicted in Figure 3.11 b.

3.3.4 Spin-polarised low-energy electron microscopy

Spin-polarised low-energy electron microscopy (SPLEEM) is a method that images the magnetic structure of surfaces by utilising spin-dependent electron scattering and reflection. As the name suggests, the experimental setup is largely identical to that of a conventional low-energy electron microscope with the main difference being that a spin-polarised electron source is used instead of an unpolarised one. This additional feature gives the option to acquire both structural and magnetic information simultaneously and thus allowing to correlate the surface morphology with the material's magnetisation.

SPLEEM setup

The SPLEEM setup used in this work was provided by the National Institute of Material Science (NIMS) in Tsukuba, Japan [125, 126] and consists of a compact Elmitec LEEM instrument equipped with a spin-polarised illumination column. The system is further equipped with all necessary facilities for sample growth and characterisation such as MBE and LEED and is operated at a base pressure in the low 10^{-10} mbar. The used system further has a lateral resolution of about 10 nm [126]^e.

A schematic of the setup is shown in Figure 3.12. The SP high brightness electron source (1), consisting of an oxygen-caesium activated strained GaAs/GaAsP superlattice photocathode, has a spin polarisation of approximately 90% and a quantum efficiency of 1.6% [128, 129]. The calibration of both quantum efficiency and spin polarisation were performed prior to the measurements using a Co/W (110) sample. The beam's spin polarisation can be reversed optically by reversing the helicity of the excitation laser.

^eA newly developed aberration corrected SPLEEM even achieved a lateral resolution of down to 3.3 nm [127]

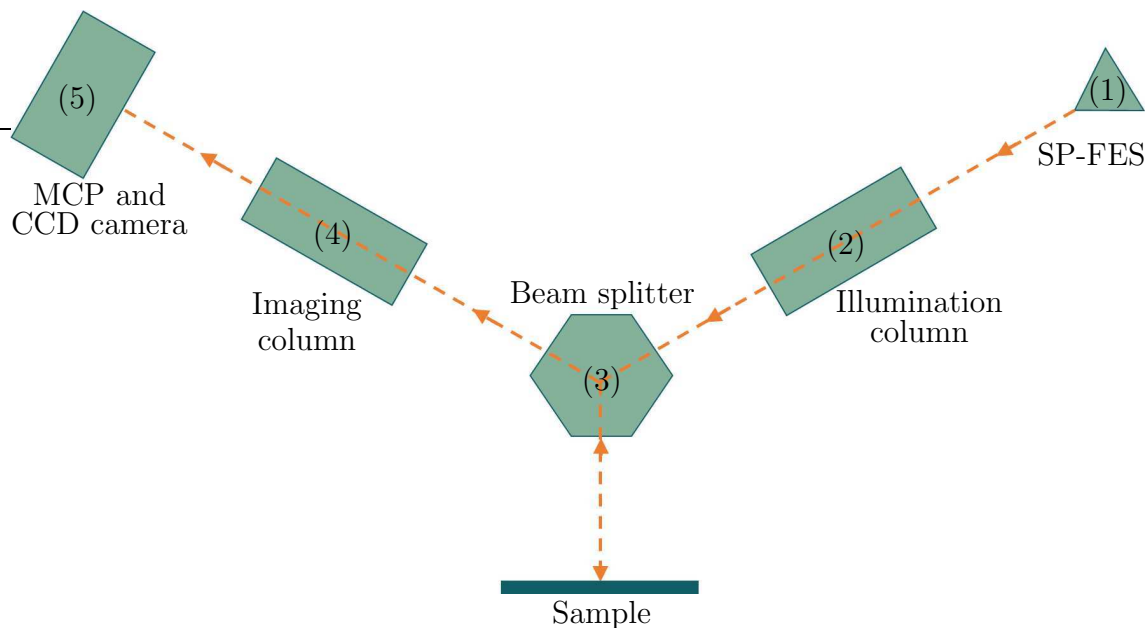


Figure 3.12: Schematics of a SPLEEM setup in which spin-polarised electrons, coming from the SP-FES, are first injected into an illumination column containing spin manipulators to adjust their azimuthal and polar orientation. Then, passing through a beam splitter, they hit the surface at normal incidence. The generated backscattered and secondary electrons are separated from the incoming beam by again passing through the beam splitter. Subsequently the electrons are collected in an imaging column and focused on a multichannel-plate detector with CCD.

The subsequent illumination column (2) consists of a spin manipulator (Wien filter) and a spin rotator (condenser lenses) which provide full control over the polar and azimuthal angle of the beam's spin direction [130]. This feature is the main strength of the technique as its capability to orient the electron beam in any space direction allows it to probe any type of magnetisation configuration.

After passing through a beam splitter, the primary electron beam hits the sample normal to its surface and gets reflected. In this geometry, only spin-spin interactions occur while spin-orbit interactions do not influence the signal [131]. Thus, the magnetic contribution to the signal results solely from exchange scattering and gives a direct microscopic image of the sample's magnetic domain structure. The typical energy of the electron beam reaching the specimen surface is only a few eV above the vacuum level, making this technique highly surface sensitive [131].

The backscattered electrons (BSEs) are then reflected normal to the surface and separated from the incoming beam by again passing through the magnetic beam splitter (3) using the Lorentz force. The magnified image of the surface is obtained by passing the BSE beam through an imaging column (4) [132]. The intensity of the reflected electron beam with the polarisation parallel or antiparallel to the sample's

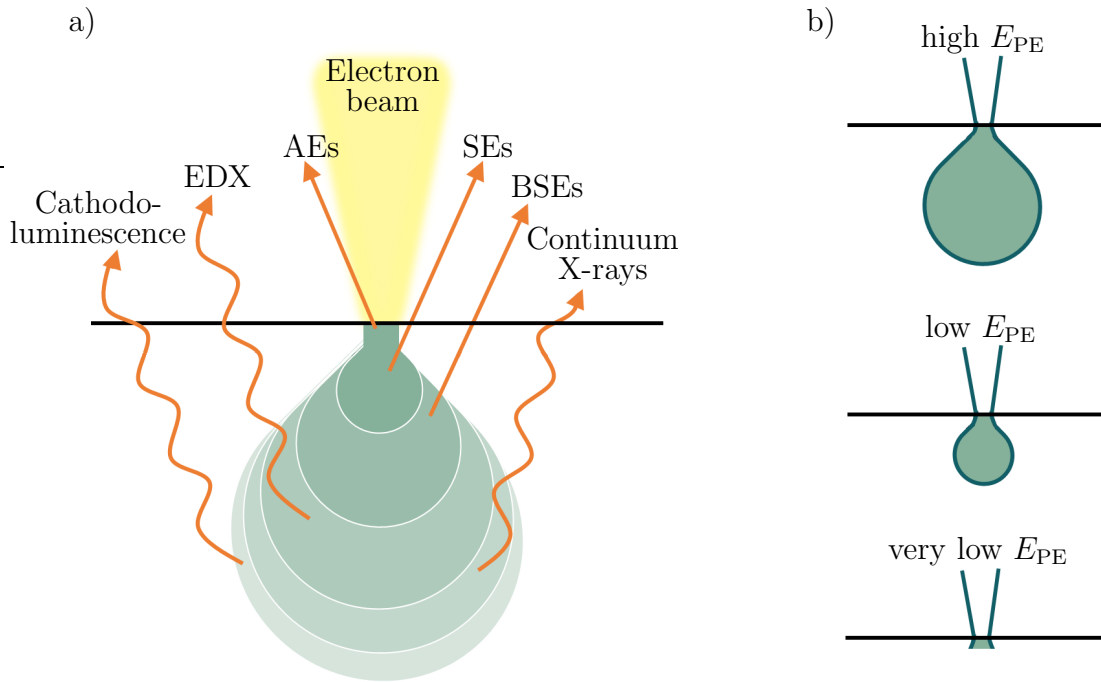


Figure 3.13: a) Schematic of various signals, such as Auger electron (AE), secondary electron (SE), backscattered electron (BSE) and energy-dispersive X-rays (EDX), emitted from different regions of the interaction volume. b) Interaction volume for different primary beam energies. The interaction volume takes a “pear”-shape whose depth increases with the electron energy and reaches an almost cylinder-shape for $E_{PE} < 20$ eV.

magnetisation is then acquired with multichannel-plate (MCP) image amplifiers and a CCD camera (5) to record images and energy-dependent reflection intensity plots.

Beam - specimen interaction

Generally, there are several different scattering processes involved when an electron beam hits a material surface, which result in a variety of detectable signals such as elastically and inelastically backscattered electrons (BSEs), secondary electrons (SEs), Auger electrons (AEs), cathodoluminescence or X-rays. These signals can usually be distinguished by their energy and stem from different depth regions within the so-called interaction volume (Figure 3.13 a). The size and shape of this volume is largely dependent upon the electron beam energy and the specimen’s atomic number. Figure 3.13 b illustrates the variation of interaction volume with respect to different accelerating voltages. As can be seen, high accelerating voltages result in a “pear”-shaped interaction volume with deep penetration length and a large lateral excitation region, causing the loss of detailed surface information of the sample. This interaction volume decreases with decreasing acceleration voltage. At very

low electron beam energies below 20 eV, such as for the experiments presented in Chapter 5, the volume is less of a pear-shape but rather a small cylinder of only a few nanometre depths and with a very narrow lateral expansion.

The two types of electrons, BSEs and SEs, which are of further interest for this dissertation both stem from a region within a few nanometres of the material surface. The former are of interest as they are the main contributors to the magnetic contrast in SPLEEM images. Usually, those BSE are defined by having energies above 50 eV, but a more accurate description would define them as electrons that still have approximately 90% of the initial energy of the primary electron (PE). This is important here, as the investigated PE energy only ranges up to 20 eV [133]. The latter is also of importance for the main goal of building novel spin-polarised field emission sources and to widen the understanding of the interaction processes of spin-polarised low-energy electrons with matter.

Origin of the magnetic contrast in SPLEEM images

The basis of the magnetic contrast is mainly caused by two phenomena: (1) the spin-dependent exchange interaction between the spin polarisation \vec{P} of the incident beam and the magnetisation direction \vec{M} of the target material and (2) the difference in spin-dependent inelastic mean free path (IMFP) for electrons parallel or antiparallel to the material's spin orientation [131, 132].

In the case of the first phenomenon, the spin-spin interaction between \vec{P} and \vec{M} can be represented by an exchange potential V_{ex} . This potential is a consequence of the Pauli exclusion principle and is thus spin-dependent, meaning that electrons parallel ($\uparrow\uparrow$) or antiparallel ($\uparrow\downarrow$) to the material's magnetisation experience different interaction potentials, $V_{\text{ex}}^{\uparrow\uparrow}$ and $V_{\text{ex}}^{\uparrow\downarrow}$, respectively. As a result, the electrons are elastically backscattered at different intensities ($I^{\uparrow\uparrow} \equiv I^{\uparrow}$, $I^{\uparrow\downarrow} \equiv I^{\downarrow}$) which are proportional to $\vec{P} \cdot \vec{M}$. From this, the exchange scattering asymmetry can be defined as

$$A = \frac{I^{\uparrow} - I^{\downarrow}}{I^{\uparrow} + I^{\downarrow}}. \quad (3.5)$$

This difference in V_{ex} is the main cause for spin-dependent elastic scattering of the electron beam. Here, one has to note that the exchange potential is not only spin- but also energy-dependent, as can be seen in Figure 3.14 a (taken from Ref. [132]). Previous studies of different solid-state materials demonstrated that the exchange potential changes non-monotonically with energy [134].

The second phenomenon concerns the inelastic scattering of the primary beam. Here, one has to consider the difference in IMFP ($l^{\uparrow\uparrow} \equiv l^{\uparrow}$, $l^{\uparrow\downarrow} \equiv l^{\downarrow}$) for electrons

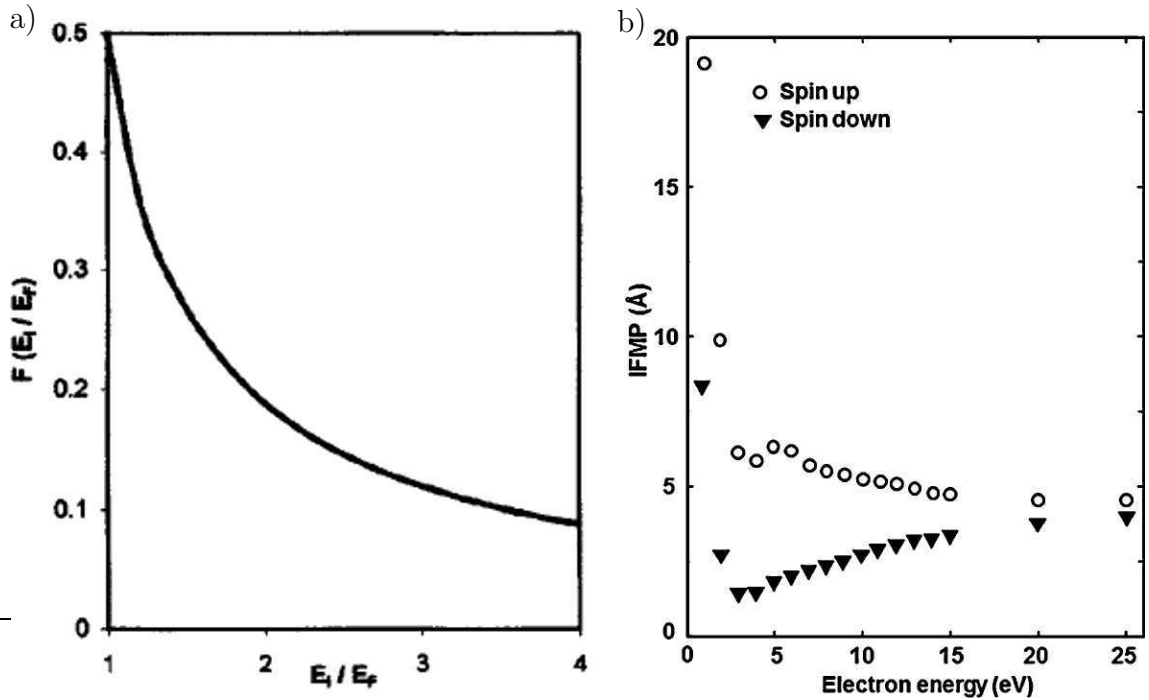


Figure 3.14: a) Energy dependence of the exchange potential for a free electron gas relative to its value at the Fermi level. b) Calculations for iron's energy-dependent IMFP for the majority and minority electrons above the Fermi level. Both are taken from Ref. [132].

with spin parallel and antiparallel to \vec{M} . In general, the difference in IMFP is caused by the difference in density of unoccupied states just above the Fermi level. In a ferromagnet, this number differs and the DoS for unoccupied states is higher for the minority spin bands than for the majority states (see Section 2.2). Thus, minority electrons are more effectively scattered than majority electrons. This effect can be seen in Figure 3.14 b, which shows the calculated values of l^\uparrow and l^\downarrow versus beam energy for Fe (taken from Ref. [132]). Similar to the exchange potential, the IMFP is highly energy-dependent for low energies but the difference almost vanishes for energies above 20 eV from the vacuum level where $l^\uparrow \approx l^\downarrow$. Additional interactions affecting the contrast mechanism, such as the reflection of slow electrons from surfaces or quantum well resonances in very thin films can enhance, reduce, or even invert the magnetic contrast. However, the full discussion of these effects would exceed the scope of this brief introduction and can be found in Ref. [45, 135, 136]. As seen in Figure 3.14, both phenomena become less effective as the electron energy increases. Hence, the best magnetic contrast in SPLEEM is usually obtained for low-energy electrons, with energies of a few eV.

The total electron yield, consisting of both BSE and SE, will be collected by the MCP amplifier and give an image of the sample surface using the CCD camera. Here

one has to consider, that taking a single image only provides topological information and a second image, with the equivalent topological information but opposite spin-polarisation, is needed to get the magnetic information. By subtracting these two images, the topological information cancels, while the pure exchange asymmetry of the sample's electron intensity remains. This means, that a SPLEEM image with no magnetic contrast ($|\vec{M}| = 0$) will have 50% grey colour, while bright or dark features in the images result from the different scattering intensities and represent magnetic contrast. However, one has to note that an incident electron beam with a spin-polarisation perpendicular to \vec{M} would also result in 50% grey colour by virtue of the scalar product between \vec{P} and \vec{M} .

Electron spectroscopy with SPLEEM

Generally, there are several ways in which a SPLEEM can be used for spectroscopy purposes. These techniques are useful to measure, *inter alia*, the unoccupied band structure of magnetic or non-magnetic materials, to investigate electron energy losses, and to probe the electronic and magnetic properties of buried magnetic interfaces.

One such spectroscopy method utilises the information gained from elastically backscattered, *i.e.* reflected, electrons in relation to the primary beam energy. In this method, the primary energy is scanned over a certain energy range, and the reflected BSE yield is measured, which gives an indication of scattering losses due to material properties such as the band structure and thickness. The minimum energy these BSEs can have is defined by the material work function and thus this technique also gives information about the local material specific surface work function. If the energy of the incident electron beam is smaller than the work function, the beam gets totally reflected (mirror mode) above the sample surface. Using this information, the initial beam intensity I_0 is defined and the spin-dependent reflectivities, $R_{\uparrow}(E)$ and $R_{\downarrow}(E)$, can be normalised by $I_{\uparrow,\downarrow}(E)/I_0 = R_{\uparrow,\downarrow}(E)$. One additional application, which will not be further explored in this work, is the possibility to measure thickness-dependent oscillations in the reflectivity of ultra-thin films. These oscillations are caused by reflections at the vacuum/film interface and at the film/substrate interface, which may interfere and give rise to constructive or destructive interference patterns [137].

Additional capabilities come from the SPLEEM's ability to filter the electrons emitted from the surface by their energy. In this energy-filtered SPLEEM the inelastically scattered electrons are investigated, as they contain information about surface plasmon energies, bulk plasmons, surface magnons, or other spin-dependent

excitation processes. Due to these processes, electrons undergo energy losses when hitting the surface of a crystal. While a certain part of the beam is reflected or only loses a small amount of energy, some fraction enters the crystal and gets inelastically scattered. Here one has to distinguish between two different types of low energy electrons: primary electrons which have lost the majority of their energy due to scattering and “true” secondary electrons. To analyse these electrons’ energy spread, an energy analyser is needed. In the setup used here, the energy can be scanned by adjusting the retarding bias of a grid in front of the MCP to effectively filter the electrons reaching the detector. As the low-energy electrons leaving the surface are accelerated inside the imaging column, the retarding bias needs to be in the order of kV [138]. An example of such an energy loss spectrum is shown in Figure 3.15 in which the elastic peak (used for reflection mode) and the SE peak are visible. After a certain energy loss, electrons will have insufficient energy to overcome the surface potential barrier and the intensity falls to zero.

To assure a high energy resolution, one has to further select a suitable beam aperture in the dispersive plane which acts as an energy bandpass. Its size is chosen

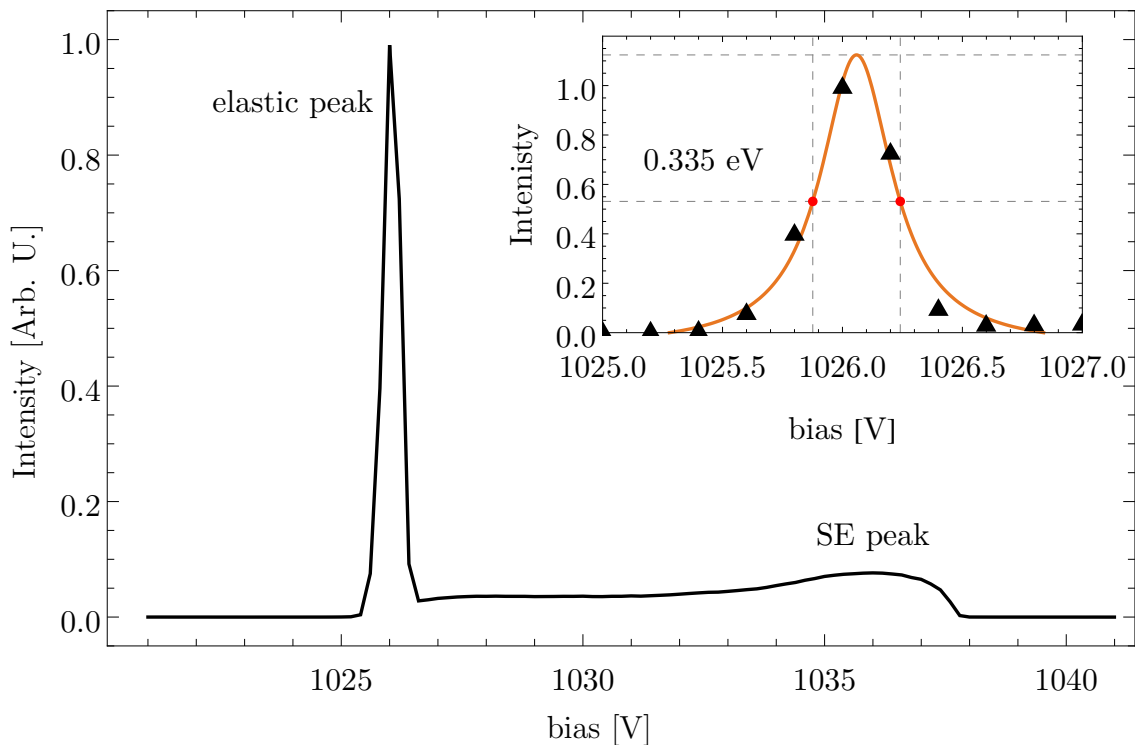


Figure 3.15: Typical energy loss spectrum for a primary beam energy of 15 eV, showing the elastic peak of reflected electrons and the secondary electron peak. The inset shows the calculation of the FWHM (●), the data points (▲) and the fitted Lorentzian function (orange line) used to determine the energy resolution of 335 meV.

such that it allows a high energy resolution while still collecting a high electron count. Here, an aperture of 60 μm was found to provide the best energy resolution and a good electron yield. The elastic peak was measured to have a full width at half maximum (FWHM) of 0.335 eV using a Lorentzian fit function, as shown in the inset of Figure 3.15. Assuming an energy spread of about 0.1 eV for the primary beam, the aperture provides a good spectrometer resolution.

By combining the primary beam energy scan with the selective energy filter, it is possible to investigate the change in secondary electron yield for SEs of a certain kinetic energy in relation to the primary beam's polarisation and energy. This can be done by, *e.g.* measuring the maximum SE peak intensity emitted from the sample, which corresponds to the most probable energy loss, but it can be adjusted to any SE energy. This novel application was developed within this work and will further be called energy-selective secondary electron yield (ESSEY) mode. For the measurements presented here, these ESSEY scans were conducted for the energy of maximum SE yield. Thus, three initial energy loss scans are performed for different beam energies and the energy-dependent SE peak position is determined. This shift is found to be linear, while the exact peak position was found to be material-dependent (see Chapter 5 for more details). Based on this linear correlation between SE peak position and primary beam energy it is possible to measure the spin-dependent maximum secondary electron yield for a variety of different beam energies by only recording the intensity of the SE peak.

The advantage of this technique is the very short data acquisition time. Compared to the full energy loss scan, which takes hours for a single spectrum, the complete ESSEY scan only takes about 30 min. This acquisition time is short enough for the sample to not be contaminated during the measurement and influences of adsorbates can be neglected for the interpretation. The results of these experiments are presented in Chapter 5.

3.3.5 Mott polarimeter

Mott polarimetry is a very useful characterisation technique capable of measuring the spin polarisation of an incoming beam of electrons. In comparison with the previously described SPLEEM, which is based on an initially spin-polarised electron beam, this technique is based on a spin-sensitive detection scheme. The brief introduction given here is based on descriptions found in review articles on Mott polarimetry [139–141] and Mott scattering [142, 143].

As the name suggests, the idea of the Mott polarimeter is based on Mott scattering, an effect first predicted by Sir Nevill Mott in 1929 [144]. Generally, this

scattering process refers to the collision and subsequent scattering of electrons off the Coulomb field of heavy nuclei. The direction of scattering is further influenced by the spin-orbit coupling between the nucleus and the electron. This relation can be seen from the semi-classical scattering potential, V_S , which essentially consists of the electrostatic Coulomb potential, V_C , and the spin-orbit potential, V_{SO} ,

$$V_S = V_C + V_{SO} = \frac{Ze}{r} + \frac{Ze^2}{2m_e^2c^2r^3} \vec{L} \cdot \vec{S}, \quad (3.6)$$

with r being the nucleus-electron separation and c being the speed of light.

Since V_{SO} contains the scalar product $\vec{L} \cdot \vec{S}$, it has different signs for electrons of the same orbit but different spin directions. This means that the resulting scattering potential would be higher or lower for electrons with one particular spin compared to the other, depending on which side of the atom they pass. This effect is illustrated in Figure 3.16 a. These different scattering potentials subsequently lead to different scattering intensities and a scattering asymmetry, which can be defined by

$$A_{\text{Mott}} = \frac{N_L - N_R}{N_L + N_R}, \quad (3.7)$$

where $N_{L,R}$ are the electron counts in the left and right detector per data acquisition period.

The component of electron polarisation perpendicular to the scattering plane as defined by the detectors is given in turn by

$$P = \frac{A_{\text{Mott}}}{S_{\text{eff}}(\theta, E)}. \quad (3.8)$$

Here, $S_{\text{eff}}(\Theta, E)$ is called the effective Sherman function which depends on the target material, polar scattering angle θ , incident electron energy E , energy loss of the scattered electrons and other geometric details of the device.

A simplified schematic of how the Mott polarimeter measures the scattering asymmetry is shown in Figure 3.16 b. This so-called retarding potential Mott polarimeter^f scatters electrons at energies between 20 keV to 25 keV off a high- Z target such as gold or thorium (1), which results in a left-right asymmetry with scattering angles of $\theta = \pm 120^\circ$ (2). Therefore, two (or four) detectors (3) are located symmetrically to either side of the incident beam path. The arrangement used in this work consists of four channeltron electron multipliers for an improved electron count and signal sensitivity. Furthermore, additional retarding grids (4) are used to deceler-

^fThe setup has been described in more detail in Ref. [145].

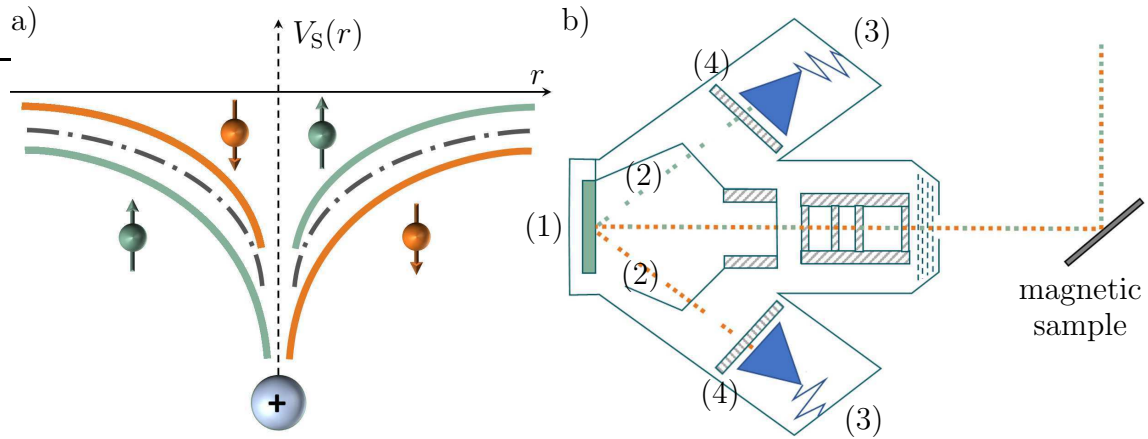


Figure 3.16: a) Schematic of the spin-dependent change in scattering potential, when SOC is taken into account. The corrected potentials, for spin up and spin down electron are shown in blue and orange, respectively. b) Simplified schematic of the retarding potential Mott polarimeter, in which a spin-polarised beam hits a thorium foil (1) and undergoes spin-dependent scattering (2) before being detected by several channeltron electron multipliers. Additional retarding grids (4) are used to filter out inelastically scattered electrons.

ate the electrons prior to reaching the detectors which allows for inelastic scattering events to be electrostatically filtered out. This in turn eliminates the need for energy analysis by the electron detectors. Utilising this measurement technique, it should be possible to quantify the level of spin-polarisation from a variety of SP-FESs.

4 | **Ab-initio study of field emission properties from low-dimensional emitters**

This chapter details the simulation results acquired by the atomistic-continuum model technique which was developed in the course of this dissertation (see Chapter 3.1). In the first part, new insights into the field emission properties of a (5,5) CNT, such as the charge density, potential energy, local density of states and spatial distribution of individual orbitals, are presented. Further, the energy and occupation of orbitals and the Fermi level are analysed with and without an applied field. The underlying work has been done in collaboration with the “Theory of Condensed Matter” group in the Cavendish Laboratory and published in *Journal of Electron Spectroscopy and Related Phenomena* as “Modelling a capped carbon nanotube by linear-scaling density-functional theory” [146] and *Ultramicroscopy* as “Analysis of a capped carbon nanotube by linear-scaling density-functional theory” [147]. The second section will detail simulations of a different emitter type consisting of a four-sided tungsten pyramid. These will further highlight the strength of the multi-scale atomistic-continuum simulation method and give details on the emitter’s properties.

4.1 Characterisation of a capped (5,5) CNT

All simulations reported henceforth, unless otherwise stated, use the LDA functional, and a cut-off energy of 1000 eV. Furthermore, the NGWF had cut-off radii of $12 a_0$ and the PAW method from the ABINIT dataset was used to represent the atomic cores [148]. Most energies will be reported relative to the Fermi level which is treated here as identical to the chemical potential as explained in the following section.

4.1.1 Fermi level and metallic radius

To correctly compare the individual simulations with and without externally applied electric fields, one has to define a point of reference for the potential. Usually, the ONETEP code relates the calculated potential to the chemical potential [88], μ , which describes the change in free energy when electrons are either added to or removed from the system. This concept is similar to the Fermi level in solid-state materials, where $\mu = E_F$ at 0 K. This means, that inducing additional electrons will change a simulation's reference potential, which makes the comparison of the individual results less clear.

However, as the simulations do not only describe an isolated CNT molecule but represent a whole emitter system, one can assume the CNT to be in a simple circuit with a cathode. In this system, the voltage of the cathode and CNT is held fixed as the anode-cathode voltage is varied. In this case, the Fermi level of the CNT remains constant as the external field varies. Thus, by calculating the Fermi levels for different applied fields, it is possible to compare the potential distributions around the tip by aligning their Fermi levels.

As shown in Eq. (2.10) these calculated potentials consist of three parts. Firstly, it includes the electron-electron interaction or Hartree potential and secondly, it contains the “external” potential caused by the ion cores. Here, the usually Coulombic potential of the core electrons is replaced by pseudopotentials which approximate the potentials to simplify the computational procedure. These pseudopotentials will only match the more realistic Coulomb potential above a certain radius from the core. Lastly, the potential also includes the effects of electron exchange and correlation (XC), also known as many-electron effects. These correct the calculation by including non-classical terms that can not be calculated from electrostatic interactions. This functional consists of an exchange part, which partially corrects for self-interaction of one electron with itself and also contains the effects of the Pauli exclusion principle, and a correlation part which corrects further for many-electron effects.

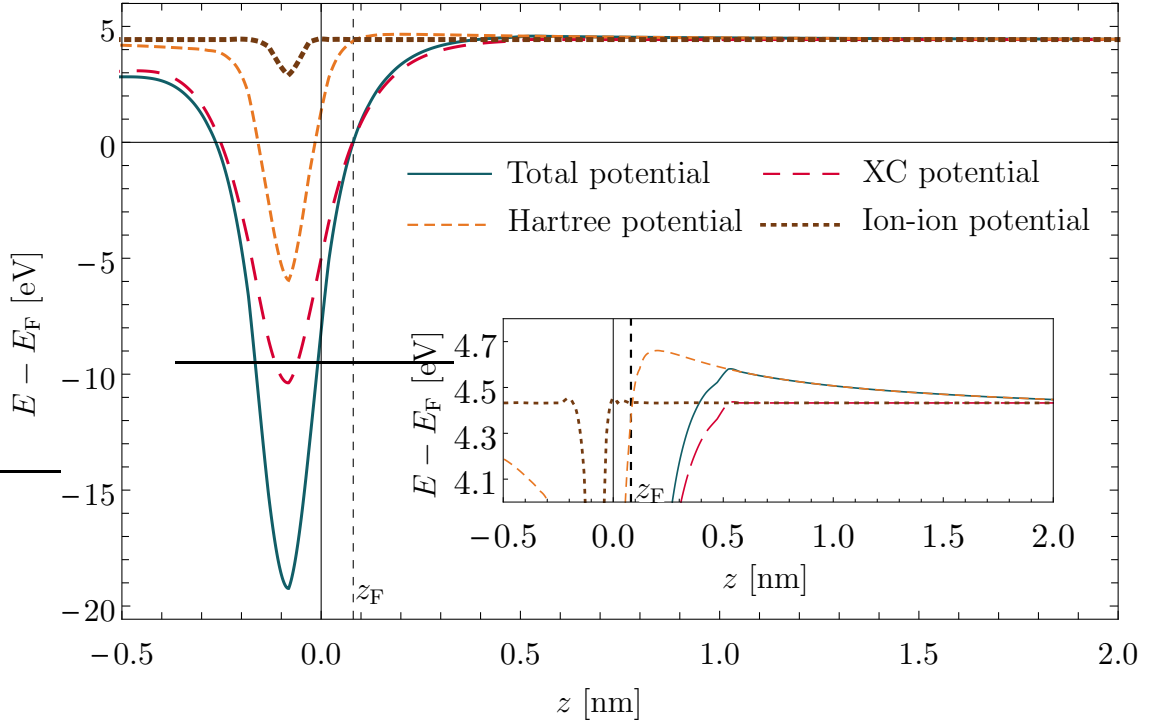


Figure 4.1: Display of the different contribution to the overall potentials at zero applied field: Hartree, XC and pseudopotential along the CNT axis, going through the centre of the top C pentagon (see Figure 2.7 a). The axial position at which the total potential equals the Fermi level is indicated by the black dashed line and denoted by z_F . The equipotential surface containing z_F , surrounding the ions but at about 0.175 nm from them, defines the surface of the metallic CNT. The inset shows an enlargement of the plot-range close to the vacuum level and the long- or short-range properties of the different potentials.

Figure 4.1 shows a one-dimensional plot of the different parts of the potential energy calculated with ONETEP along the z -axis of the CNT. Here, the solid blue line represents the overall potential energy of the system, consisting of the Hartree potential (short dashed, orange line), the local pseudopotential (dotted, brown line) and the exchange-correlation potential (long dashed, red line). One thing to note is that the plotted depth of the individual potentials changes along different directions through the CNT. This means, that the particular direction displayed here is going through the centre of the top C pentagon and will not pass through any atoms directly. In this case, the XC potential has a higher influence than the Hartree potential. Furthermore, the local pseudopotential is very small as this is a short-range interaction and there are no ion cores close to the plotted line. If the potential is plotted either along another direction or along the same direction at a different xy position going through a C core, the influence of the core and Hartree potential become much stronger than the XC effects in the core region.

Nevertheless, the figure demonstrates, that the influence of the pseudo- and exchange-correlation potentials is short-ranged around the ion cores and does not have an effect on the potential at the boundary, while the Hartree potential is contributing over a long distance. This can better be seen in the inset, which shows an enlarged view of the plot-range around the Fermi level. The combination of both the Hartree and the XC potential give the potential barrier its distinct shape, and without accounting for XC effects, the barrier would be much lower. Including many-electron effects also has a large influence on the width of the potential well and subsequently the position at which the potential intersects with the Fermi level (black dashed line). This is also the point at which the Hartree potential increases beyond the chemical potential. In the case of a metallic material, this increase would indicate the creation of surface dipoles.

Based on these results in conjunction with the definition of the Fermi level to be the level below which the probability of occupation of orbitals is more than 50%, this location was chosen to represent a coherent definition of the metallic isosurface (hereafter labelled z_F) of the model. As mentioned in Section 3.2.1, this was important to correctly match the atomistic with the macroscopic model.

The validity of this definition is displayed in Figure 4.2, which shows a compar-

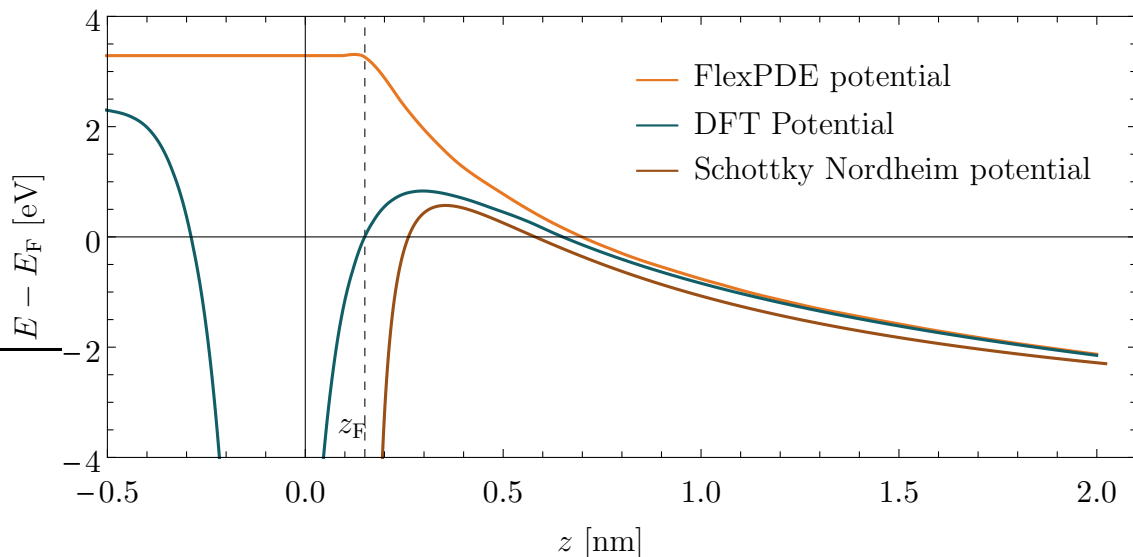


Figure 4.2: Comparison between the one-dimensional potential along the centre of the CNT found using the multi-scale model (DFT), the Poisson solver (FlexPDE) and a classical calculation for a spherical emitter with $r = 0.527$ nm (Schottky Nordheim barrier). All potentials were calculated for an applied field of 0.16 V/nm. The models diverge significantly around the ion core but agree well at larger distances. The black dashed line shows the defined metallic radius which was used for the classical models.

ison of the simulated potential distribution for an applied field of 0.16 V/nm using ONETEP (blue line) and the semi-classically calculated potential by FlexPDE solving Poisson’s equation (orange line). The latter is raised by the work function, as explained in Section 3.2.4. It illustrates, that both models match very well and are converging to the same boundary value which was set by the multi-scale simulation procedure (Section 3.2.4). The DFT potential however diverges quite significantly from the classical model close to the emitter surface, where the DFT potential exhibits a potential well. This effect is not present in the FlexPDE potential of the conducting rod as it does not take the ion cores or the work function into consideration but considers the field inside the conductor to be zero. The brown line represents a calculation of a classical potential as described by a Schottky-Nordheim barrier for a spherical conductor of radius $r = 0.527$ nm. All calculations are further adjusted to the Fermi level. Even though this model works reasonably well at a larger distance from the core, the barrier close to the ion cores diverges significantly from the ONETEP results.

Overall, the figure proves that, even though classical calculations work sufficiently well at a certain distance from the metallic surface, the more advanced atomistic-continuum model using DFT is needed to accurately represent the emitter tip region. Furthermore, defining the potential’s intersection with the Fermi level to define the metallic surface is a good approximation for all further simulations. The validity of this definition can further be seen in Section 4.1.2 (Figure 4.4) which shows, that the charge density is almost zero beyond z_F .

4.1.2 Electron charge density

One property of great interest for field emission is the CNT’s charge distribution in the absence and presence of an applied field. Thus, this section will first discuss the simulated charge density without external fields, as shown in Figure 4.3. As no external potential is applied, this charge represents the chemically induced electrons in the molecule. Here, the isosurfaces of a) 1%, b) 0.25% and c) 0.02% of the global maximum charge density of $717 e/\text{\AA}^3$ are plotted.

The first thing to note is that most of the electron density is situated around the carbon cores (Figure 4.3 a), which represents bound electrons. Those electrons are highly localised and will not contribute to the CNT’s conductivity. Following the decrease in charge density from 1% to 0.025% in Figure 4.3 b one can see that the electron charge is further located between the carbon atoms, forming the covalent bonds. In contrast, Figure 4.3 c illustrates that only a very small percentage of the overall electron density forms a delocalised sheet along the CNT body. This sheet lies

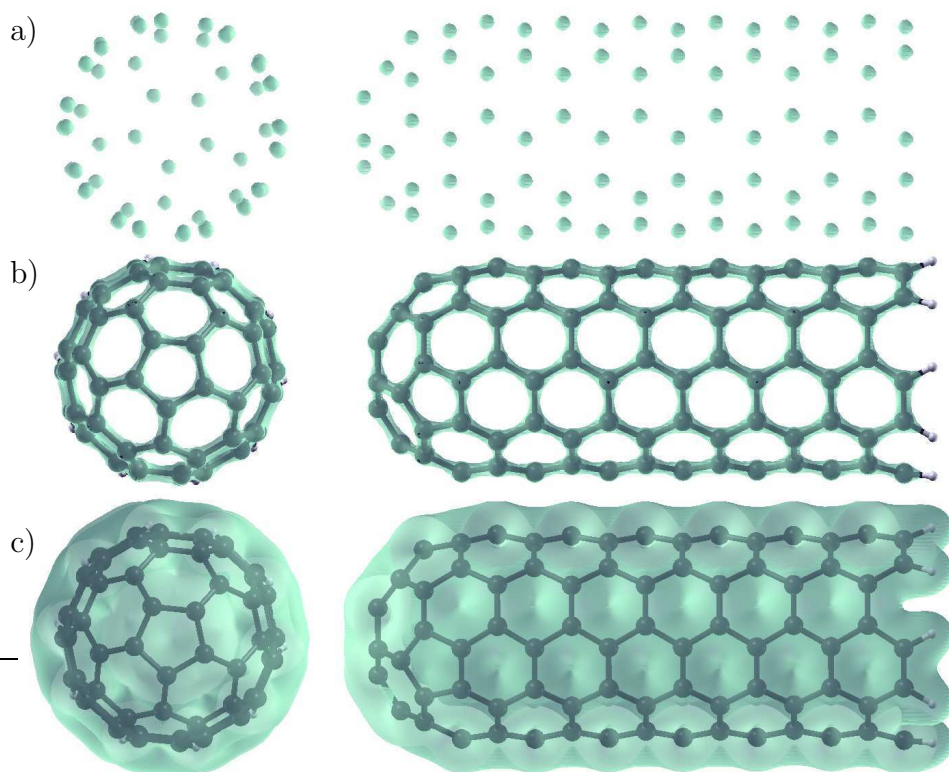


Figure 4.3: Electron density isosurfaces for zero applied field. The isosurfaces are at a) 1.00%, b) 0.25%, c) 0.02% of the global maximum charge density of $717 e/\text{\AA}^3$. In b) and c), isosurfaces are in green with the atomic frame of the CNT added. The views on the left are from the cap end.

at about 0.175 nm from the carbon cores and provides a path for electric charges to move along and around the CNT's surface. It also demonstrates, that in the absence of an applied field, the valence electrons are distributed evenly throughout the surface. Any additional charges, which might be induced due to an external electric field will be added to this outer sheath.

Figure 4.4 illustrates the correlation between potential energy and the electron density. Both quantities are plotted along the CNT's z -axis, going through the top pentagon ring. The plot confirms that, as mentioned above, most of the electron density is localised around the cores where the potential energy is lowest. The electron density falls off to near-zero at the Fermi equipotential, labelled z_F (black dashed line) with some charges spilling into the potential barrier ($E > E_F$), which might be caused by the finite temperature of $T > 0\text{K}$ of the system. The inset shows an enlargement of the plot around z_F and reveals an electron charge spilling of approximately 0.13 nm into the barrier (coloured area beyond z_F).

To further investigate very small changes in the electron charge between carbon atoms, a Mulliken population analysis was carried out. This analysis is based on

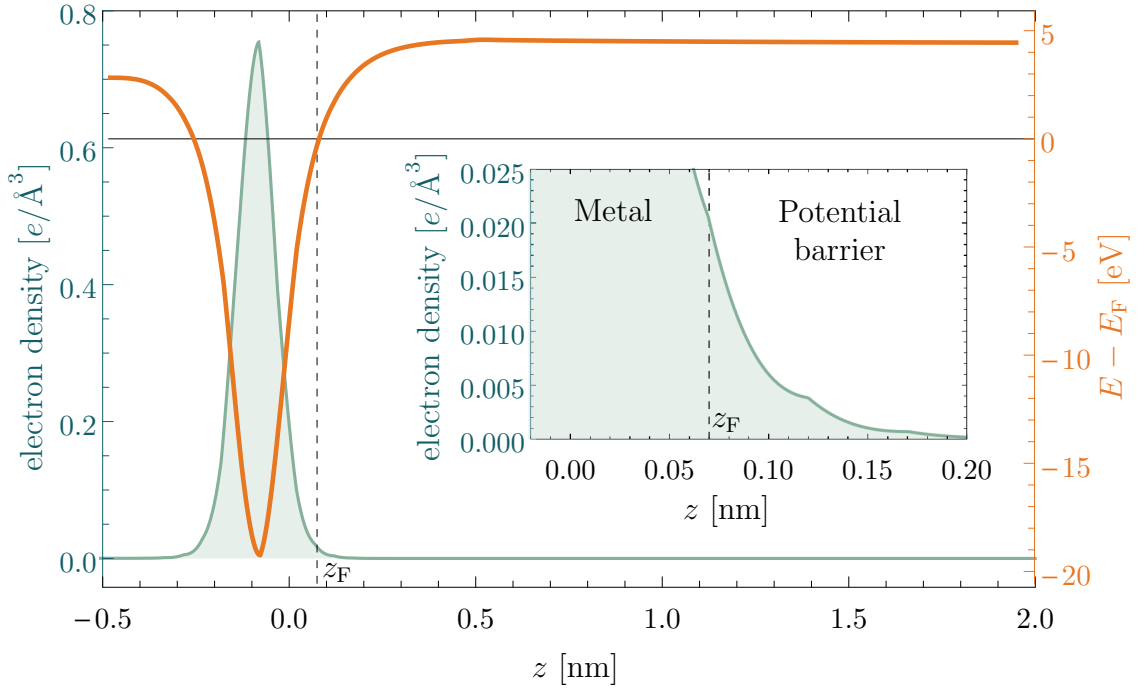


Figure 4.4: Relation between the charge density (blue) and the electrostatic potential (orange) along the CNT axis. The centre of the C atoms of the hemispherical cap are at $z = -0.08$ nm. The inset shows the spilling of electron charge into the barrier region ($z > z_F$).

the formalism described by Segall *et al.* [149] and provides a means of estimating partial atomic charges and the bonding, antibonding, or non-bonding nature of molecular orbitals. However, it suffers from a heavy dependence on the basis set used and the lack of a well-defined complete basis set limit, as well as possibly producing unphysical numbers of electrons, such as occupation numbers greater than two, which is forbidden by the Pauli principle [150]. However, the Mulliken population analysis still yields a useful qualitative description of the direction of charge transfer and the overall charge distribution of the CNT.

The plots in Figure 4.5 show the mean Mulliken charge population of each carbon layer along the CNT axis. One thing to note is the increase in negative charges at the apex, with a maximum charge transfer of $-0.007e$ and $-0.008e$ for the 2nd and 5th layer, respectively (Figure 4.5 top). These minor changes are too small to be visible in Figure 4.3 a-c. The reason for this shift in electron charges at the tip of the CNT is based on this region's increased curvature. The symmetry break and altered bond length at the high curvature surface result in the existence of additional localised states at the tip of the capped CNT. These states are filled by tube electrons as the tip experiences a decreased Coulomb repulsion compared to the tube. The idea is that the electrons along any surface repel each other due to

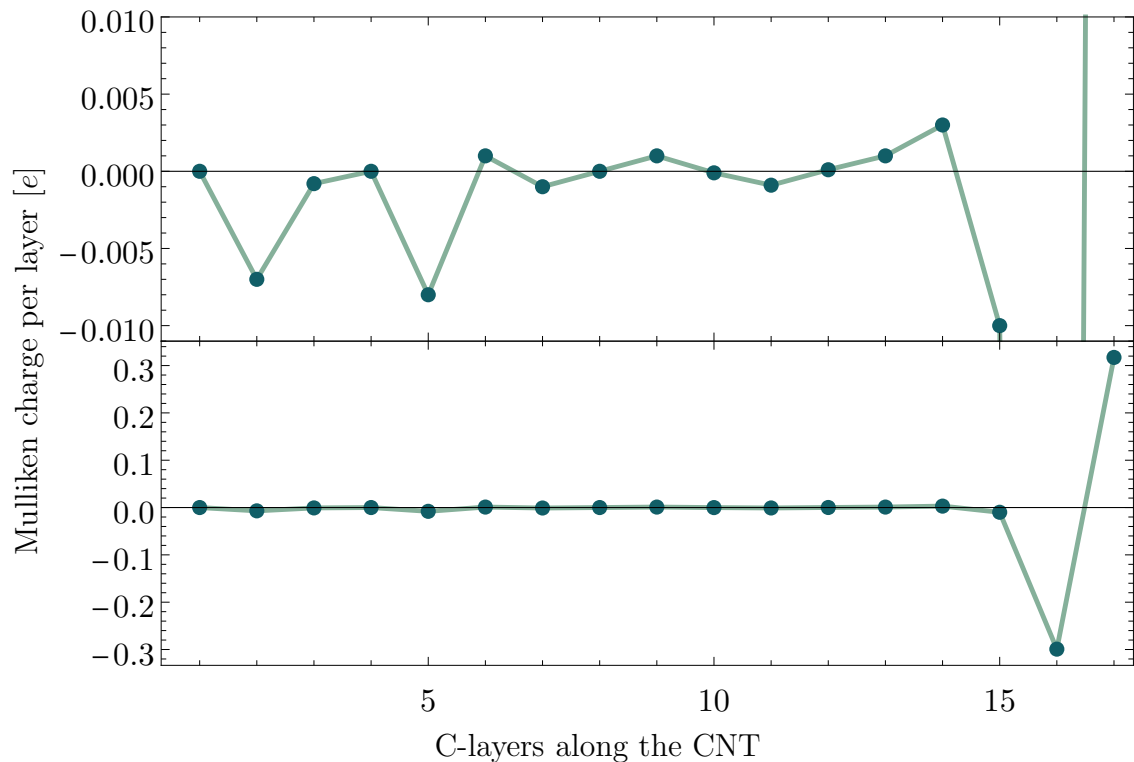


Figure 4.5: Mulliken charge population of the capped (5,5) CNT without an applied electric field. The values represent the mean Mulliken charges of each layer indexed as shown in Figure 2.7. The top plot is an enlargement of the bottom plot.

the Coulomb force. However, for electrons along a planar surface, this repulsive force is directed parallel to the surface, whereas for electrons along a curved surface, some part of this vectorised repulsive force is directed perpendicular to the surface and thus does not contribute to the electron’s separation. As a result, electrons along highly curved surfaces can accumulate more densely, since the repulsive force is effectively reduced. This is further verified as the “tube-layers” just before the cap have lost negative charge, indicated by the positive spike in Mulliken charges. The 5th layer is also a special case, as it represents the last tube-layer going from the symmetrical tube into the hemispherical tip. It can be seen that the break in symmetry leads to an increase of electrons. The bottom plot in Figure 4.5 shows the effect of the hydrogen atoms on the charge transfer along the CNT. It can be seen that the hydrogen atoms are positively charged in contrast to the CNT tip. The high increase in negative charges for the bottom C-layer before the hydrogen termination indicates, that the H atoms push electrons into the CNT body.

4.1.3 Electron charge density with applied field

The next step was to investigate the change in charge density in an applied field, where the total charge now consists of both chemically and electrically induced electrons. A three-dimensional illustration of the change in electron charge density for a background field of 0.162 V/nm, which induces three additional electrons into the DFT box, is shown in Figure 4.6 a. The magnitude of the change in density represented by these isosurfaces is $\pm 5 \times 10^{-3} e/\text{\AA}^3$, which is about 3×10^{-3} of the static charge density of the surface in Figure 4.3 b. Here, the positive excess electron charge is shown in orange, representing areas that have gained electron charge, whereas the green regions have lost electrons and thus carry a conventional positive

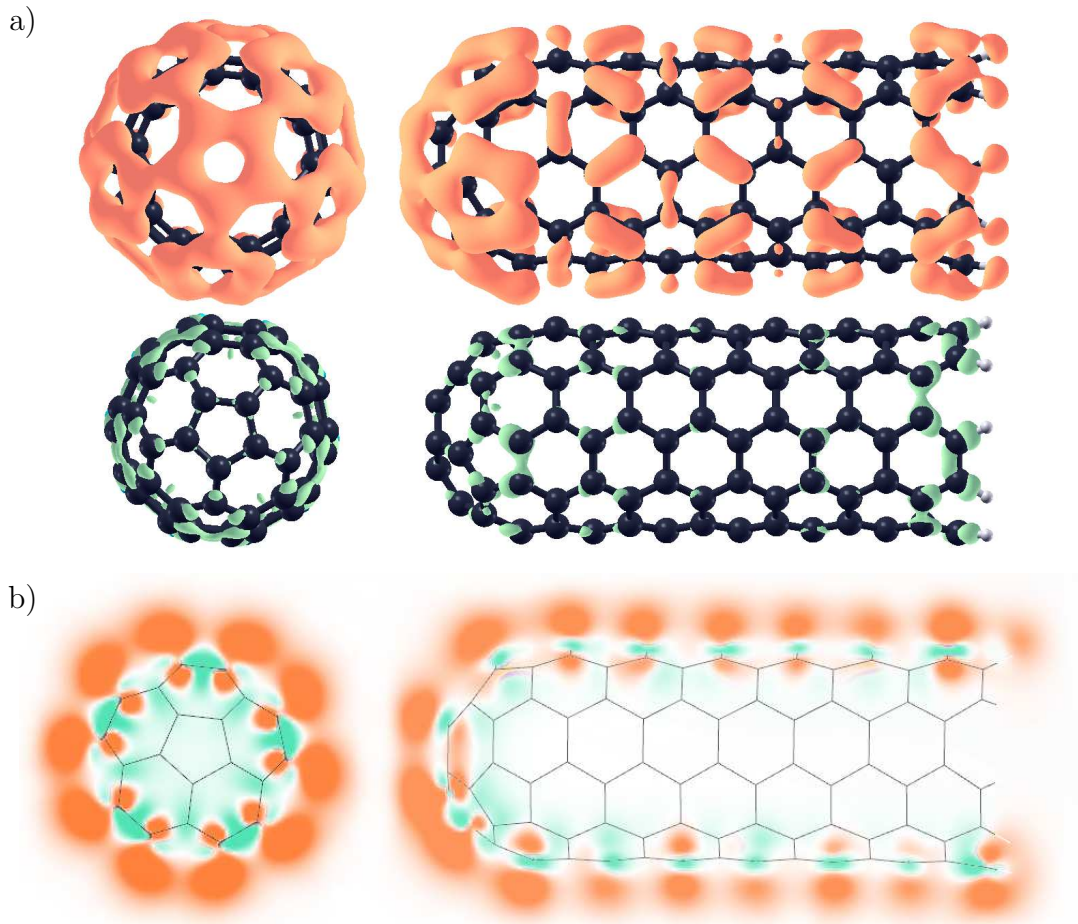


Figure 4.6: Change in electron density on application of 0.162 V/nm inducing three additional electrons. Here, orange (green) indicated an increase (decrease) in charge density. a) The upper isosurface indicates an increase by $5 \times 10^{-3} e/\text{\AA}^3$, while the lower represents a decrease by $5 \times 10^{-3} e/\text{\AA}^3$, relative to zero-field values. b) A 2D cut-plane along the CNT axis showing the dipole nature of the change in charge density upon applying an external electric field.

charge. The figure shows, that the induced excess electrons are mainly localised around the tip of the CNT. Comparing both plots in Figure 4.6 a indicates that the π -orbitals, which lie perpendicular to the CNT surface, have gained electron charge during charge redistribution, whereas the σ -electrons, lying in-plane, seem to have lost charge.

This can further be validated by Figure 4.6 b, which displays the two-dimensional change in electron density for a plane that includes the CNT axis and at least one of the atoms in the top layer (see Section 2.3.1). One can further see that the charge rearrangements display the nature of dipoles (or higher multipoles). This means that the π -orbitals of the carbon hemisphere tip can be easily polarised and extend further into the vacuum space under the applied electric field, resulting in the charge redistribution.

4.1.4 Local density of states

The density of states (DoS) describes the number of states at each energy level that is available to be occupied by electrons, making it another important quantity for understanding any field emission system. In finite systems, however, such as the CNT discussed here, the density distribution is discrete and exhibits local variations. Thus, one uses the projected or local density of states (LDoS).

To better compare the LDoS for the different CNT regions, all values are normalised by dividing the number of states by the total number of atoms in the respective region (*i.e.* tip, tube, and complete model). Furthermore, as only the orbitals close to the Fermi level contribute to field emission, all figures show only

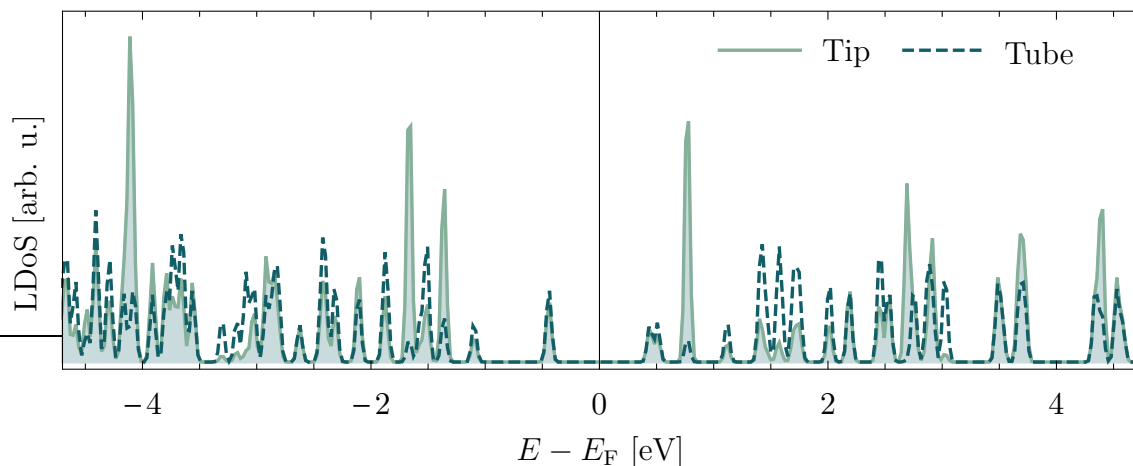


Figure 4.7: Local density of states as a function of energy near the Fermi level, for the tip (filled light blue region) and the tube (dashed, dark blue line) without an applied field.

the densities of states from -5 eV to 5 eV around E_F . The energy levels are fitted with a Gaussian function of 0.025 eV (300 K) FWHM.

As the model is a finite, heterogeneous structure, the first thing to investigate is the difference in LDoS between tip and tube region. This difference is shown in Figure 4.7, in which the density of states for the tip is represented by the filled, light blue area and the tube by the dark blue dashed line. Here, one can see that the tip region has a slightly higher LDoS compared to the tube, particularly in the close vicinity of E_F , with peaks at about -1.6 eV, -1.4 eV and 0.7 eV. This enhanced density indicates that the number of available states increases for highly curved surfaces, which means additional local states are introduced at the tip. As discussed in the previous section, this forces electrons to accumulate at the apex of the emitter.

Figure 4.7 further indicates that the investigated CNT only has states near the Fermi level at about ± 0.5 eV but none at E_F , resulting in a band gap of approximately 1 eV. This shows that although a $(5,5)$ armchair CNT is supposed to be metallic [107], this specific capped armchair CNT is semiconducting as it has an energy gap between its highest occupied molecular orbital and lowest unoccupied molecular orbital. The reason for this band gap is the finite nature of the investigated molecule.

As has been shown in literature, a infinite $(5,5)$ CNT is metallic and thus exhibits no band gap, however, the investigated model's finite size constrains the wavelengths of the electronic states in such a way that there are no allowed states at the Fermi level. Due to this effect, it has been found that the band gap of a finite CNT tents

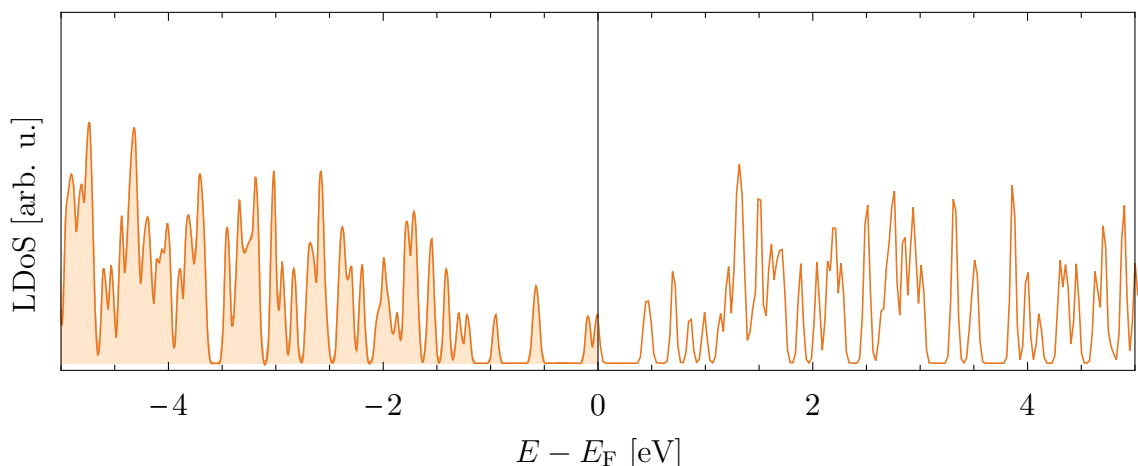


Figure 4.8: Total local density of states as a function of energy near the Fermi level, for the full 28-layer CNT without an applied electric field. The existence of local states at E_F validates the model's metallic nature.

to oscillate as a function of number of C atoms and length [151,152]. To investigate this effect, the LDoS of a longer 28-layer capped (5,5) single-walled CNT, consisting of 260 C atoms arranged in 4 tip-layers and with 24 tube-layers, was simulated and compared to the shorter 16-layer CNT (4 tip-layers and 12 tube-layers, as shown in Figure 2.7).

As can be seen in Figure 4.8, the long CNT has an increased LDoS compared to the short CNT with additional localised states at the Fermi level. This result shows that the longer molecule exhibits the expected metallic behaviour, which validates the hypothesis that the finite nature of the CNT influences the LDoS of the model. Despite the evident energy gap for the shorter 16-layer CNT, this model represents a reasonable proxy for a metallic CNT. Firstly, because it only represents the tip of a much longer CNT system, as described by the used BC, which would allow for more states at the Fermi level. Secondly, because it has been found that relevant material properties such as work function and electrostatic potential are the same for the 16-layer CNT and the metallic 28-layer CNT.

The next step was to investigate how the LDoS would behave in an external field. For this, electric fields of 0.054 V/nm, 0.108 V/nm and 0.162 V/nm, where each field adds one additional electron to the system, are applied. The change in LDoS relative to the Fermi level is plotted in Figure 4.9 for the four tip carbon layers. Here one has to consider, that the value of E_F changes as additional electrons are induced in the system. Hence, the LDoS is adjusted according to the value found by ONETEP for each field (see Section 4.1.1). The figure demonstrates that the energies of local

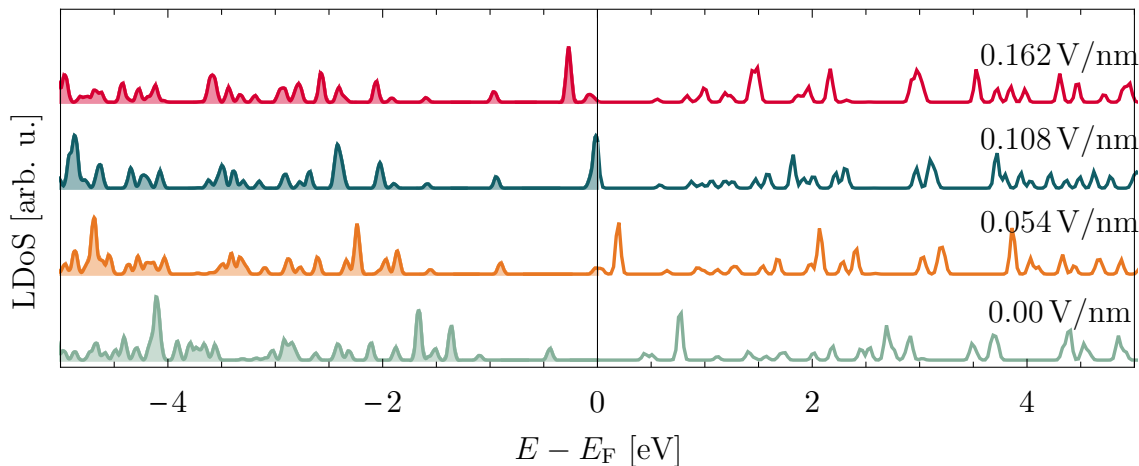


Figure 4.9: Local density of states as a function of energy near the Fermi level, for four values of applied field. Each field induces one additional electron into the system. The normalised density has been collected from the top four layers of the CNT's tip.

orbitals are lowered under the influence of an applied external field, with some of them even dropping below the Fermi level. Subsequently, newly induced electrons from the cathode can occupy these local orbitals. Furthermore, the shift of the band-gap-like valley results in an increase in LDoS around the Fermi level. Consequently, the system's corresponding emission probability increases as the applied electric field increases.

4.1.5 Energy levels

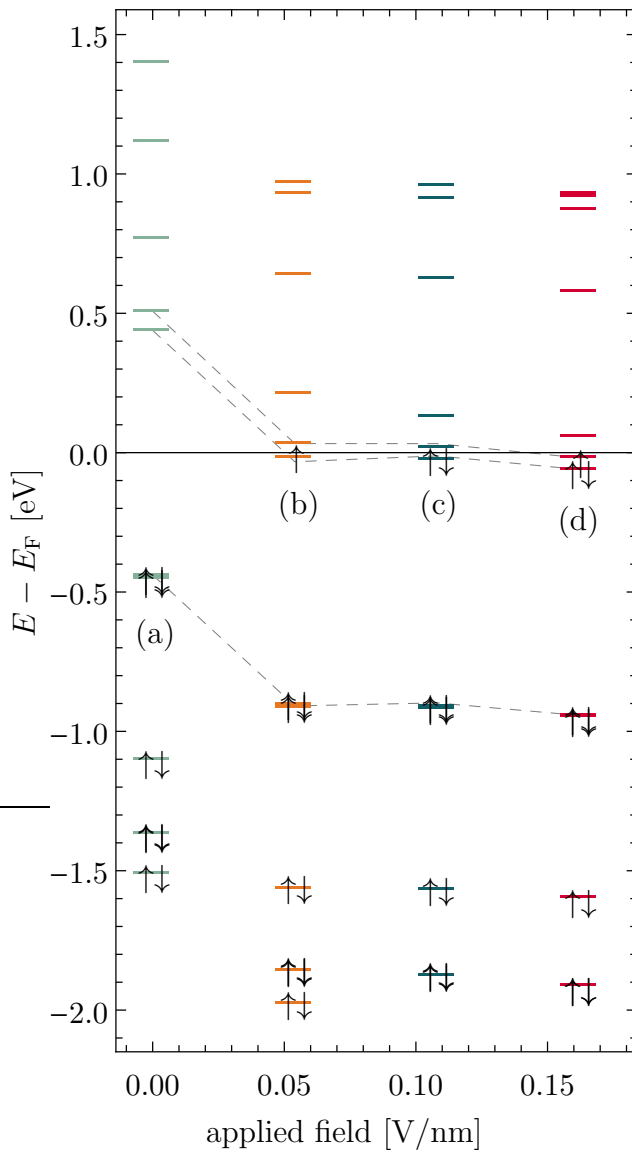


Figure 4.10: Change in orbital energies with applied field. The dashed lines indicate energy changes in HOMO and LUMO. The arrows represent spin-up and spin-down electrons.

Another way of assessing a material's field emission behaviour is to investigate the exact changes in energy of individual molecular orbitals around the Fermi level. Here, especially the change in the highest occupied molecular orbital (HOMO), which is a molecule's highest energy orbital that still contains electrons, and the lowest unoccupied molecular orbital (LUMO), which is the next highest energy orbital which an electrically induced electron would occupy, are of interest. The energy difference between the HOMO and LUMO, *i.e.* the HOMO-LUMO gap, ΔE_{HL} , is generally the lowest energy needed for electronic excitation in a molecule. The existence of such a gap for the CNT investigated here again shows that it is indeed semiconducting. Even though the information gained by investigating the exact change in molecular orbitals is similar to the LDoS they will give a few more details about the material not obtainable

from Section 4.1.4. As mentioned in Section 4.1.1 the Fermi level of the CNT remains constant as the external field varies. Thus, one can compare the energy levels by aligning their respective Fermi levels. Figure 4.10 shows the orbital energies when adjusted to such a constant Fermi level. Here one can see clearly that the energies of local orbitals decrease under the applied external field with some of them being lowered even below E_F . This results in external electrons being induced from the cathode to subsequently occupy these local orbitals. Generally, two electrons with opposite spin can occupy an orbital which is indicated here by up and down arrows. The orbitals labelled with (a), (b), (c) and (d) correspond to the highest occupied molecular orbitals discussed in Section 4.1.6.

Although DFT is known to under or overestimate the real band gap of a material, it is still worth investigating the relative change in ΔE_{HL} when examining field emission properties. As previously mentioned in Section 4.1.4, the CNT model shows semiconducting properties with a small HOMO–LUMO gap of 0.87 eV without an applied field. However, ΔE_{HL} decreases when an external field is applied and thus demonstrating a more metallic behaviour with gaps as small as 0.007 eV for 0.162 V/nm.

4.1.6 Molecular orbitals

As mentioned in the previous section, field emission mainly occurs from the HOMO and LUMO which are the closest states to the Fermi level. Thus, their spatial distribution along the capped (5,5) CNT and their properties are of particular interest. Therefore, this section will analyse these two molecular orbitals in more detail.

The change in spatial distribution for the HOMO for four externally applied electric fields is presented in Figure 4.11 a-d, where all isosurfaces are plotted for an amplitude of $\pm 0.0004 (e/\text{\AA}^3)^{1/2}$. As can be seen in Figure 4.11 a, the HOMO distribution without an applied field resembles an extended delocalised π -state that covers the entire surface of the CNT. Its distribution around the tube contains a component that is independent of azimuthal angle and it is non-zero on the axis. This azimuth-independent component disappears when an external field is applied (Figure 4.11 b-d). On successively inducing additional electrons with alternate spins into the DFT box, the HOMO exhibits changes in identity, energy level and spatial distribution. This suggests that the distribution of emitted current can also be expected to vary with the applied field.

While the structure analysed here is non-periodic on the scale of its total length, it has a periodicity similar to that of a (5,5) CNT of infinite length on the scale of the interatomic bonds. Thus, the structure has a periodicity and bond properties

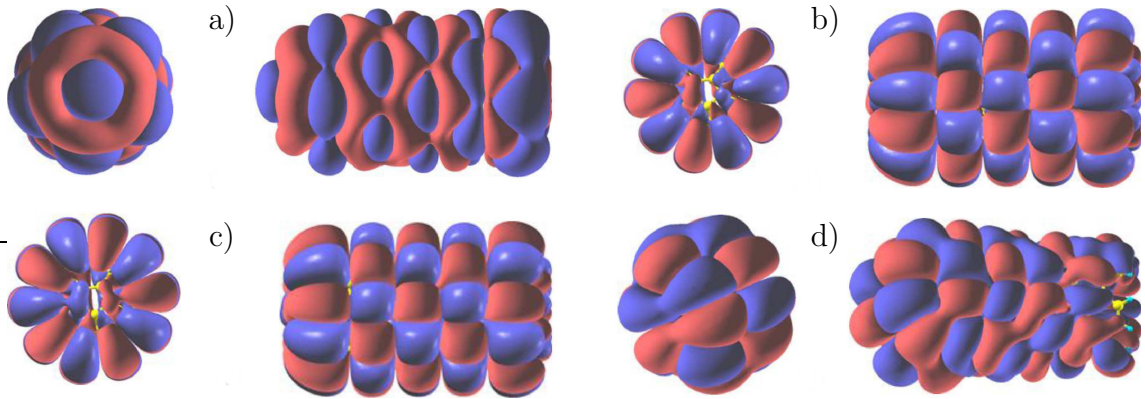


Figure 4.11: HOMO isosurface for the (5,5)CNT at amplitude of $\pm 0.0004 (e/\text{\AA}^3)^{1/2}$, a) in zero field, b) in 0.054 V/nm, c) in 0.108 V/nm and d) in 0.165 V/nm. Figure reproduced from reference [147].

related to those of graphene, whose behaviour can be described in terms of the hybridisation of the different orbitals (see Section 2.3.1). The s -, p_x - and p_y -orbitals merge to form planar sp^2 -hybrids, which then form covalent σ/σ^* -bonds with adjacent carbon atoms, while the remaining out-of-plane p_z -orbitals form delocalised π/π^* -bonds. These lie above and below the atomic frame with energies close to the Fermi level, and thus providing a conducting path over the whole of the graphene sheet. Inspection of the orbitals in Figure 4.11 b-d shows that the HOMO's axial wavelengths are similar but do not correspond to the width of either one or two hexagons in the CNT structure. This suggests that electrons in the HOMOs are sufficiently delocalised to form the orbitals of Figure 4.11 without being influenced or constrained by the hexagonal structure of the atomic lattice.

Figure 4.12 shows the distribution of the charge densities for the HOMO and LUMO with and without an applied electric field. The isosurfaces are chosen to represent 25% of the total charge density. In the case of a CNT without an applied field, it can be seen that, while the HOMO and LUMO are mainly localised along the tube, the states also spill into the tip region, building an extended state (Figure 4.12 a). Figure 4.12 b illustrates the HOMO's and LUMO's charge densities under 0.162 V/nm electric field. Here, the electron charge of both the HOMO and LUMO are localised at the tip of the structure and leak out from the atomic frame along the z -axis. This can be understood by considering the different alignments of the p_z -orbitals along the molecule. While the p_z -orbitals along the tube lie perpendicular to the applied field, the top pentagon ring has its p_z -orbitals parallel the electronic field. Thus, the orbitals at the tip are easier to polarise than the orbitals along the tube. As field emission mainly occurs from the orbitals closest to the Fermi level, the HOMO in Figure 4.12 b indicates the emission area and pattern for

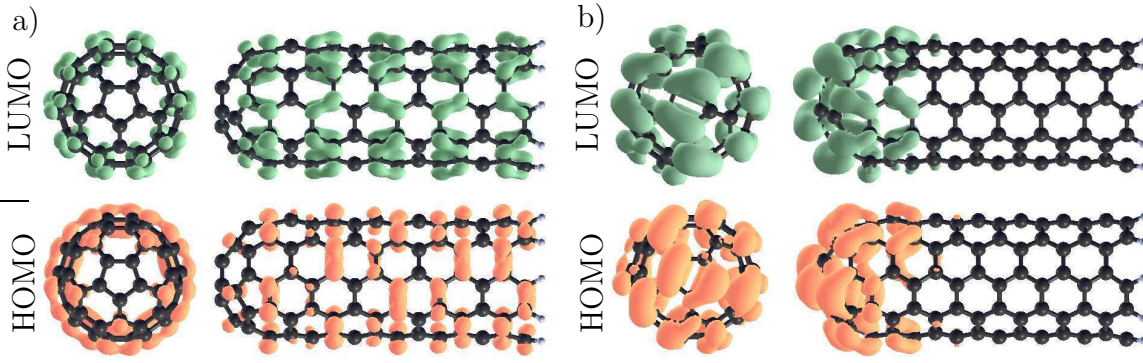


Figure 4.12: Electron charge densities of the HOMO and LUMO at a) zero applied field and b) with an applied field of 0.165 V/nm . The isosurfaces represent 25% of the total charge density of $0.0019 e/\text{\AA}^3$.

this particular CNT configuration for 0.162 V/nm applied field. As all additionally induced electrons will fill up the LUMO first, the figure also demonstrates that these charges will be localised at the tip.

4.1.7 Binding energy

Another simulation parameter worth investigating is the change in binding energy of the system under an applied field as this value reflects the bonding strength between atoms and thus represents the CNT's stability. Here, the binding energy E_B can be obtained from the following formula

$$E_B = (E_{\text{tot}} - nE_{\text{sg}}), \quad (4.1)$$

where E_{tot} represents the total energy of the system gained from the converged simulation, while E_{sg} represents the energy of a single atom multiplied by the number of atoms in the system. For the individual elements used in this dissertation, an atomic energy of $5.3890 E_h$ for C and $0.4454 E_h$ for H was found.

Figure 4.13 shows the change in total binding energy of the system as a function of the applied field strength. As can be seen, the binding energy of the CNT is 1519.4 eV without an applied electric field and increases up to 1531.9 eV in an external field of 0.18 V/nm . This increase suggests that the CNT exhibits an improved stability when exposed to an electric field. One possible reason for this effect could be the change in charge distribution along the CNT, as more electrons are induced into the system which improves the shielding of the atomic cores. Another cause for the increased stability could be a structural relaxation process in which the atomic cores find an energetically more favourable position. However, experiments

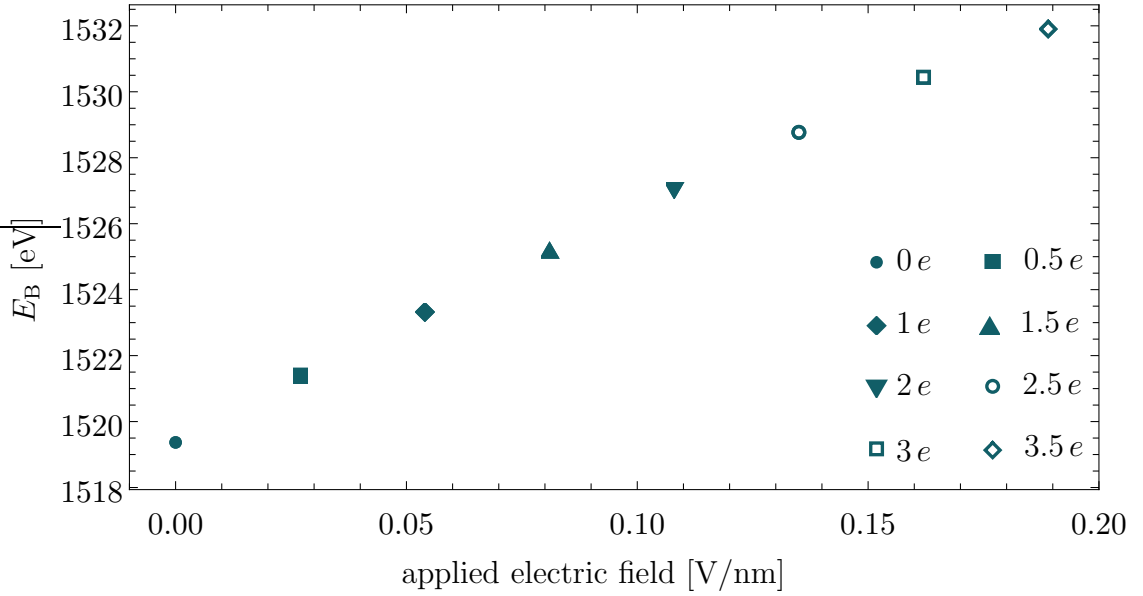


Figure 4.13: Changes in total binding energy of a capped (5,5) CNT under the influence of externally applied electric fields. Each field induces additional $0.5e$ into the model.

have shown that CNTs tend to break and possibly disintegrate under high electric fields [153]. Thus, the increased stability is expected to decrease after a certain threshold voltage.

4.1.8 Potential barrier with applied field

One parameter of great significance for the field emission properties of any emitter is the shape, width and height of the potential barrier. Thus, this section will give a detailed investigation of the changes in potential barrier with different applied fields. All potentials are again aligned by their respective Fermi levels. By doing so, the potential distribution near the atomic cores is found to vary very little with applied field.

A 2D and 3D representation of a longitudinal plane through the DFT box for an applied anode-cathode voltage of 16 V is shown in Figure 4.14. This plane contains the CNT axis and passes through one of the carbon atoms at the top pentagon ring (as indicated in Figure 2.7 a). Here, the contour-lines are plotted in steps of 0.2 eV, while the colours represent the potential energy with respect to the Fermi level, with orange being above and green being below E_F . The red dashed line in both the 2D and 3D image indicates the crossing of the potential energy through the Fermi equipotential, thus the region between these lines is defined as the effective tunnel barrier.

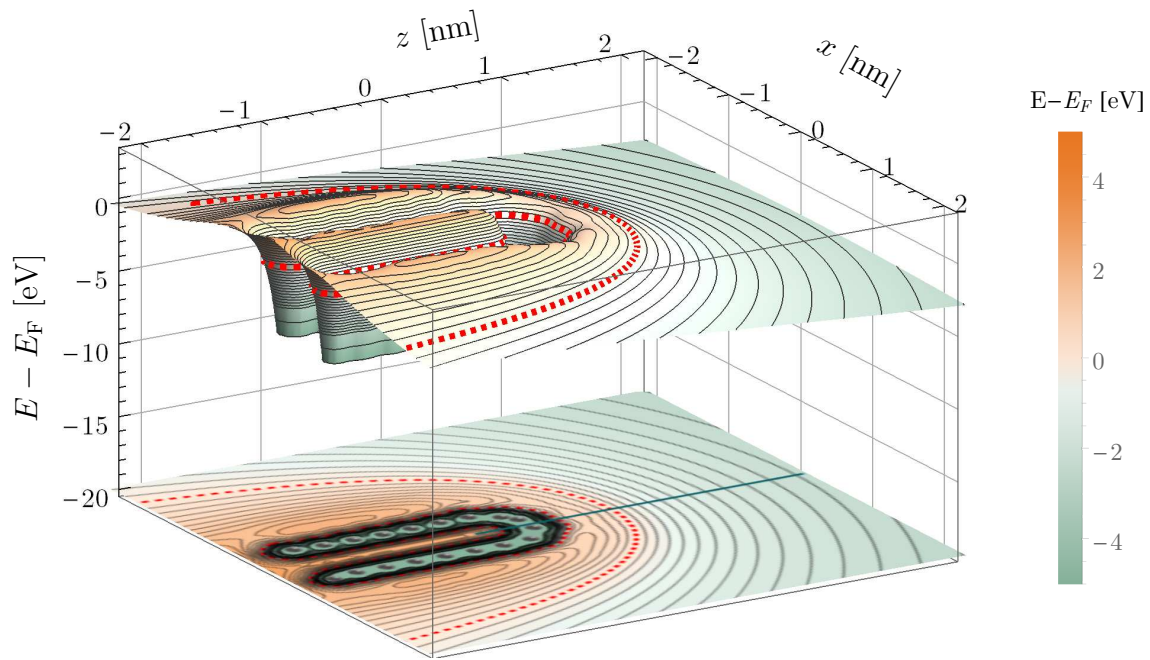


Figure 4.14: 2D and 3D representation of a section containing the CNT axis, showing the potential energy ($E - E_F$) for a background field of 0.162 V/nm and with three excess electrons. The red dashed outline is the crossing through the Fermi level. Equipotentials above and below E_F are at intervals of 0.2 eV. The coloured line starting from ($z = 0.5$ nm, $x = 0$ nm) indicates the directions of the 1D potentials shown in Figure 4.15. The grey dots in the 2D plot indicate the positions of the carbon cores.

As can be seen from the 3D plot, the potential barrier becomes finite upon applying an external field. The contours also indicate that both the potential barrier height and width are lowered and narrowed more at the CNT's apex than at the walls. This is expected as the external field produces a larger component normal to the apex than normal to the tube wall. Increasing the applied field will lead to a further decrease of barrier height and width, which will be more pronounced at the tip apex than at the tube walls. This shows that firstly any possible emission will happen in the apex region first and secondly that the emission current density will be much greater at the apex than from the tube walls. Furthermore, it can be seen that the potential energy is lowest at the atom cores where most of the electrons are located^a.

Figure 4.15 shows one-dimensional plots of the total potential energy relative to the Fermi level along the green line, indicated in Figure 4.14. This line was plotted for eight values of background field: 0 V/nm, 0.026 V/nm, 0.054 V/nm, 0.081 V/nm, 0.108 V/nm, 0.135 V/nm, 0.162 V/nm and 0.189 V/nm and lies along the axis, going

^aThe potential is clipped at -5 eV for better visualisation.

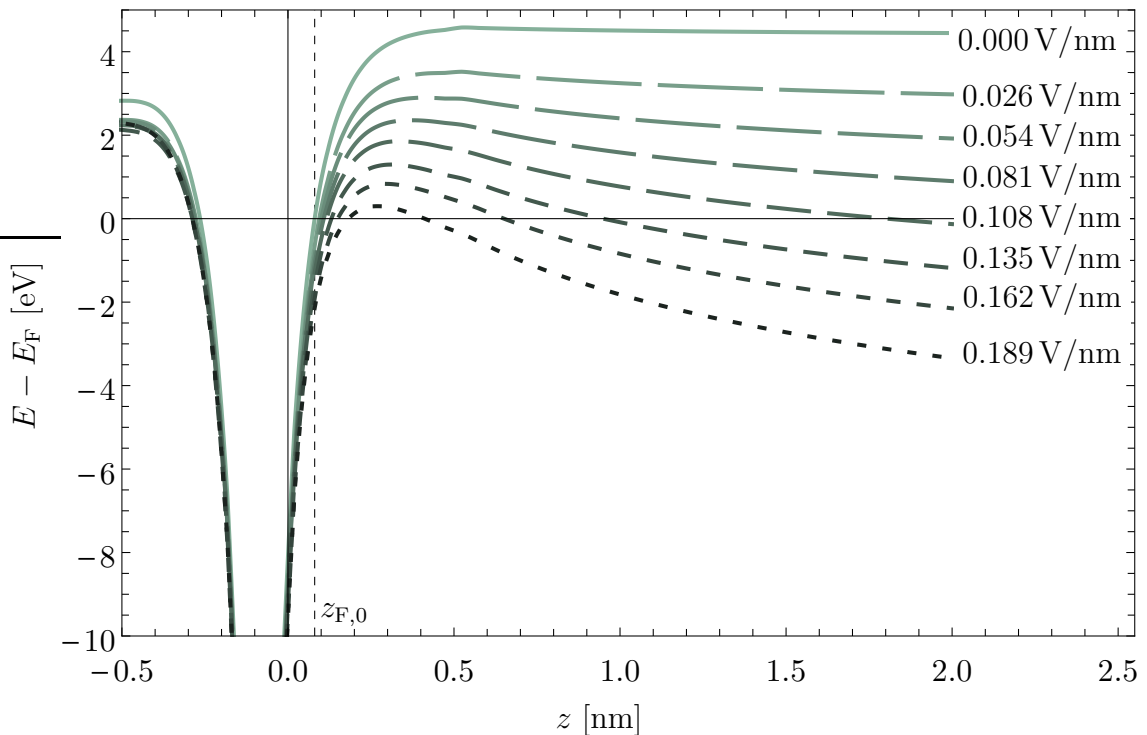


Figure 4.15: Potential energy at 100 K, along the z -axis indicated in Figure 4.14, for eight values of applied electric field inducing additional charges from zero to $3.5e$ in increments of $0.5e$. The black dashed line indicates the Fermi equipotential at zero field ($z_{F,0}$).

through the centre of the topmost pentagon ring, with the C cores located at about $z = -0.08$ nm. The first thing to note is that, as expected, the potential barrier decreases with increasing applied field. Any further increase in external field strength would lower the potential barrier below the Fermi level, which would induce full emission from one or more orbitals. This feature is currently not implemented in the DFT code as this would require time-dependent DFT, whereas the current code is limited to stationary systems.

At some point in the intermediate range of applied field, the tunnel barrier becomes sufficiently narrow for electrons to tunnel through, leading to the onset of field emission. The tunnel barrier width at E_F for 0.108 V/nm, 0.135 V/nm, 0.162 V/nm and 0.189 V/nm is plotted in Figure 4.16 a. It can be seen, that the simulated tunnel barrier width decreases exponentially with increasing field. At a field of 0.189 V/nm the barrier width is as small as 0.08 nm, which should be sufficiently narrow for electrons to tunnel through. However, the simulations in their present form do not give the exact threshold field at which emission occurs. Furthermore, the figure compares the simulation results (green dots) with results from classical calculations (orange triangles) using the Schottky-Nordheim equation in Table ??, which ap-

proximates the CNT apex as a spherical conductor. The comparison shows similar behaviour for both models, however, the classical model underestimates the tunnel barrier width, which in turn would give an underestimation for the threshold field at which field emission occurs. This discrepancy between the DFT results and the classical calculations seems to decrease for higher fields.

Generally, as with all polarisable systems, applying an electrostatic field to the CNT causes an increase in its dipole moment at the tip. This in turn creates a change in local-field near the negatively charged apex. As a result, the potential barrier height is reduced, as shown in Figure 4.16 b. Here, the simulated barrier height is compared to classical calculations and reveals that both behave almost identical, following a linear decrease. However, the classical potential is continuously smaller than the simulated results. One reason for this discrepancy could be because the classical calculations do not take changing surface dipoles and XC effects into account. These effects on the change in barrier height can only be retrieved with the DFT calculations. Based on the barrier height and the slope one can also calculate the field enhancement factor. With the external field of 0.162 V/nm, the maximum accelerating field in the barrier region is about 2.9 V/nm. This field is about 0.23 of that obtained using the classical enhancement factor calculated using Eq. (2) from

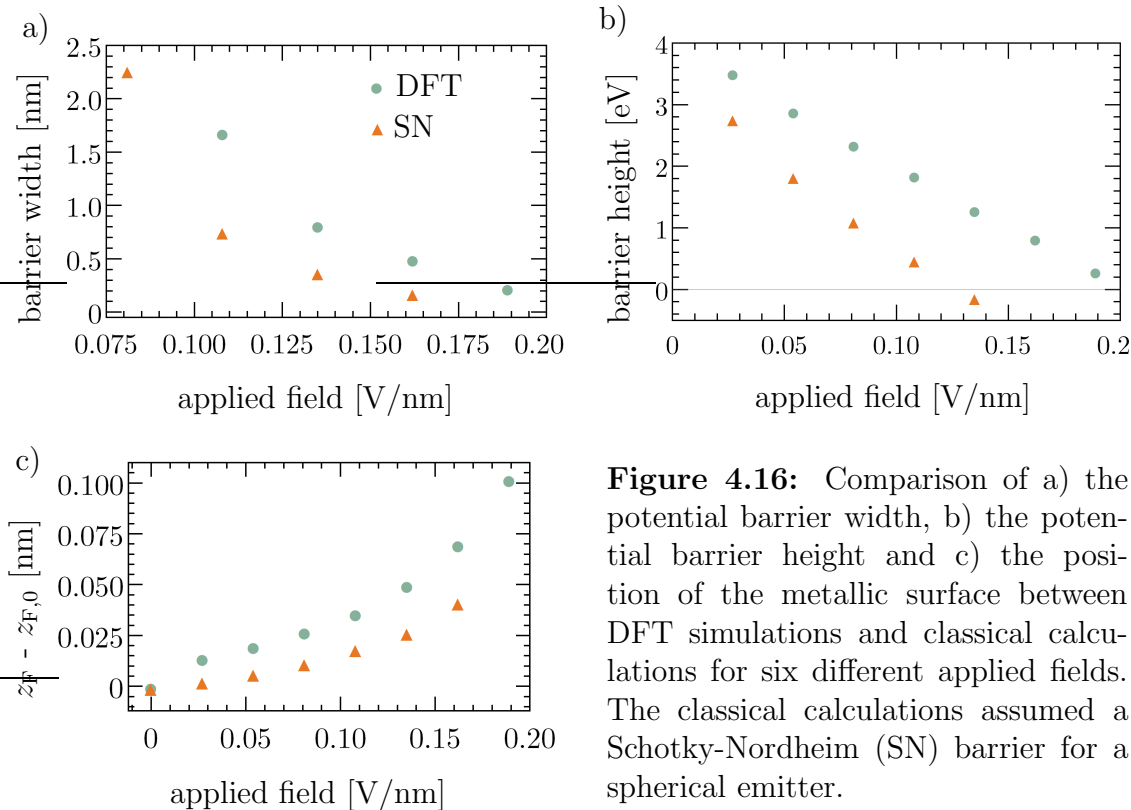


Figure 4.16: Comparison of a) the potential barrier width, b) the potential barrier height and c) the position of the metallic surface between DFT simulations and classical calculations for six different applied fields. The classical calculations assumed a Schotky-Nordheim (SN) barrier for a spherical emitter.

Ref. [154].

As mentioned in Section 4.1.2, the material's surface is defined by the Fermi level's isosurface. This means that all additional charges induced by the external field increase the radius of this delocalised sheet of electrons. This effect can be seen by the changing location of the intersection of the potentials with the Fermi equipotential (z -axis) in Figure 4.15. Here, the point of intersection moves slightly away from the C cores, increasing from $z = 0.0806$ nm in zero field (labelled as $z_{F,0}$) to $z = 0.18$ nm in a background field of 0.189 V/nm. Figure 4.16 c shows the plotted change in Fermi equipotential along the z -direction relative to $z_{F,0}$. It can be seen, that z_F increases exponentially as more electrons are induced which will accumulate at the tip. Again, the classical calculations follow the same trend but underestimate the change in z_F compared to the ONETEP simulations. While the DFT simulations take a change in electron charge and subsequent change in metallic radius into account, classical calculations only consider static dimensions for the emitter model.

4.1.9 Work function

The work function of a material is another very important parameter when investigating the field emission properties of a structure. It is defined as the difference in energy between the vacuum potential and the Fermi level in the CNT via

$$\Phi = E_{\text{vac}} - E_{\text{F}}. \quad (4.2)$$

Here, the vacuum potential is chosen as the uniform potential at a distance of many interatomic spacings from all the cores, in zero field.

To analyse the influence of exchange and correlation effects on the behaviour of the work function three simulations will be compared. In the first calculation the LDA with the PW92 functional [118] is used, the same calculation was then performed using the GGA with the PBE functional (Perdew, Burke and Ernzerhof [155]) and the third was done by omitting the contribution from XC effects. In the third case, the terms remaining in the energy functional then only include the energy due to the external field together with the electrostatic energy, which consists of the kinetic energy, the Coulomb term (valence electrons) and the core term (nuclei and electrons from inner shells).

The comparison of these calculations is shown in Figure 4.17, which reveals a clear difference between all three results when they are aligned by their respective Fermi levels. Here, the first thing to note is, that on the axis at $z > 0.15$ nm the work

function without XC, which results from the dipole effect of negative charge outside the framework of atomic cores, is significantly lower with Φ being about 2.49 eV. This value is much less than any work function found by including XC effects and less than experimentally measured work functions. Only when exchange-correlation effects are taken into account in the calculation of E does the work function increase to about 4.45 eV for the LDA and 4.22 eV for the GGA simulation. The position and shape of the edge of the potential differ for the simulation without an XC functional. Here, the curvature is higher and reaches its constant value at about 2.5 Å from the core.

The two simulations using different XC functionals are very similar in shape and value. Both have the same curvature and reach a constant value at about 5 Å from the C cores. They only differ due to their simulated work function, which only varies by 0.23 eV. However, the LDA simulation with $\Phi = 4.45$ eV is in better agreement with other calculations using different DFT codes. These simulations have yielded work functions for an infinite (5,5) CNT of 4.53 eV [156], 4.63 eV [157] and 4.685 eV [158], while simulations for a hemispherically-capped (5,5) CNT found 4.78 eV [159].

Analysing the simulations' behaviour close to the nuclei at about $z = -0.1$ nm in Figure 4.17 one can see, that in all three cases the potential drops below the

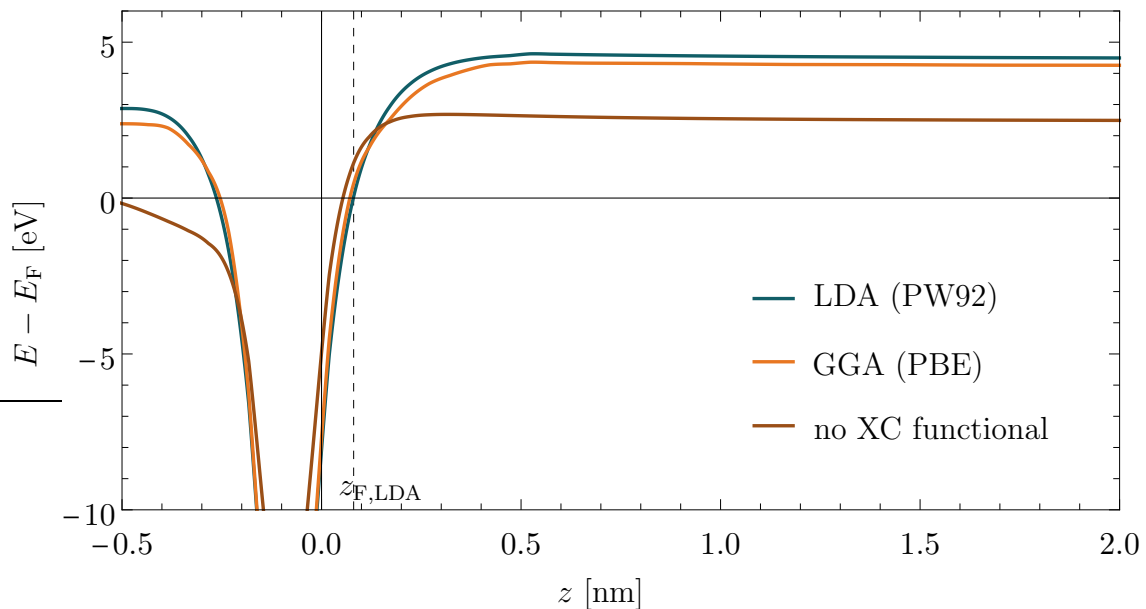


Figure 4.17: Comparison of the simulated potential energy along the CNT axis using an LDA, GGA and without a XC functional, which result in work functions of 4.45 eV, 4.22 eV and 2.49 eV, respectively. The black dashed line indicates the Fermi equipotential at zero field using the LDA functional ($z_{z,LDA}$).

Fermi level by many electronvolts. However, as the calculations presented here use pseudo-potentials to estimate the potential in the core region, the potentials shown in that region should not be assumed to be an accurate representation of the potential. Furthermore, the exact value of the potential well is determined by the plotted direction (see Section 4.1.1).

To summarise, the results gained from these initial atomistic-continuum simulations gave a deeper insight into material properties and size-related effects which are important to predict and design point-like field emission sources. In particular field- and shape-dependent charge density redistributions and potential barrier shapes, are imperative when considering novel field emitters. Using these results, predictions about an emitter's FE properties like the emission pattern, brightness or threshold voltage can be made.

4.2 Initial analysis of a W pyramid

This section will focus on another type of field emitter based on a tungsten needle. This was done, as not only is W one of the most commonly used materials for field emission but also it can be etched into ultra-sharp tungsten tips, which only have a single atom at the apex.

4.2.1 Geometry optimisation

The first step in any simulation is to design an adequate DFT model which represents the emission area of the macroscopic model and to optimise its geometry. Here, the emission tip of the W cone is approximated by a four-sided pyramid. For this, the atoms were arranged in a bcc lattice with the $[100]$ direction pointing along the pyramid axis and the pyramid faces corresponding to the $\{110\}$ surfaces, as shown in Figure 4.18 a. This orientation was chosen as the $\{110\}$ surfaces were found to be the energetically most stable structure with about 2.1 J/cm^2 [160]. The next step was to determine a sufficient size for the model to represent the macroscopic structure while still being small enough to be simulated in a reasonable amount of time. Here, previous simulations regarding the number of atomic layers in the pyramid, which are not shown here, indicated that if the pyramid is too small it behaves like a non-metallic molecule, while larger pyramids would take too long to simulate. Thus, for the simulations presented here, a pyramid was chosen which consists of six pyramid-layers and a bottom layer totalling 116 W atoms and which is terminated with 36 H atoms, as depicted in Figure 4.18 a. This model exhibited the most promising results regarding its metallic behaviour, while keeping the simulation time reasonably low.

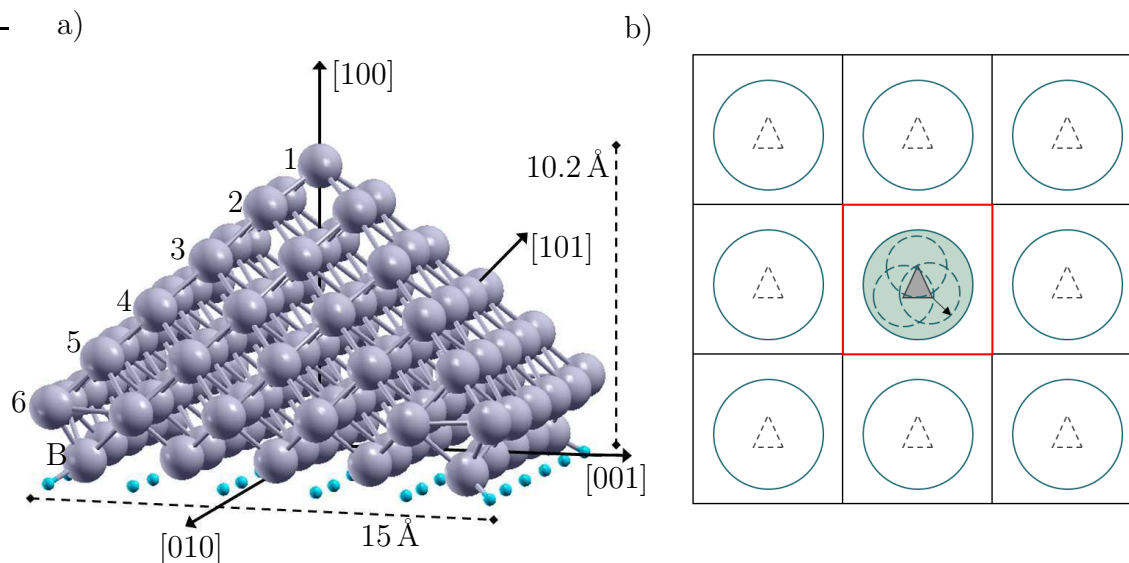


Figure 4.18: a) 2D image of the four-sided W pyramid showing its dimension and crystallographic directions. b) Schematic of the periodic “Coulomb cut-off” boundary condition where the main cell is indicated in red and periodically repeated images are shown in black. For these boundary conditions to be used, the distance between the simulation models must be large enough such that their respective overall Coulomb potential (light green circle), which is a combination of individual Coulomb potentials around the atoms, does not overlap with other models. The grey triangle represents the W pyramid model.

The problem with simulations involving W atoms lies with their large number of electrons. Compared to the C atoms used in the CNT, where each has 6 electrons, W has 74 electrons per atom, which increases the computation time immensely.

For the geometry optimisation of this specific structure, periodic boundary conditions were used based on the “Coulomb cut-off” approach^b. This approach uses a truncated form of the Coulomb potential which confines it within a certain radius. This way it is possible to use periodic boundaries while preventing any part of the simulation cell from feeling the potential from any neighbouring copy [161]. Here, a spherical cut-off type was used with a radius of 30 Å based on the initial W pyramid model’s dimensions. As the W pyramid has a base width of about 15 Å and a total height of 10.2 Å prior to the geometry optimisation, the large cut-off radius ensured, that each Coulomb potential around an individual atom can “feel” the Coulomb potential of all other atoms. The whole simulation cell had a size of 66 Å × 66 Å × 66 Å to ensure that the combination of all Coulomb cut-off potentials around the atoms lie within the cell. This can be better illustrated pictorially as shown in Figure 4.18 b, which shows a two-dimensional grid where the red cell is the

^bThis procedure was used based on discussions with experts from TCM.

primary cell, while the black cells are the repeated images. The light green circle indicates the overall Coulomb cut-off sphere which is a combination of all individual Coulomb cut-off spheres (dashed circles) around the atoms. The grey triangle represents the pyramid model.

The DFT simulations of the geometry optimisation were done using a cut-off energy of 1000 eV and Perdew, Burke and Ernzerhof (PBE) as the XC functional [155]. Further, each W atom had 10 NGWFs with cut-off radii of $14 a_0$, while H had 1 NGWF with $14 a_0$ radius. Moreover, three different approaches to the geometry optimisation were used in which (a) all atoms can move and fully relax, (b) the bottom layer and the H atoms are kept at a fixed position, while the rest can move and (c) layer 6 plus the bottom layer and the H atoms are kept in fixed positions while the other atoms can move. The idea behind this approach was that if all atoms can move freely, they will find atomic positions which will represent the optimised positions for the molecule-like model instead of for the larger macroscopic structure. The small model has a very high surface-to-bulk ratio and metals are known to exhibit surface relaxation effects, meaning that the atomic bond length changes compared to the bulk value [162, 163]. Thus, the pyramid’s bottom layers were fixed in their “bulk”-position to simulate the pyramid’s attachment to the macroscopic model.

For (a) the initial atomic positions were based on the bcc lattice constant for W found in literature, while for (b) and (c) they are based on an initially converged structure using the molecular mechanics code GULP [164]^c. As these molecular mechanics (MM) simulations do not take account of the charge density due to electrons, other than by models for potential around ions, they are computationally less demanding than DFT and thus faster but are also less accurate than the computed solutions in ONETEP. By using this approach, it was possible to simulate a large pyramid, consisting of 100 layers, and to find the optimised atomic positions for its top seven layers, which were used as initial positions for the DFT simulations. This approach had the advantage, that the positions found via MM represent a larger structure and have already been optimised prior to the DFT optimisation. Thus, the simulation model of (b) and (c) ought to converge faster than (a).

The results of the three different geometry optimisation approaches are shown in Figure 4.19, which illustrates the decrease in the system’s energy with each optimisation step. Here the optimisation process is done by alternately optimising the locations of the ions and the NGWFs defining electron orbitals. Thus, an individual optimisation step is indicated by a sudden increase in energy, where the atomic po-

^cThese simulations were done by D. H. Phillips.

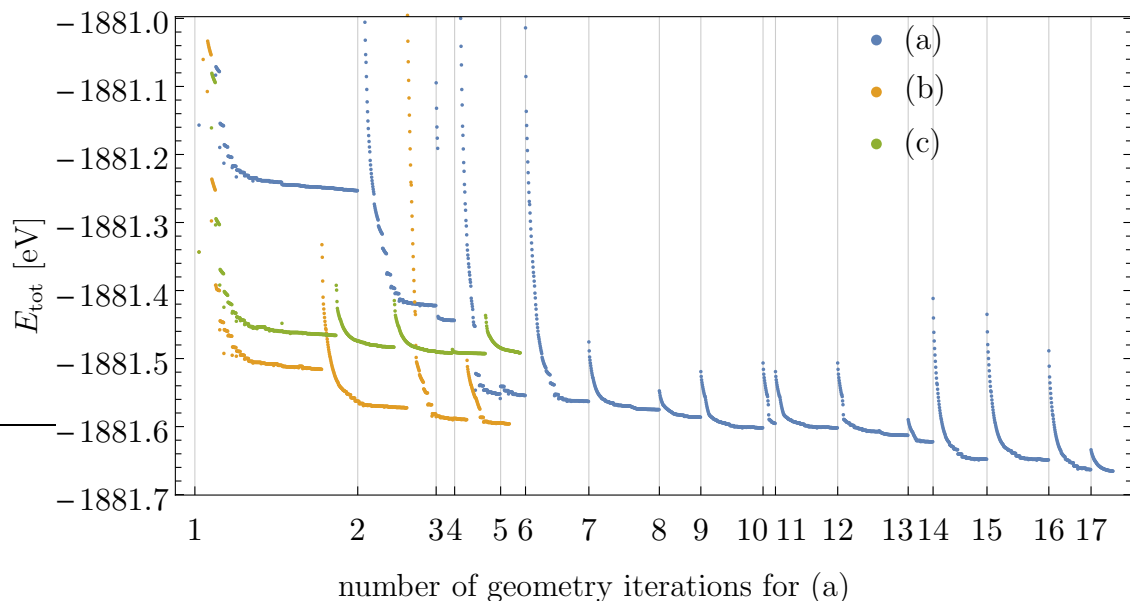


Figure 4.19: DFT simulations demonstrating a decrease in total energy due to the optimisation of the atomic position. Here, in (a) all atoms can move, in (b) the bottom layer and the H atoms are kept at a fixed position, while the rest can move and in (c) layer 6 plus the bottom layer and the H atoms are kept in fixed positions while the other atoms can move. The gridlines specify separate iterations of each optimisation step of (a), indicated by the sudden increase in energy.

sitions were changed and the subsequent decrease where the simulation rearranges the NGWFs to fit the new atomic position. The figure illustrates, that approach (a) had initially the highest energy and thus the worst initial atomic positions, but it decreased fast with every optimisation circle. The most suitable initial position was found for (b), where the H and bottom layer were held at a fixed position. For this model, the system’s energy decreased steadily with every iteration and was lower than (a) and (c). Approach (c) had initially a lower energy than (a) but decreases less than the other two cases and is ultimately the most difficult model to relax, indicating that the structure’s base is too restrained. Ultimately, even though the geometry convergence improved, none of the models did fully converge in a reasonable amount of time.

To identify the areas which prevent the structure from convergence the force, F_W , acting on each atom is plotted in Figure 4.20 a and b for the first and the last geometry optimisation step, respectively. In these figures atoms with larger forces ($F_W > 1 \text{ eV}/\text{\AA}$) are depicted in red, with medium forces ($0.5 \text{ eV}/\text{\AA} < F_W < 1 \text{ eV}/\text{\AA}$) in orange and with low forces ($F_W < 0.5 \text{ eV}/\text{\AA}$) in green. It can be seen from Figure 4.20 a that initially most atoms had large forces. In particular, the surface atoms which have a broken symmetry and dangling bonds. After 17 geometry

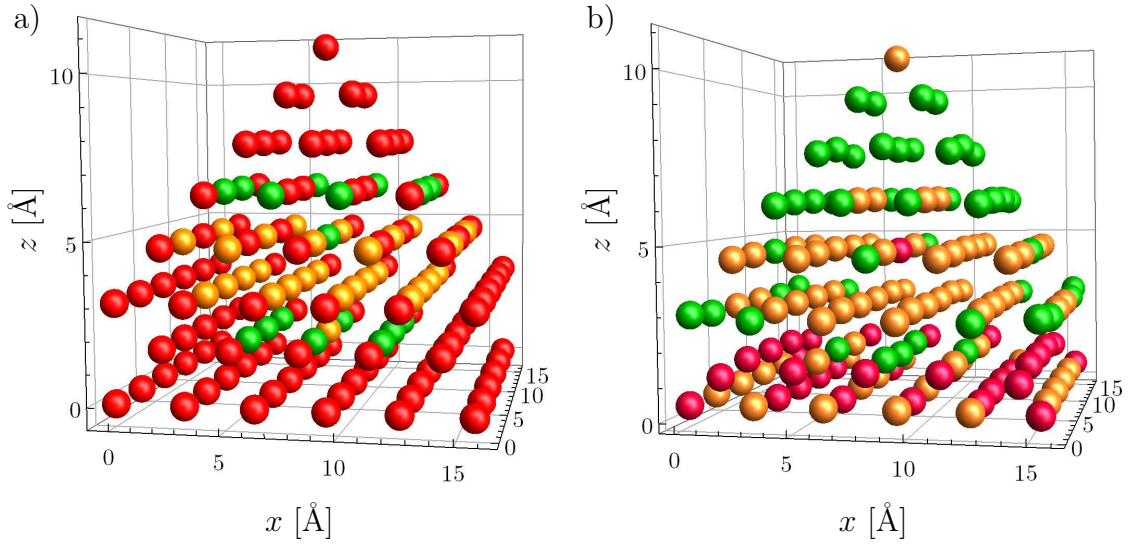


Figure 4.20: Plot of the atomic W model a) after the first and b) the 17th geometry optimisation iteration. Here, the colours indicate the atomic forces acting on the individual atom, with large forces ($F_W > 1 \text{ eV/\AA}$) being depicted in red, medium forces ($0.5 \text{ eV/\AA} < F_W < 1 \text{ eV/\AA}$) in orange and low forces ($F_W < 0.5 \text{ eV/\AA}$) in green.

optimisations (Figure 4.20 b), almost all atoms have relaxed. Here, the top four layers have very low forces acting on them which is aided by the change in atomic distance between the 1st and 2nd atomic layer of the pyramid from 1.58 \AA to 1.32 \AA (surface relaxation). The bottom of the pyramid is still showing difficulties with their position. Specifically, the bottom and H layer exhibits large forces, while the fifth- and sixth-layer exhibit moderate forces. This analysis indicates that the structure's starting position from a bulk-like lattice constant is not a good starting point.

However, even without a perfectly converged structure, it was possible to conduct further investigations regarding the structure's field emission properties. Here one has to remember that the aim of the dissertation is to design a suitable multi-scale simulation procedure, capable of simulating different nano-sized emission structures with varying geometry and material. Thus, the following sections will use the atomic positions of the incompletely converged structure from procedure (a) as the base for further simulations.

4.2.2 Multi-scale model with applied field

The atomistic-continuum simulation method was used to model this new emitter setup, in the same way as described in Chapter 3.1. Here, the macroscopic geometry

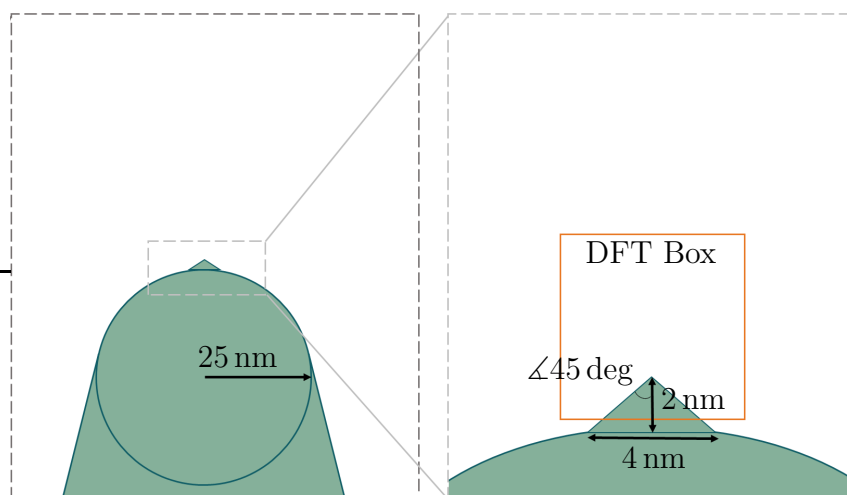


Figure 4.21: The tip is modelled by a truncated cone capped by a hemisphere, which has a small cone on top (left). The small cone approximates the dimensions of the DFT model and partially lies inside the DFT box (right).

was based on that of chemically-etched W tips, typical dimensions of which were measured using SEM images (not shown here). Based on these dimensions a model was designed, using FlexPDETM, in which the large emitter is approximated by a truncated cone with a hemisphere at its tip, situated between two parallel planes. To model the atomically sharp tip, a small cone is located on top of the hemisphere with the tip centred on the emitter axis. This design results in a rotationally symmetric model to minimise the calculation time.

For the classical model presented here, the supporting cone stands normal to and in the centre of the cathode plane and the hemispherical end has a radius of roughly 25 nm. The cathode plane and emitter are kept at 0 V, while the anode voltage is varied depending on the simulation. The distance from the anode to the apex of the small cone was chosen to be 1000 nm.

The small cone on top of the hemisphere approximates the previously discussed atomically sharp four-sided pyramid. Hence, its dimensions and angles were adjusted to match the metallic surface (Fermi equipotential) found by the geometry optimisation in Section 4.2.1 but its height was extended to protrude through the DFT box. The final cone had a base width of 4 nm and a height of 2 nm, of which 1.5 nm lie within the DFT box. The apex region with all its dimensions is depicted in Figure 4.21. The right-hand image shows an enlargement of the junction between pyramid and hemisphere. The red frame in the figure indicates the size and position of the DFT box in relation to the macroscopic model. This cubical box of side 5 nm is defined around the cone apex and does not include the hemisphere below.

The FlexPDE model is rotationally symmetric around the cone axis. Thus, the program only has to solve the Poisson equation in two dimensions after discretising the region using a triangular mesh. The generated model and the corresponding mesh are displayed in Figure 4.22 a) for the full structure (left) and an enlargement (right)

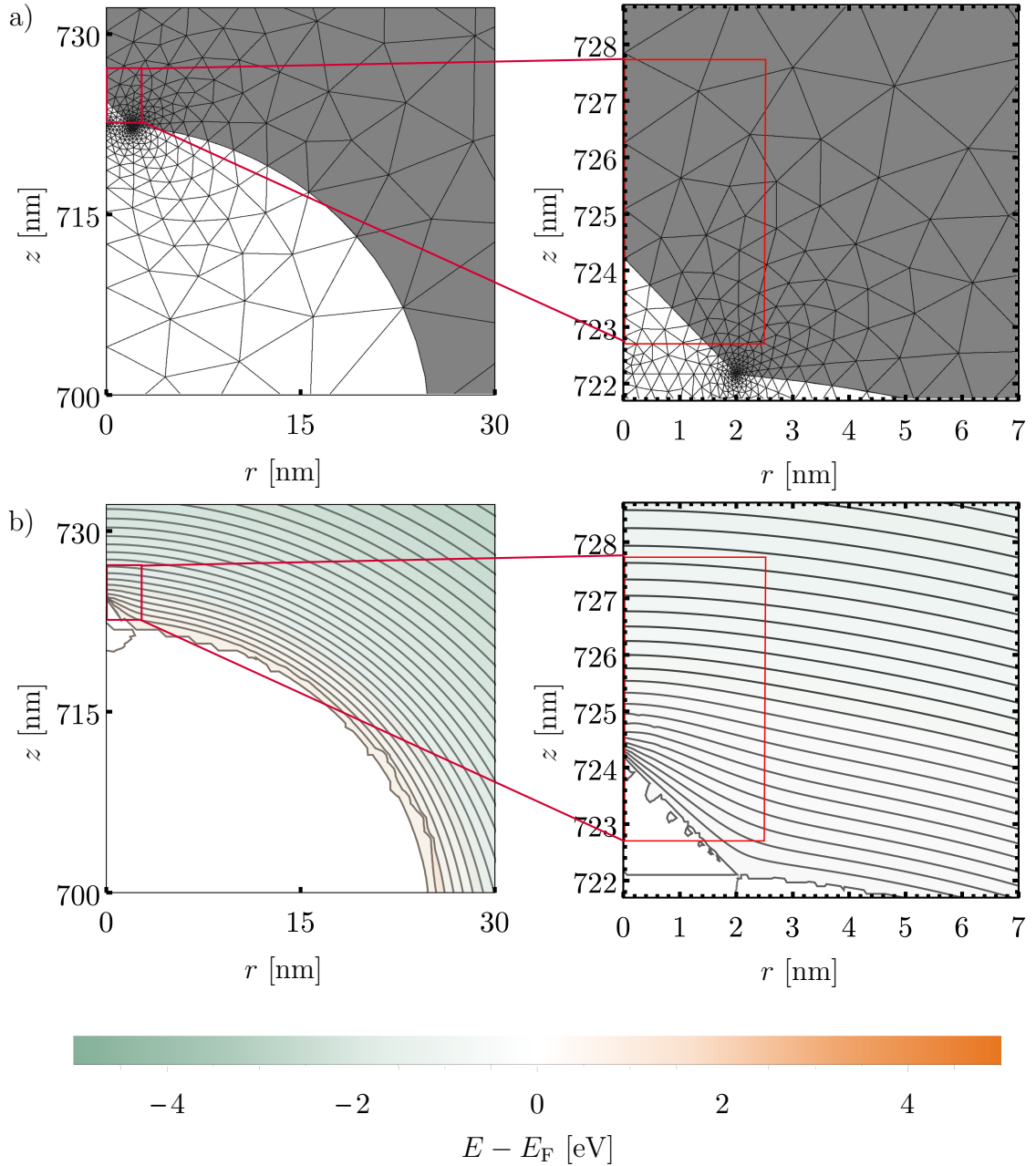


Figure 4.22: a) Part of the rotationally symmetric FlexPDE model showing the adaptive mesh distribution around the top of the emitter (left) and the small cone at the apex (right). b) The electrostatic potential isocontours at intervals of 0.1 V (left) and 0.05 V for a field of 0.0087 V/nm around the top of the emitter (left) and the small cone at the apex (right). The red frame indicates the size and position of the DFT box.

of the cone at the apex (right), as found for an error limit of 1.5×10^{-4} . As can be seen, the adaptive mesh refinement procedure generated a fine mesh around the small conical tip structure.

The corresponding electrostatic potential is displayed in Figure 4.22 b which shows the equipotentials in intervals of 0.1 V/nm (left image) and 0.05 V/nm (right image) for the apex region of the “W-pyramid-on-a-cone” model and an enlarged view of the small cone. The colour scale represents the electric potential with respect to the Fermi level for an applied anode-cathode voltage of 15 V, which corresponds to a background field of 0.0087 V/nm. As described in Chapter 3.1, to accurately

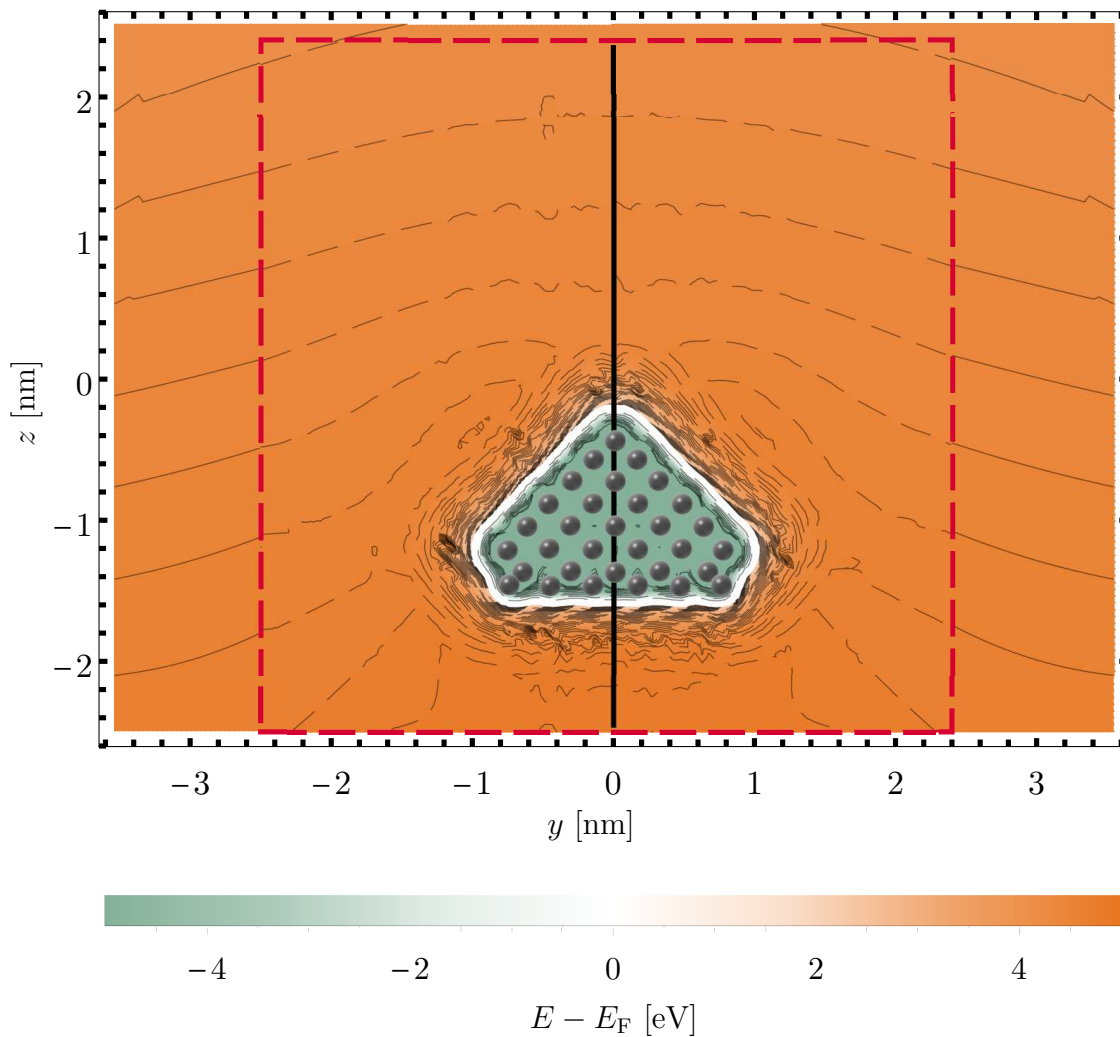


Figure 4.23: Section through the W-pyramid, showing the DFT potential energy superimposed on the classical macro model (raised by the work function) for a background field of 0.0087 V/nm. The equipotentials above (below) E_F (white line) are at intervals of 0.1 eV (1 eV). The atomic positions are mapped in grey onto the model for visualisation. The red frame indicates the size and position of the DFT box. The black line shows the directions of the 1D potentials shown in Section 4.2.6.

simulate the emitter properties the electrostatic field distribution in conjunction with the induced charge within the DFT box are extracted and used as boundary conditions for the DFT calculation. This was done by converting FlexPDE’s cylindrical coordinate systems into Cartesian coordinates first and then matching the mesh of the boundaries as described in Section 3.2.4.

The final DFT simulations were conducted using the induced charges, the matched boundary conditions for an externally applied field and an EDFT smear width of 100 K. For the XC functional the GGA was chosen using the PBE functional. All simulations had a cut-off energy of 1000 eV and NGWF with cut-off radii of $14 a_0$ and the PAW method from the ABINIT dataset were used to represent the atomic cores [148]. The atomistic-continuum multi-scale solver again used ONETEP’s open boundary condition algorithms. The combination of the macro and nano-model is illustrated in Figure 4.23 and demonstrates the matching between the boundaries. Here, the boundary of the DFT box is indicated by the red frame, where the simulated DFT potential energy for a background field of 0.0087 V/nm, inducing $0.25 e$ electrons, is superimposed on the FlexPDE potential, which is raised above the Fermi level by the work function. In the figure, the equipotential lines above and below E_F are at intervals of 0.1 eV and 1 eV, respectively. The white outline in the DFT potential represents the Fermi equipotential.

Using the simulation results it was possible to gain information about the emitter system’s density of states, the highest occupied molecular orbital and lowest unoccupied molecular orbital, the electron charge density and the electrostatic potential around the tip. The individual results will be discussed in more detail in the following sections.

4.2.3 Local density of states

A representation of the local density of states for the W-pyramid including the top six layers is plotted in Figure 4.24 a. As in Section 4.1.4, only the densities of states from -5 eV to 5 eV around E_F are plotted, as they would contribute to any potential field emission. The energy levels are again fitted with a Gaussian function of 0.025 eV (300 K) FWHM.

As can be seen, the model exhibits localised states at the Fermi level, which confirm the expected metallic behaviour of the material. Furthermore, the number of peaks indicates a high density of states around the Fermi level, which represents a metallic band-like behaviour than the individual orbitals of a molecule.

A more detailed analysis of the LDoS for each pyramid layers without an applied field is shown in Figure 4.24 b. Here, the energy is normalised by the number of atoms

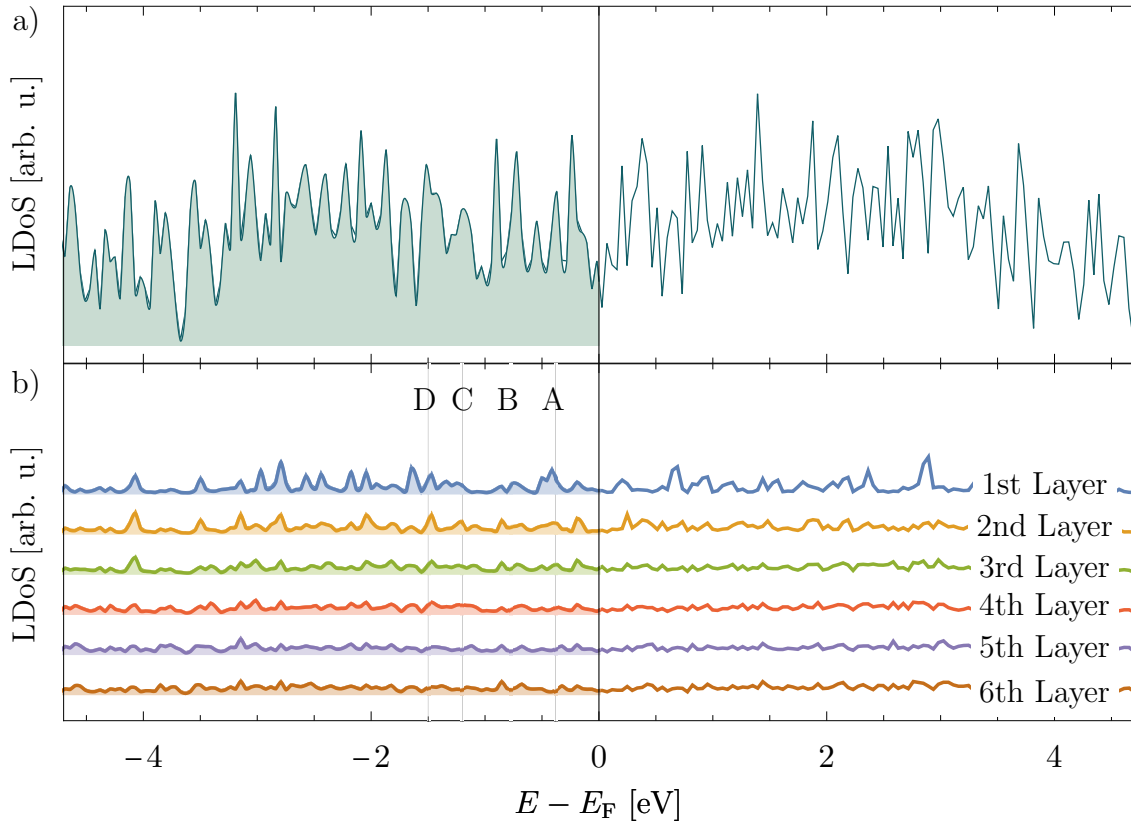


Figure 4.24: Local density of states of a) the combined and b) the individual top six layers of the pyramid as a function of energy near the Fermi level, fitted with a Gaussian functions of 0.025 eV FWHM. The existence of local states at E_F validates the model’s metallic nature. Additional surface states corresponding to the experimentally found Swanson humps are labelled A - D.

in each layer for better comparison. It can be seen that there are additional states for the top layers, which either are not present or not as dominant in the lower layers. As the top layers have altered coordination numbers and a different atomic distance, their electronic structure is altered compared to the bulk, which can lead to increased electron emission from those layers. Such an effect was experimentally found in 1966 by L. W. Swanson [165] for the $\langle 001 \rangle$ direction. E. W. Plummer and J. W. Gadzuk attributed this so-called “Swanson hump” to surface state emission [166]. Based on this theory, the simulated LDoS suggests such a hump to occur even for the $\langle 110 \rangle$ orientation.

The corresponding energies at which a Swanson hump was found were reported to be around -0.37 eV below the Fermi level (dominant peak) [166, 167], and several weaker peaks at about -0.73 eV [166], -1.2 eV [168] and -1.5 eV [166]. These values correspond very well with surface states found in Figure 4.24 b labelled A - D, respectively.

4.2.4 Charge density with and without applied field

This section will discuss the simulated charge density distribution with and without an external field. Two isosurfaces for a) 0.0001% and b) 0.00005% of the global maximum charge density of $395\,010\,e/\text{\AA}^3$ without an applied field are depicted in Figure 4.25. Here one can see, that similar to the CNT most of the electron density is localised at the atomic cores (Figure 4.25 a). These electrons are bound and do not contribute to the conductivity of the system. Only a very small percentage of the overall electron density forms a delocalised conducting sheet covering the W-pyramid, as illustrated in Figure 4.25 b. This evenly distributed sheet allows electrons to move freely and thus giving it its metallic character.

Although the percentage of 0.00005% of electrons contributing to the conductivity of the W-pyramid seems very low, it corresponds to $19.75\,e/\text{\AA}^3$, compared to $0.14\,e/\text{\AA}^3$ for the conducting sheet of the CNT (0.02% of $717\,e/\text{\AA}^3$). Moreover, this low percentage is expected as most of the 74 electrons in W are core electrons. Here one has to note, that these percentages are not exact numbers as the transition of the isosurfaces from bound to delocalised electrons is continuous, nevertheless, they give an estimate of how many electrons contribute to the conductivity.

Figure 4.26 illustrates the change in electron charge density with an applied background field of 0.0087 V/nm , which induces $0.25e$ in addition to the chemically present electrons. These three-dimensional isosurfaces represent the change in magnitude of $\pm 2 \times 10^{-4}\,e/\text{\AA}$, where the positive excess electron charge is shown in orange (areas which gained electron charge), whereas the green represents a loss in electron charge. The first thing to note is that most of the electron charge was re-

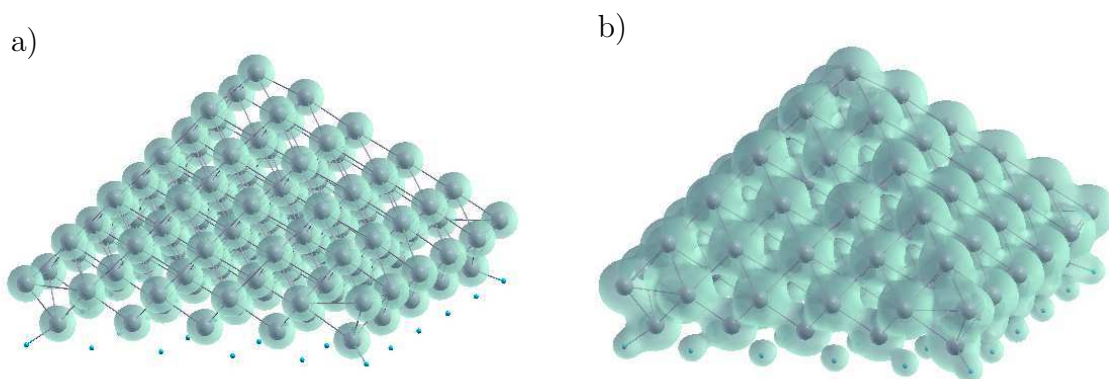


Figure 4.25: Electron density isosurfaces for zero applied field. The isosurfaces are at a) 0.0001% and b) 0.00005% of the global maximum charge density of $395\,010\,e/\text{\AA}^3$. In a) the charge density is localised around the atomic cores while in b) it forms a conducting sheet.

distributed around the corners and the tip of the pyramid. As can be seen from the side-view, these electrons have moved away from the atomic cores in the direction of the applied field as it acts as an attractive force on the electrons. Further, there is an accumulation of excess charge around the edges of the pyramid base. This however is an unrealistic effect when considering the full emission tip and is caused by the finite size of the limited DFT pyramid model. As can be seen in Figure 4.26 the increased electron charge density around the corners is not only caused by the additionally induced charges but also by a redistribution of the bound core electrons (green isosurface).

Here one should note, that the depicted change in electron density represents the overall changes of all electrons of the whole model from all orbitals. In the case of field emission, the emitted electrons will mainly occur from around the Fermi level. Thus, the next step is to investigate the highest occupied molecular orbital and lowest unoccupied molecular orbital.

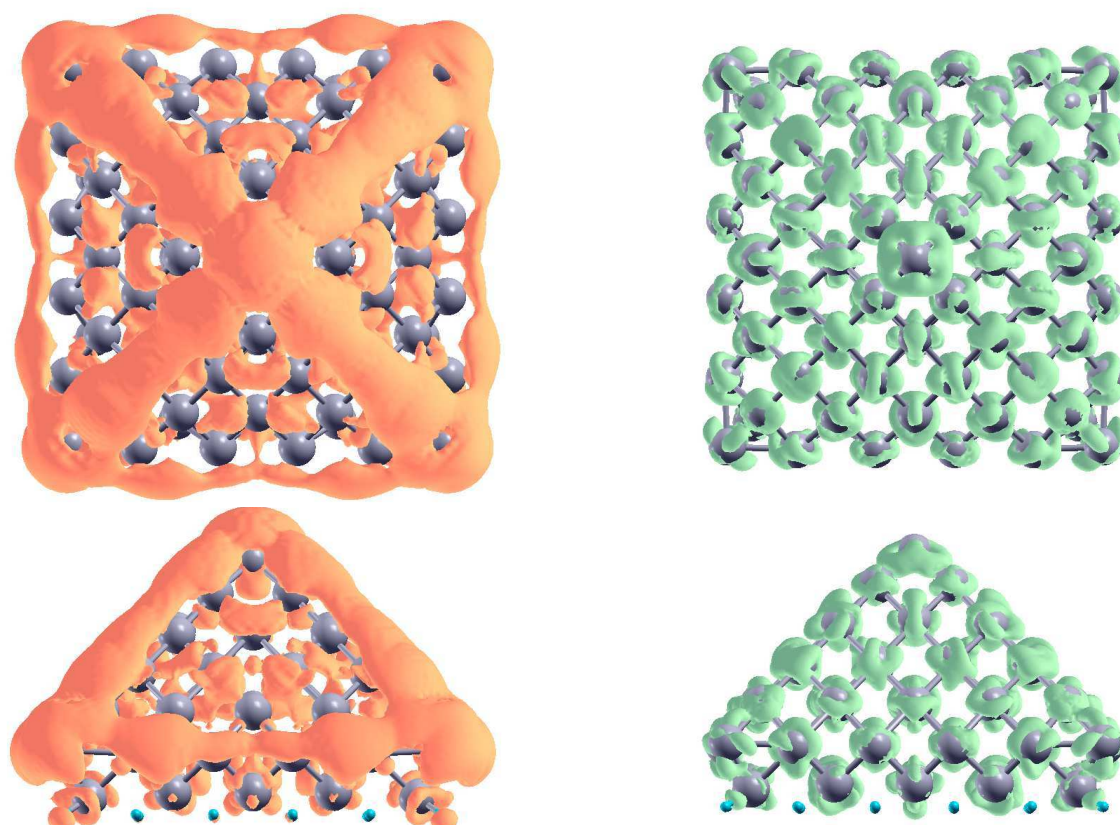


Figure 4.26: Change in electron density on application of 0.0087 V/nm inducing 0.25 additional electrons. The orange isosurface indicates an increase by $2 \times 10^{-4} e/\text{\AA}$, while green represents a decreased by $2 \times 10^{-4} e/\text{\AA}$, relative to zero-field values. The views are from a direction perpendicular to the axis of the pyramid.

4.2.5 Molecular orbitals

While the CNT has a clear semiconductor-like band gap without an applied field (Section 4.1.4), the W tip exhibits metallic behaviour. Therefore, the notion of highest occupied molecular orbital or a lowest unoccupied molecular orbital is probably not realistic for this model but should rather be treated with an electronic band structure. However, as the molecule itself is a non-periodic structure with a limited number of electrons in the model one can simulate individual orbitals. A plot of the isosurface of the HOMO for $\pm 0.003 (e/\text{\AA}^2)^{1/2}$ is shown in Figure 4.27. It exhibits a quadrantal distribution that is consistent with the four faces of the W pyramid. Here the HOMO is more prominent along the edges than in the middle of the pyramid.

A better way of analysing a potential emission area and the emission pattern is to plot the HOMO's distribution of charge densities. This is illustrated in Figure 4.28 for both the HOMO (orange) and LUMO (green) without an applied electric field. These isosurfaces represent 5% of the total charge density. As can be seen, the HOMO is mainly situated along the corners of the pyramid, while there is only little electron charge at the centre and the sides. In the case of the LUMO the electrons are situated in four corners of the pyramid and around the tip of the pyramid, which itself is again charge free. For this simulation, the LUMO needs to be considered for electron emission as firstly, additionally induced electrons would occupy this orbital, which in turn would become the new HOMO, and secondly because electrons are likely to occupy this orbital at $T > 0$ K, as there is no band gap in the material (Section 4.2.3). Thus, a resulting emission pattern would be influenced by both orbitals.

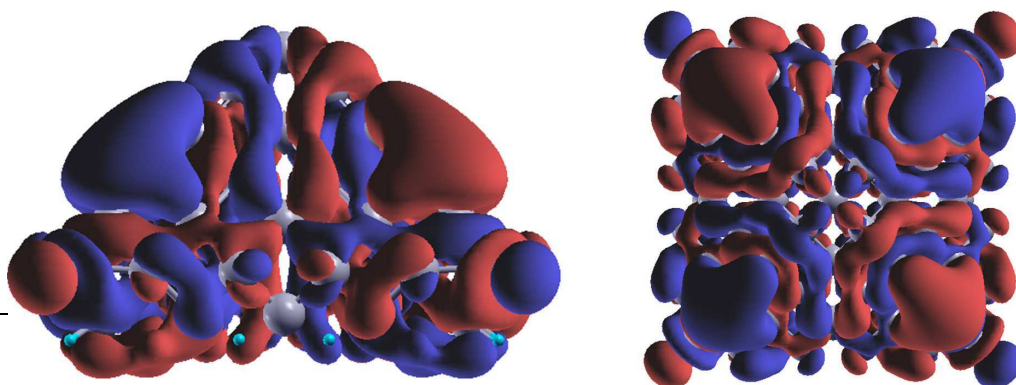


Figure 4.27: HOMO isosurface for the W-pyramid at an amplitude of $\pm 0.003 (e/\text{\AA}^2)^{1/2}$, without an externally applied field. Here, red and blue depict the positive and negative isosurfaces, respectively.

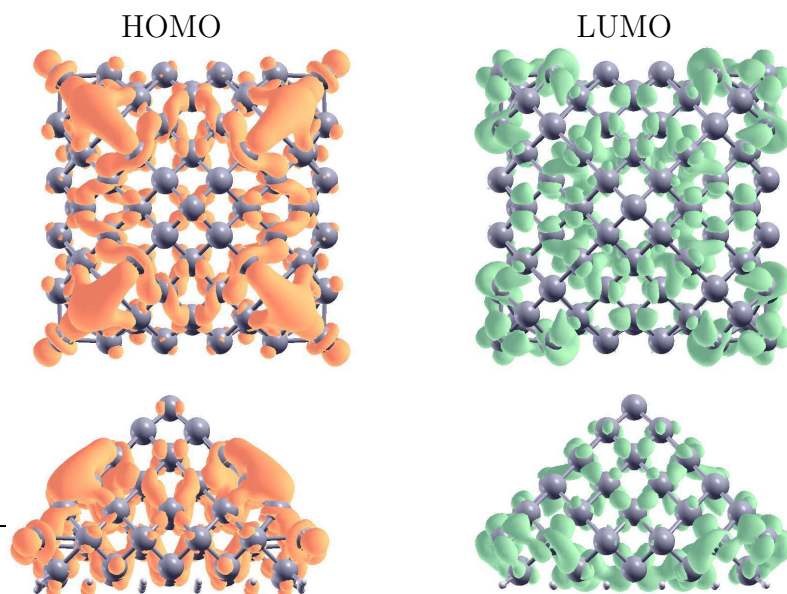


Figure 4.28: Electron charge densities of the HOMO (orange) and LUMO (green) at zero applied field. The isosurfaces represent 5% of the total charge density of $0.0024 e/\text{\AA}^3$.

Figure 4.29 a) shows a field-electron-microscope image of a typical emission pattern from the (110) surface of a W-tip taken from Figure 1 in Ref. [169]. The comparison of this pattern with the charge densities from the LUMO in Figure 4.28 shows qualitative agreement of the emission regions with volumes defined by isosurfaces of one orbital's electron charge amplitude. Even though there is still some

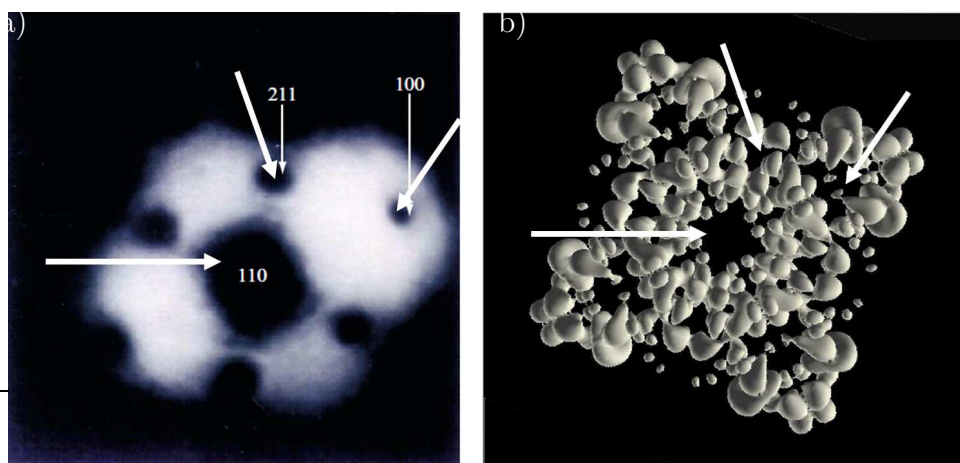


Figure 4.29: Comparison of the emission pattern between a) the experimental emission pattern of a W-tip along the (110) direction (field-electron-microscope image taken from Figure 1 in Ref. [169]) and b) the simulated charge density of the LUMO without an applied field of a four-faced W-pyramid. The arrows indicate similar features between the images.

inaccuracy in the calculation it is encouraging that the plots agree on the locations of zero emission.

4.2.6 Electric potential

As mentioned in Section 4.1.8, the change in potential barrier outside the metallic surface is of special interest for the investigation of field emission sources. Thus, Figure 4.30 shows the one-dimensional profile of the potential through the centre of the pyramidal model in the direction of the electric field (z -axis) as indicated in Figure 4.23, with zero and 0.0087 V/nm applied electric field.

The first things to note are the four potential wells at approximately -1.4 nm , -1 nm , -0.7 nm and -0.4 nm , which correspond to the position of the atomic cores where most of the electron charge is situated. However, as the calculations use pseudo-potentials to estimate the potential in the core region, the depth of the potential well should not be assumed to be an exact representation. Nevertheless, the plot exhibits the expected shape as predicted by the “muffin-tin” approximation of a crystal lattice [170]. The dashed orange line ($z_{F,0}$) indicates the point of intersection of the Fermi equipotential with the z -axis without an applied field,

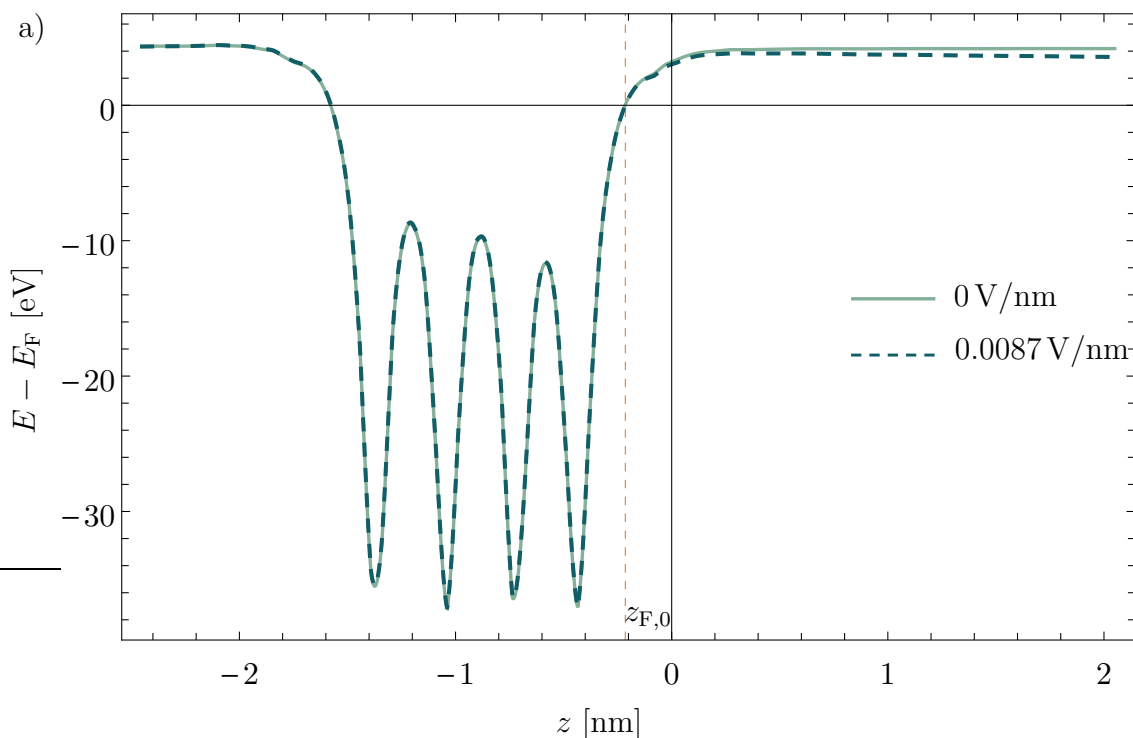


Figure 4.30: Potential energy at 100 K, along the z -axis indicated in Figure 4.14, for zero and 0.0087 V/nm of applied electric field inducing additional charges from zero and $0.25 e$, respectively.

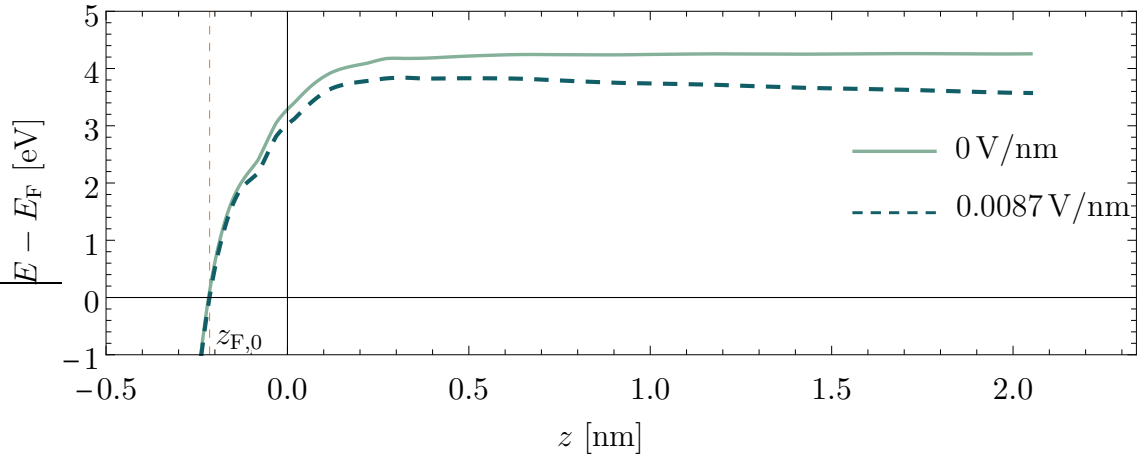


Figure 4.31: Enlarged view of the potential energy for the region $-0.5 \text{ nm} < z < 2 \text{ nm}$, along the z -axis indicated in Figure 4.14, for zero and 0.0087 V/nm applied electric field inducing additional charges from zero and $0.25 e$, respectively.

which again defines the model’s metallic surface (see Section 4.1.1). This isosurface lies at $z = -0.2145 \text{ nm}$ and is 2.2 \AA away from the top W atom’s core. As demonstrated in the previous Section 4.1.8 all additional field-induced charges would increase the radius of this conducting sheet of electrons. However, as an applied field of 0.0087 V/nm only induces $0.25 e$ the change in z_F is too small to be seen here.

Comparing the potential with and without an applied field illustrates the expected lowering of the potential barrier due to the electric field. This effect can better be seen in Figure 4.31, which shows an enlargement of the potential barrier just after the top W core. Even though the field of 0.0087 V/nm is too small to estimate a model which would best describe the decrease of the potential barrier, higher electrical fields will ultimately lower the potential barrier further until the tunnel barrier is narrow enough for electrons to tunnel through and induce field emission. Calculations of the field enhancement give a factor of $\gamma = 9.37$ with $F_M = 0.0087 \text{ V/nm}$ and $F_L = 0.0816 \text{ V/nm}$ (slope of potential for $z > 0.1 \text{ nm}$ in Figure 4.31).

Both potentials are aligned with respect to their corresponding Fermi level, which was found by the DFT simulations and give work functions of 4.27 eV at zero field and 4.31 eV at 0.0087 V/nm . These values agree well with the lowest experimental values of work function found for W (310) [169].

4.3 Conclusion

This chapter presented the results obtained by using the atomistic-continuum simulation method described in Section 3.1 and highlighted its capabilities to analyse field emission relevant material properties for zero external field and for applied fields that are below the threshold for electron emission.

In the first section calculations for a single-walled, capped (5,5) CNT have been presented, which have given detailed estimates of the atomic properties that are otherwise not available from classical approximations. The second section presented the initial results and considerations regarding the simulation of an emission model using a more complex geometry and heavier atoms; namely a four-sided W-pyramid.

The thus obtained results include the spatial distribution of charge density, showing a low-density sheath which provides a conducting path for electrons to move along the model and which screens the core potential from external fields. Upon applying an external field, additional charges are induced and accumulate at the apex. The distribution and relative energies of individual orbitals including the HOMO and the LUMO have been investigated and exhibited good agreement with the experimentally found emission pattern. It was shown that by inducing additional charges, the distribution of the HOMO and the LUMO changes, which has an effect on the distribution of current charges and might lead in turn to a change in current density distribution for different applied fields. Further, the local density of states was analysed which showed that the modelled system's number of orbitals needs to be sufficiently large to be considered a bulk-like structure. Smaller models with fewer electrons exhibited size-related effect, such as a band gap. It was shown that both models indicate the existence of additional surface states which might be correlated with experimentally found effects like the "Swanson hump". Moreover, the influence of varying externally applied fields on the potential barrier was presented. The changing field and the correlated increase in induced charges on the CNT changes the height and width of the potential barrier above the Fermi level. A comparison with numerically calculated classical potentials indicates that these classical calculations overestimate the change in barrier width and height. Lastly, the influence of exchange and correlation effects on the distribution of the total potential was shown, indicating that the choice of XC functional has some small influence on the potential close to the atomic nuclei, while omitting it changes the results dramatically. The work function value, which is the part of the total change of E (between ion sites and vacuum) that is above the Fermi level, is realistic only when XC is included.

Hence, as can be seen from these results, the atomistic-continuum simulation method is a powerful tool to gain detailed insights into a material's field emission-related properties.

5 | Spin-polarised secondary electron emission spectroscopy

For this dissertation, three different material systems were investigated to study the interaction of spin-polarised electron beams with magnetic materials. In particular, ultra-thin Fe on Ag(001) and on W(110) samples were chosen as their ferromagnetism would cause spin-selective interactions. Thus, the following chapters will present the preliminary investigations into each sample using SPLEEM and the newly-developed energy-selective secondary electron yield (ESSEY) mode and discuss their results.

5.1 SPLEEM investigation of ultra-thin Fe films on Ag (001)

The material system of an ultra-thin iron film on an Ag (001) substrate is a well-known heterostructure that has been intensively studied with regard to both growth mechanism [171–173] and spin-polarisation [174–176]. Due to the lack of *d*-orbital overlap between Fe and Ag, the Fe layer is a close approximation to a free-standing, two-dimensional magnetic film [171], making it an ideal model-system for theoretical and experimental studies of spin-polarised electron beam interactions with ferromagnetic materials.

5.1.1 Sample preparation of Fe/Ag (001)

The magnetic properties and crystalline quality of a thin film strongly depend on the initial conditions of the substrate prior to the growth process. Therefore, any substrate has to be polished and cleaned carefully to assure optimal growth condition before Fe is deposited. Here, the substrate used in the following experiments was a 1-mm-thick Ag single-crystal with a side-length of about 6.5 mm, oriented within 1° along the [001] surface normal direction. As this substrate was exposed to air for a substantial amount of time, the first step was to remove the thick oxidation layer employing silver polishing paste. Afterwards, acetone cleaning and subsequent ultrasonication for approximately 5 min was used to remove any dust particles and organic contaminations. As acetone tends to leave a residue, this step is followed by an isopropanol rinse. After this initial crude cleaning process, the sample was cleaned following a well-established procedure via sputter annealing in Cambridge, which consists of repeated cycles of 500 eV/10 μA^a Ar⁺ ion sputtering and subsequent annealing at 400 °C for 0.5 hours each. Further sputter annealing was done at the National Institute of Material Science in Japan in a multi-chamber UHV system that provides a variety of facilities for sample preparation and characterisation.

Prior to the deposition of Fe the sample's chemical cleanliness was confirmed employing LEEM and scanning AES, where no impurity peaks were detected. The surface's crystalline quality and crystallographic symmetry directions were analysed using LEED. As seen in Figure 5.1 a the LEED image displays a sharp fourfold (1x1) pattern acquired using an energy of 49 eV, indicative of a clean single-crystalline Ag (001) surface. The low background further confirms its smooth surface.

In the next step, a thin iron film of only a few MLs was deposited reproducibly

^aTarget current.

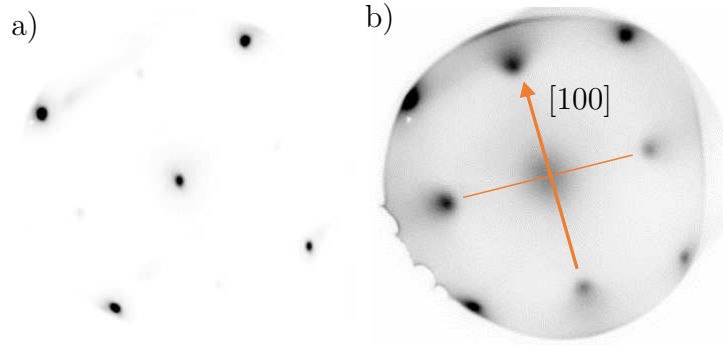


Figure 5.1: Low-energy electron diffraction pattern of a) the pure Ag(001) substrate and b) the Fe/Ag(001) structure for a primary electron energy of $E_0 = 49$ eV. The orange arrow indicates the crystallographic [100] directions.

using MBE at a rate of about 0.16 ML/minute using an Omicron EFM-3 electron-beam evaporator. The deposition rate was measured by direct observation of the periodic intensity oscillations during growth via SPLEEM, which arise due to the periodic nucleation, growth and completion of atomic monolayers, which can be used for very precise film thickness measurements [177]. During the deposition, the substrate temperature was held at about 243 K using nitrogen gas from a reservoir of liquid N_2 . This was necessary since Fe and Ag are miscible when grown at room temperature, as the surface energy of Ag is only about half the value of Fe (Ag: ~ 1.3 J/m², Fe: ~ 2.9 J/m²) [173, 178]. This would result in a “wetting-layer”, as Ag segregates to the Fe surface. Keeping the sample at a low temperature during the deposition will decrease the amount of Ag contamination on the surface. Hence, the growth “recipe” has to be strictly followed to be able to compare the results obtained from samples originating from different growth runs. After the growth, the sample is left to heat up to room temperature for further experiments.

Figure 5.1 b shows the (1x1) LEED pattern of 8 ML Fe on Ag(001) for a primary electron energy of $E_0 = 49$ eV. The high intensity of the spots confirms that the Fe layer was grown epitaxially on the Ag(100) surface. The directional relationship of the materials was found to be that the bcc-Fe(001) $\langle 100 \rangle$ axis is parallel to the fcc-Ag(001) $\langle 110 \rangle$ axis [173]. Comparing the two images in Figure 5.1 shows that the LEED spots became slightly diffuse after Fe growth indicating that the deposition resulted in the formation of Stranski–Krastanov growth [172].

5.1.2 Onset of the magnetic domain structure and orientation

Magnetic thin films have been found to have altered properties compared to bulk-like samples. The magnetic anisotropy, in particular, can vary in the ultra-thin film regime, when the surface anisotropy dominates the effective anisotropy, as can be seen in Eq. (2.27) [176]. Thus, to analyse a sample's thickness-dependent magnetisation dynamics and to ensure an in-plane (ip) magnetisation, the evolution of ferromagnetism during film growth was observed. This was done by monitoring the spin-asymmetry, as defined by Eq. (3.5), which can be obtained by taking continuous sequences of images of the surface during the deposition of the ferromagnetic thin film. For each set of two consecutive images, the spin's orientation vector \vec{P} of the electron beam was changed to be either parallel or antiparallel to the film's in-plane easy-axis of magnetisation, *i.e.* the [100] direction for Fe.

The results are shown in Figure 5.2, which displays the *in situ* evolution of the in-plane spin-asymmetry during the growth process of Fe from 0 ML to 8 ML^b. The first thing to note in Figure 5.2 is that there is no measurable ip spin-asymmetry for thicknesses $L < 4$ ML. This is due to a thickness-induced spin reorientation transition in which the magnetisation first points out-of-plane (oop) for thin films below 4 ML (maximum magnetisation at 3 ML), while the ip magnetisation only starts to occur at 3 ML and reaches its saturation value at about 4 ML [176].

This is in good agreement with the experiments presented here, where some regions start to exhibit an in-plane magnetic contrast at around $L \geq 4$. As the layer-plus-island growth mode (see Section 3.3.1) results in islands and terraces with varying thickness, the four regions of interest (RoIs) analysed in Figure 5.2 show slightly different onsets of ip magnetisation. While some regions (red and green lines) have reached the critical layer thickness to exhibit a spin reorientation from oop to ip after 4 ML [176], other regions (blue and grey) are still below the threshold thickness and have a predominantly oop magnetisation. Thus, they only show a magnetic contrast after five pseudomorphic monolayers. These values are in good agreement with results found by R. J. Hicken *et al.*, who investigated ultra-thin epitaxial Fe/Ag(100) films via magneto-optical Kerr effect (MOKE) and found that the first magnetic signal was usually observed for $L \approx 4$ ML [171]. After an average thickness of about $L \geq 7$ ML the sample investigated here exhibits a homogeneous magnetisation, at which stage the asymmetry converged to its maximum value.

The dotted lines in the plot, labelled A - D, indicate four different stages during

^bDue to the Stranski–Krastanov growth mode a monolayer can only be given as an average.

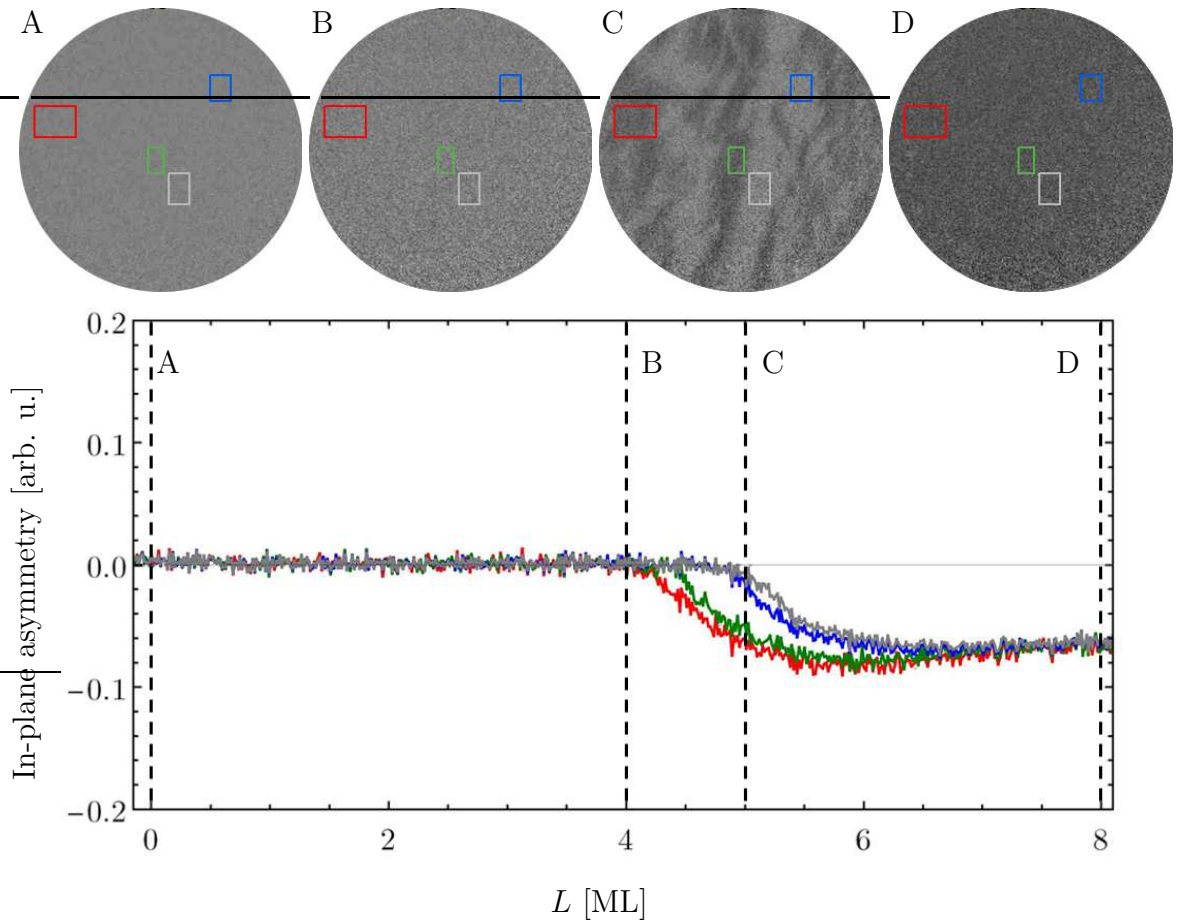


Figure 5.2: *In situ* observation of the thickness-dependent changes in spin-asymmetry during Fe growth (0.16 ML/minute) monitored for two ip (red, green) and two oop magnetised (blue, grey) regions. The SPLEEM images A-D show different stages during the growth process of Fe/Ag (001) and indicate the four RoIs which correspond to the asymmetry plot. They were taken for a FoV of $30\ \mu\text{m}$ and with an incident electron beam of 4.5 eV, whose polarisation was parallel to the sample's easy axis.

the growth process and correspond to the four SPLEEM images, which are labelled accordingly. These and all further SPLEEM images show the remanent state of the sample after the in-situ growth, meaning that no external magnetic field was applied. Here, the images were taken with an incident beam energy of 4.5 eV for a field of view (FoV) of $30\ \mu\text{m}$ and a beam polarisation parallel to the sample surface along the $[100]$ direction. Generally, in SPLEEM images the occurrence of bright and dark features indicates magnetic domains with opposite magnetisation and are caused by the spin-dependence of the reflection intensities (see Section 3.3.4). Areas of grey colour represent regions without magnetic contrast ($A = 0$), where $|M| = 0$ or $\vec{P} \perp \vec{M}$. The four RoIs are indicated by the four rectangles in each image with

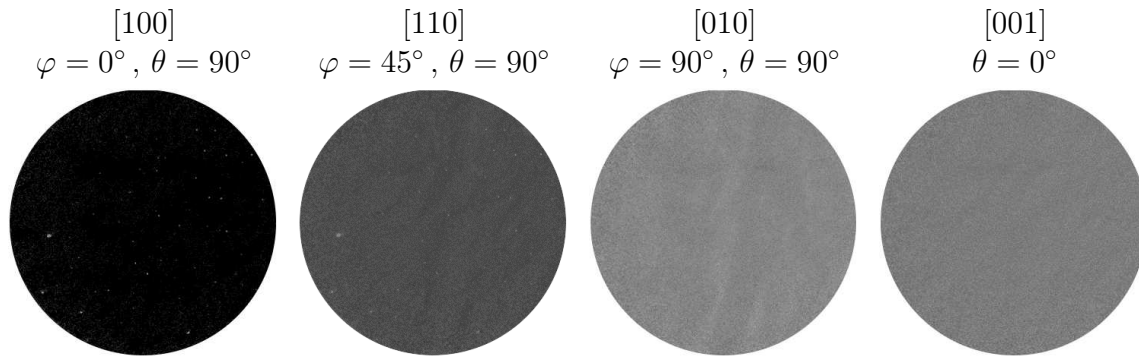


Figure 5.3: SPLEEM images of Fe/Ag(001) for varying angles of the incident beam's electron spin polarisation P . The first three images were taken with P having a polar angle parallel to the sample surface ($\theta = 90^\circ$) and azimuthal angles (φ) of 0° , 45° and 90° . The fourth image has $\theta = 0^\circ$ and is hence parallel to the surface normal. The change in brightness in these images shows that the asymmetry is proportional to $P \cdot M$ and that the sample has an in-plane magnetisation along the [100] direction.

their respective colour representing the corresponding plot lines.

It can be seen from image A, that no magnetic contrast appears at the beginning of the Fe deposition in all RoIs. Image B shows a snapshot of the sample at 4 ML, after which point ip magnetic contrast starts to appear. Image C shows the sample at about 5 ML Fe coverage at which stage several magnetic domains have become visible. Here, the dark regions have a thickness above the spin reorientation and thus have an ip magnetisation (RoI-red, RoI-green), while the grey areas are still magnetised out-of-plane (RoI-blue, RoI-grey). This behaviour is caused by the island-layer growth mode of Fe on Ag(001). The contrast reaches its maximum in image D, where the sample exhibits a homogeneous ip magnetisation within the FoV and all RoI have reached maximum magnetic contrast.

Figure 5.3 shows four SPLEEM images obtained for varying angles of incident electrons. The first three images are taken using incident electrons with a spin polarisation parallel to the sample surface ($\theta = 90^\circ$) and different azimuthal angles φ . Here, the first image is taken at $\varphi = 0^\circ$ and depicts the maximum magnetic contrast, thus indicating $P \parallel M$. This corresponds to the sample's magnetic easy axis, which is the [100] direction. The magnetic contrast in the second image ($\varphi = 45^\circ$) is decreased, as seen by the change in brightness. This is expected as the magnetic contrast can be represented by a cosine function of the azimuthal angle [130]. The third image ($\varphi = 90^\circ$) shows almost no magnetic contrast. This indicates that the electron beam's spin polarisation is perpendicular to the sample magnetisation. The analysis of these changes in brightness shows that the magnetic contrast in SPLEEM

images follows qualitatively $P \cdot M$. The last image is taken at a polar angle of $\theta = 0^\circ$. As there is no visible magnetic contrast the electron beam's spin polarisation has to be perpendicular to the sample's magnetisation ($P \perp M$) which thus lies in-plane with no oop component. For all further measurements, the spin polarisation of the illuminating electron beam was adjusted to be aligned with the magnetic easy axis of the film, *i.e.* the [100] direction. Based on this alignment, the spin direction of the incoming beam will further be defined with respect to the majority and minority spins of the sample. Here, I^\uparrow represents a beam alignment parallel to the majority spin direction of the sample.

5.1.3 Spin-dependent energy loss spectra

To investigate the interactions of spin-polarised electron beams with magnetic samples, spin-polarised electron energy loss (SPEEL) experiments were conducted, as explained in Section 3.3.4. The first investigation was performed on a pure Ag (001) substrate and on a sample of 5 ML Fe on Ag (001) which, owing to the Stranski-Krastanov growth mode, exhibited both ip- and oop-magnetised regions [174–176]. Here, two regions of interest (RoIs) are defined, further labelled RoI-ip and RoI-oop, which correspond to the red and grey squares in Figure 5.2, respectively. These represent areas from which the intensities at a given electron energy, MCP bias and spin orientation are extracted.

Figure 5.4 presents three SPEEL spectra taken for a primary beam energy of $E_0 = 15 \text{ eV}$ with a beam polarisation aligned parallel (orange) and antiparallel (blue) to the sample magnetisation. Each individual measurement point took about one to ten seconds, depending on the primary beam energy and has an error of approximately 0.66 eV.

The first thing to note is that these spectra are dominated mainly by two distinct features. The first is the quasi-elastic peak which is represented by a large intensity at zero energy loss. The second one is a broader peak between 8 eV to 12 eV for $E_0 = 15 \text{ eV}$, which will further be called the secondary electron (SE) peak. These two peaks differ in their origin as the elastic peak represents the elastically reflected primary electrons, *i.e.* backscattered electron (BSE), which have not undergone any energy losses, while the electrons contributing to the SE peak are created by inelastic scattering events inside the material and thus have a broader energy distribution than the BSE. It is important to note that the SE peak consists of a combination of “true” secondary electrons and a background of inelastically scattered primary electrons, which can not be separated easily. The SPEEL spectra drop to zero when the electrons have insufficient energy to overcome the material-dependent work

function. The three plots have been normalised by their elastic peak intensity and the background has been subtracted.

In the case of Ag (001) (Figure 5.4 a) the spectrum exhibits no measurable intensity difference between I^\uparrow and I^\downarrow . This demonstrates that the sample exhibits no significant spin-dependent interactions. The upper inset in the figure shows an enlargement of the SE spectrum^c, while the lower plot shows the spin-asymmetry, A . Both these plots show no distinguishable difference between the two spin spectra, again indicating no detectable spin polarisation within experimental errors over the examined energy loss region. The small peak at about 3.8 eV is the surface plasmon excitation energy loss of Ag [179].

The two energy loss spectra of 5 ML Fe on Ag (001) for RoI-oop and RoI-ip, shown in Figure 5.4 b and Figure 5.4 c respectively, demonstrate that depositing Fe results in a clear change in the spectrum compared to pure Ag. Firstly, the Ag surface plasmon excitation at 3.8 eV disappeared and secondly the intensity of the SE peak doubles in relation to the elastic peak intensity, going from 4% to 8%. As this increase appears in both RoIs, it indicates that the effect is independent of the magnetisation direction of Fe and that it is a material-dependent property related to the material's band structure. In comparison to Ag (001), which exhibits a band gap along the [001] direction and thus elastically reflects most electrons, Fe (001) has no band gap along this direction thus allowing electrons to enter the sample to be inelastically scattered, resulting in the creation of more SEs (see Section 5.1.4). As there was no detectable spin-asymmetry in neither Figure 5.4 a nor Figure 5.4 b one can further conclude that there is no spin-dependent component arising from the Ag (001) surface or from the Fe/Ag (001) interface and that the spin-asymmetries are solely caused by the in-plane ferromagnetism in the Fe layer.

While the plot for RoI-oop exhibits no difference between I^\uparrow and I^\downarrow for neither the elastic peak nor the SE peak and the spin-asymmetry averages to zero, the RoI-ip shows a clear difference between these two intensities. Here, the elastic peak for I^\uparrow is higher than for I^\downarrow , and the spin-asymmetry, shown in the inset, yields about -12% close to the elastic peak. The reason for this negative spin-asymmetry lies in the fact that we are effectively examining the reflectivity of the sample in dependence of the primary beam polarisation and not the material's polarisation P . This reflectivity is determined by the sample's spin-dependent DoS, as explained in more detail in Sec. 5.1.4. This means that, in the case of Fe (001), there are less minority states available just above the Fermi level causing I^\downarrow to exhibit a higher reflectivity compared to I^\uparrow and resulting in a negative spin asymmetry. This value

^cFor these plots only every other plot marker is shown for better visualisation.

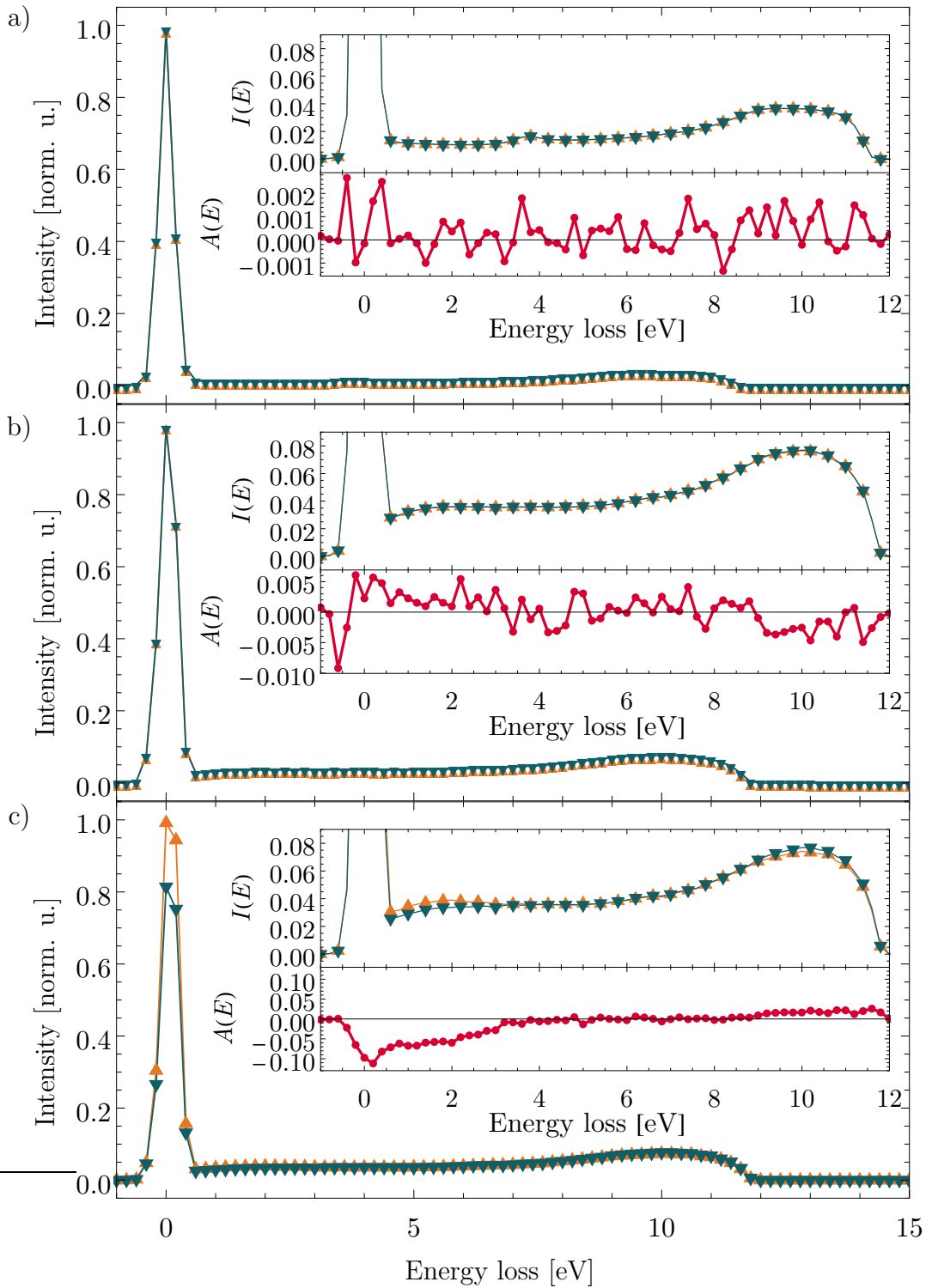


Figure 5.4: SPEEL spectra of a) a clean Ag(001) surface and b) an oop- and c) an ip magnetised region of 5 ML Fe/Ag(001) for a primary beam of $E_0 = 15$ eV. The main plots show the full spectrum for I^\uparrow (\blacktriangle) and I^\downarrow (\blacktriangledown), the upper insets show an enlargement of the secondary electron spectrum and the lower insets show the spin-asymmetry A (\bullet). All plots are normalised by their elastic peak.

decreases slowly to zero at about 2.5 eV. Another feature in the plot is the small but broad intensity peak from 1 eV to 2.5 eV. The scattering-asymmetry in this energy range is caused by Stoner excitations, as explained later, and corresponds to the ferromagnetic exchange splitting. Examining the broader SE peak, ranging from 8 eV to 12 eV in the inset, shows that this peak as well exhibits a spin-asymmetry. However, compared to the elastic peak, I^\downarrow is higher than I^\uparrow . This effect is apparent in the plotted asymmetry, which has now changed its sign with respect to the elastic peak and yields a value of about 2%, which is about ten-times larger than the noise level^d. The effect of the change in sign and asymmetry will be discussed in more detail in Section 5.1.5.

For the following experiments, a fully magnetised 8 ML-thick Fe/Ag (001) sample was used to yield a higher electron count than the previously discussed 5 ML-thick sample. At this thickness, the Stranski-Krastanov growth mode is still present, but the sample's average thickness is large enough to form a continuous ferromagnetic film with an ip magnetisation, as shown in Figure 5.3. Using this sample, three SPEEL scans at primary beam energies of $E_0 = 10$ V, 15 V, and 20 V have been measured and are shown in Figure 5.5. These spectra are normalised by their so-called mirror intensity I_0 . This can be done by operating the SPLEEM in mirror mode, meaning that 100% of the electron beam is reflected as the impinging electrons have an energy below the sample's work function (see Section 5.1.4). Thus, this normalisation gives the relation between the total number of impinging electrons and the number of inelastically scattered electrons *i.e.* the electron yield profile in correlation to a certain beam energy.

Comparing the elastic peaks between the three spectra reveals a significant change in intensity and spin-asymmetry for the backscattered electrons. The elastic peak at $E_0 = 10$ eV is only 8.7% of the mirror intensity, meaning that about 91.3% of the impinging electrons get inelastically scattered and lose energy. This percentage increases further with increasing primary beam energy, going from 91.3% at 10 eV to 95.2% for the majority and 96.8% for the minority at 15 eV to 97.6% for the majority and 98% for the minority spins at 20 eV. The cause of this decrease in BSE intensity is the material's band structure as explained in detail in Section 5.1.4. Examining the scattering asymmetries at the elastic peak shows that there is almost no difference in I^\uparrow and I^\downarrow at $E_0 = 10$ V and that I^\downarrow is higher than I^\uparrow for both $E_0 = 15$ V and 20 V. Based on the analysis in Section 5.1.4 it can be deduced that I^\uparrow (I^\downarrow) corresponds to a beam alignment parallel (antiparallel) to the majority spins.

^dThe noise level was approximated by the A in RoI-loop in Figure 5.4 b.

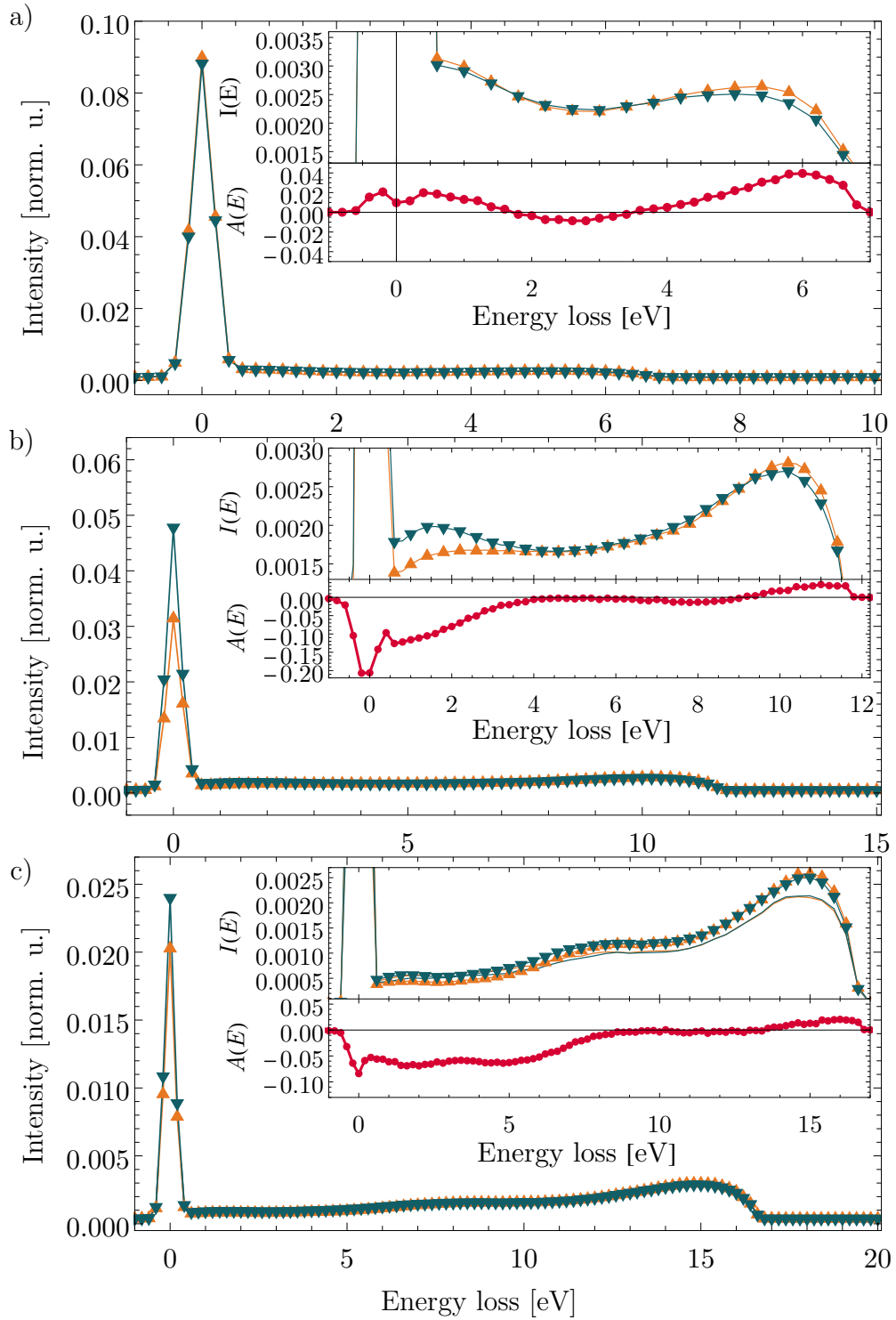


Figure 5.5: Energy loss spectra of 8 ML Fe/Ag (001) for primary beam energies of a) $E_0 = 10$ eV, b) 15 eV and c) 20 eV. The main plots show the full spectra for I^\uparrow (\blacktriangle) and I^\downarrow (\blacktriangledown). The insets show enlargements of the secondary electron spectra and the spin-asymmetry (\bullet). The lines in c) show the spectrum for 5 ML Fe/Ag (001). All plots are normalised by the mirror intensity.

As briefly mentioned in the preceding discussions, the peak at about 1 eV to 3 eV is caused by inelastically scattered primary electrons, which have lost some of their initial energy due to Stoner excitations. In these electron-hole pair excitations, an incident electron of a given spin occupies an unoccupied state of the material and an electron of opposite spin is excited and can be detected [180]. As there are more minority states available above the Fermi level, it is more likely that an incident electron with minority-spin orientation drops into an empty minority-spin state and excites an electron of the occupied majority-spin band, as indicated in Figure 5.6. The latter electron then leaves the sample with a kinetic energy equal to the energy of the incident electron minus the energetic difference between the spin-split states [181]. The opposite process, *i.e.* a spin-flip for a primary electron with spin parallel to the majority-spin band, has comparatively low probability but is non-negligible in Fe [182]. However, Stoner excitations can take place with or without a spin-flip event [182]. Thus, to further analyse the amount of spin-flip to non-spin-flip events one would need to detect the spin of the scattered electrons, *e.g.* by employing a Mott polarimeter. It would then be possible to determine the contribution from losses in which the incident electron's spin is flipped in the course of the scattering event. However, in the experiments presented here it is only possible to determine that the decreased spin-asymmetry, compared to the elastic peak, indicates that an electron beam parallel to the minority-spin direction triggers more scattering events, as would be expected. The Stoner excitations have a maximum scattering-asymmetry at around 2 eV, which is in very good agreement with the spin split

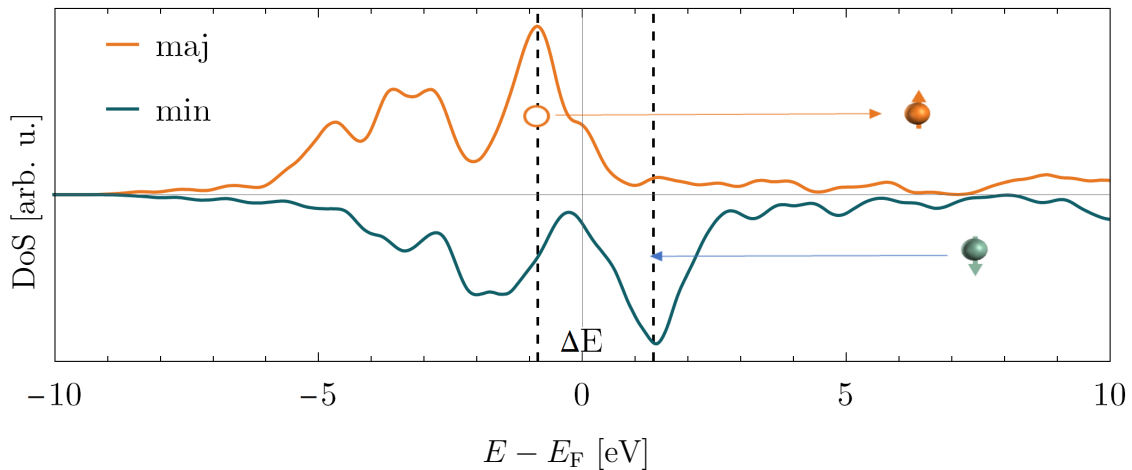


Figure 5.6: The DFT-calculated spin-resolved density of states of Fe. The Stoner excitation process is sketched onto the simulated DoS and the dashed lines indicate the exchange splitting of about $\Delta E = 2.3$ eV.

of $\Delta E = 2.3$ eV in the DoS calculated by the DFT program CASTEP^e, shown in Figure 5.6. Using Eq. (1.1), the simulated DoS further has a spin polarisation of about 35% at the Fermi level, which agrees well with experimentally found values of about 33% [183,184].

The broad intensity peaks at high energy losses correspond again to the energy distribution of the secondary electrons, where the maximum represents the most probable energy loss. These SEs usually leave the sample with a broad energy distribution between 1 eV to 10 eV [185], as the secondary cascade of collisions produces more and more secondary electrons at progressively lower energies. It can further be seen that the SE peak exhibits a larger intensity for I^\uparrow than for I^\downarrow in all three plots. This means that the SE yield is higher if the incident beam is aligned parallel to the majority spins. This effect will be discussed in more detail in Section 5.1.5. Comparing the maximum scattering-asymmetry of the SE peak for different primary energies shows that it only decreases slightly, from 3.9% to 3.2% and to 2.0% for the consecutive energy loss scans compared to the large changes in elastic peak asymmetry.

Another larger shoulder at around 10 eV, which exhibits no spin-asymmetry, is visible in the SPEEL spectrum for $E_0 = 20$ V but is absent in the other two spectra at lower primary energies. This feature is also visible in the SPEEL spectrum of 5 ML Fe/W(001) as shown in Figure 5.5 c. However, this peak is absent in the spectra of Fe/Ag(001) at $E_0 = 20$ V (see Section 5.2.3), indicating that the peak is related to the crystallographic direction of Fe(001) and is possibly a feature of the sample's surface or band structure. The absence of this peak in the spectrum of pure Ag(001) (Figure 5.4 a) further shows that the substrate has no influence on this effect. The exact origin of this peak could not be determined in the course of this work. To further analyse the potential origin of this feature, SPEEL scans for higher primary energies could reveal whether this is a higher energy feature related to multiple scattering or an effect of the band structure several electronvolts below the Fermi level.

As discussed in Section 3.3.4, these energy loss scans can be used to determine the energy-dependent maximum SE peak positions, which are indicated by the black arrows in Figure 5.7. These, and all following peak positions, are determined by using a spline-fit between data points and a Gaussian filtering, which then gives the maximum value. Here, the standard deviation is about 0.5 eV. Due to the linear correlation between maximum peak position and primary beam energy, shown in the inset, it was possible to measure the spin-dependent asymmetry and the change

^eSee Section 5.1.4 for further details on the simulation parameters.

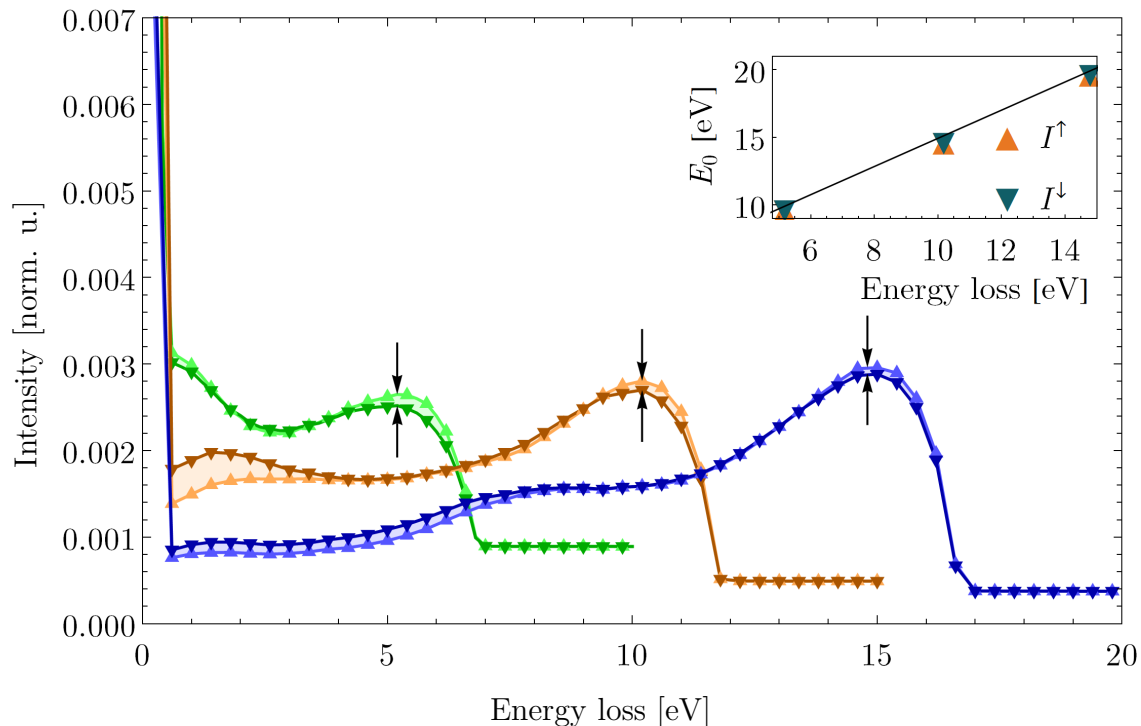


Figure 5.7: Enlarged view of the secondary electron peaks for the three SPEEL spectra of Fe(8 ML)/Ag(001) at $E_0 = 10$ eV, 15 eV and 20 eV. The black arrows indicate the SE peak position for each scan. The inset shows the linear correlation between the primary beam energy and the maximum SE peak energy. All plots are normalised by their mirror intensity.

in maximum secondary electron yield for a certain energy in relation to the primary beam alignment for a variety of different beam energies in a short period of time. The results of these measurements will be discussed in Section 5.1.5.

5.1.4 Reflectivity scans and band structure probing

As part of the experiments, energy-dependent reflectivity scans were performed that allow to scan the unoccupied electronic states above the Fermi level and to determine which orientation of the incident beam ($I^{\uparrow,\downarrow}$) is parallel to the sample's magnetisation by rotating the spin direction of the primary beam. For this the primary beam energy was varied from 0 eV to 25 eV in steps of 0.5 eV by varying the potential difference between the Fermi levels of the photocathode and the sample and the elastic peak *i.e.*, the reflectivity, was recorded. Such spectra for 8 ML-thick Fe/Ag(001) and pure Ag(001) are shown in Figure 5.8. Both spectra are normalised by their mirror reflection via $R(E) = I(E)/I_0$.

The first thing to note is that the backscattering of electrons is not a simple

monotonic function, but varies strongly with energy and is dependent on the material's electronic band structure. The plateau at the beginning of the spectrum indicates the energy range in which the incident electrons are totally reflected above the surface (mirror mode) due to the retarding field and the difference in potential barrier. The threshold energy of this region predominantly depends on the difference between the emitter's and the material's work function and thus allows to measure the material's local work function employing Φ_{emitter} . In the experiments presented in this chapter, the emitter consists of a CsO₂-activated GaAs/GaAsP super-lattice with $\Phi_{\text{emitter}} = 1.6 \text{ eV}$ ^f while Fe (001) has a work function of $\Phi_{\text{Fe}(001)} = 4.64 \text{ eV}$ [186]. Hence, the threshold energy of about 3 eV agrees well with the expected value. As Ag (001) has a very similar work function ($\Phi_{\text{Ag}(001)} = 4.64 \text{ eV}$ [186]) to Fe (001) both spectra exhibit the same threshold energy. This further means that the impinging electrons have a kinetic energy of 0 eV at a beam voltage of 3 V. The small decrease in the mirror intensity prior to the threshold energy is caused by the sample's topography, such as scattering from steps and edges on the sample surface, and by local variations of the work function. The energy dependence for $E_{\text{kin}} > 0 \text{ eV}$ can be interpreted in terms of the density of unoccupied states and the energy-dependent inelastic mean free path.

In the case of the Ag (001) sample, the spectrum exhibits a slow decrease from 0 eV to 2.5 eV, after which the reflectivity drops significantly. This can be understood in terms of the electronic band structure shown in Figure 5.8 b. This DFT-simulated band diagram of an infinite Ag crystal along the [001] direction was obtained using the software CASTEP [187] and is adjusted by the vacuum energy. For these, and all further CASTEP simulations in this chapter, pseudopotentials were employed with a kinetic cut-off-energy of 300 eV and the LDA in CA-PZ (Ceperley, Alder [188] parameterised by Perdew and Zunger [76]) was chosen for the exchange correlation energy. The Brillouin zones of the unit cells were sampled by a 12 x 12 x 12 k-point mesh. In case of Fe, the system had a spin polarisation of two.

The figure demonstrates that the high reflectivity and sudden drop are related to a band gap of 2.5 eV above vacuum level in the spectrum (dashed line). In this gap, the incoming electrons are only able to penetrate slightly into the crystal as evanescent waves, as there are no allowed states available, causing strong elastic scattering.

The two spectra for the Fe (001) film for spin-up and spin-down beams show a decrease in reflectivity from 0 eV to 3 eV and exhibits a clear spin-asymmetry of about 5% at 1 eV. At this low energy, the IMFP is highly spin-dependent, meaning

^fKnown from discussions with Dr. Suzuki, who is an expert in the experimental setup.

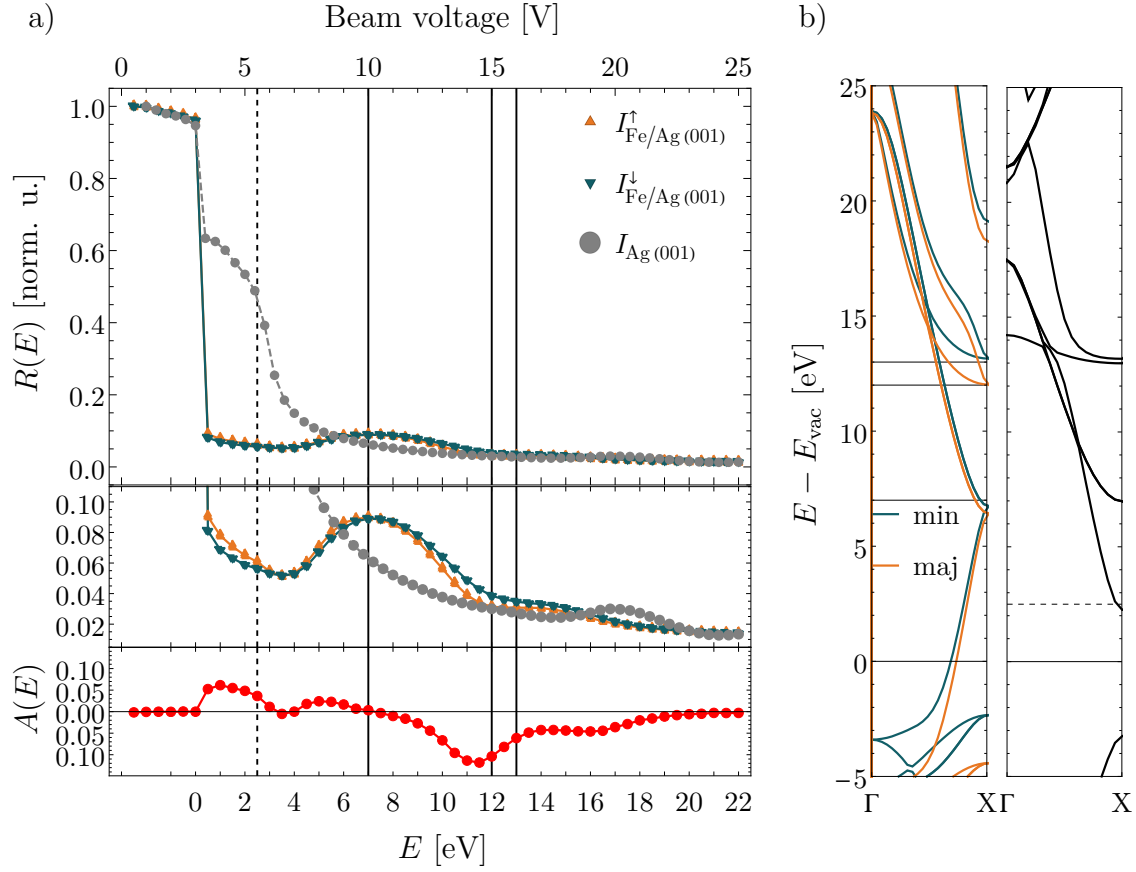


Figure 5.8: a) Primary electron intensity (top), an enlarged view of the low reflectivity region (middle) and the spin-asymmetry (bottom) versus incident beam energy for 8 ML Fe/Ag(001). b) Spin-dependent DFT-calculated band structures of an infinite Fe (left) and an infinite Ag (right) crystal along the [001] direction. The energy reference is taken at the vacuum level, which is 4.64 eV above E_{F} . The solid (dashed) lines correlate features in the spectra with electron bands in Fe (001) (Ag (001)).

that usually minority electrons have a three-times shorter IMFP compared to the majority electrons due to the higher density of unoccupied minority states around the Fermi level in the crystal. Therefore, an electron beam with a polarisation parallel to the minority electrons is more likely to be inelastically scattered than one parallel to the majority electrons. Above 3.5 eV, both partial reflectivities exhibit an increase again with a broad peak at 7 eV which is related to a drop in available states.

The scattering-asymmetry exhibits a large intensity peak at about 11.5 eV of approximately -12%. As can be seen in the band diagram, at this point the majority electrons have a higher DoS than the minority states. This causes the latter to exhibit a higher reflectivity, causing the increased asymmetry. The minority spins have a band onset at about 12.5 eV, at which point the minority and majority spins

have an equal DoS and the spin-asymmetry reaches a stable value. This analysis shows the correlation between reflectivity and band structure. Moreover, based on this analysis and the spin manipulation of the primary beam it is possible to determine which beam polarisation corresponds to an alignment parallel or antiparallel to the sample’s majority-spin electrons. As defined by Eq. (3.5), a positive (negative) spin-asymmetry indicated a higher majority (minority) electron reflection. It can further be seen that, as the incident beam energy increases, the asymmetry decreases. This is caused by the reduction in spin-dependence of the IMFP at higher beam energies and when the electron kinetic energy becomes large compared to the exchange splitting in the density of states of the d -bands. Thus, this effect on the scattering asymmetry limits SPLEEM to energies below 20 eV.

Despite the presence of band gaps, none of the spectra displays a total reflection like the mirror mode. This reduced reflectivity is caused by several reasons [189]: (1) although the incident electron beam only penetrates the crystal as an evanescent wave in a band gap region, it still has a finite penetration depth and electron may suffer inelastic scattering and energy losses, (2) the surface potential barrier and additional surface states can cause inelastic scattering, (3) crystallographic imperfections, such as atomic steps, ad-atoms and vacancies can lead to scattering. One should further consider the influence of additional surface states which would reduce the reflectivity and which were not considered in the current DFT simulations.

5.1.5 ESSEY-SPLEEM mode

Using the linear correlation between primary beam energy and the SE peak’s maximum intensity position, energy- and spin-dependent secondary electron yield measurements were performed, as explained in Section 3.3.4. Based on the peak maximum’s energy, the investigated SE electrons have a kinetic energy of about 1.9 eV above vacuum level, which represents the most probable SE energy loss value. The primary beam energy was varied from 10 eV to 20 eV in steps of 0.5 eV. This energy range was chosen, as primary beam energies below 10 eV do not create “true” secondary electrons, while energies above 20 eV exhibit almost no difference in spin-dependent IMFP [190, 191]. The resulting energy-selective secondary electron yield spectrum is shown in Figure 5.9.

Generally, low-energy secondary electrons are created if a primary electron gets inelastically scattered and loses energy creating electron-hole pairs (Stoner excitations). These excited electrons can in turn excite other electron-hole pairs and thus create a secondary electron cascade which, depending on their energy, momentum, and starting depth, will be emitted from the solid. The thus created SEs

give valuable information about inelastic scattering processes and the band structure of a material below the Fermi level. Due to the low primary beam energy, the SEs in the experiments presented here will come primarily from the valence band as secondary electron emission involving inner electron shells can be neglected as they cannot take place due to the insufficient energy of the primary beam [189]. However, here one should consider that it is difficult to distinguish between inelastically scattered electrons and “true” secondary electrons for an energy range below 50 eV. Other inelastic scattering processes, such as electron-phonon scattering and magnon excitation involve only small energy losses and thus do not contribute to the SE peak [138].

The first thing to note in Figure 5.9 is that the energy-selective secondary electron yield (δ_{ESSEY}) for electrons with an energy of 1.9 eV is higher if the incident electrons are aligned parallel to the majority-spin direction of the sample over the whole energy range under investigation. The reason for this effect is based on the spin-dependent band structure, DoS, the IMFP and the subsequent scattering. As

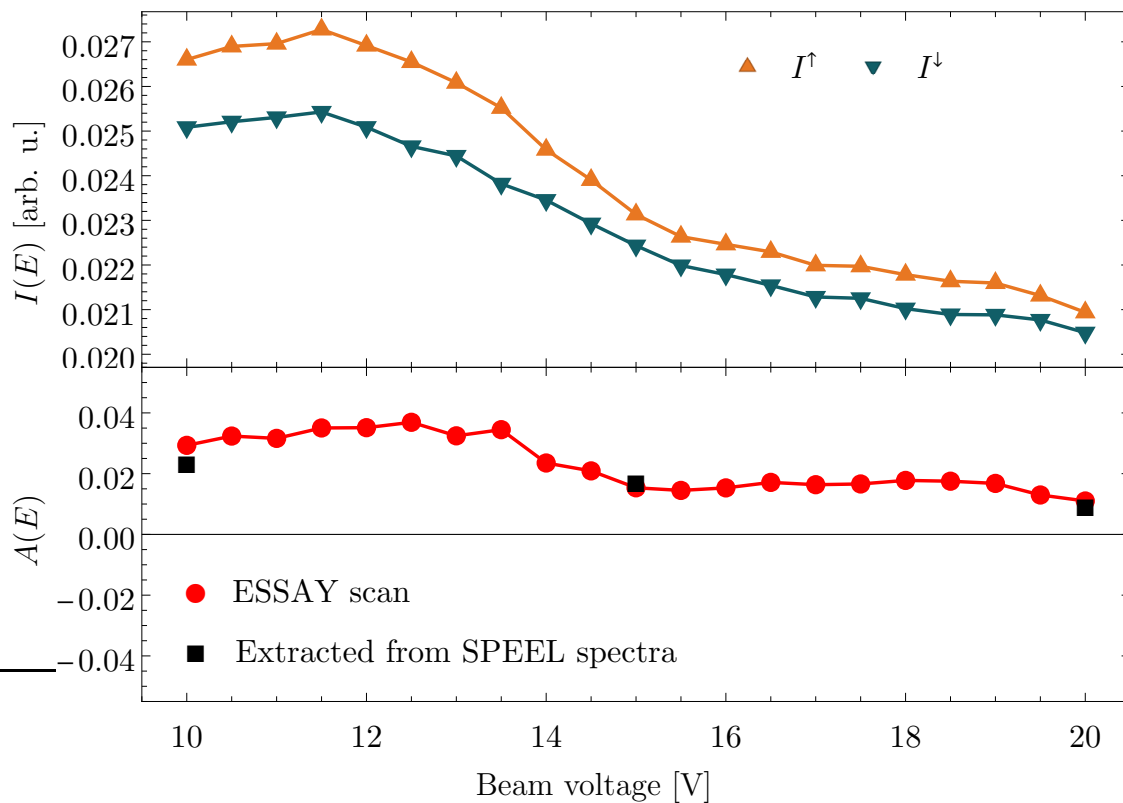


Figure 5.9: Energy-selective secondary electron yield spectrum of Fe/Ag (001) (top) and spin-dependent asymmetry in SE yield (bottom) versus primary electron beam voltage. The black squares represent the asymmetry values extracted from the three energy loss scans.

can be seen from Figure 5.8 the primary electrons parallel to the sample magnetisation (spin-up) had a lower reflectivity in the energy region from 10 eV to 20 eV than electrons with antiparallel orientation (spin-down). This means that more spin-up electrons penetrated into the material and were inelastically scattered, thus creating more SEs. Furthermore, as was shown in Figure 3.14 b spin-up electrons can penetrate deeper into the material and thus have a bigger interaction volume. At the same time, spin-down electrons that enter the crystal have a larger probability of scattering into unoccupied spin states and thus exhibiting Stoner excitations. This increased inelastic scattering can cause momentum changes in the emitted electrons and thus large scattering angles. Hence, the detected signal would be attenuated if the momentum change is larger than that accepted by the angle-limiting aperture. However, as these Stoner excitations can trigger secondary electron cascades the difference in scattering asymmetry reaches a maximum of only about 3.5% at $E_0 = 12.5$ eV. Here one should keep in mind that it is not possible to distinguish between true SE and inelastically scattered primary electrons. Thus, this increased intensity for I^\uparrow could also be due to an increased background of inelastically scattered primary electrons. It is generally a safe approximation to assume that an electron's spin is conserved during scattering and emission of electrons parallel to the majority electrons as pure Coulomb scattering does not flip spins and only exchange and spin-orbit scattering events can flip spins. This means that electrons with I^\uparrow and which have undergone non-flip excitations have a higher probability than minority electrons to pass the surface barrier to be detected. To validate these considerations, one would need to investigate the spin-polarisation of the emitted electrons, *e.g.* using a Mott polarimeter. This would give indications of the amount of Stoner excitations and would potentially allow determination of the number of true SEs.

The second thing to note in the spectrum is the slight decrease in SE yield with increasing primary energy. It will be shown in Section 5.2.5 and Section 5.3.4 that this behaviour is consistent in all experiments and is again caused by the energy dependence of the IMFP of the electrons. As can be seen from a universal curve such as in Ref. [192], electrons with very low energies below 50 eV exhibit a decrease in IMFP with increasing energy. As the primary beam energy used in the experiments presented here lies within this energy regime, the primary electrons can travel longer into the crystal before getting scattered at $E_0 = 10$ eV than for 20 eV. Thus, the interaction volume decreases, which results in the creation of fewer SEs. However, here one needs to consider that the ESSEY scans do not represent the total SE yield but only the yield of electrons with an energy of 1.9 eV. Thus to validate

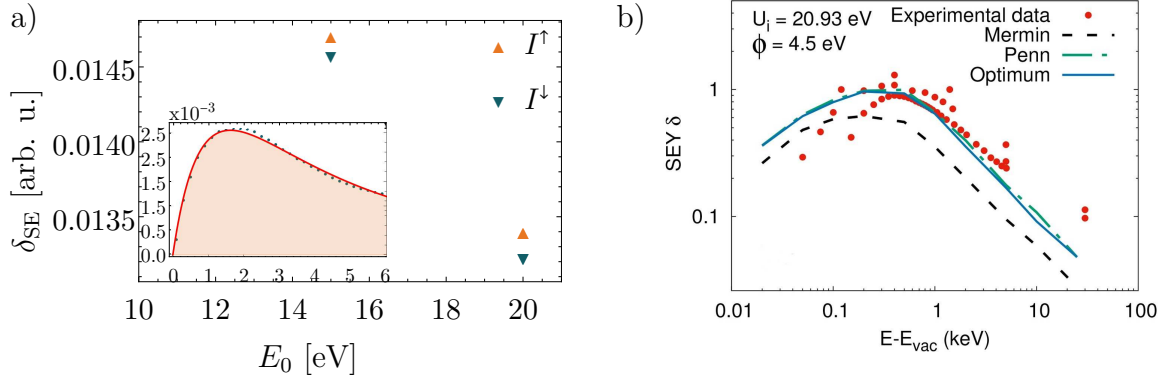


Figure 5.10: a) Calculated SE electron yield versus primary beam energy. The yield was calculated by fitting Eq. (5.1) to the experimental data as shown in the inset. b) Comparison of the secondary electron yield for Fe taken from Figure 5 b in Ref. [192].

this tendency, the SE peaks obtained from the SPEEL spectra were fitted using the following equation for the energy distribution

$$\frac{dj(E)}{dE} = \kappa \frac{E}{(E + \Phi)^4} \quad (5.1)$$

and the area was integrated. Here, κ is a normalised constant [192]. The resulting SE yield for $E_0 = 15$ eV and 20 eV are shown in Figure 5.10 and the inset shows a fitted curve for $E_0 = 20$ eV. Due to the Stoner peak, it was not possible to fit the SE peak for 10 eV. Nevertheless, the two values indicate a slight decrease in SE yield. This effect is unexpected compared to the experimentally and theoretically found primary-beam-energy-dependent total electron yield for $E_0 > 100$ eV [192–195]. As shown in Figure 5.10 b, taken from Figure 5 b in Ref. [192], the SE yield from Fe exhibits an initial increase for low primary beam energies which peaks at around 300 eV before decreasing again. However, these measurements were done for higher primary energies than the ones used in this work.

The sudden decrease in Figure 5.9 between 13 eV and 16 eV could be correlated to the band structure and decreased DoS at this beam energy, as was found for the reflectivity (see Figure 5.8), but the exact origin of this feature could not be determined in the course of this work. Investigating the asymmetry, which corresponds to the spin-dependent difference in SE yield, shows that in this energy range the asymmetry drops from about 4% to 1%, but otherwise A only decreases slightly. This slight decrease could be caused by the decrease in spin-dependence of the IMFP for increasing energies, as seen in Figure 5.8. The plot shows that $l^\uparrow \approx l^\downarrow$ at $E_0 = 20$ eV and thus the interaction volume for I^\uparrow and I^\downarrow becomes equal. On the contrary, I^\uparrow

has a larger IMFP and consequently a larger interaction volume at lower energies. This effect coincides with I^\downarrow having a higher chance to trigger an SE cascade due to their higher probability to trigger Stoner excitations, which would also reduce the asymmetry as it compensates for the difference in reaction volume. As can be seen in Section 5.2.5 and Section 5.3.4, this tendency was found for all three samples under investigation.

Moreover, as can be seen from Figure 5.9, the scattering asymmetry gained from the ESSEY scans is in good agreement with the asymmetry calculated from the SE peaks of the three individual energy loss scans (black squares in the plot). This shows that this measurement technique is a fast and reliable way to determine the energy-selective secondary electron yield for a spin-polarised electron beam in relation to the orientation to the sample's majority spins.

5.2 SPLEEM investigation of ultra-thin Fe/W (110)

To investigate the changes in magnetic properties of ultra-thin Fe for a different crystallographic direction, the second sample was chosen to be Fe/W (110). This material system, especially in the ultra-thin coverage regime, has been extensively studied both experimentally as well as theoretically and exhibits a rich variety of structural, electronic, and magnetic properties [196–201]. Furthermore, W is a well-known field emission source that can be covered by a ferromagnetic layer to act as a potential SP-FES [62, 64, 65].

5.2.1 Sample preparation of Fe/W (110)

The preparation of the W (110) substrate, used in this work, was done by a standard cleaning procedure in which the substrate is heated in low-pressure oxygen at 1400 K and subsequently repeatedly flashed to about 2000 K. The surface quality prior to the Fe deposition was checked with LEEM and LEED. Figure 5.11 a shows that the cleaning procedure yielded a sharp (1x1) LEED pattern with low background indicating a smooth and well-ordered single-crystalline W surface.

Generally, the growth process of Fe on W (110) is very complex and can range from pseudomorphic over Stranski-Krastanov to Frank-Van der Merwe mode, whereby the exact growth morphology is strongly dependent on certain growth conditions such as temperature, film thickness or post-annealing [198–201]. In this work, a deposition rate of 0.15 ML/minute was used, which was again monitored by observing the sample's intensity oscillations during growth using the SPLEEM. The substrate was kept at about 500 K during deposition. Compared to the previously discussed

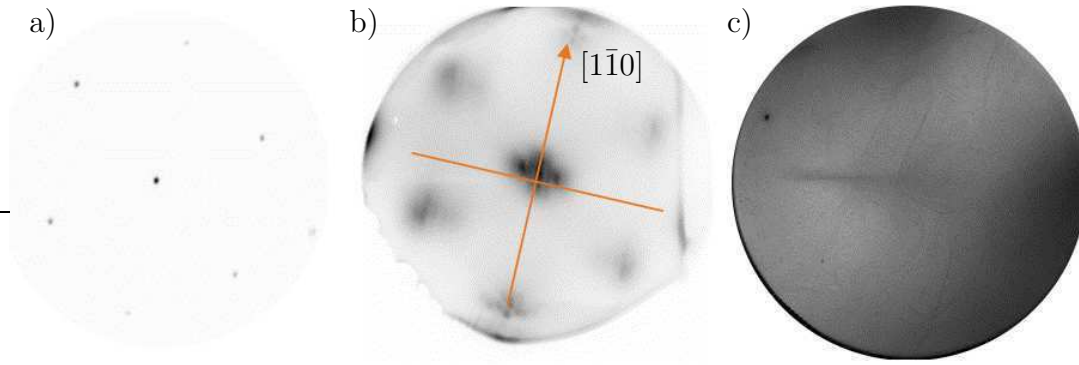


Figure 5.11: Low-energy electron diffraction pattern of a) the pure W (110) substrate and b) the 5 ML Fe/W (110) structure taken at room temperature and at a primary electron energy of $E_0 = 100$ eV. The orange arrows indicate the crystallographic $[1\bar{1}0]$ directions. c) Topographic images of the Fe/W (110) substrate in which atomic steps appear as dark lines. All images were taken for a FoV of $30 \mu\text{m}$.

heterostructure of Fe/Ag (001), Fe/W (110) has the advantage of being immiscible thus allowing for an elevated deposition temperature [198]. These growth conditions resulted in a more homogeneous film thickness of Fe over the surface with large, atomically flat regions and a low density of steps. This can be seen in Figure 5.11 c, which shows the topographic image of the sample after the deposition of 5 ML Fe for a FoV of $30 \mu\text{m}$. Here, the continuous and flat terraces appear bright, while the darker curved lines and bands represent the monoatomic or multilayer steps. The relative step depth can be approximated by its shade, as deeper steps result in more diffuse scattering and hence appear darker in the image. Thus, the figure shows that the sample has low step heights and that the resulting terraces are large regions of constant thickness.

Figure 5.11 b shows the LEED pattern after the deposition of 5 ML of Fe taken with a primary energy of 100 eV, which exhibits satellite reflections that coincide with the position of the clean W pattern. These can be attributed to periodic lattice distortions between Fe and W caused by the lattice mismatch of about 9.4% ($a_{\text{Fe}} = 2.866 \text{ \AA}$, $a_{\text{W}} = 3.165 \text{ \AA}$), as discussed in detail in Ref. [200]. The existence of this pattern is indicative of pseudomorphic Frank-Van der Merwe growth.

5.2.2 Onset of magnetic domain structure and orientation

Similar to Section 5.1.2, Figure 5.12 shows the *in situ* development of the in-plane spin-asymmetry during sample growth for an incident beam energy of about 7 eV. Here, the first traces of magnetic contrast occur after about 1.45 ML, hence indicating the onset of ip magnetism in the sample. This value is in good agreement

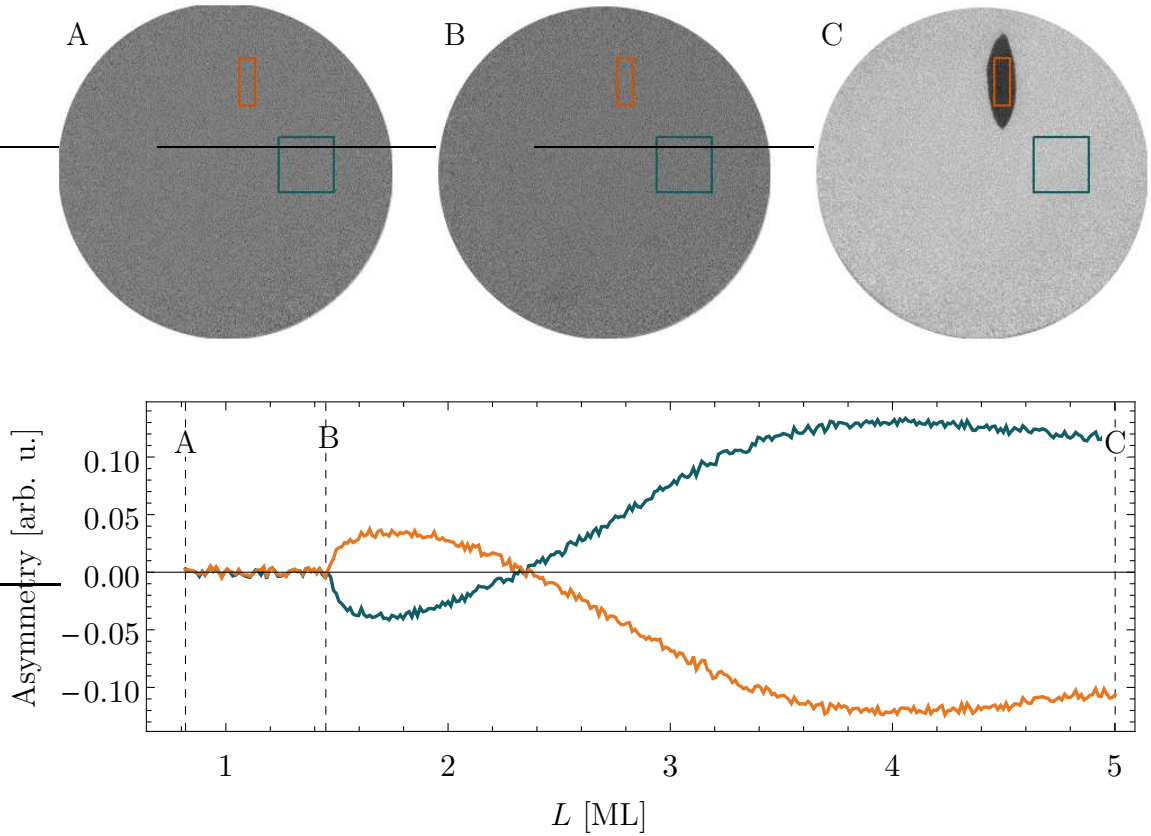


Figure 5.12: Evolution of the thickness-dependent spin-asymmetry during Fe growth (0.15 ML/minute) monitored for two antiparallel domains. The SPLEEM images (A - C) show different stages during the growth process of Fe on W (110), as marked in the asymmetry plot. They were taken for a FoV of $30\ \mu\text{m}$ and with an incident electron beam of 7 eV, whose spin-polarisation direction was parallel to the sample's easy axis.

with the previously reported value of 1.5 ML in Ref. [202]. As the initial W sample had a smooth surface and low step density, iron's pseudomorphic growth leads to a simultaneous onset of ip magnetism in both RoIs (orange and blue), which differs from the time-delayed onset in the Fe/Ag (100) sample.

After reaching a local maximum at around 1.7 ML the asymmetry decreases again and switches sign at about 2.4 ML. This effect could be caused by spin-dependent interference of the electron beam in the Fe thin film. A similar effect was found for both Fe and Co on W (110), where the asymmetry exhibits quantum size oscillations with changing electron beam energy [126, 201, 203], which were attributed to the spin-dependent interference of the electron beam in the thin film, or a spontaneous reorientation due to magnetic domain merging. Here, the asymmetry reaches its maximum value at $L = 4\ \text{ML}$, after which it starts to decrease again. This is expected, as the surface roughness increases with film thickness, which in turn results

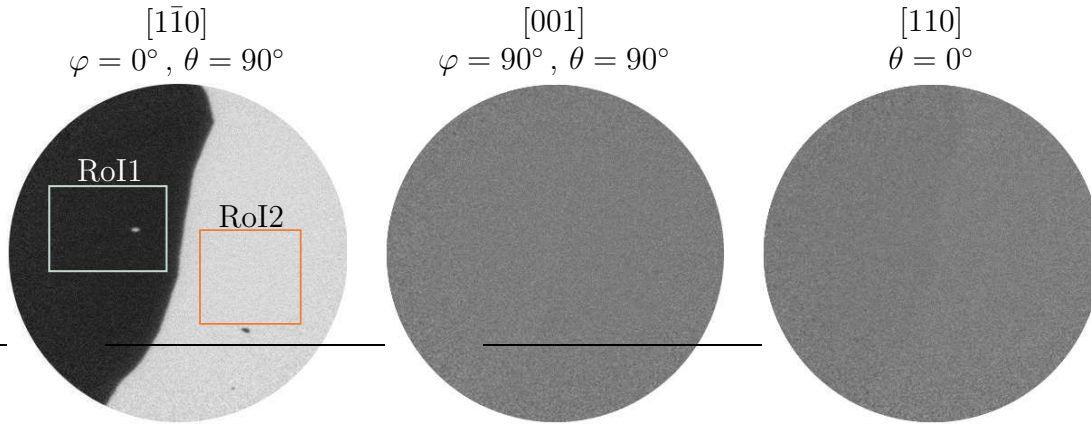


Figure 5.13: SPLEEM images of Fe/W (110) for a polar angle of 0° (left) and 90° (middle) at an azimuthal angle of 90° and one for an azimuthal angle of 0° (right). The analysis shows that the sample has an in-plane magnetisation with its easy axis along the $[1\bar{1}0]$ direction. The right image indicates the existence of a Néel wall boundary between the domains.

in a decrease of the reflectivity [203].

The dotted lines in the plot, labelled A-C, correspond to three different stages during the growth process and are correlated to the three SPLEEM images shown above the plot, which are labelled accordingly. These images were taken with an incident beam energy of 7 eV and for a FoV of $30\ \mu\text{m}$. As expected, no magnetic contrast appears in the beginning of the Fe deposition in image A, which has a homogeneous grey colour. Image B was taken just when the magnetic contrast started to emerge. Image C shows the sample after the deposition of 5 ML Fe, at which point it exhibits almost maximum magnetic contrast. In this image, the bright and dark features indicate the existence of two magnetic domains with opposite magnetisation direction. The brightness of the domain depends on the projection of the beam polarisation onto the local surface magnetisation vector.

The three SPLEEM images in Figure 5.13 show the angular-dependent change in magnetic contrast. Here, the first image was taken for a polar angle of $\theta = 90^\circ$, meaning that the incident electrons have a spin polarisation parallel to the sample surface, and an azimuthal angle of $\varphi = 0^\circ$, which is parallel to the sample magnetisation. As before in Figure 5.12, the bright and dark contrast shows the existence of magnetic domains, which have an opposite magnetisation direction. By using the crystallographic information gained from LEED, it was found that \vec{M} lies along the sample's $[1\bar{1}0]$ direction. Thus, this corresponds to the sample's easy axis caused by its strong surface anisotropy. Above a certain critical thickness, the sample's easy axis would switch to lie along the $[001]$ direction as expected for bulk Fe [199]. The

second image was taken at $\varphi = 90^\circ$ and thus along the [001] direction. As there is no visible magnetic contrast one can assume that this direction is perpendicular to the sample's magnetisation. The last image at $\theta = 90^\circ$, shows the sample's out-of-plane component. Here, most of the magnetic contrast again vanishes as the incident beam's spin polarisation becomes perpendicular to the magnetisation. However, the slight contrast in brightness between the two domains indicates some spin canting at the surface. Furthermore, a "faint line" at the boundary between the two domains becomes visible. This indicates that the boundary seen here creates a Néel wall where the magnetisation smoothly rotates from the direction of the first domain to the direction of the second. As this domain wall rotates the magnetisation in and does not have an oop component there is no strong contrast visible.

5.2.3 Spin-dependent energy loss spectra

As previously described in Section 5.1.3 energy loss spectra for $E_0 = 10$ eV, 15 eV and 20 eV were measured. Here, two regions of interest, corresponding to the two domains seen in Figure 5.13 and labelled RoI1 and RoI2, were chosen as they had a low step density and a homogeneous film magnetisation. For both regions, the primary beam's spin polarisation was set to be parallel and antiparallel to the domain magnetisation. The resulting SPEEL spectra, normalised by the mirror intensity, are shown in Figure 5.14. Here, one can see that the spectra for both regions are identical for the respective primary energy but opposite in sign, as in RoI1 I^\uparrow is parallel to the majority electrons and antiparallel in RoI2.

Comparing the elastic peak in the three spectra for RoI1 shows that neither the reflectivity nor the spin-asymmetry exhibit significant changes with regards to incident beam polarisation or energy. In case of $E_0 = 10$ eV the reflectivity is about 6% and about 3% for both $E_0 = 15$ eV and 20 eV, which is again correlated to the unoccupied band structure of the sample and will be discussed in Section 5.2.4. As the band structure differs for different crystallographic directions the reflectivity for Fe(110) differs from Fe(001). However, similar to Fe/Ag(001) the elastic peak intensity decreases with increasing primary beam energy. The spin-asymmetry stays relatively constant at about 5% for all three primary energies.

The energy loss region after the elastic peak, between 1 eV to 3 eV, is again attributed to the inelastically scattered primary electrons which have undergone Stoner excitations. For these, the scattering-asymmetry is relatively constant at about 5% which is similar to the values of the Fe/Ag(001) sample. This might indicate that the inelastic scattering due to Stoner excitations is independent of the material's direction-dependent band structure and only depends on the overall

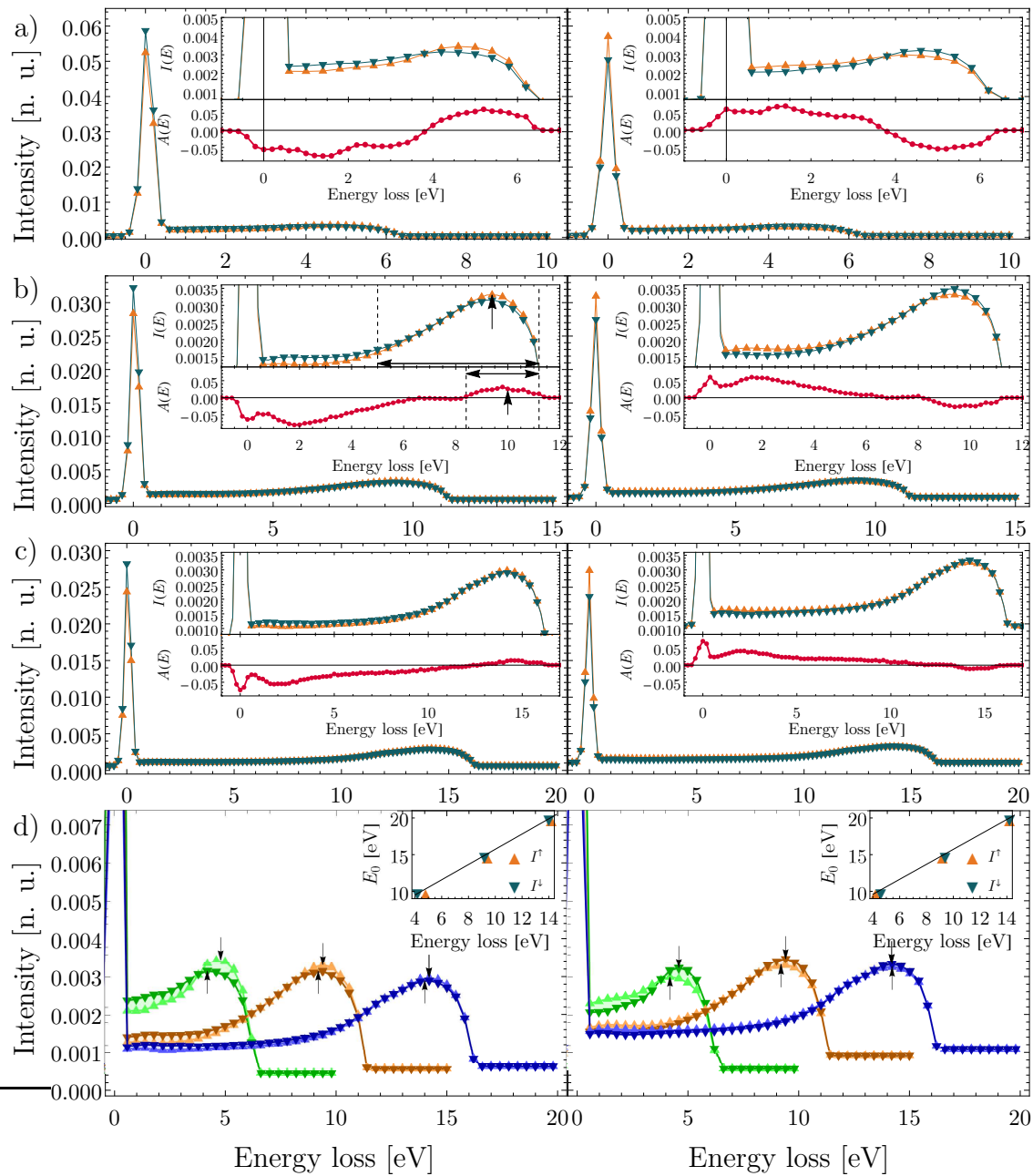


Figure 5.14: Energy loss spectra of RoI1 (left) and RoI2 (right) of a 5 ML Fe/W(110) sample for primary beam energies of a) $E_0 = 10$ eV, b) 15 eV and c) 20 eV. The main plots show the full spectrum for intensities I^\uparrow (\blacktriangle) and I^\downarrow (\blacktriangledown), while the upper insets show an enlargement of the secondary electron spectrum and the lower insets show the spin-asymmetry A (\bullet). The arrows in b) indicate the difference in width and maxima position between SEs and A . d) Enlarged view of the secondary electron peak for the three energy loss spectra at $E_0 = 10$ eV, 15 eV and 20 eV. The black arrows indicate the SE peak position for each scan. The inset shows the linear correlation between E_0 and the energy of maximum SE yield. All plots are normalised by their mirror intensity.

DoS. However, as will be seen in Section 5.3.2, the Ag wetting-layer influences the scattering-asymmetry of electron-hole pairs. The Stoner excitations exhibit a maximum asymmetry at around 2 eV, which agrees well with the exchange split of 2.3 eV in the DoS (see Figure 5.6). After this maximum, the scattering asymmetry falls off smoothly towards higher energy losses until the SE energy regime. As a Stoner excitation can trigger subsequent Stoner excitations, the scattering asymmetry exists over a large energy range.

The broad intensity peaks at high energy losses can again be attributed to the creation of secondary electrons. Here one should note that the SE peak has a width of about 6 eV and the SE peak, *i.e.* maximum SE yield, lies at about 2 eV to 2.2 eV above the vacuum level (point at which the intensity drops to zero). In contrast, the corresponding peak in the spin-asymmetry has a width of approximately 2.5 eV and a maximum at about 1.5 eV above the vacuum level. This difference in peak position and width between maximum SE yield and maximum asymmetry is indicated for RoI1 in Figure 5.14 b. While the creation of SE can be described by a Gaussian approximation such as Eq. (5.1), the asymmetry is governed by the spin-dependent difference in the IMFP. As can be seen in Figure 3.14, the difference in IMFP for spin-up and spin-down electrons is highest for low-energy SE and decreases with increasing energy. This agrees well with the behaviour of the scattering-asymmetry, which peaks for electrons with an energy of about 1.5 eV above the vacuum level and then decreases to almost zero for SEs of 3 eV above the vacuum level. It can further be seen that, in all three plots, the SE peak exhibits a larger intensity for I^\uparrow than for I^\downarrow , as previously found in Fe/Ag(001). This means, that the energy-selective secondary electron yield is higher if the incident beam is aligned parallel to the majority spin direction. Comparing the scattering-asymmetry of the SE peak for different primary energies shows that it only decreases slightly, from 5.5% to 1.9% and 1.0% for the consecutive SPEEL scans compared to the large changes in elastic peak asymmetry.

The SPEEL spectra are again used to determine the energy-dependent maximum SE peak position for both RoIs, which are indicated by the black arrows in Figure 5.14 d. However, here one can see that the maximum SE peak position differs slightly for I^\uparrow and I^\downarrow , which becomes more apparent for lower primary beam energies, and which is not observable for either Fe/Ag(001) or Ag/Fe/W(110). The exact cause of this effect could not be determined in the course of this work. However, it could be just be due to the the overall spin-resolved spectra rather than by a fundamental effect. As the peak position differs for I^\uparrow and I^\downarrow the average between the two peak positions was taken as the energy for the ESSEY measurements

discussed in Section 5.2.5.

5.2.4 Reflectivity scans and band structure probing

As in Section 5.1.4 the energy-dependent reflectivity was measured for primary beam energies from 0 eV to 20 eV in steps of 0.5 eV. The spectra of 5 ML Fe/W (110) and pure W (110), adjusted by their vacuum energy and normalised by the mirror intensity, are shown in Figure 5.15. The threshold energy of the mirror intensity for the two materials differs as it is correlated to the respective work function. W (110) exhibits a threshold energy of about 4 eV which corresponds to a work function of 5.6 eV and agrees well with experimental values of $\Phi_{\text{W}(110)} = 5.44$ eV [186]. Fe/W (110) has a threshold energy of about 3.5 eV corresponding to a work function of $\Phi = 5.1$ eV which is again close to the experimentally found work function of $\Phi_{\text{Fe}(110)} = 5.07$ eV [186]. Thus, the difference in threshold energy between the two materials is representative of the difference between their respective work functions.

The pure W (110) sample exhibits two distinct features, which are directly related to the band structure. The first reflectivity peak between 0 eV and 6 eV correlates to a band gap in W (110), as can be seen in the band structure of an infinite W crystal in Figure 5.15 b. The intensity decreases, as states become available for electrons to scatter into after 6 eV. The second reflectivity peak at 14 eV can be attributed to an energy region with low DoS.

Comparing the corresponding SPEEL spectra for a beam alignment parallel (orange) and antiparallel (blue) to the sample magnetisation for the two RoIs shows that their respective behaviour matches very well. This is also demonstrated by the symmetry of the asymmetry plots with inverted signs. The scattering-asymmetry between 0 eV to 2.5 eV is due to the difference in spin-dependent IMFP. Thus in this energy region, the beam with polarisation parallel to the majority spins exhibits a higher reflectivity. At 2.5 eV the asymmetry drops to zero as the energy lies within the band gap, meaning that there are neither majority nor minority states available. The band diagram also shows that the majority and minority states have different band onsets. Here, the majority band has an onset at lower energies (3.5 eV) than the minority band (5 eV). Thus in this energy region electrons whose spins are parallel to the majority electrons can penetrate into the crystal and occupy states, while the minority electrons are still strongly reflected. This also correlates to the maximum spin-asymmetry in the spectra. The asymmetry decreases further and stays constant above 5 eV, when there is an equal number of majority and minority states available. Based on these results, it is possible to conclude that I^\uparrow is parallel and I^\downarrow is antiparallel to the majority spins in RoI1 and *vice versa* in RoI2. Furthermore,

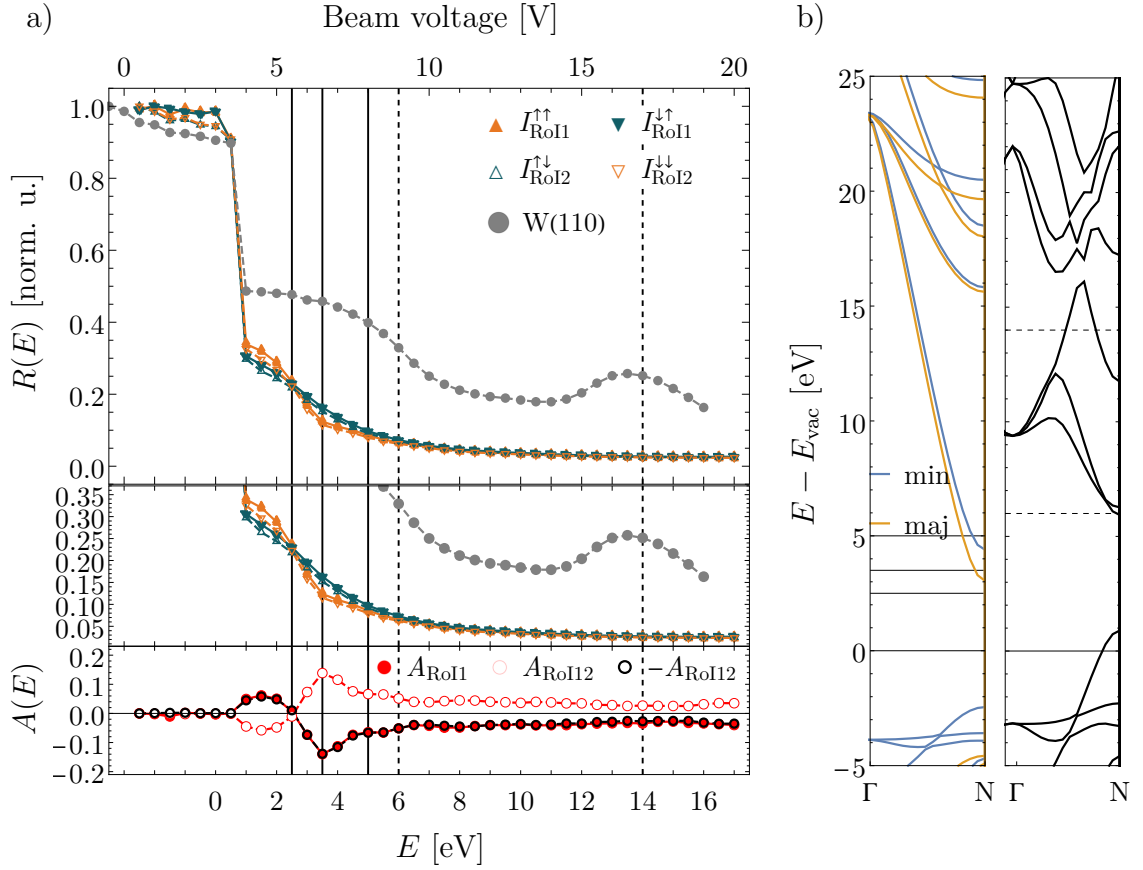


Figure 5.15: a) Primary electron intensity (top) and spin-asymmetry (bottom) versus incident beam energy for 5 ML Fe/W(110). b) DFT-calculated band structures of an infinite Fe (left) and an infinite W (right) crystal along the [110] direction. The energy reference is taken at the vacuum level. The solid (dashed) lines correlate features in the spectra with electron bands in Fe(110) (W(110)).

one can note that the reflected intensity for Fe(110) is significantly higher than for Fe(001), due to the band gap along the [110] direction.

5.2.5 ESSEY-SPLEEM mode

Similar to Section 5.1.5 the linear correlation between the primary beam energy and the maximum SE peak intensity is used to acquire an energy-selective secondary electron yield spectrum for SEs with an energy of 1.7 eV above the vacuum level. This again represents the most probable SE energy loss value for this material system. The primary beam energy was varied from 10 eV to 20 eV in steps of 0.5 eV and the measured spectrum is shown in Figure 5.16.

Here one can see that the SE yield is higher if the polarisation of the primary beam is parallel (orange lines) to the sample magnetisation for both regions of interest. The reasons for this are the same as given in Section 5.1.5. This difference

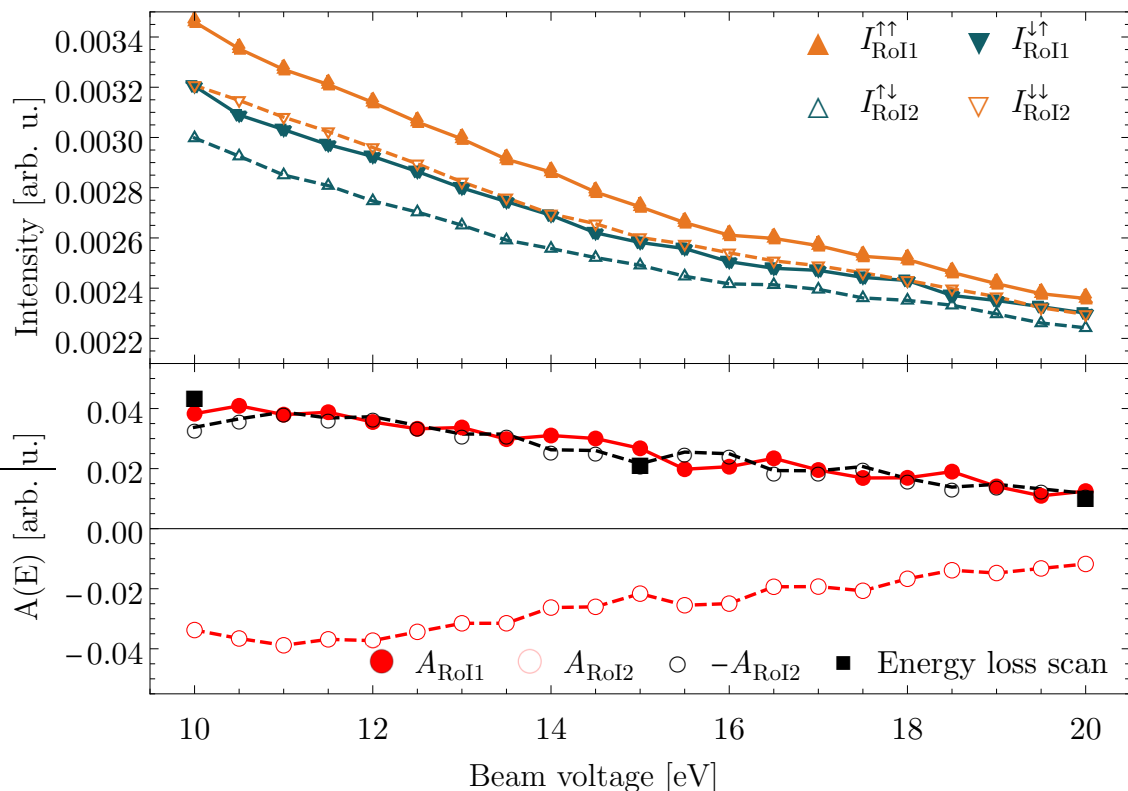


Figure 5.16: Energy-selective secondary electron yield spectrum of Fe/W (110) versus primary electron beam energy and the corresponding spin-dependent asymmetry in SE yield. The black squares represent asymmetry values extracted from the three SPEEL scans.

decreases with increasing primary energy, as can be seen from the plotted asymmetry, which drops from 4% at $E_0 = 10$ eV to about 1% at $E_0 = 20$ eV. Furthermore, the asymmetry is similar in both RoIs but exhibits the same inverted features, as can be seen at around 15.5 eV. This could indicate a fine structure in the energy-selective SE yield. To further analyse the origin of such features, the ESSEY scans should be measured with a smaller energy increment and aided by a spin analysis using a Mott polarimeter. However, the validity of the ESSEY measurement can again be seen when comparing the thus obtained asymmetry with values found by the SPEEL scans, which agree very well (see Figure 5.16).

The second thing to note is the monotonic decrease in SE yield. Compared to the results for Fe/Ag (001) the values do not show a sudden drop but follow an almost linear behaviour. The same tendency can be observed in Figure 5.17 a which shows the calculated SE yield δ_{SE} (see Section 5.1.5). These values show a decrease with increasing beam energy, similar to the SE yield values found by the ESSEY scan.

Integrating over the whole SPEEL spectrum gives an indication of the total number of electrons δ_{tot} . As seen in Figure 5.17 a, the total electron yield shows a higher

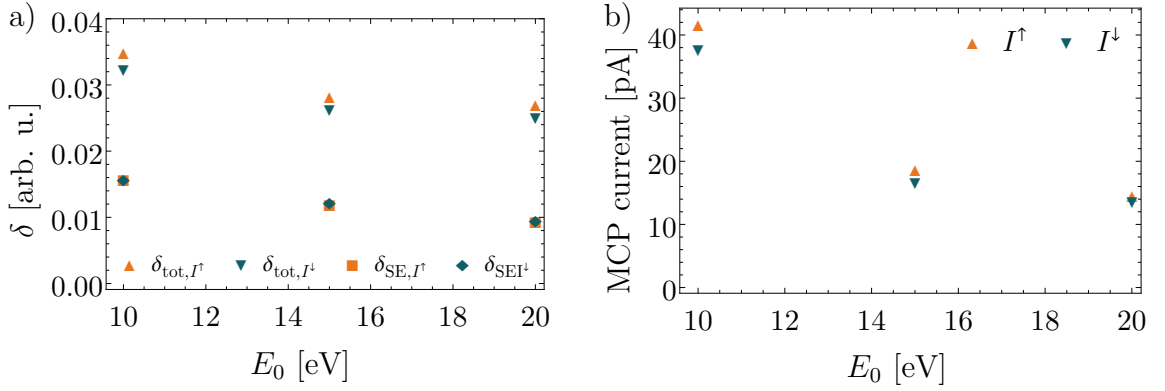


Figure 5.17: a) Total electron yield and SE electron yield versus primary beam energy. b) Measured MCP voltage versus primary electron beam energy. Here, the measured dark current was subtracted.

number of electrons for a beam alignment antiparallel to the sample magnetisation. This is primarily caused by the higher reflectivity of I^\downarrow as explained in the preceding section. Using the measured MCP current, as seen in Figure 5.17 b in conjunction with the calculated total electron yield would give the actual number of created electrons. Using Eq. (5.1) would allow quantifying the number of created SEs.

5.3 SPLEEM investigation of ultra-thin Ag/Fe/W (110)

To investigate the influence of an Ag wetting-layer on top of the Fe and to test if Ag would influence the SE polarisation and yield, a third sample was analysed. Here, a 5 ML-Fe/W (110) sample with an additional 1 ML-thick Ag overlayer was measured.

5.3.1 Sample preparation of Ag/Fe/W (110) and magnetic orientation

The growth procedure of this epitaxial bilayer is almost the same as the one previously reported for Fe/W (110) in Section 5.2.1. In brief, the W (110) substrate was cleaned by successive flash heating circles in a low-pressure oxygen environment, followed by UHV flash heating up to 2000 K. Then, the substrate was cooled down to about 500 K and 5 ML Fe was deposited at a rate of about 0.13 ML/minute. Immediately after Fe, 1 ML of Ag was deposited onto the Fe/W (110) sample at the same rate. Even though Ag would generally grow in Stranski-Krastanov mode on Fe(110), it was found that the first two layers form a continuous film, especially at

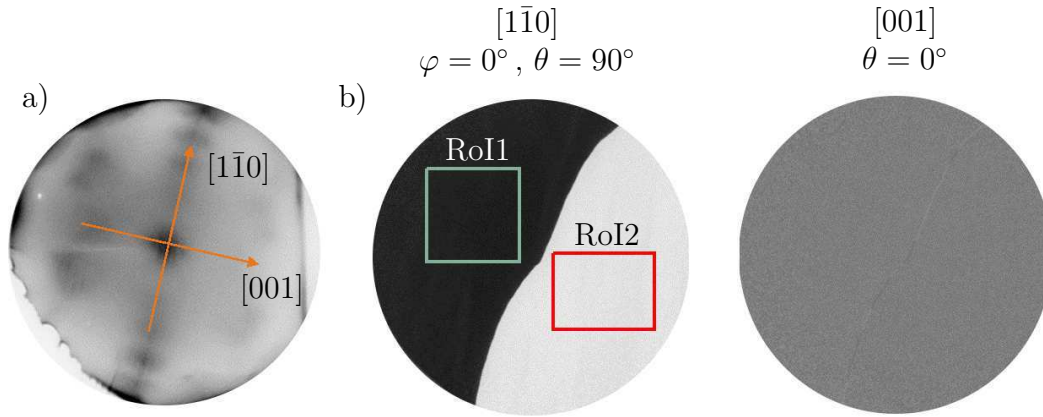


Figure 5.18: Analysis of a 1 ML-Ag/5 ML-Fe/W (110), a) LEED pattern for a primary beam energy of $E_0 = 100$ eV. The orange arrows indicate the crystallographic directions. b) Left: SPLEEM image along the sample's easy axis. The grey and red rectangles indicate RoI1 and RoI2, respectively; Right: SPLEEM image taken perpendicular to the easy axis, which shows the existence of a Bloch wall. All images were taken for a FoV of $30 \mu\text{m}$.

elevated temperatures [204]. Further, as mentioned in Section 5.1.1, Ag has a lower surface energy than Fe and thus there should be no interdiffusion with Fe wetting the Ag layer [178]. LEED images of the sample after the deposition, taken at room temperature and with an energy $E_0 = 100$ eV, are shown in Figure 5.18 a. It can be seen that Fe's satellite peaks are still visible in the LEED pattern, but are more diffuse than the pattern in Figure 5.11 b. This is due to the additionally deposited Ag overlayer on the Fe surface, which grows epitaxially with a (111) surface on Fe (110) [205]. The onset of magnetism is the same as reported in Section 5.2.2.

Moreover, the Ag/Fe/W (110) heterostructure was again found to have an in-plane magnetisation with its easy axis along the $[1\bar{1}0]$ direction as can be seen by the left SPLEEM image in Figure 5.18 b. The right image of Figure 5.18 b was taken for a polar angle of $\theta = 90^\circ$ and an azimuthal angle of $\varphi = 90^\circ$, which is perpendicular to the sample's easy axis. In contrast to the second image in Figure 5.13, this image shows the existence of a Bloch domain wall where the magnetisation smoothly rotates about the normal of the domain wall, going from ip to oop to ip. Thus, there was an observable magnetic contrast for the oop direction.

5.3.2 Spin-dependent energy loss spectra

Plotted in Figure 5.19 are the six energy loss spectra for RoI1 (left) and RoI2 (right), which correspond to the green and red regions in Figure 5.18 b, respectively. Similar to Section 5.2.3, the two RoIs show very similar behaviour and magnitude but with

inverted intensities. As with Fe/W (110), comparing the three SPEEL spectra taken at energies of $E_0 = 10$ eV, 15 eV and 20 eV for *e.g.* RoI1 shows that the secondary

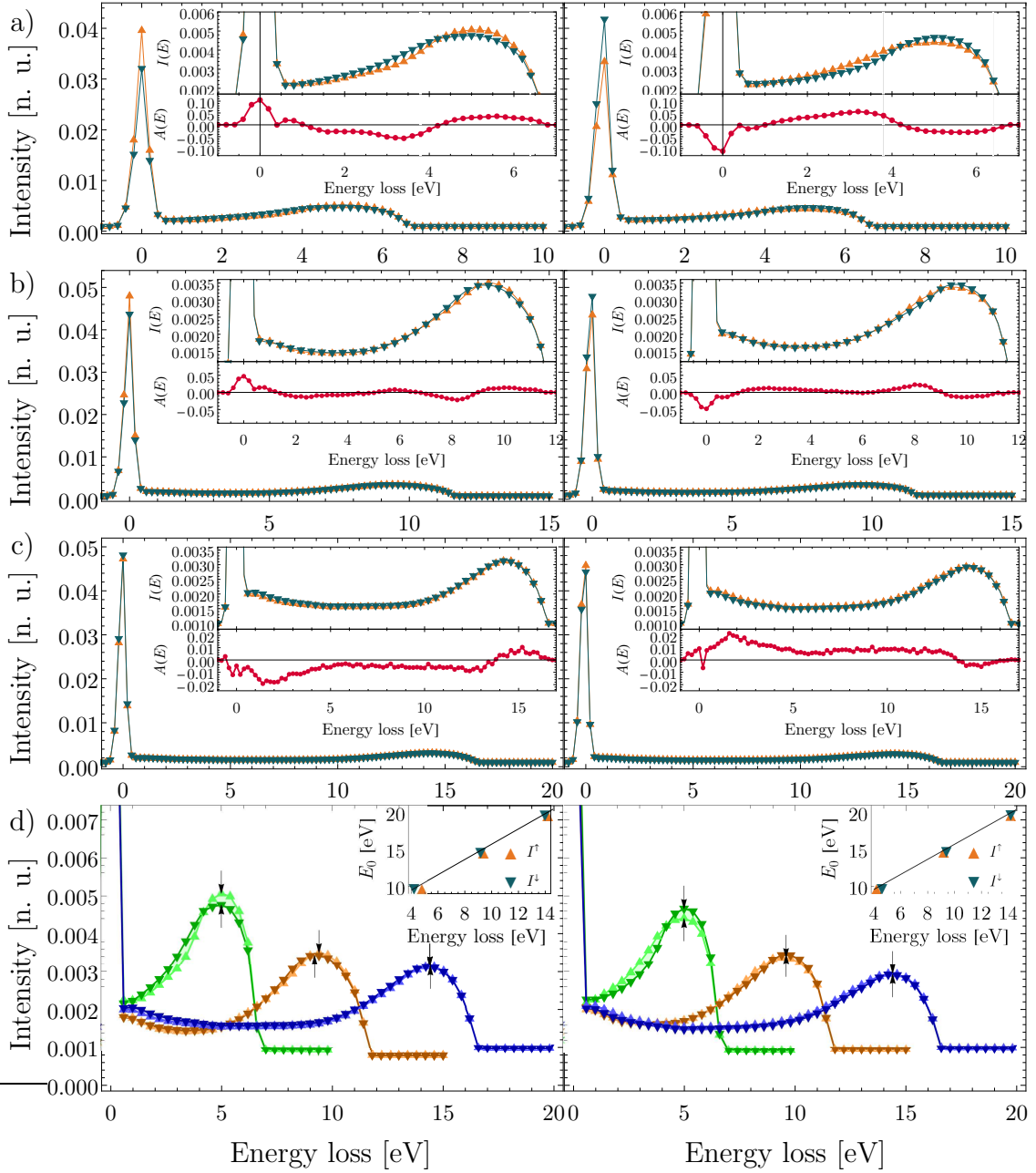


Figure 5.19: SPEEL spectra of RoI1 (left) and RoI2 (right) of a Ag(1 ML)/Fe(5 ML)/W (110) sample for primary beam energies of a) $E_0 = 10$ eV, b) 15 eV, and c) 20 eV. The main plots show the full spectrum of I^\uparrow (\blacktriangle) and I^\downarrow (\blacktriangledown), while the upper insets show an enlargement of the SE spectrum and the lower insets show the scattering-asymmetry A (\bullet). d) Enlarged view of the secondary electron peaks for all three energy loss spectra. The black arrows indicate the SE peak position for each scan. The inset shows the linear correlation between E_0 and the energy of maximum SE yield. All plots are normalised by their mirror intensity.

electron yield decreases with increasing primary beam energy. Furthermore, the insets of the scattering-asymmetry illustrate the expected decrease in asymmetry for both the elastic and the SE peak with increasing energy. While the asymmetry of the elastic peak reduces from 10% to 5% and to 1%, the asymmetry of the SE peak decreases from 3% to 1.5% and to 0.5%. It is noticeable that, in contrast to the Fe/Ag (001) and Fe/W (110), the asymmetry for both peaks has the same sign. However, there is a change in sign in the asymmetry before the SE peak's maximum, which is caused by the different slopes for I^\uparrow and I^\downarrow in this energy region. This is particularly visible in the insets in Figure 5.19 a. A similar but less pronounced effect was also found for Fe/Ag (001), which has Ag atoms on the surface due to segregation. As Fe/W (110) does not exhibit such a feature one can conclude that the effect is caused by the Ag surface atoms. However, the exact origin of this effect could not be determined in the scope of this work and would need further investigation in which *e.g.* the thickness of the Ag surface layer is varied.

Figure 5.19 d again shows a direct comparison of the SE peak area normalised by the mirror intensity of the three SPEEL spectra. These measurements were further used to determine the correlation between electron beam energy E_0 and the SE peak position (indicated by the black arrows) and to adjust the bias voltage of the retarding grid in front of the MCP for the ESSEY scan. This linear correlation is plotted in the inset in both figures. As can be seen by the black arrows and the data points in the inset, the SE peak positions for I^\uparrow and I^\downarrow are very similar, unlike for the Fe/W (110) sample, which makes the ESSEY measurement more precise.

Figure 5.20 shows a more detailed comparison of the SPEEL spectra and the scattering-asymmetries of the three investigated samples at a primary beam energy of $E_0 = 20$ eV and normalised by their mirror intensity. The first thing to note is the difference in maximum SE peak position, which changes for all three samples. This change in energy is related to the material work function and should follow $E_{\max} = E_F + \frac{4}{3}\Phi$ [206]. However, the found peak values were at about 4.9 eV for Fe/Ag (001), 5.4 eV for Fe/W (110) and 5.4 eV for Ag/Fe/W (110). This would correspond to a smaller factor of about 1.07.

The height of the SE peaks relative to each other has been found to vary with different beam energies. The same was observed for the scattering-asymmetry, which was highest for Fe/Ag (001) at $E_0 = 20$ eV and smallest at $E_0 = 10$ eV. Comparing the point of maximum scattering-asymmetry in the SE region with the point of maximum SE yield again shows that they do not align, as discussed in Section 5.2.3. Furthermore, as mentioned in Section 5.1.3 the shoulder in the spectrum of Fe/Ag (001) is not visible for the other two samples, indicating that this effect is

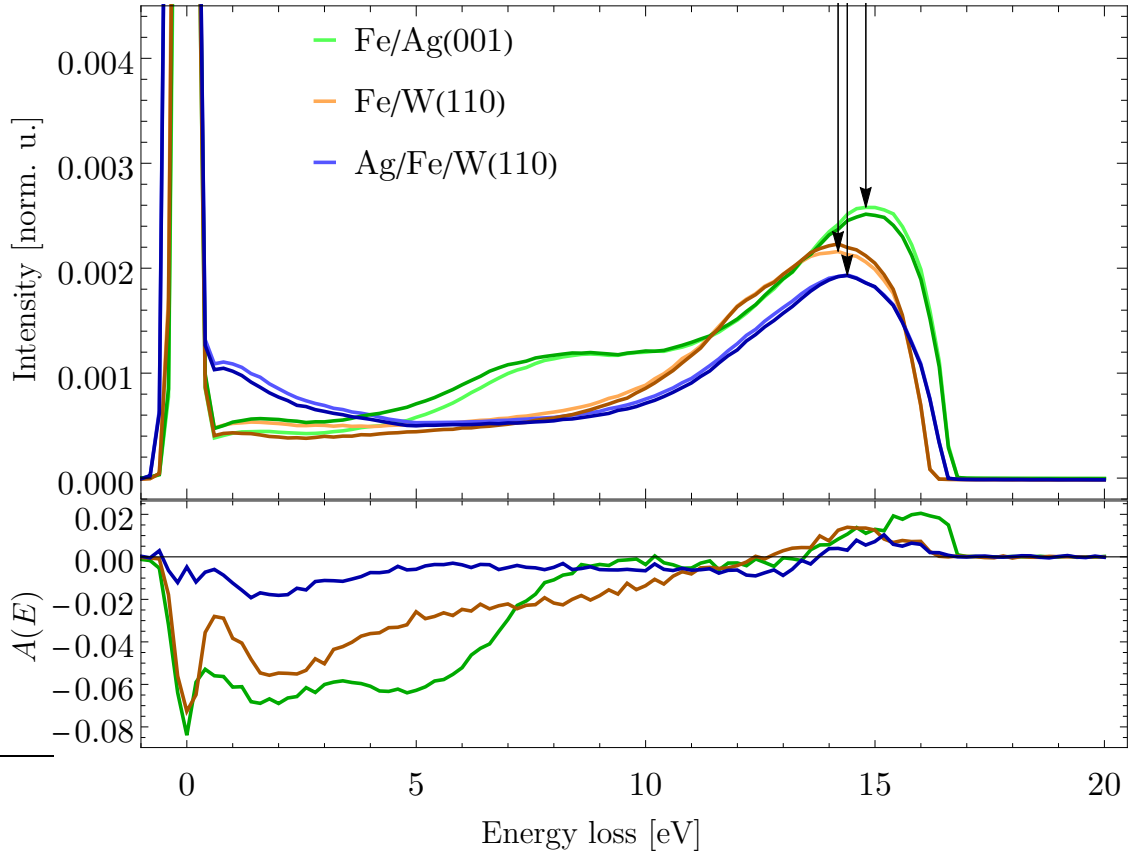


Figure 5.20: Comparison of the SPEEL spectra of Fe/Ag (001), Fe/W (110) and Ag/Fe/W (110) taken at a primary beam energy of 20 eV (top) and the corresponding scattering asymmetry (bottom). The SE peak positions are indicated by black arrows. All plots are normalised by their mirror intensity and the background was subtracted.

caused by the crystallographic direction of the material.

Comparing the scattering-asymmetry of the Stoner excitation peaks shows, that the maximum position is similar in all three samples and lies at around 2 eV, which is the average exchange splitting of Fe. Even though the comparison of the absolute value of the asymmetry between the samples containing 8 ML Fe(001) and 5 ML Fe(110) is difficult, a comparison of Fe(110) with and without an Ag-overlayer shows that the spin-dependent scattering-asymmetry is weaker if Ag is present. This effect was observed for all investigated primary beam energies and is especially apparent in the energy region of Stoner excitations and the secondary electrons. Such a change in spin-polarisation caused by thicker Ag-overlayers of about 12 ML was found to be related to the breaking of the spin degeneracy due to the spin-dependent coupling between Ag and Fe states at the interface [207]. Other experiments observed a Ag-induced spin-reorientation from ip to oop after the deposition of just one monolayer

[208]. This would cause the detectable spin-asymmetry to vanish, as seen by the ip-oop magnetised regions of the 5 ML Fe/Ag (001) sample in Section 5.1.3. Thus, to investigate the damping of the spin-dependent scattering further one should also investigate the sample's oop component.

5.3.3 Reflectivity scans and band structure probing

Like in the previous sections of Fe/Ag (001) and Fe/W (110), the energy-dependent reflectivity was measured for Ag(1 ML)/Fe(5 ML)/W (110) and pure W (110), which are shown in Figure 5.21 a. The inset shows the different threshold energies for Ag/Fe/W (110), Fe/W (110) and pure W (110) with incident beam energy. This comparison shows that the sample of Ag/Fe/W (110) has the lowest threshold of just 3 eV. This is expected, as Ag (111) has a work function of about $\Phi_{\text{Ag}(111)} = 4.7 \text{ eV}$, which is lower than the work functions of Fe (110) and W (110). However, to get more precise values, the increments of the primary beam energy should be reduced. Moreover, it can be seen that the energy ranges of increased reflectivity of Ag/Fe/W (110) are similar to the ones of Fe/W (110) shown in Figure 5.15 and thus the interpretation of the Ag/Fe/W (110) and W (110) spectra follows the one given in Section 5.2.4 and will not be reiterated here. This also means that there seem to be little to no influence of the Ag monolayer on the energy range in which stronger reflectivity occurs. This is further indicated by the band diagram for Ag along the [111] direction in Figure 5.21 b. As there is no band gap, the Ag-overlayer should have no influence on the reflectivity. However, the DFT simulation was carried out for an infinite crystal, which has a different band structure than a monolayer. Thus, for a more detailed analysis, a more realistic multilayer model of all three materials and a vacuum surface should be performed.

Even though the magnitude of reflectivity of both Fe/W (110) and Ag/Fe/W (110) are the same, the spin-dependent scattering-asymmetries are different. This can be seen in the bottom plot of Figure 5.21 a, which compares the scattering asymmetries of RoI1 and RoI2 of the Ag/Fe/W (110) with RoI1 of Fe/W (110) and which shows that the presence of the Ag-overlayer on Fe dampens the spin-asymmetry. Furthermore, the plot shows that the asymmetry changes sign at about 5.5 eV and thus indicating a higher reflectivity for primary electrons with a spin-polarisation parallel to the sample's magnetisation. In contrast, Fe/W (110) did not exhibit such a change in sign. For a more detailed analysis, the spin-asymmetry should be qualified using a Mott polarimeter.

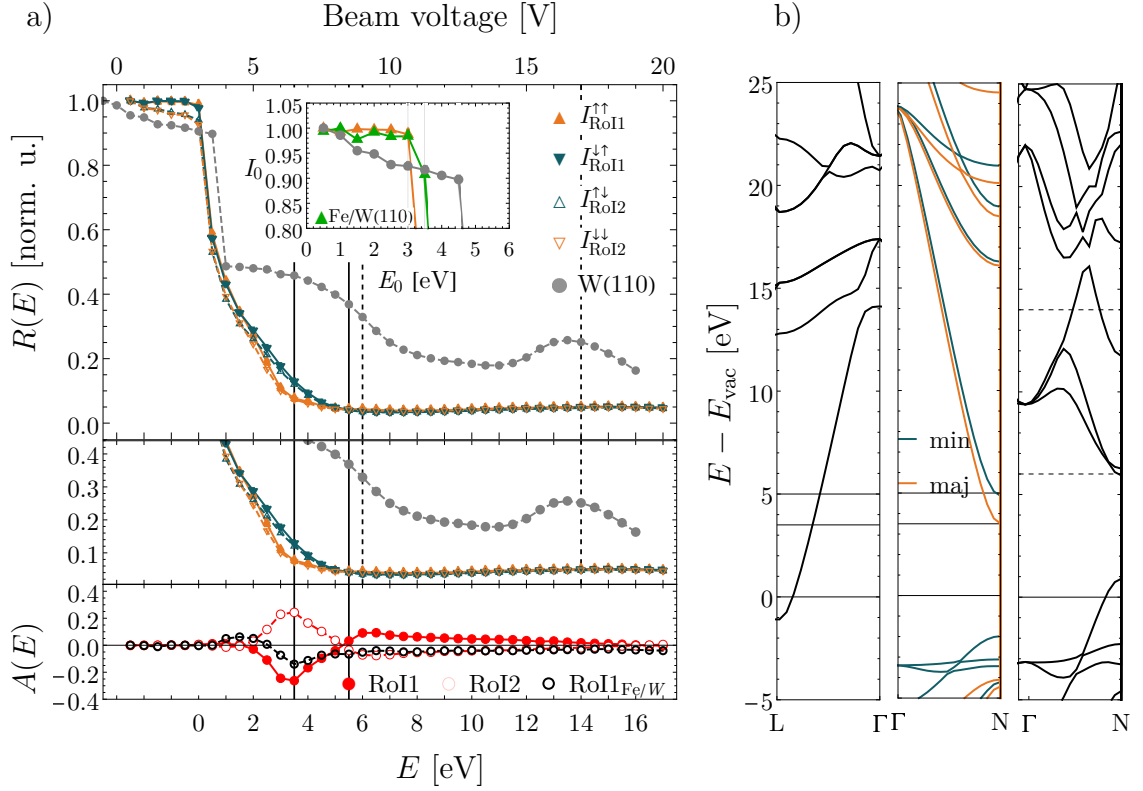


Figure 5.21: a) Primary electron intensity (top) and spin-asymmetry (bottom) versus incident beam energy for Ag(1 ML)/Fe(5 ML)/W(110) and W (110). b) DFT-calculated band structures of an infinite Ag (left) along the [111] direction, Fe (middle) and W (right) crystal along the [110] direction. The energy reference is taken at the vacuum level.

5.3.4 ESSEY-SPLEEM mode

As in previous sections, the energy-selective secondary electron yield scan was conducted for SE electrons having an energy of about 1.9 eV above the vacuum level and the primary beam energy was varied from 10 eV to 20 eV in steps of 0.5 eV. The corresponding energy-selective secondary electron yield spectrum is shown in Figure 5.16.

The plot again shows the same decrease in SE yield as the other two materials. However, the relative intensity of it is higher for the case of a Ag-overlayer compared to the bare Fe/W (110), which could be caused by two effects. The first being the reduced work function of Ag (111) of $\Phi_{\text{Ag}(111)} = 4.7$ eV compared to $\Phi_{\text{Fe}(110)} = 5.07$ eV for Fe (110). This results in more electrons being able to leave the sample surface. The second effect can be attributed to the larger yield for Ag compared to that for Fe [209]. The asymmetry again decreases with increasing primary beam energy but is lower than for the bare Fe/W (110). Here it decreases from 3% at $E_0 = 10$ eV

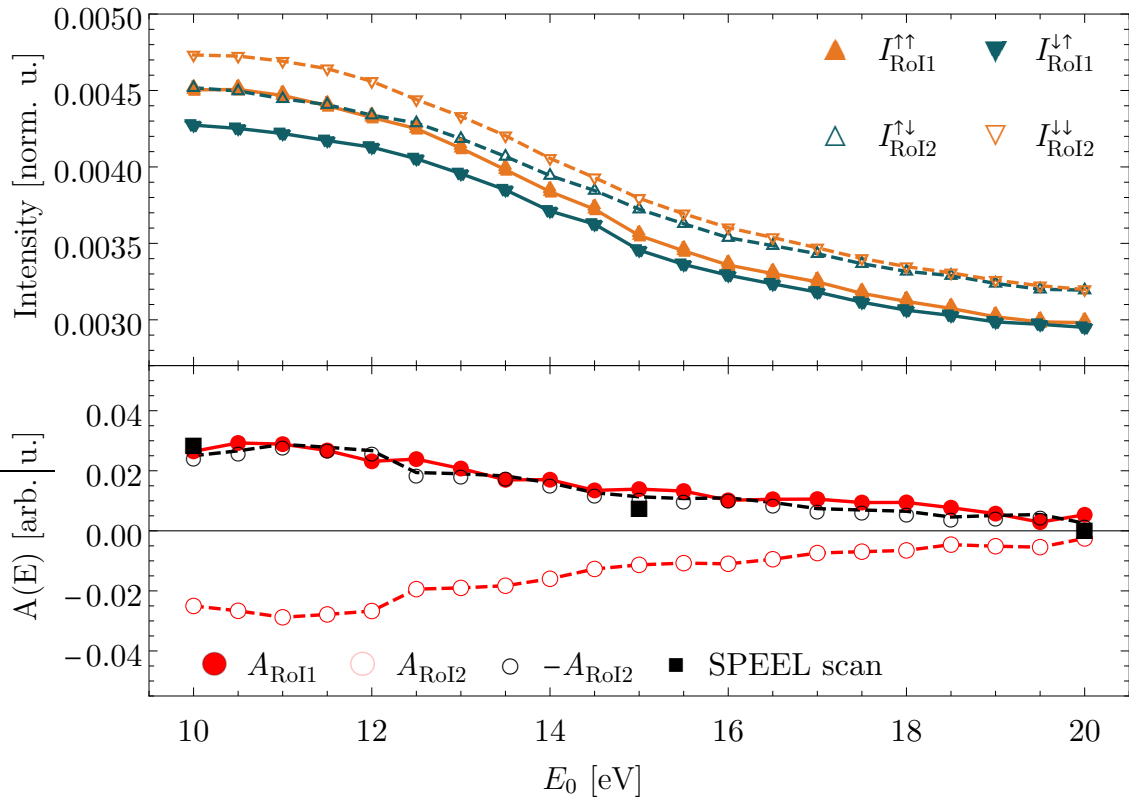


Figure 5.22: Energy-selective secondary electron yield spectrum of Fe/W (110) versus primary electron beam energy and the corresponding spin-dependent asymmetry in SE yield. The black squares represent the asymmetry values extracted from the three energy loss scans.

to 0.5% at 20 eV. This could be due to the relative decrease in polarised secondary electrons from the Fe substrate and the relative increase in mostly unpolarised secondary electrons from the Ag-overlayer. This would reduce the difference in IMFP.

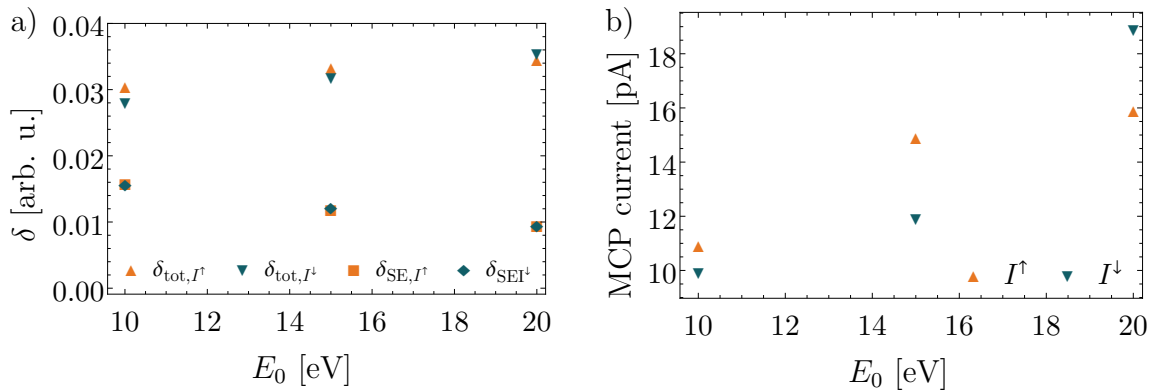


Figure 5.23: a) Total electron yield and SE electron yield versus primary beam energy. b) Measured MCP voltage versus primary electron beam energy. Here, the measured dark current was subtracted.

Again, the found asymmetry via ESSEY agrees well with the values extracted from the SPEEL spectra.

As in Section 5.2.5, the SE yield was calculated and exhibits a decrease, as shown in Figure 5.23 a. This is again similar to the measured ESSEY scans and validates their correctness. In contrast to Fe/Ag(001) and Fe/W(110) the total electron yield (integration of the energy loss spectrum) increases with increasing energy. Furthermore, δ_{tot} is higher for I^\uparrow than for I^\downarrow at $E_0 = 10$ eV and 15 eV and lower at 20 eV. This behaviour is the same as found for the elastic peaks seen for RoI1 in Figure 5.19. The corresponding MCP current is plotted in Figure 5.23 b.

Figure 5.24 shows a comparison between the maximum SE peak intensity and the corresponding ESSEY values. This plot shows that in the case of Ag/Fe/W(110) these measurements agree well with each other. However, this fit did not work as well for Fe/W(110) and did not work at all for Fe/Ag(001). Thus, more measurements would be needed to optimise the measurement parameters and to investigate the discrepancy further.

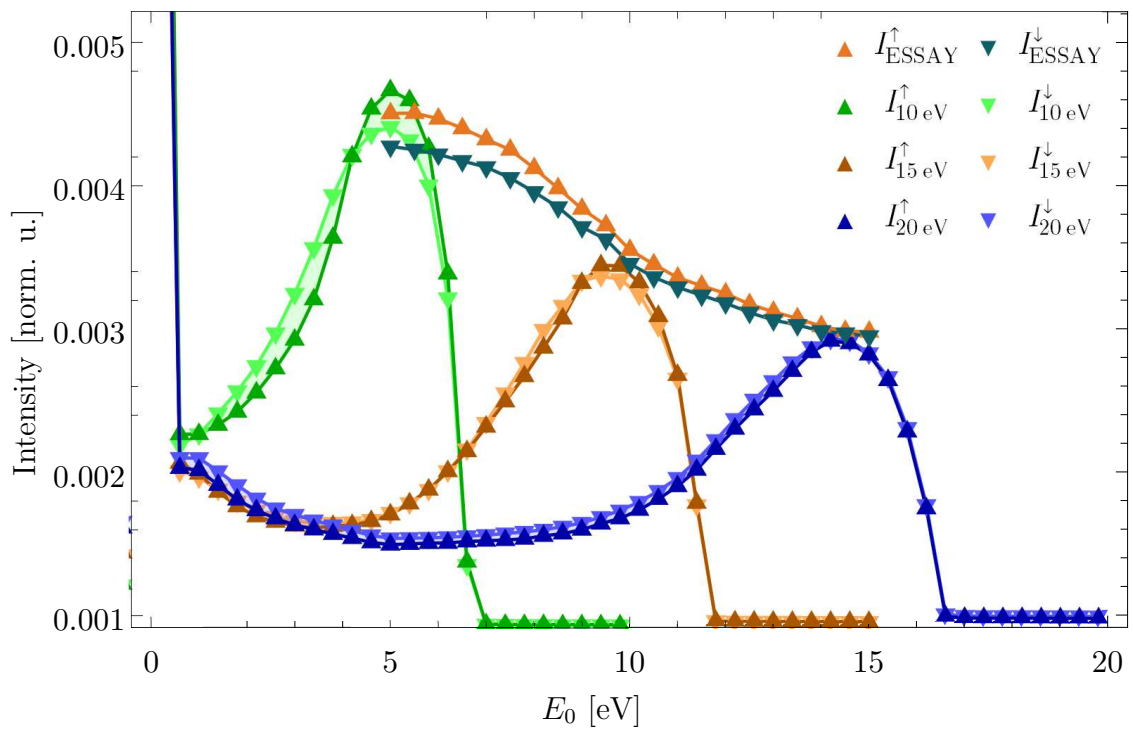


Figure 5.24: Comparison between the ESSEY scans of Ag/Fe/W(110) and the corresponding energy loss spectra. The two measurement techniques show very good agreement.

5.4 Conclusion

This chapter firstly presented the thorough characterisation of the growth mode and magnetisation of three ferromagnetic material systems. Secondly, it provided extensive spin- and energy-dependent studies of the interaction of spin-polarised low-energy electron beams with ferromagnetic and non-magnetic material using a SPLEEM.

The main material systems under investigations were heterostructures of: Fe(8 ML)/Ag(001), Fe(5 ML)/W(110), and Ag(1 ML)/Fe(5 ML)/W(110). Monitoring the intensity oscillations during sample growth gave precise measurements of the critical onset thickness for in-plane ferromagnetism to occur. While Fe/Ag(001) had a critical thickness of about 4 ML the Fe/W(110) sample started to exhibit in-plane ferromagnetism already after 1.5 ML. This difference in critical thickness is caused by the difference in magnetocrystalline anisotropy for the different samples. Furthermore, it was found that the easy axis of the Fe/Ag(001) sample lies along the [001] direction and along the $[1\bar{1}0]$ direction for both Fe/W(110) and Ag/Fe/W(110). To maximise the signal and the magnetic contrast, for all further experiments the electron beam polarisation was chosen to be either parallel or antiparallel to the sample's easy axis.

Energy-dependent reflectivity scans were performed by varying the primary beam energy between 0 eV to 20 eV and measuring the intensity of the elastically backscattered electrons. These measurements gave information on the samples' work functions, which were in good agreements with experimentally found values. The experiments further allowed to investigate the density of unoccupied spin states above the Fermi level for all three samples. Thus, this technique is a complementary tool to photoemission techniques, which address the electronic structure below the Fermi level. The interpretation of the reflectivity spectra was aided by density functional theory simulations of the respective material. These simulations showed a clear correlation between reflectivity peaks and band gaps in the electronic structure. Furthermore, the spin-dependent asymmetry could be correlated to the energy difference in the onsets of majority and minority electron bands, which results in an increased spin-asymmetry. Thus, this feature would allow to determine the optimal settings of the electron beam for magnetic domain imaging. In case of Fe/Ag(001) a maximum contrast would be achieved with a primary beam energy of 11.5 eV and of 3.5 eV in the case of the Fe/W(110) sample. However, a quantitative interpretation would require a full LEED theory calculation for the crystal, which takes effects such as the altered surface potential, the surface potential barrier and the damping of

the wave by inelastic scattering into account [210]. The combination of reflectivity and band structure indicated the direction of magnetisation and determines which electrons correspond to the majority and minority electrons, which is important for the ESSEY scans.

Energy loss scans for three different primary beam energies were conducted by adjusting the retarding voltage of the MCP grid. In these measurements, Stoner excitations appeared as a broad feature extending from low energies up to several eV. It was observed that these peaks had only little fine structure and the spin asymmetry has been almost independent of the sample system and primary beam energy. The maximum intensity of the Stoner excitations was found to be around 2 eV to 2.5 eV, which is in very good agreement with the value of the exchange splitting in Fe, which was simulated using DFT. However, to completely analyse the Stoner excitations, it would be necessary to not only use an incoming spin-polarised electron beam but also a spin detector for the scattered electrons. Nevertheless, the decreased spin-asymmetry, which had a negative sign, indicates that, even though Stoner excitations are present in both spin-flip channels in Fe, the excitations had higher intensity for incoming minority electrons. The SE peak in the energy loss spectrum had a width of about 6 eV and the maximum peak intensity, which corresponds to the most probable energy loss, was found to be about 1.9 eV above the vacuum level. These values were found to be independent of the material system. Furthermore, the energy loss spectra gave information on the material-dependent work function, which were in good agreement with experimentally found values.

Taking three energy loss spectra the primary-beam-dependent maximum SE peak intensity was found and used to measure the energy-selective secondary electron yield spectra. Based on this approach the new measurement mode of ESSEY for spin-polarised low-energy electron microscopy was developed. These measurements gave information on the changes in electron yield at a certain energy, which is correlated to inelastic scattering processes. Generally, all experiments exhibited a decrease in SE yield and of the scattering-asymmetry with increasing E_0 . Moreover, the SE's intensity was found to be consistently higher if the primary beam polarisation was aligned parallel to the sample magnetisation. The experiments further demonstrated that the presence of an Ag-overlayer decreased the spin-dependent asymmetry.

One of the advantages of this technique is the fast data acquisition time compared to the energy loss spectra. As these take an average of about one hour per primary energy, measuring multiple spectra leads to the problem of sample contamination over time. The absorption of hydrogen or oxygen would result in a decrease in spin dependence compared to a clean Fe film [136] and thus influence the interpretation of

the results. Therefore, by only measuring the energy- and spin-dependent SE peak position it was possible to decrease the measurement time to only a few minutes for a large primary beam energy range. Thus, this chapter presented initial experiments regarding SE yield and inelastically scattered electrons which, although not sufficient for a detailed and theoretically complex analysis of scattering processes, demonstrated an interesting capability of a conventional spin-polarised low-energy electron microscopy.

Overall, the here presented experiments indicated that in order to build a SP-FES from a Fe-coated W tip the Fe layer would need to have a minimal thickness of 4 ML to exhibit a strong ip-magnetisation. Moreover, such an emitter should be grown with the (001) surface normal to the emitter axis as the (110) direction has a large band gap at the Fermi level. Additionally, this chapter further gave insights into the interactions of polarised electrons, which would be emitted from a SP-FES, and a magnetic material. Effects such as Stoner excitations, band structure probing and secondary electron yield are some material properties which could be determined using a SP emitter. However, to further analyse the potential origin of many of the here discussed effects and features additional analysis of the spin polarisation of the emitted SE would be needed. Here one could, for example, use a Mott polarimeter.

6 Experimental setup for spin-polarised field emission experiments

To analyse the spin-polarised field emission properties from a variety of emitters, a pre-existing UHV chamber with attached Mott polarimeter was refurbished and improved. The present experimental chamber was mainly developed by K.P. Kopper in 2007 [145] but has not been used in the years following 2013, which made a complete restoration necessary. Therefore, the first section's main focus is to describe the restored experimental UHV setup and its functionalities, followed by a more detailed list of all necessary steps taken to remodel and refurbish the experimental equipment for field emission studies. The second section outlines the initial considerations in the design process of a novel "field emission sample holder" suitable for field-induced emission experiments from nano-sized FESs.

6.1 UHV-MBE chamber with attached Mott polarimeter

The experimental system in its present state is shown in Figure 6.1 and consists of two parts, the pumping chamber (lower section under the table) and the experimental chamber which contains the MBE facilities and the Mott polarimeter (upper section on the table). The two parts are connected through a DN 200CF (ConFlat) flange to allow maximum pumping efficiency.

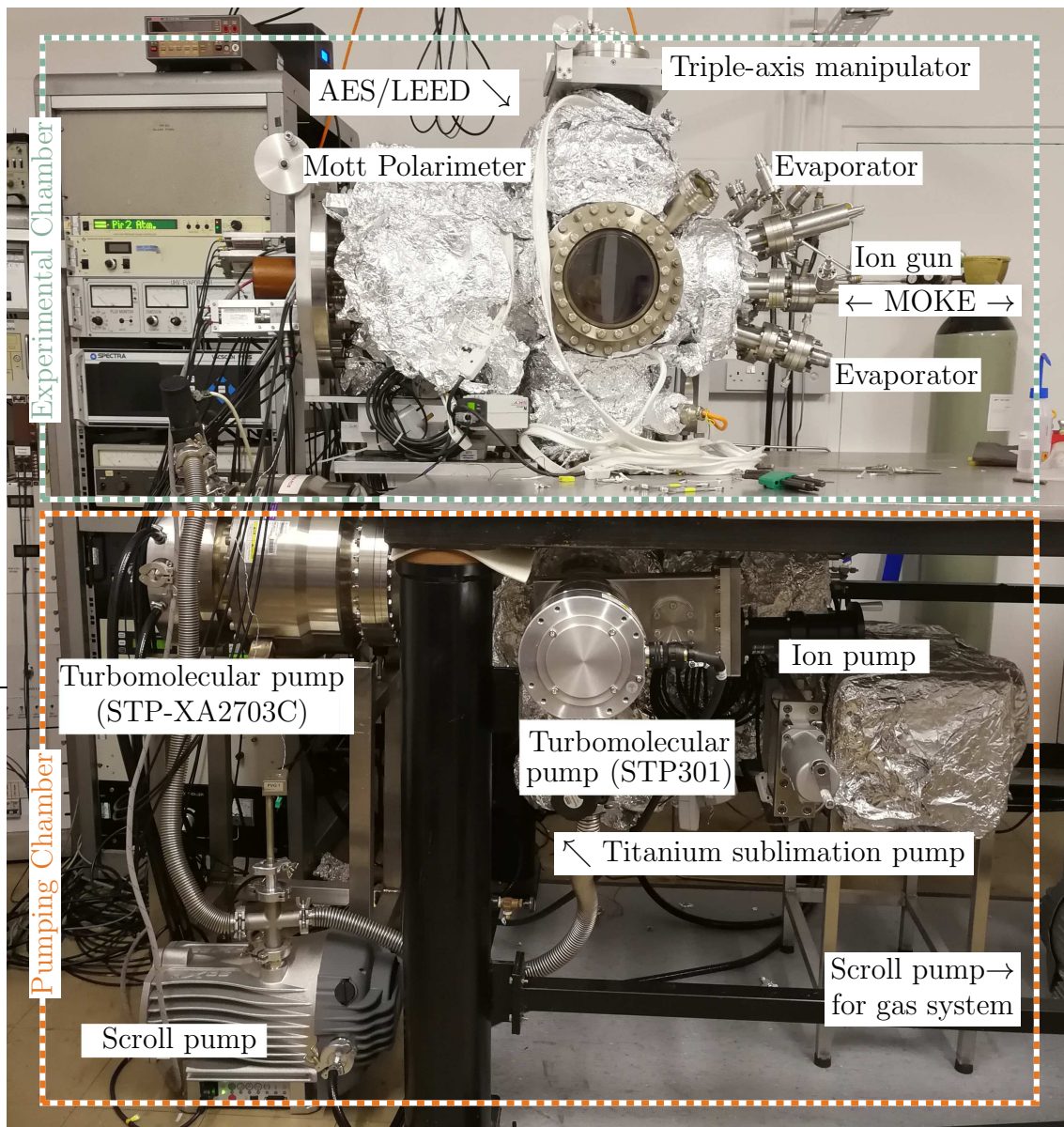


Figure 6.1: Picture of the complete Mott/MBE UHV chamber in the Cavendish Laboratory after the refurbishment of all its components.

6.1.1 Pumping chamber

To avoid surface contamination of freshly prepared samples due to adsorbates it is necessary to reduce the number of molecules impinging on the sample during the experiment. Therefore, all experiments had to be carried out under vacuum conditions. Generally, vacuum can be subdivided into groups according to the pressure range as follows:

Rough vacuum	1000 to 1 mbar
Medium vacuum	1 to 10^{-3} mbar
High vacuum	10^{-3} to 10^{-9} mbar
Ultra-high vacuum	10^{-9} to 10^{-12} mbar
Extreme vacuum	$<10^{-12}$ mbar.

By using the kinetic theory of gases [211] one can calculate that it takes a monolayer of adsorbates about 1.5 hours to form at a pressure of 1×10^{-9} mbar. However, many experimental techniques, such as Mott polarimetry, take much longer, which makes it necessary to work under UHV conditions in the low 10^{-10} mbar range. Thus, the newly designed UHV system has an improved pumping performance, a hydrocarbon-free vacuum, a reduced energy consumption and a smaller carbon footprint compared to the previous setup.

To provide ultra-high vacuum conditions for the experiments, the following pumps were mounted onto the pumping section of the chamber:

- A magnetically levitated Edwards STP-XA2703C turbomolecular pump, which provides a very high pumping speed of 2650 L/s keep the FESs clear of contamination with gaseous adsorbates like H_2 molecules. It has the further advantage of hydrocarbon-free pumping to avoid sample contamination with pumping oil.
- A magnetically levitated Edwards STP301 (300 L/s) turbomolecular pump, which provides additional pumping to maintain UHV and to increase pumping speed in the initial pumping down phase.
- A Varian VacIon Plus 300 StarCell ion pump (240 L/s), which is especially suited for small molecules such as H_2 and N_2 . It provides additional pumping speed and can be used to provide UHV conditions even with all other pumps decoupled from the system (standby mode). This is useful in case some experiments are sensitive to vibrations coming from the turbomolecular pumps. The ion pump itself can be isolated from the system during Ar^+ sputtering cycles using a gate valve.

- A titanium sublimation pump periodically supplements the system and can be combined with a liquid nitrogen cold trap to provide additional pumping speed during experiments.

Roughing is accomplished by a state-of-the-art dry scroll pump (Edwards nXDS15i), which provides a backing pressure of 7×10^{-3} mbar for both turbomolecular pumps. Being lubricant-free within the vacuum envelope and hermetically sealed means a totally hydrocarbon clean and dry vacuum to prevent cross-contamination. Furthermore, to achieve optimal UHV conditions, the system undergoes a 72-hour, 150°C bake-out routine, while the Mott channeltrons are kept below 100°C . After the subsequent out-gassing procedure, the system has a base pressure in the low 10^{-10} mbar range, which is independently measured with both a Bayard-Alpert ionisation gauge and a Pirani gauge. A schematic of the finished vacuum assembly with all its components is depicted in Figure 6.2.

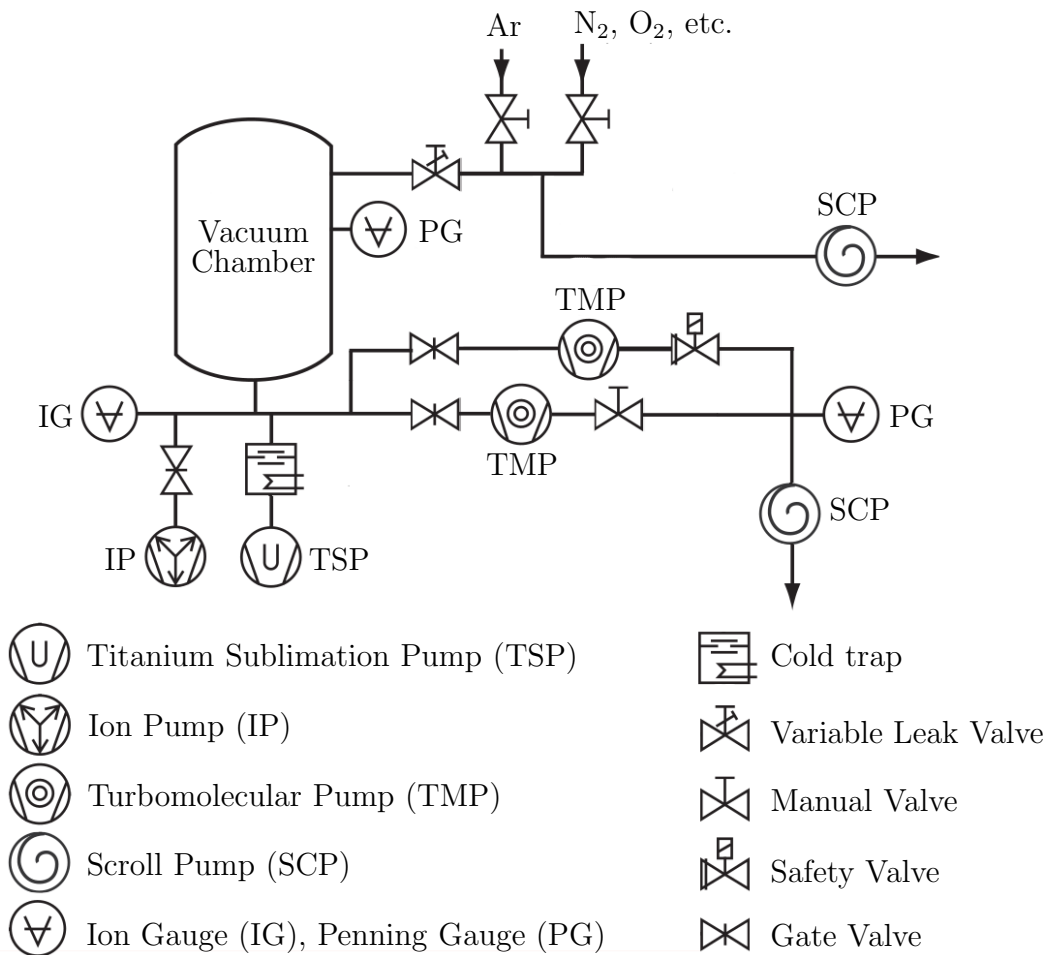


Figure 6.2: Schematic of the pumping section of the apparatus with emphasis on vacuum generation and gas handling, consisting of vacuum pumps, valves and suitable pressure gauges.

An additional Vacscan residual gas analyser (mass spectrometer) provides information on the composition of any residual gas molecules still present in the vacuum chamber and is a useful tool to verify the quality of the bake-out process or to detect leaks in the system. Most pumps can be isolated from the system using manual valves *e.g.* for bake-out. An electromechanical safety shut-off valve is used to protect the system and keep it in medium vacuum range in case of a blackout. Additional protection is guaranteed by adding an uninterruptible power source to the system, which will provide energy for up to 12 hours in case the mains power fails. As can be seen in Figure 6.2 the system is further equipped with two gas lines, allowing the use of Ar gas for sputtering and high purity nitrogen to vent the system, while keeping oxidants and water vapour to a minimum.

6.1.2 Experimental chamber

The experimental section of the chamber shown in Figure 6.1 is made from Mu-Metal which is a nickel-iron alloy (77% Ni, 14% Fe, 5% Cu and 4% Mo) to shield the experiments from external magnetic stray fields including the Earth's magnetic field. It was measured, that the shielding reduces the earth's ~ 500 mG ambient magnetic field, to about 20 mG in the region around the sample. This low magnetic field is especially important as the emitted SP electrons are highly susceptible to external disturbances.

The chamber is further equipped with an argon ion sputtering gun and two evaporators, currently holding Co and Fe, allowing for *in situ* cleaning and sample fabrication. The connected Specs ErLEED 150 combined LEED/AES system, gives the possibility to analyse and monitor the sample surface's crystalline structure and chemical composition before and after growth. As part of the system's improvements, a quartz crystal microbalance was added to the system to control and check the growth rate of the evaporators in real-time. The sample's magnetisation during and after fabrication can be observed via longitudinal MOKE measurements. Here, the laser beam enters and exits through two windows at an angle of $\pm 45^\circ$ to the sample normal. All the before mentioned components are used to allow *in situ* growth and characterisation of different samples, making this a very versatile MBE system.

In addition, the experimental chamber holds a low-energy retarding-potential Mott polarimeter, which is of importance for the objective of this dissertation, due to its ability to measure spin-polarised low-energy primary and secondary electrons (see Section 3.3.5). The idea is to use it in combination with a specially designed sample holder to characterise the spin polarisation of electrons emitted from a variety



Figure 6.3: Picture of the current triple-axis manipulator, which allows for precise linear and rotational positioning of the sample within the experimental chamber with a resolution of 0.1 mm and 1° . It further includes a thermocouple to measure the sample’s temperature and electrical connections to measure induced currents.

of SP-FESs, as will be explained in more detail in Section 6.2. The Mott polarimeter is attached to the system through a custom-made bellows which allows the position of the polarimeter inside the chamber to be changed by moving it into or withdrawing it from the restricted working area. This feature is especially important to find the optimal position to focus the emitted electrons from the sample to the detector. The initial design was taken from Prof. F. B. Dunning’s group at Rice University [140] and was implemented and improved for the present chamber in Cambridge by Dr. K. P. Kopper [145].

The top flange holds a triple-axis manipulator, as seen in Figure 6.3, which is mounted on three linear motion stages at right angles to each other. It is connected to the vacuum system via a flexible bellows allowing the sample to be positioned in x -, y - and z -direction with a resolution of about 0.1 mm. Furthermore, the sample can be rotated around its azimuthal and polar (the manipulator’s z -axis) angle within 1° , allowing for precise linear and rotational positioning of the sample within the experimental chamber.

6.1.3 Refurbishment and improvements

In the following, a detailed description of the system’s refurbishment and improvements is listed:

- **Issue:** During the refurbishment process it was found that the experimental part of the UHV chamber in its original design was insufficiently stabilised on the table. This meant that it was not possible to simply remove the old pumping system without the risk of damaging the experimental part.

Improvement: Special height-adjustable stabilising mounts were designed, built and installed on three sides to ensure safe handling of the chamber. An

image of the design can be seen in Figure 6.4 a.

- **Issue:** The original pumping stage of the system had a tiny leak and thus could not go to ultra-high vacuum. Unfortunately, this leak was found to be related to the system's cold trap, which was permanently welded to the pumping stage body thus making it impossible to replace it.

Improvement: A completely new UHV chamber body was used, consisting of a seven-way spherical cross as seen in Figure 6.4b. As the initial state of contamination or cleanliness of the part was unknown, the part was sent to be cleaned and polished by ITL Ltd., a company that specialised in UHV components. The refurbished UHV body was then mounted onto the experimental chamber and used to attach all UHV related pumps.

- **Issue:** The original system was equipped with two diffusion pumps (EO2K and EO4K) which had several drawbacks. The first being that these pumps, although very powerful, use evaporated oil to pump vacuum and are thus prone to hydrocarbon contamination which might lead to sample-surface contaminations. The second being that, due to the age of the larger EO4K pump its indispensable cooling system was broken, rendering it unusable for UHV applications.

Improvement: The oil diffusion pumps were replaced with two magnetically levitated turbomolecular pumps. These pumps have the advantage of hydrocarbon-free pumping, low vibration operation and being almost maintenance-free. With the new pumps, the chamber can be pumped down to low 10^{-7} mbar in 45 minutes.

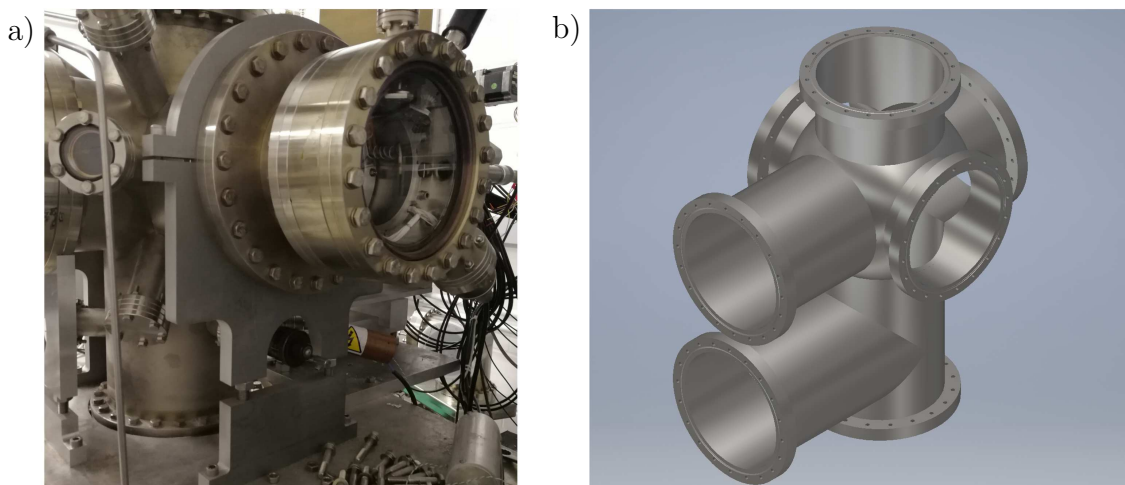


Figure 6.4: Picture of a) one of the new height-adjustable stabilising mounts and b) the new UHV chamber body.

- **Issue:** Due to the extended exposure to air over several years, all pressure gauges were either broken or in need of refurbishment.

Improvement: The ion gauge and Penning gauge in Schematic 6.2 were cleaned and all filaments were either exchanged or fixed. The re-installed gauges are completely operational again providing a pressure measurement range of atmosphere down to 10^{-11} mbar.

- **Issue:** It was found that the Varian Starcell ion pump was unexpectedly heating up during its regular operation mode. This might have been caused by the extensive use and prolonged exposure to air over the years where material deposits may form flakes with sharp points resulting in unwanted field emission currents, short circuits and electrical discharges. These deposits are formed when ionized gas molecules undergo chemical reactions with the active gases and getter material to form stable compounds that are deposited on the internal walls of the pump. These deposits not only increased the probability of damaging the pump but the heating also causes the vacuum to decrease as the adsorbed material in the pump is partially evaporated and re-released into the UHV system.

Improvement: The ion pump was completely disassembled and all element cells were cleaned via sonication in acetone and subsequent IPA rinsing. All electrical high voltage connections were checked and cleaned to avoid any short circuits. After the deposits were removed the materials were outgassed. The refurbished ion pump was fully functional and could keep the system in the low 10^{-9} mbar after bake-out even without any other pump running.

- **Issue:** The newly purchased Edwards STP301 comes without an additional cooling system but relies on ambient cooling for heat dissipation. Unfortunately, it was found that the pump exhibited a significant rise in temperature when running for prolonged periods of time even under UHV conditions.

Improvement: To avoid any damage to the pump a new water-cooling shroud was designed, fabricated, and fitted. This work was done in collaboration with the workshop, as the non-magnetic stainless steel parts had to be welded. The finished cooling system was fitted to the pump and provides sufficient heat exchange (Figure 6.5 a).

- **Issue:** The large Edwards STP-XA2703C pump has a pumping volume of 2650 L s^{-1} with 27500 rpm (revs per minute) and thus will cause danger if anything would suddenly obstruct the rotor blades *i.e.* if the sample or other components would fall into the pump.

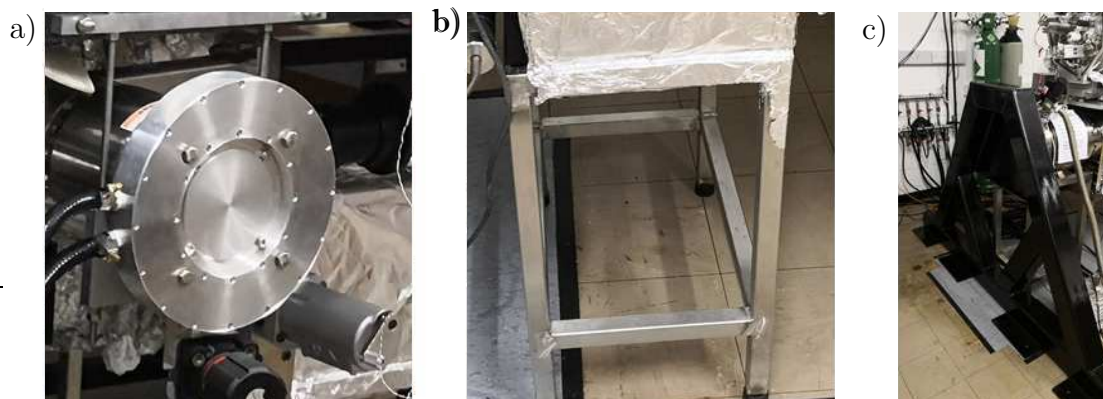


Figure 6.5: Picture of a) the new cooling shroud for the STP301 pump, b) one of the new height-adjustable stands for the turbomolecular pump and the ion pump, and c) the new STP-XA2703C pump's safety frame.

Improvement: To avoid any risk to both people and equipment, the pump was mounted horizontally onto the system. As it weighs about 80 kg a new height-adjustable stand was designed and built to hold it in position (Figure 6.5 b). It was important to adjust everything to the right height, as the heavy weight creates a massive torque on the UHV system. This might cause leaks or more severe damage. Furthermore, because of the dangerous rotational torque a special frame was designed and fabricated in the mechanical workshop which was permanently attached to the concrete floor (Figure 6.5 c).

- **Issue:** The Specs ErLEED LEED/AES system was not able to focus the beam and the fluorescent screens did not work properly. After dismantling the whole system, it was found that the problems were caused by severe mechanical damage. The ceramic insulation spacers which electrically separate the screens were broken, causing the system to short circuit.

Improvement: The LEED/AES system was taken apart and the ceramic spacers between the grids were replaced. The newly made spacers were installed and the SPECS system was again mounted onto the chamber. The mended system was fully functional again and it was possible to run full AES scans and LEED pattern analysis after recalibrating all system settings (*e.g.* gain, offset, crossover-point, *etc.*) and the sample position.

- **Issue:** It was found that the argon ion sputter gun had a heat-induced short circuit. As the ion gun's voltage was increased and the system's temperature rose, the filament wires extended and touched the grounded anode and shielding and thus created a short circuit. Then it was not possible to strike

a plasma or to sputter the sample.

Improvement: The ion gun was taken apart and the filaments were replaced. Special care was taken to correct the filament's length to avoid any more issues for the system caused by heat-induced elongation. After the disassembly of all components, the sputter gun had to be re-calibrated and the new sample position and focus were found. The finished system was able to sputter the substrate and thus clean it prior to the sample growth.

- **Issue:** Due to heavy use in the past, initially none of the shutters *i.e.* for the ErLEED system, the Mott detector, the main viewport, the sputter gun and the evaporators were working properly. While this was not difficult to fix, the restoration was imperative for the MBE process. Without the shutters, the evaporated material would cover and destroy most of the other components in the system, such as the LEED screens which are for example protected by an integral multi-segment shutter mounted in front of all grids.

Improvement: The chamber was opened, and all shutters were repaired, cleaned and securely reattached. The finished system was fully functional, and all components could be individually closed or opened when necessary.

- **Issue:** As part of this dissertation a new sample holder assembly capable of inducing FE in a SP-FES had to be designed. This novel sample holder assembly, as described in Section 6.2, has an overall thickness of about 45 mm and thus would not fit through the originally designated flange opening.

Improvement: To facilitate the new sample holder design a new reducer flange was mounted, adapting the DN 160CF UHV body flange to a DN 63CF flange port through which the sample manipulator with attached sample holder would easily fit.

- **Issue:** The newly implemented reducer flange for the sample manipulator had a longer port length than the previously used flange, causing the sample to be displaced from the focal point of the UHV chamber. The reach of the manipulator arm was too short, causing the sample to not be positioned in the focal point of the experimental chamber any more.

Improvement: To adjust the sample position to be in the focal point of the evaporators, Mott detector, sputter gun *etc.* a sample holder extension was designed and fabricated as seen in Figure 6.6. The new adaptor made it possible to operate the system again.

- **Issue:** The attached thermocouple, which is used to measure the sample temperature, was broken as well as the electrical connection which is used to

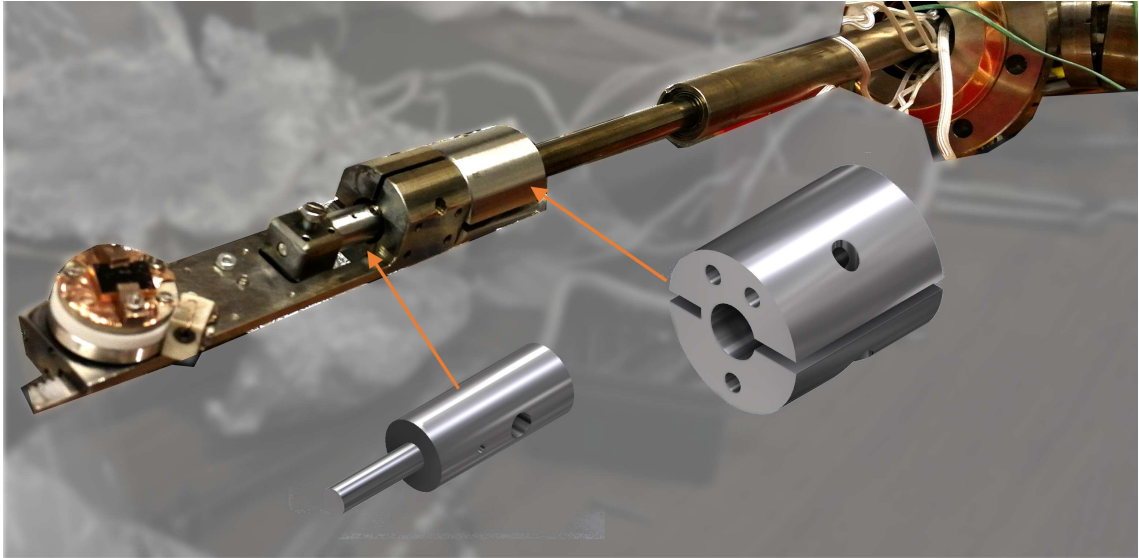


Figure 6.6: Picture of the extended sample manipulator assembly including CAD images of the individual parts.

measure the sample's target current during sputtering. Furthermore, the electrical connections to the W-wire ceramic plate which heats the system were non-operational.

Improvement: The entire electrical connections and wiring from the feed-through to the sample holder were redone and tested. The refurbished system was able to correctly measure the temperature, the currents and to anneal the sample to over 200 °C.

- **Issue:** Due to the heavy use over the years, the sample holder assembly's ceramic plates which hold the sample and electrically insulate it from the sample manipulator were worn out. More specifically, the tapped holes which held the screws were stripped, making it impossible to mount a sample.

Improvement: As no documents or mechanical drawings were available, all ceramic segments were measured and new mechanical drawings of all components were made and subsequently machined out of Macor ceramic. The fixed sample holder was again able to hold a sample in position.

In summary, almost all components of the pre-existing UHV-MBE chamber were replaced, redesigned, or underwent major repairs and improvements. The finished system was again able to achieve UHV conditions and to prepare and analyse samples using all its components.

6.2 Novel sample holder for field emission experiments

The general setup to induce and measure field emission is comprised of the emitter (cathode) and an opposing anode between which a sufficiently high voltage is applied. Here either the anode or the cathode may be grounded to suit the experimental setup. The generated electrons are subsequently accelerated towards the anode which in general has a concentric hole through which the electrons escape to be detected. To extend the basic emission setup to act as an electron gun, either an additional Wehnelt electrode or a suppressor electrode is used to focus the electrons into a beam. For the latter, the emission tip protrudes through the suppressor electrode which is at a more negative potential than the tip and thus prevents electron emission from the tip shank.

For the purpose of testing and measuring SP-FESs in the framework of this dissertation, a customised “field emission sample holder” (FE-holder) was designed based on the above-mentioned simple cathode-anode system and which could be mounted onto the pre-existing sample manipulator assembly. This new FE-holder would allow for a spin-polarised electron beam to be emitted from a nano-sized emitter and to be collected and analysed by the Mott polarimeter. A schematic of the concept is shown in Figure 6.7.

To minimise fabrication efforts, the new FE-holder was designed to fit onto the pre-existing sample manipulator. This also had the advantage of re-using the manipulator’s rotation capabilities, making it possible to change the electron spin di-

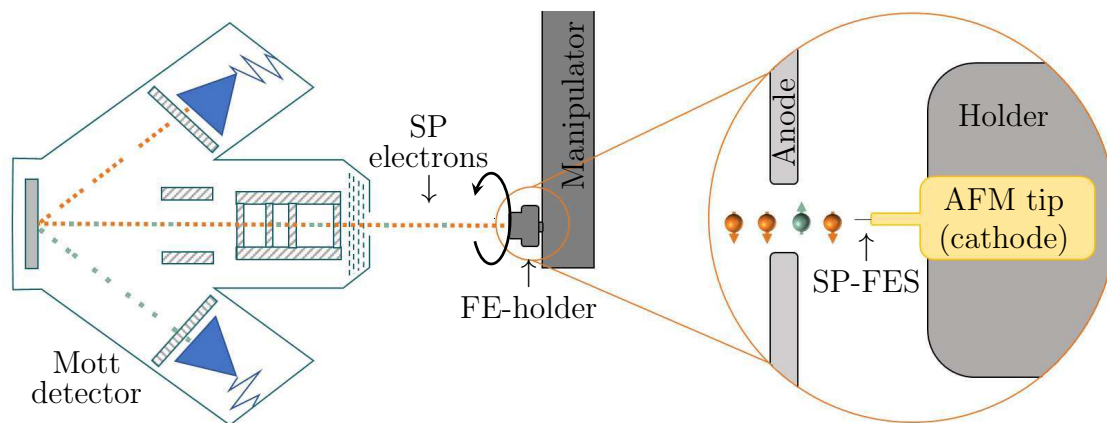


Figure 6.7: Conceptual representation of the measurement setup, which can be used to analyse the spin-polarising properties of point-like emitters. The setup consists of a specialised FE-holder which is mounted onto the pre-existing manipulator and a Mott polarimeter.

rection mechanically by simply rotating the sample holder plate. Furthermore, the FE-holder had to be versatile in the sense that it should be usable for different kinds of emission tip samples. Therefore, commercially available conducting atomic-force-microscopy (AFM) probes with tip-less cantilevers should be used onto which the nano-sized emitters would be attached, as indicated in Figure 6.7. This approach would have the advantage of utilising the AFM probes' standardised dimensions and thus making it easy to mount the samples in the specially manufactured holder.

6.2.1 Field emission holder design

This section investigates different design aspects of the FE-holder assembly which in its core components consist of an anode, a cathode (the specimen under test), a heating element and spacers. All parts were designed with Autodesk[®] Inventor[®] Professional 2018 [212] and the simulations were done using COMSOL[®] 5.4 [213].

The anode

One of the main components of the assembly is the non-magnetic 304 stainless steel anode, which is used to extract electrons from the sample. Here, a cylindrical or “top-hat” geometry was chosen with a 1 mm hole or aperture in the middle through which the electrons can be emitted (see Figure 6.8 a). The large openings on all four sides of the anode allow for vacuum to be pumped more efficiently around the sample and to eliminate the creation of air-pockets. The largest opening also acts as a feed-through for the electrical connection of the heater and the sample (cathode).

One important design consideration was the shape of the aperture and its impact on the number of transmitted electrons. This was important as sharp edges and corners can result in strong electric fields which might negatively affect the FE-holder's electron yield. Therefore, two models, one with a chamfered hole (CH) as seen in Figure 6.8 b and rounded corners at the upper surface and one with a straight hole (STR) with sharp corners (Figure 6.8 c), were computed with COMSOL. For both cases, the applied cathode voltage was varied from -1 kV to -10 kV, while the anode was kept at ground potential. This was done to keep the outside of the FE-holder assembly field free.

To design the sample holder to be as versatile as possible and to be capable of accommodating a variety of emission sources, the emission tip was emulated by a 100 nm by 100 nm inlet from which electrons were released into the system. This way the FE-holder assembly will be optimised for SP-FESs with radii up to 50 nm. Furthermore, to be close to the real experimental conditions, the electrons were

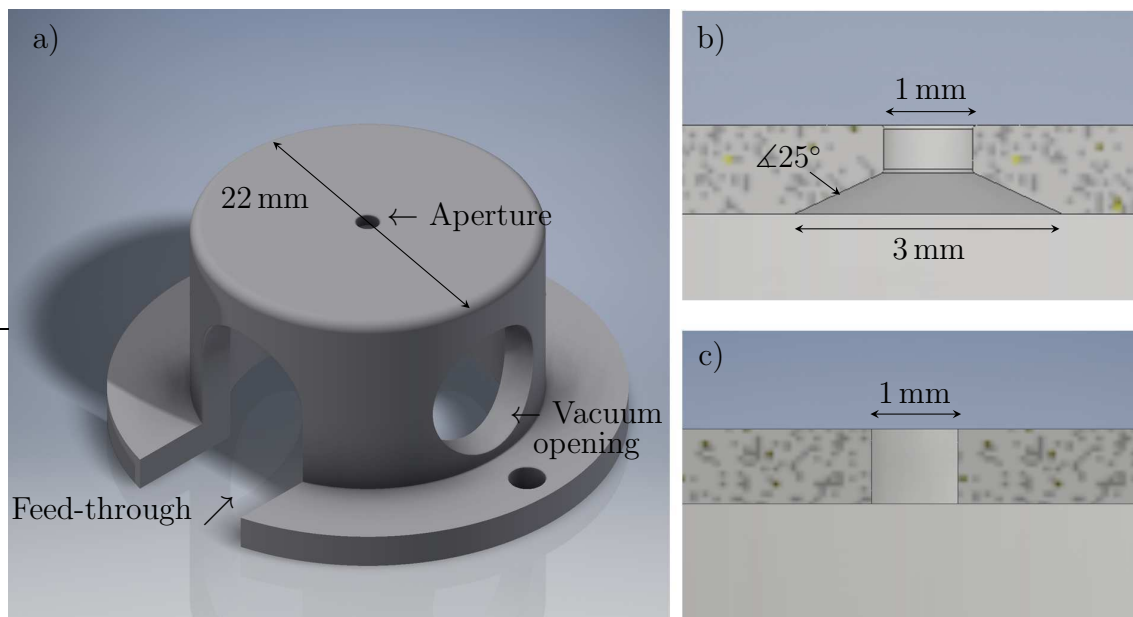


Figure 6.8: a) CAD model of the “top-hat” anode with a 1 mm aperture and the necessary feed-throughs. b) Chamfered aperture design with rounded corners at the upper surface. c) Straight aperture design with sharp corners.

launched with a non-uniform velocity with initial energies ranging from 0 meV to 0.1 meV.

The simulated results are plotted in Figure 6.9 and show an increase in transmitted electrons with increasing electric field going from about 40% at -1 kV up to almost 100% after about -4 kV for both apertures. These results were obtained by counting the electrons arriving on the top boundary opposite from the release point and thus give the number of particles transmitted from the aperture. This increase results from the improved focus of the electron beam with higher fields as demonstrated in the two insets which show the electron trajectories. Comparing the trajectories clearly shows that the divergence of the electron beam is much higher for -1 kV which in turn blocks a significant number of electrons from escaping the anode.

Even though both designs yield similar results, it was found that the electron count was consistently lower for the straight aperture compared to the chamfered design. Thus, the aperture’s surface facing the emitter was chosen to be chamfered and all corners were rounded. In addition, all steel components were polished to prevent corona discharge and electric arcing from unwanted protrusions.

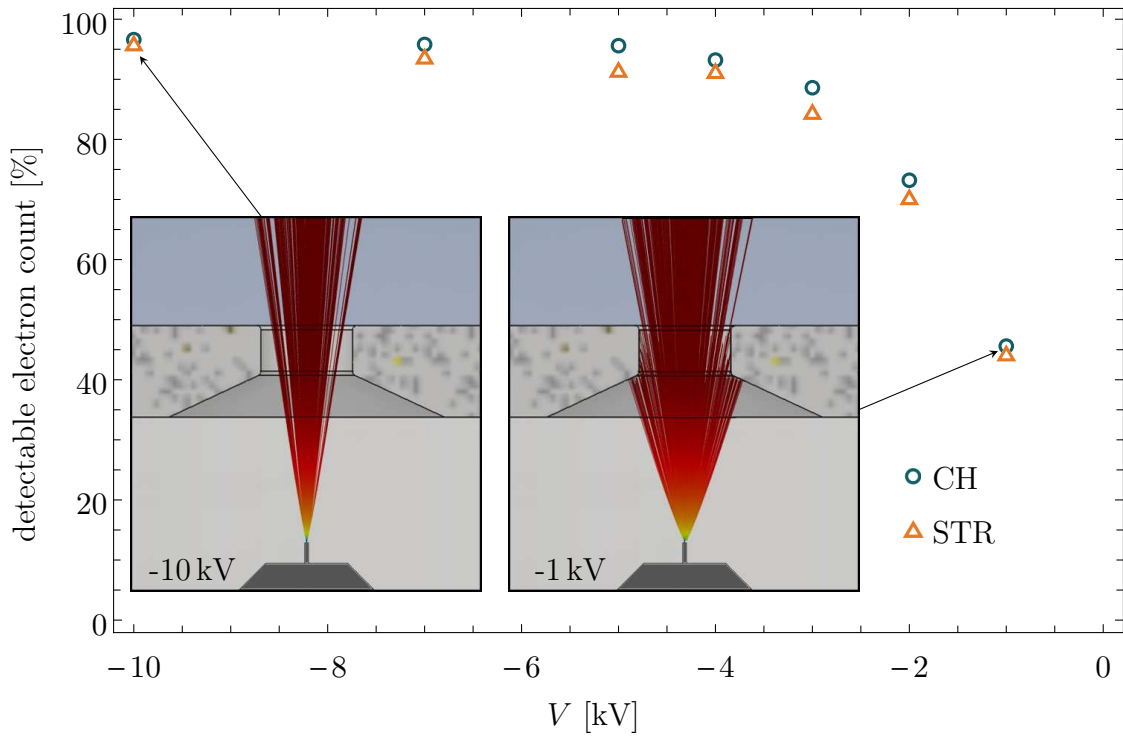


Figure 6.9: Increase in detectable electron count with increasing applied voltage for a chamfered (CH) and a straight (STR) aperture. The insets demonstrate that the increase results from an improved focus of the electron beam.

The sample holder base

The insulating sample holder base, as seen in Figure 6.10 was machined out of Macor. This material has the advantage of being an excellent insulator while being easily machinable. The holder has a total height of 12 mm and a radius of 11 mm. Its special feature lies in the form-fitted recess which was measured to hold commercially available AFM probes. This ensures that both the sample positioning and anode-cathode distance are reproducible, which allows easy comparison of emission current between different samples. Furthermore, the sample is easily alignable on axis with the central hole, allowing the maximum number of electrons to be emitted through the anode's aperture.

Another design consideration was the attachment of the anode to the sample holder base without creating a short between cathode, anode or sample manipulator. The issue was that it is inadvisable to attach the anode via screws to the ceramic holder directly, as the continuous use would quickly strip the threaded ceramic holes, rendering the sample holder unusable. Therefore, a special recess was added, which embeds a threaded metallic counter plate to avoid any electric shorts.

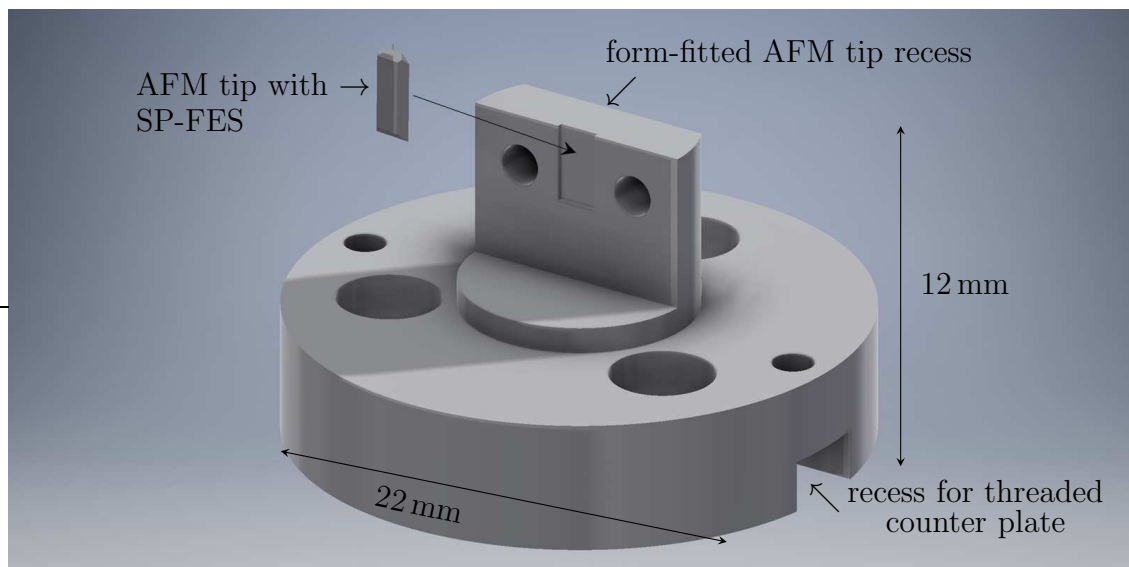


Figure 6.10: CAD model of the sample holder base. It has a special recess to fit AFM samples on axis with the central anode aperture and another recess at the bottom for a threaded counter plate to attach the anode to the base without creating a short circuit with the sample manipulator.

The spacers and suppressor electrode

Another very important parameter for field emission is the anode-cathode distance, d_{AC} , as it for example influences the field enhancement factor β [214] and the electron trajectories. Thus, simulations were performed including additional spacers between sample holder base and anode to vary the emitter-anode distance from about 0.5 mm to 5.5 mm to find the optimal parameter. Here, d_{AC} is defined as the distance measured from the top of the AFM cantilever to the bottom of the anode, as indicated in the insets in Figure 6.11.

Figure 6.11 shows the change in number of detectable electrons with varying distance for the case of a constant voltage of -5 kV and a constant electric field of -3.36 kV/mm. For both cases the number of electrons leaving the anode aperture decreases significantly for $d_{AC} > 1.5$ mm (dashed line in Figure 6.11). As can be seen from the insets, which show the electron trajectories, some of the electrons get blocked by the anode before leaving the aperture to be detected if d_{AC} becomes too large. Based on these simulations the final anode-cathode distance was chosen to be 1.5 mm for the actual design to be fabricated. However, as the theoretical predictions might differ from actual experimental values, several C-shaped spacers with varying thickness were fabricated which allow the anode-cathode distance to be changed in steps of 0.5 mm if necessary. These spacers were made from 304 stainless steel and were 0.5, 1, 1.5, 2 and 2.5 mm thick and can be placed between the anode

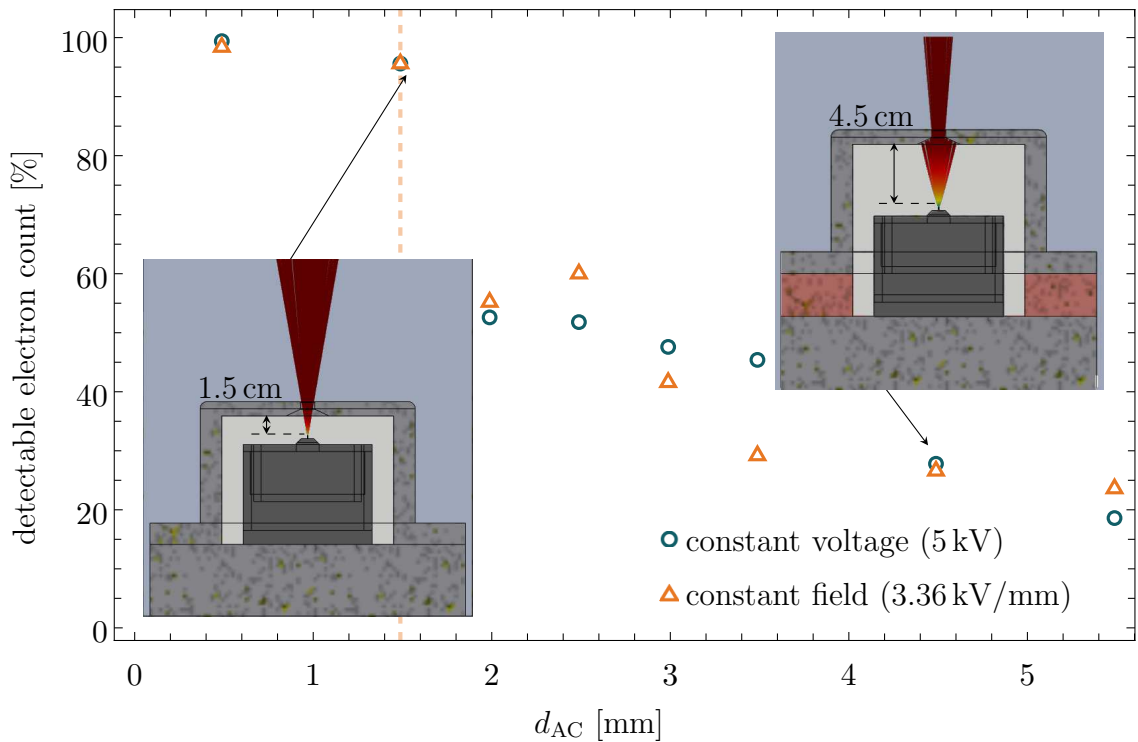


Figure 6.11: Decrease of detectable electron count with increasing anode-cathode distance. The black dashed line indicates the distance chosen for the final design. The insets show the electron trajectories and indicate that the majority of electrons get blocked by the anode before leaving the aperture if d_{AC} is too large. The red area in the right inset indicates the additional spacer thickness.

and the sample holder base.

Furthermore, as can be seen in Figure 6.12 a, the electric field inside the sample holder assembly is not perfectly symmetric around the emission tip which causes slight deflections of the electron trajectories. This asymmetry forces the electrons to not only have a velocity in the z -direction but to also have a velocity component in the x -direction. This in turn results in a loss of detectable electrons as they get blocked by the anode as shown by the electron trajectories in the xz -plane. One way to overcome this issue is to introduce a suppressor electrode, as seen in Figure 6.12 b, through which the emitter protrudes and which is held at a slightly more negative potential than the emitter itself. This plate not only restricts electrons emitted from the tip shaft but also helps to form a uniform and symmetrical electrostatic field distribution inside the sample holder assembly. Simulations for a suppressor electrode held at -1 kV lower than the cathode are shown in Figure 6.12 c and demonstrate an increased electron count compared to the simulations without.

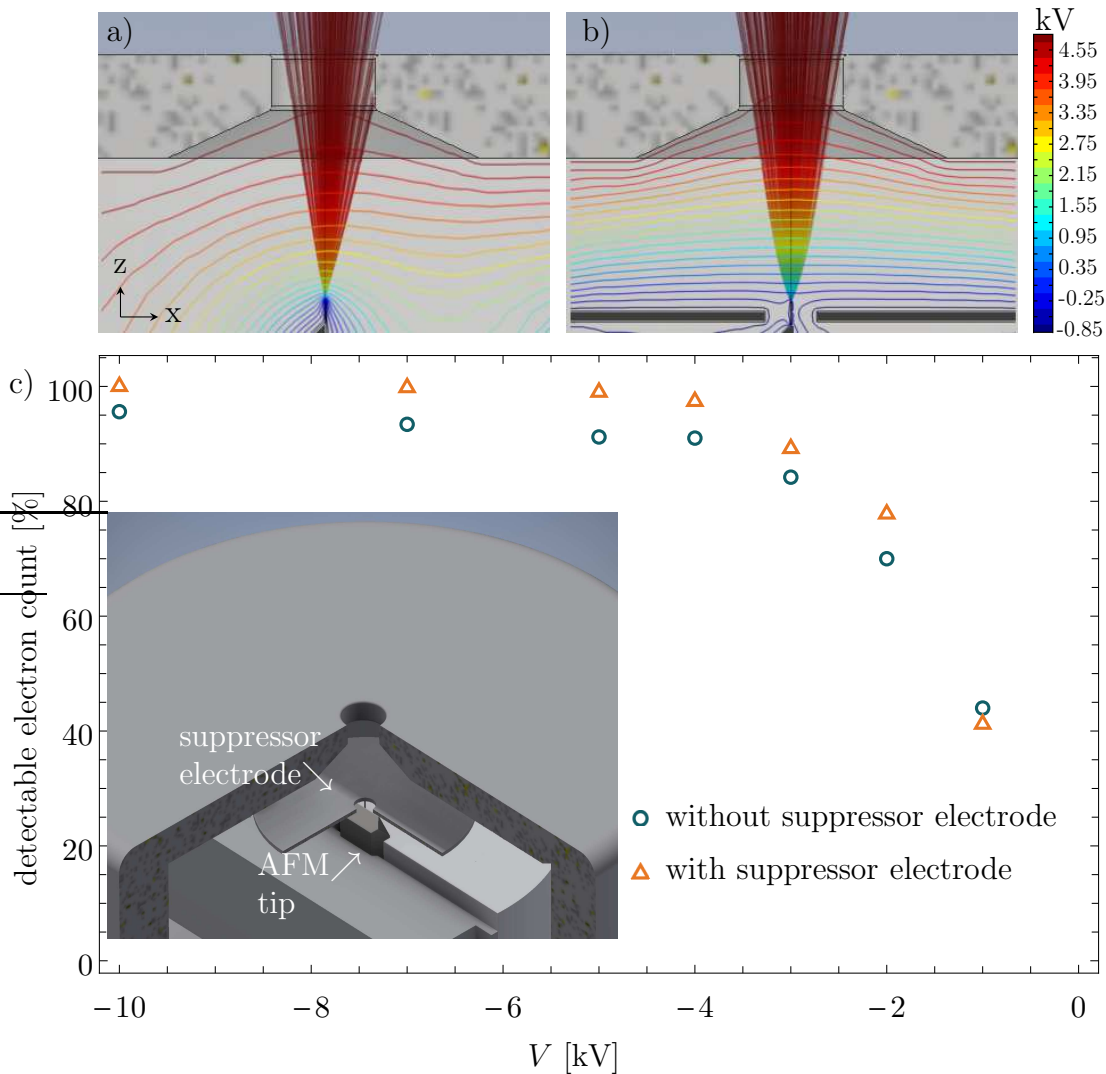


Figure 6.12: COMSOL simulations of the electron trajectories a) without and b) with a suppressor electrode. c) Comparison between the detectable electron count with and without a suppressor electrode. The inset shows the placement of the suppressor electrode within the FE-holder assembly.

The sample heating

Incorporated inside the FE-holder assembly, mounted directly in front of the primary sample, are a small resistive heater and a thermocouple which can be used for active temperature control and monitoring. The heater consists of a piece of tantalum (Ta) foil which is held in place by a ceramic clamp and a threaded counter plate, see Figure 6.13. The electrical connections to allow heating are spot welded to the Ta foil. The heating can be used either to anneal the emitter after exposure to air during sample transport or to support electron emission due to thermal excitation. Furthermore, the same connections can be used to either apply a potential or to

ground the sample to induce field emission.

The finished assembly

After careful considerations based on the COMSOL simulations, a final FE-holder design was chosen. A schematic view of the entire designed setup and how the components are assembled is shown in Figure 6.13. The real manufactured components are shown in Figure 6.14 b. As the main restriction in the design was imposed by the available space of the DN 63CF flange the entire assembly including the sample manipulator is only 45 mm high and 22 mm wide.

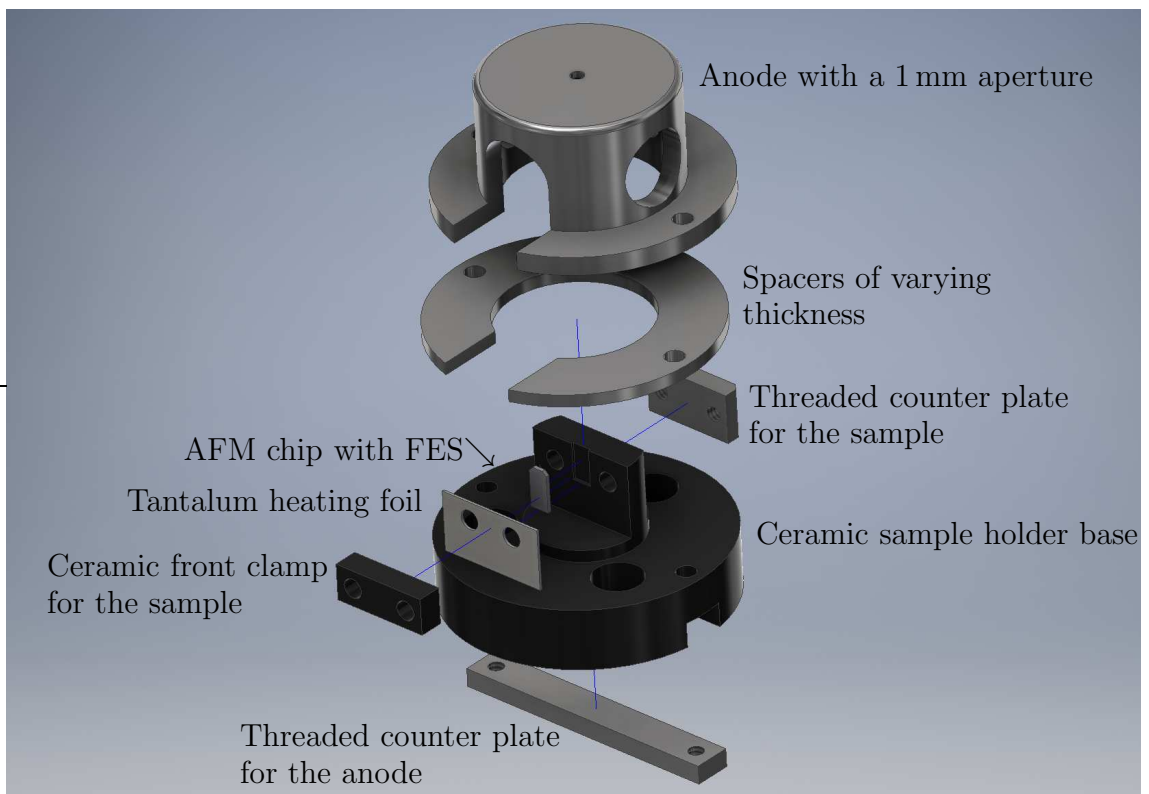


Figure 6.13: CAD design of the new FE-holder assembly which can be used to analyse spin-polarised FES.

6.3 Conclusion

This chapter detailed all necessary steps taken to build and design a fully functional experimental setup to measure spin-polarised field emission from different nano-sized emission sources. In this process most components of the pre-existing ultra-high vacuum MBE/Mott chamber were either replaced, rebuilt, or underwent major repairs.

The refurbished system is again able to achieve and hold pressure in the low 10^{-10} mbar range thanks to a completely redesigned pumping system. By using state-of-the-art magnetically levitated turbomolecular pumps and scroll pumps, the system is completely hydrocarbon free guaranteeing a clean and dry vacuum environment, which is essential for FE experiments. Moreover, the experimental chamber is again capable of preparing high-quality crystalline samples via molecular beam epitaxy. The substrates can further be cleaned prior to the growth process using sputter-annealing cycles and their quality can be determined pre and post deposition using AES and LEED. The newly implemented quartz crystal microbalance allows to precisely monitor and tailor the film thickness during deposition.

To facilitate the analysis of SP-FESs, after extensive COMSOL simulations, a novel compact field emission holder was designed for mounting onto the pre-existing triple-axis manipulator. The finished assembly is depicted in Figure 6.14 a. The design is further capable of quickly changing between the FE-holder and the regular sample holder used to analyse magnetic thin film samples. The finished FE-holder prototype is expected to effectively collect most of the electrons emitted from the SP-FESs at radii up to 50 nm, for analysis by the Mott polarimeter.

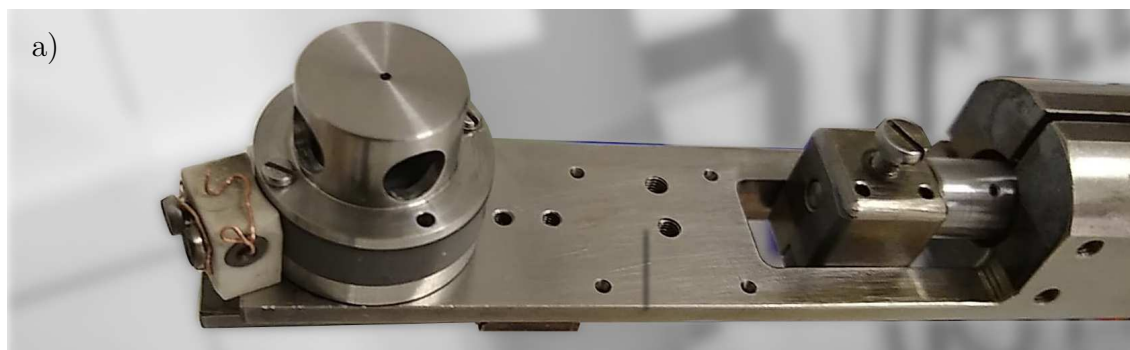


Figure 6.14: a) The finished field emission holder assembly mounted onto the triple-axis manipulator. b) Some of the individual components after the fabrication.

7 | Theoretical investigation of potential spin-polarised field emission sources

The next step in the process of achieving and analysing spin-polarised field emission from point-like sources was the development of the emitter design and a fabrication concept. Thus, this chapter will outline the initial considerations and general design idea of an iron-based field emission source with an in-plane magnetisation which is inert against an oxidising environment. The design process will further be aided by micromagnetic simulations to find the optimum dimensions of the ferromagnetic layer.

7.1 Preliminary design considerations for spin-polarised field emitters

The design, proposed in this dissertation, is based on the spin-polarised electron emission from a magnetic material. Here, a thin ferromagnetic layer on top of a non-magnetic material acts as a spin filter for unpolarised electrons before being emitted. Figure 7.1 shows a schematic of the first of two proposed emitter fabrication processes.

As a first step, a well-known field emission source such as GaAs or W is used as the base material which is either grown or etched into pillar-like structures with sub-micrometer radii (1). In the second step, a ferromagnetic material, such as Fe, Co, or Ni is deposited onto these pillars in such a way that the material's magnetisation lies perpendicular to the surface normal (2). This layer will provide the necessary spin-polarisation due to the FM's spin-dependent density of states around the Fermi level. The in-plane (ip) magnetisation direction is necessary as the Mott polarimeter, used to characterise the emitters, is only sensitive to the component of polarisation perpendicular to the incident beam's momentum. The sample's magnetisation direction can be tailored by adjusting the FM layer's dimensions and thus utilising its shape anisotropy (see discussion in Section 7.2).

To avoid contaminations and oxidation, in the next step an inert capping layer

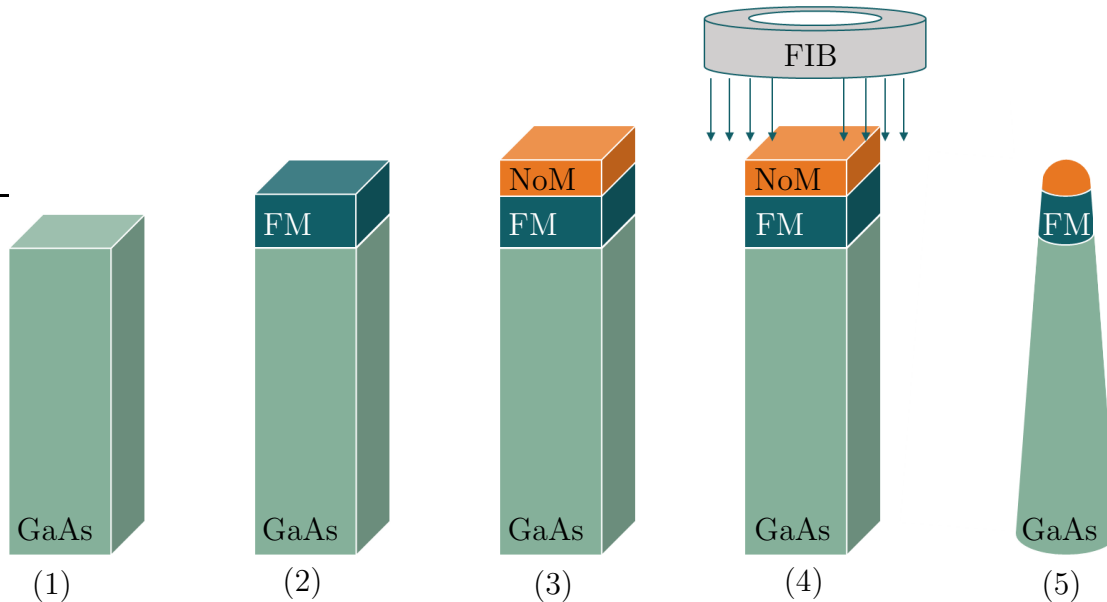


Figure 7.1: Principal design idea for a point-like spin-polarised field emission tip with an in-plane magnetised ferromagnetic (FM) layer and a passivating noble metal (NoM) cap. The emitter can be thinned down using annular focused ion beam (FIB) milling.

will be grown on top of the FM layer (3). This step is necessary as ferromagnetic materials are known for their high reactivity with adsorbates and fast oxidation times which can have profound effects on the material's properties [215–221]. It was, for example, found that gaseous adsorbates such as nitrogen reduced the polarisation of emitted SE from a Co/Cu(001) sample by about 20% compared to a clean surface [219].

One possibility for such a passivating layer could be a noble metal (NoM), such as gold, silver, or platinum. These materials have the advantage of being resistant to oxidation and having a high temperature stability [222]. Gold in particular is suited for the proposed emitter design as it was found that for efficient spin transmission across interfaces the conductance at the FM/NoM interfaces needs to be matched. This is the case for an Au/Fe interface as the lack of d -states in the majority subband of Fe above the Fermi level results in a good matching of the s - p wave functions between the two materials [223]. This further leads to a spin-filtering effect due to the high transmittance for majority electrons across the Fe/Au interface compared to minority electrons [223, 224]. However, the thickness of the NoM layer has to be adjusted to be less than the spin diffusion length (l_{sd}) [225]. This is important, as upon applying an external field, the spin-polarised electrons are injected from the FM material in the non-magnetic NoM layer to be emitted. If this layer is thicker than l_{sd} the injected SP electrons will have lost their polarisation before being emitted. Thus, in the case of Au, the layer thickness should be less than $l_{sd} = 30$ nm [226]. However, as the coating of Fe with NoM is not trivial, the exact thickness or the necessity of additional adhesion layers like Ti would need to be experimentally determined. Furthermore, as can be seen from the figure, the here proposed process leaves the sides of the FM layer uncoated. However, the oxidation of metals is known to be limited in depth. This means that an oxide covering layer with a well-defined thickness will form and thus prevent the underlying metal from further oxidation, resulting in a self-stabilized bilayer structure [227]. Hence, Section 7.2 will discuss the magnetic properties of both iron and iron-oxide layers.

The last step in the SP-FES fabrication process is to reduce the radius of the pillar to create a sharp apex to enhance emission (4). This can be done by utilising a procedure commonly used for the preparation of atom-probe tomography specimens. In this process, a focused beam of gallium ions is used to “mill” the specimen surface via a sputtering process with nanometer precision (annular focused ion beam (FIB) milling) [228]. In the initial rough-milling step the micropillar is sharpened by repeatedly removing ring-shaped areas. This step is followed by finer milling in which the ion current, as well as the ring diameter of the milling pattern, is gradually

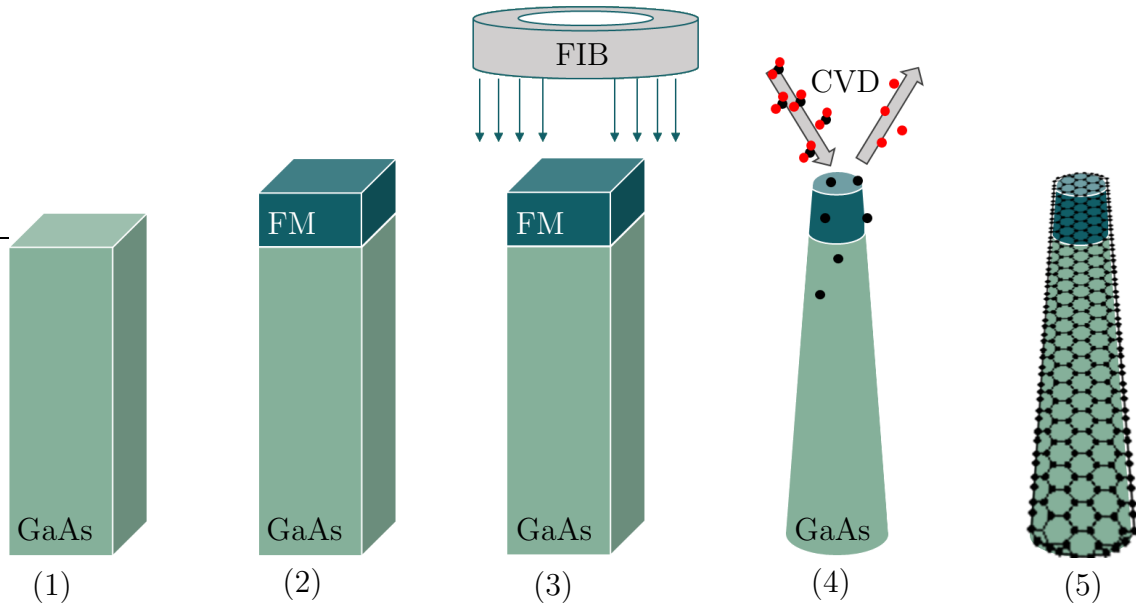


Figure 7.2: Principal design idea for a point-like spin-polarised field emission tip with an in-plane magnetised ferromagnetic (FM) layer and a passivating graphene layer.

reduced. Finally, a polishing step using an ion beam with an inner mask diameter of zero is used to reduce the level of gallium implantation and to adjust the NoM capping layer's thickness. The finished design is depicted in Figure 7.1 (5).

An alternative concept to fabricate SP-FES is depicted in Figure 7.2, in which the micropillar would be milled down prior to the capping-layer deposition (3). Then graphene could be grown using, for example, chemical vapour deposition (CVD) (4) to form a passivating layer (5) [71, 229, 230]. Recent reports have demonstrated that a single graphene layer, when deposited on an Fe film, keeps it from oxidation while keeping its SE spin polarisation almost unchanged [231]. This was further verified by other reports on graphene-passivated Ni and Co samples, which were found to preserve the spin polarisation for electrons flowing perpendicularly through the graphene. However, a graphene-passivation layer on Ni can induce a spin-filtering effect which results in the reversal of the detected spin polarisation compared to an uncoated Ni sample. This effect is most likely caused by the difference in Fermi surfaces between graphene and Ni. As Ni only has minority spin states at graphene's K point only these electrons will have a continuous transport channel, while the majority electrons are filtered out [232]. It was further reported that graphene on intercalated Co significantly increased the material's magnetocrystalline anisotropy due to the hybridisation of the Co and graphene electron orbitals [233], which might lead to an unwanted magnetisation direction for the SP-FES.

Keeping these effects in mind, graphene is a promising candidate for an oxygen-

resistant coating-layer as demonstrated by extensive research on graphene-coated AFM tips which exhibited enhanced conductivity and robustness without increasing their radii. These AFM tips were coated using a variety of different techniques such as direct CVD, transfer of CVD grown graphene or using liquid-phase exfoliated graphene [234]. However, the synthesis of well-ordered epitaxial graphene on metal surfaces often requires high processing temperatures, which might cause unwanted interfacial intermixing. Furthermore, depending on the deposition technique, graphene can form clusters instead of a single layer [234], thus creating an uneven emission surface.

All these deposition techniques were demonstrated on structures with radii larger than the here desired needle-like geometry with radii below 10 nm. Thus, another procedure to fabricate point-like field emission tips with an oxidation-resistant graphene layer might be to use magnetic nanowires sheathed inside a CNT. An extensive review by Liu *et al.* showed that it is possible to encapsulate materials such as Fe and Ni inside a CNT via electromigration [235]. However, depending on the aspect ratio of the ferromagnetic filling, its magnetisation direction will most likely lie along the long axis of the emitter, which is unfavourable for the SP-FES design proposed here. Nevertheless, the graphene-coating, as depicted in Figure 7.2 (5), might be a viable option to keep the SP-FES free from oxidation while maintaining a high spin polarisation.

7.2 Micromagnetic simulations

This section will provide a detailed investigation of the correlation between the ferromagnetic layer's dimensions and its magnetisation direction. This is important, as the layer should be in a single-domain state with a maximum in-plane component of \vec{M} to sufficiently work as a spin-polarised field emitter, while its diameter should be minimised to ensure point-like emission. To achieve these properties for the FM layer different parameters have to be considered, such as thickness, crystallinity, and the material. Thus, to gain insight into a sample's magnetic behaviour, several micromagnetic calculations were performed using the GPU-based program MuMax3 [236] to analyse which combination of parameters will yield the most promising emitter for SP emission.

7.2.1 Simulation parameters

The MuMax3 program calculates a system's spontaneous magnetisation in the absence of an external magnetic field by minimising its total energy. This calculation

causes the magnetisation vector for each simulation cell to point towards the system's energy minimum, which represents a stable direction for \vec{M}^a , while taking parameters such as exchange interactions and shape anisotropy into account. Thus, for all simulations presented, the spontaneous magnetisation evolved from an initial configuration of randomly oriented cells in the absence of any external fields to obtain the sample's ground-state.

To simulate the sample's geometry, its shape is discretised in three dimensions using a grid of orthorhombic cells in which each cell has a uniform magnetisation. Here, the whole simulation cell has the dimensions of $42 \text{ nm} \times 42 \text{ nm} \times 22 \text{ nm}$, while each individual cell size was set to 1 nm^{3b} , creating a grid of $42 \times 42 \times 22$ cells. The magnetic model itself resembles a cylindrical shape, as the previously described FIB milling process will result in such a particular geometry with varying height and diameter. Due to the orthorhombic cell shape used by the finite differences approach of MuMax [236] and the minimum cell size of 1 nm the realisation of a conical simulation model of an emission tip is not feasible in the given tip dimensions, since only a terrace approximation of a cone could have been realised. In the following, two different materials will be considered: iron and magnetite.

Iron was analysed, as it has decent spin-polarising properties and grows well on W (see Chapter 5). It has an exchange stiffness constant of $A_{\text{ex}} = 21 \times 10^{-12} \text{ J/m}$ [237, 238] and a saturation magnetisation of $M_s = 17 \times 10^5 \text{ A/m}$ [238, 239] at room-temperature. Moreover, a typical damping coefficient of $\alpha = 0.005$ and the gyromagnetic ratio^c of $\gamma = 1.855\,56 \times 10^{11} \text{ rad/Ts}$, which corresponds to a g-factor of 2.1, is used. In this dissertation, two cases are considered in which the first assumes a single-crystalline cylinder with a MCA constant of $K_{c1} = 48 \times 10^3 \text{ J/m}^3$ [238, 240] and the easy axes along the $\langle 100 \rangle$ directions, which correspond to the simulation model's x -, y - and z -axis. In the second case, K_{c1} is set to zero, which represents an amorphous structure without any MCA.

As the second material, Fe_3O_4 (magnetite) was investigated as a possible spin-filtering layer, as it is one of the naturally occurring oxides of Fe, in case the emission tip would be exposed to air without a passivating cap. It also exhibits the largest magnetic moment among the naturally occurring iron oxides with $2.66 \mu_B$ per formula unit [241] and a Néel temperature of 850 K . Moreover, magnetite is proposed to be a half-metal with a full spin polarisation at the Fermi level. Thus

^aGenerally, the energy minimisation functions evolve until there are no significant changes in energy any more. However, MuMax3 does not differentiate between the absolute minimum or a saddle point.

^bThis is the program's minimum cell size.

^cThe gyromagnetic ratio is defined as $\gamma = \frac{g^* \mu_B}{\hbar}$.

it was found to exhibit a high spin-polarisation of 80% near E_F for the (111) and of 50% for the (100) orientation [242,243] with a band gap of approximately 0.5 eV in the majority-spin band [244]. This reduction in polarisation from the initially predicted 100% is caused by the altered surface of the sample which, depending on the surface orientation, exhibits surface reconstruction or relaxation [245]. Such effects need to be considered when designing highly polarised FE sources based on thin films. However, this high spin polarisation still renders it a promising candidate for spin-polarised field emission. The calculation parameters for Fe_3O_4 were approximated by $A_{\text{ex}} = 1.32 \times 10^{-11}$ J/m [246], $M_{\text{sat}} = 4.8 \times 10^4$ A/m [246] and $\gamma = 1.855\,56 \times 10^{11}$ rad/Ts, corresponding to a g -factor of 2.1133. The material's easy axes lie along the $\langle 111 \rangle$ directions which were again chosen to lie along the x -, y - and z -axis. The single-crystalline model had $K_{\text{c1}} = -1.08 \times 10^4$ J/m³ [247], while the amorphous model had $K_{\text{c1}} = 0$.

Other naturally occurring forms of iron oxide, such as FeO, maghemite ($\gamma\text{-Fe}_2\text{O}_3$) and hematite ($\alpha\text{-Fe}_2\text{O}_3$), will not be considered in the scope of this work. While FeO forms very rarely, $\alpha\text{-Fe}_2\text{O}_3$ has a very small magnetic moment of less than $0.02 \mu_B$ per formula unit [241], making both unsuitable as potential SP-FESs. Even though $\gamma\text{-Fe}_2\text{O}_3$ exhibits a magnetic moment of $2.5 \mu_B$ per formula unit [241] and has been proposed to act as a tunnel barrier for spin-filtering devices at low temperatures [248] it is unstable and transforms into $\alpha\text{-Fe}_2\text{O}_3$ at elevated temperatures, thus losing its magnetic properties [249]. However, here one should note that both magnetite and maghemite have the cubic structure of an inverse spinel and will likely be both present in an oxidised tip.

7.2.2 Magnetisation direction and single-domain state

The first step in optimising the FM layer's properties to function as a SP-FES was to determine which dimensions would yield an ip magnetisation. Thus, the model geometry is varied, with the cylinder diameter, d , ranging from 1 nm to 40 nm, while the model's thickness, L , is varied from 1 nm to 20 nm, in steps of 1 nm. Here, to describe the individual model the nomenclatures "disk" and "cylinder" are used depending on the model's aspect ratio ($\tau = L/d$). Furthermore, this section will focus on the comparison between single-crystalline and amorphous Fe models to determine if one is preferable over the other when fabricating the emitter.

Iron nano-disks

First, to determine which model has ip or oop magnetisation, m_z is investigated, which is the averaged oop component of the magnetisation over all simulation cells normalised by M_s . Figure 7.3 shows m_z , as a function of thickness for single-crystalline and amorphous Fe models with diameter $d = 9$ nm. Here, $m_z = 0$ represents an ip magnetisation, whereas $m_z = 1$ represents an oop magnetisation. As can be seen from the plot, there is a hard transition between the ip (1) and oop (2) direction at a thickness of about 7 nm to 8 nm or an aspect ratio of about $\tau = 0.85$. The abruptness of the switching indicates that there is no smooth transition in which the surface spins are gradual canted when going from a cylindrical to a more disk-like shape and vice versa. Further inspection of the resulting magnetic textures confirmed that the models solely form single-domain states. This means that their dimensions are too small for domain walls and multi-domain structures to form. Two pictures of such single-domain states with different magnetisation directions are shown by the insets in Figure 7.3. Both are visualised using MuView and show

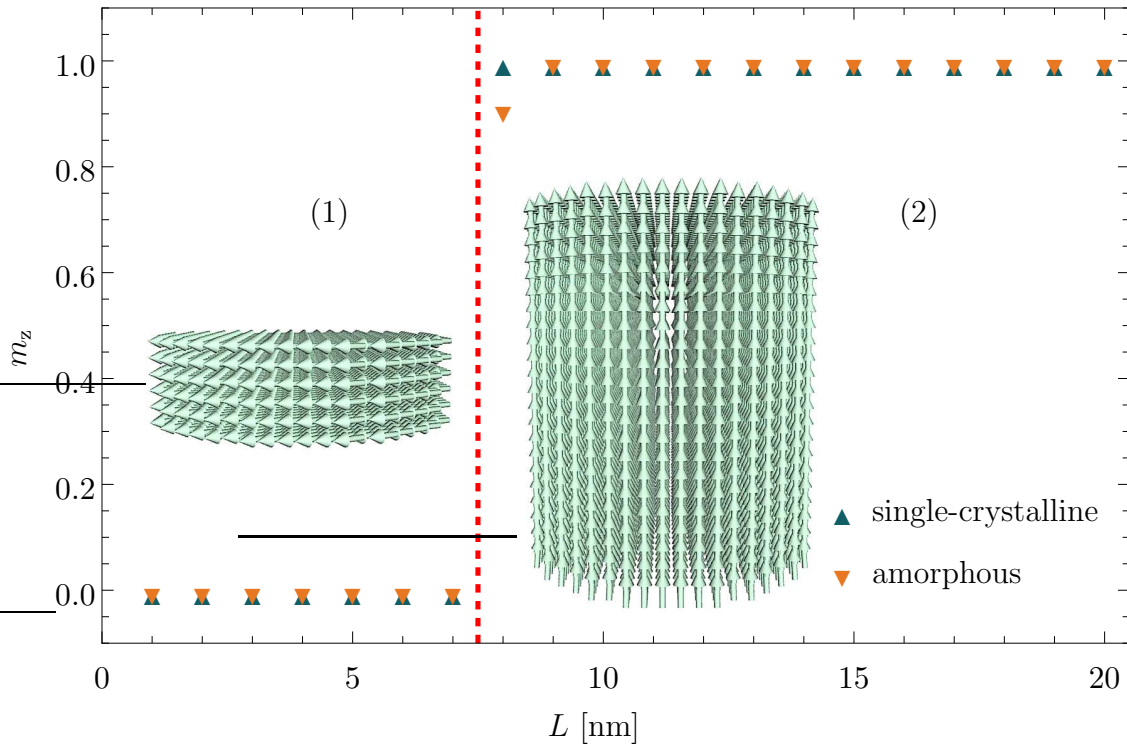


Figure 7.3: Oop-component of the magnetisation versus thickness for single-crystalline and amorphous Fe models. All models had a diameter of 9 nm. In region (1) ip magnetisation is favoured, whereas in region (2) the oop magnetisation is more stable. The two insets show the shape-dependent magnetisation direction, represented by green arrows, for two different models.

a vector representation of the total magnetisation $\vec{m} = \vec{m}_x + \vec{m}_y + \vec{m}_z$. It can be seen that these particular models form single-domain states.

However, a single-domain state does not necessarily mean uniform magnetisation as depending on the shape and dimensions, spin curling or canting can occur. It has been found both experimentally and computationally that there are three magnetic ground-states for a nano-disk, which can be classified as: a single-domain in-plane state, a single-domain out-of-plane state or a flux-closure vortex state [250, 251]. These three configurations are a result of the minimisation of the total free energy (E_{tot}) and the interplay of its various terms (see Section 2.2). Here, one has to note that these vortex states have a small oop component ($0 < m_z < 1$) due to their vortex core. This makes it impossible to precisely distinguish between the cases of a true vortex or a spin-canted ip/oop state by just analysing the m_z component. Therefore, to identify the dimensions at which such closure domains are formed, the norm of the averaged magnetisation in all three dimensions was investigated. Figure 7.4 shows such a calculation for a cylinder of single-crystalline Fe with a diameter $d = 28$ nm.

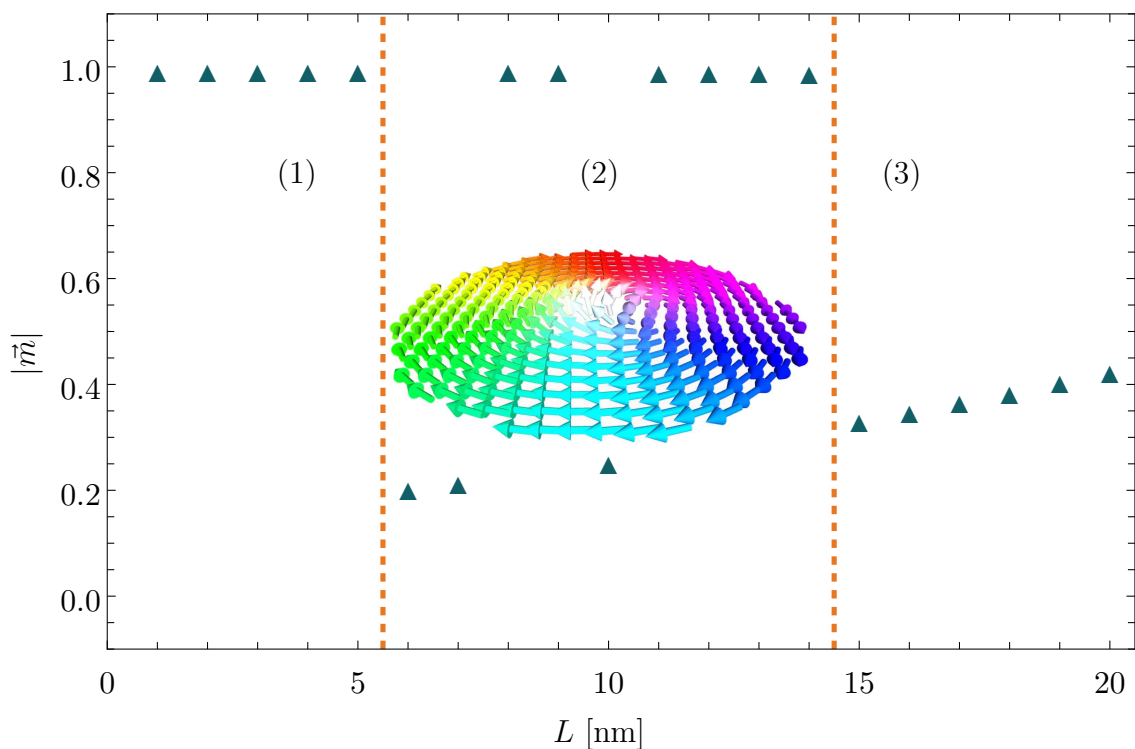


Figure 7.4: Normalised magnetisation versus thickness for single-crystalline Fe nano-disks, with a diameter of 28 nm. The sudden decrease in magnetisation indicates the formation of a vortex state. The plot can be separated into three regions: (1) in-plane, (2) unstable combination of vortex and ip states and (3) stable vortex states. The model shows a single layer of a typical vortex state, where the hue represents the ip direction and the brightness the oop component.

It can be seen, that $|\vec{m}|$ drops below 1.0 after a certain diameter which indicates the formation of a vortex state, as the ip component of the vortex averages to zero and only its core's oop component has an average value greater than zero. This also means that the gradual increase in $|\vec{m}|$ in the vortex structures with increasing disk diameter can be attributed to the changing size of their vortex core and its associated m_z component. Furthermore, this particular nano-disk's behaviour can be separated into three different regimes, wherein regime (1) the shape anisotropy dominates due to the small aspect ratio which forces the magnetisation to lie in-plane. In regime (3), larger disks with thicknesses over 15 nm form stable vortex states due to high demagnetisation fields. In regime (2), the nano-disks with thicknesses between 5 nm to 15 nm, seems to form unstable states where the magnetisation toggles between vortex and ip state. Here one has to note that these values are not absolute as the simulation starts from an initially randomised state and would need to be run several times to give a statistically significant average. This however would be computationally too demanding. Nevertheless, the simulations are representative of the overall magnetic behaviour of the modelled system. The inset in Figure 7.4 shows a single layer of such a vortex state in a nano-disk with $d = 28$ nm. The hue indicates the in-plane direction of magnetisation and the brightness indicates the magnetisation at right angles to the surface. This magnetic state is unfavourable for the application as a spin-polarised field emission source and should be avoided for the emitter fabrication.

To tailor the emitter dimensions and find the most suitable set of parameters for an ip magnetisation, a phase diagram is used as seen in Figure 7.5. Here, a good parameter to consider is the material-dependent exchange length

$$l_{\text{ex}} = \sqrt{\frac{2A_{\text{ex}}}{\mu_0 M_s}}, \quad (7.1)$$

which is a measure of the relative strength of exchange and magneto-static energy of a material [252]. The resulting m_z component of the simulated ground-state for single-crystalline and amorphous nano-disks as a function of their normalised dimensions d/l_{ex} and L/l_{ex} , with $l_{\text{ex}} = 3.4$ nm for iron, are plotted in Figure 7.5 a and Figure 7.5 b, respectively. Both phase diagrams show three regions, which can be roughly classified by their ratios as follows:

- (1) out-of-plane phase: $L/l_{\text{ex}} > d/l_{\text{ex}}$,
- (2) in-plane phase: $L/l_{\text{ex}} < d/l_{\text{ex}}$,
- (3) vortex phase: $L/l_{\text{ex}} < d/l_{\text{ex}}$ and $d \gg l_{\text{ex}}$.

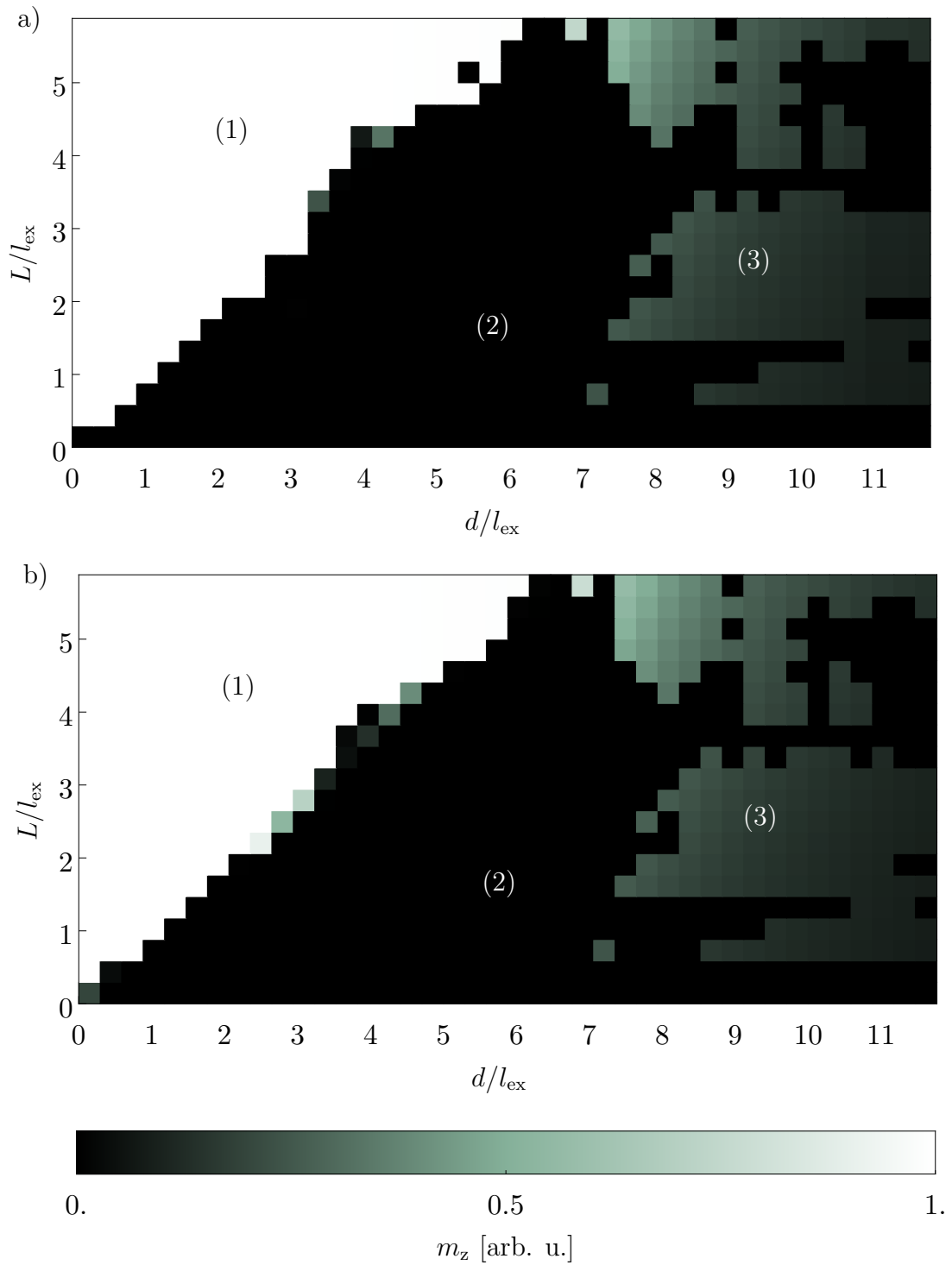


Figure 7.5: Phase diagram for a) single-crystalline and b) amorphous Fe simulation models as a function of their normalised dimensions d/l_{ex} and L/l_{ex} . The simulations can be separated into (1) out-of-plane states, (2) in-plane states and (3) vortex closure states. The colour indicates the magnitude of the magnetisation's oop component. Here, black (white) represents an ip (oop) magnetisation, while green indicates either a vortex state or spin canting.

It can be seen from both plots that iron-based nano-disks tend to form vortex states when their diameter is several times larger than the exchange length with the critical ratio being $d/l_{\text{ex}} \approx 7.35$. Simulations of spherical Fe particles found the critical ratio to be $r/l_{\text{ex}} \approx 4.242$ [94, 252]. However, structures with significant shape anisotropy, such as the disks described here, can remain in a state of uniform magnetisation for much larger dimensions [253].

Comparing Figure 7.5 a with Figure 7.5 b illustrates that there is little variation in the behaviour between single-crystalline and amorphous Fe nano-disks. To visualise any differences between the two simulations Figure 7.6 shows Δm_z which is the result of the subtraction between the two plots from one another. Here, the darker colours indicate a higher m_z component in the amorphous disk compared to the single-crystalline disk. The main difference between the simulations lies in the area $d/l_{\text{ex}} < 7$ where the uniform-magnetisation switches from ip to oop. The predominantly darker shade in Figure 7.6, meaning $\Delta m_z < 0$, indicates that single-crystalline disks change their magnetisation direction at slightly higher aspect ratios than amorphous

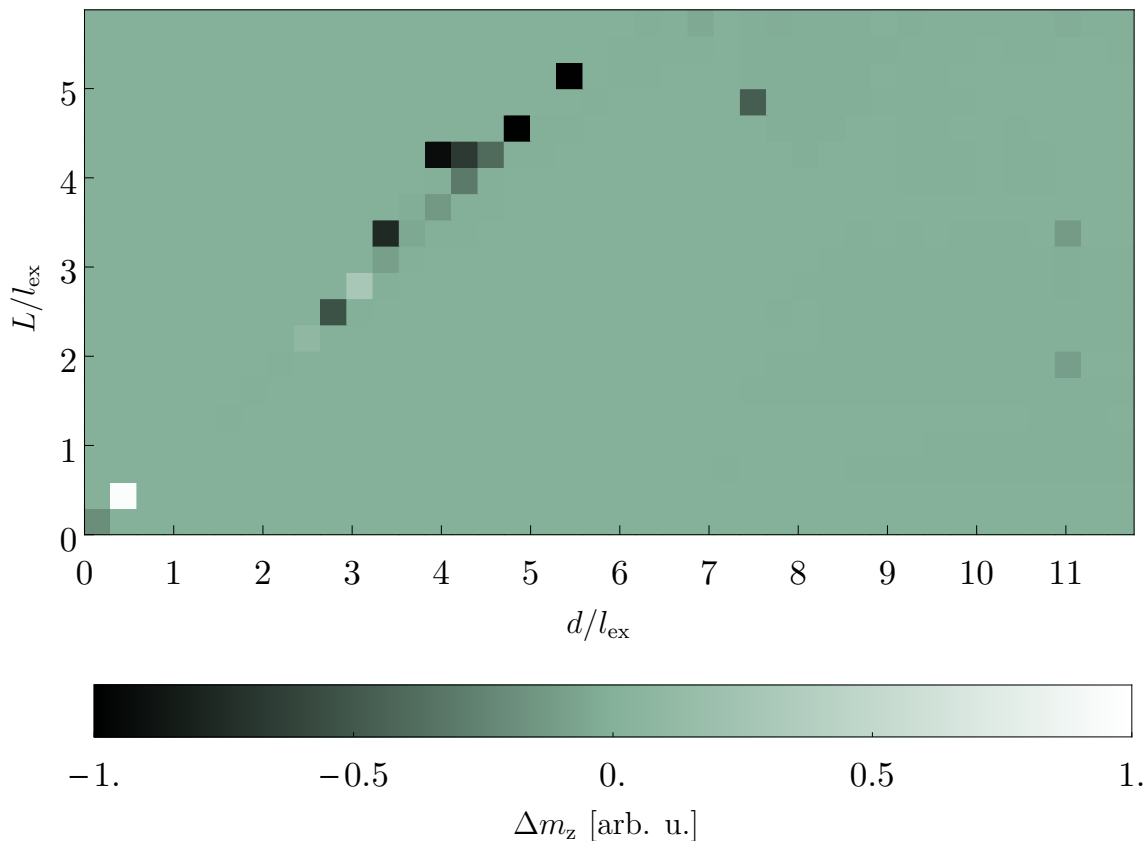


Figure 7.6: Difference in m_z components between the single-crystalline and amorphous Fe simulation models, showing that the creation of vortex states is independent of the crystallinity. Darker colours indicate $m_{z,\text{crystalline}} > m_{z,\text{amorphous}}$.

disks. This means that the MCA has a stabilising effect on the magnetisation against the shape-induced reorientation. Moreover, it is worth noting that the vortex regime ($d/l_{\text{ex}} > 7$) is very similar for both simulations, which indicates that the MCA has very little to no effect on the formation of magnetic flux closure states.

Magnetite nano-disks

Identical to the previously discussed simulations for iron, the magnetisation direction and domain-state of single-crystalline and amorphous Fe_3O_4 were investigated. Figure 7.7 shows the change in m_z component with increasing sample thickness for Fe_3O_4 nano-disks with $d = 9 \text{ nm}$. In the case of both, single-crystalline and amorphous nano-disks, the magnetisation's oop component exhibits an increase with increasing disk thickness, *i.e.* increasing aspect ratio. Compared to the behaviour of Fe (Figure 7.3), this increase happens gradually instead of abruptly, which indicates the creation of extensive spin canting at the surfaces for the magnetite models. This effect has been confirmed for Fe_3O_4 nanoparticles, which exhibit high spin canting at the particle surface [254] and is due to an interplay between magnetocrystalline

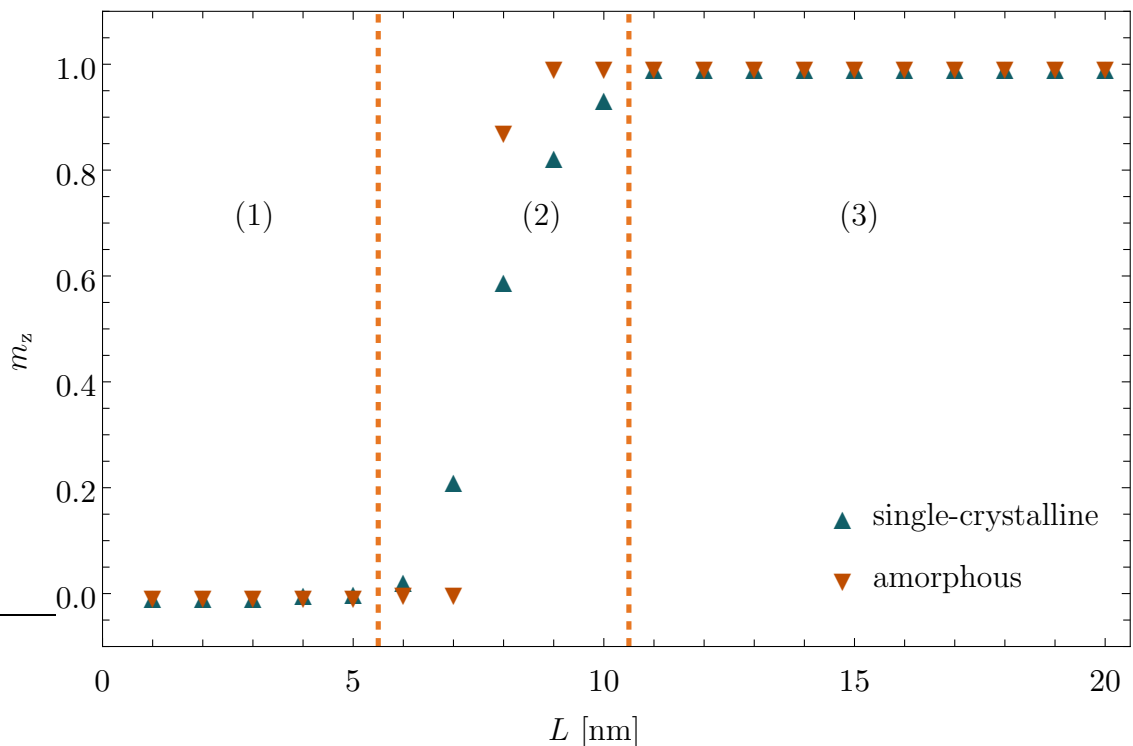


Figure 7.7: Oop-component of the magnetisation versus thickness of single-crystalline and amorphous magnetite models. All models had a diameter of 9 nm. The simulations can be separated into three states: (1) in-plane magnetisation, (2) states with extensive spin canting and (3) out-of-plane magnetisation.

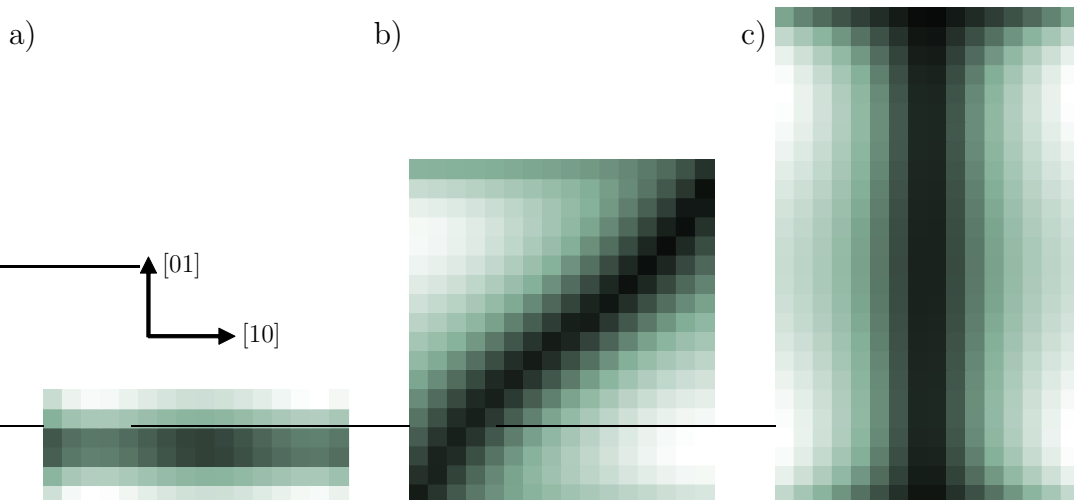


Figure 7.8: Plot of the curl of the magnetisation ($\nabla \times \vec{m}$) for three models with $d = 8$ nm and a) $L = 3$ nm, b) $L = 9$ nm and c) $L = 17$ nm. Here, the light (dark) colour indicates a high (low) spin canting.

anisotropy, dipolar, and exchange energy [255]. Thus, as can be seen from Figure 7.7, the simulated models can be separated into three different regimes in which the electron spins either lie ip (1), oop (3) or are canted (2). The reason why Fe_3O_4 shows spin canting and the previous simulations of Fe did not, lies in their difference in M_s or their respective shape anisotropy energy density, which scales with M_s^2 . This means that for the case of Fe one would have to change the model's dimensions in much smaller increments than the current 1 nm steps to see a similar spin canting effect. However, the current version of MuMax does not support smaller step sizes.

Examples of three spin configurations, corresponding to the three regions in Figure 7.7, are shown in Figure 7.8 a-c. These single-crystalline models have a diameter of $d = 8$ nm and their thicknesses are $L = 3$ nm, 9 nm and 13 nm, respectively. These figures show the normalised curl of the magnetisation ($\nabla \times \vec{m}$), which represents the magnitude of canting between adjacent cells, for a cut-plane along the xz -direction lying along the central axis of the model. Here, the bright (dark) colour represents a large (small) curl, while each pixel represents a 0.5 nm^3 cell of the model (simulated values were interpolated to reduce the cell size from MuMax's minimum cell size of 1 nm). The disk-like model in Figure 7.8 a exhibits only small spin canting along the top and bottom layer of the disk while otherwise having a uniform ip magnetisation. On the contrary, the cylinder-like model in Figure 7.8 c has a strong oop magnetisation with spin canting along its cylindrical side, while the top and bottom have a uniform magnetisation. The model in Figure 7.8 b falls within the regime of extensive spin canting (see Figure 7.7). It has an aspect ratio of about one and thus

can be approximated as an almost spherical particle. In this case, the magnetisation lies at about 45° to the surface normal. This behaviour is expected, as a spherical particle has no shape anisotropy and the direction of magnetisation is solely governed by the MCA of the material. For magnetite, the easy axis lies along the $\langle 111 \rangle$ directions or along the $\langle 11 \rangle$ directions for the two-dimensional figures shown here.

Such extensive spin canting, as illustrated in Figure 7.8 b and Figure 7.8 c will result in a reduced saturation magnetisation, which in turn will significantly reduce the practical efficiency of any spin-polarised field emission source. Hence, to achieve a uniform magnetisation it is imperative to not only identify magnetic vortex states or oop magnetisation, but also consider the spin canting at the surfaces. Therefore, to further investigate which sample dimensions result in a suitable SP-FESs phase diagrams were plotted. Figure 7.9 illustrates the changes of m_z with varying d and L for single-crystalline (Figure 7.9 a) and amorphous (Figure 7.9 b) magnetite, which shows two configurations: (1) oop and (2) ip.

Here, the first thing to note is the absence of any magnetic vortex states for either crystalline or amorphous Fe_3O_4 , compared to Fe (Figure 7.5). This can be attributed to magnetite's much higher exchange stiffness constant A_{ex} . Furthermore, as indicated by Figure 7.7 both plots exhibit extensive surface canting when going from a cylindrical to a more disk-like shape. This spin canting is predominantly happening when the model becomes almost cubic with $d \approx L$ ($\tau \approx 1$) and the model's preferred direction of magnetisation becomes rather undefined. This spin canting is also more prominent in the crystalline sample than in the amorphous one.

This shows that, for zero applied field and with no MCA, as is the case for the amorphous structures, the model's magnetic domain structure is controlled largely by the interplay between exchange and demagnetisation energies *i.e.* its shape anisotropy and thus the magnetisation transitions easier from one direction to the other. In the case of the crystalline sample, the shape anisotropy in addition to the MCA causes the model to have a higher potential barrier to overcome before changing its direction.

Based on these simulations for single-crystalline and amorphous Fe and Fe_3O_4 the model dimensions most suitable for the fabrication of viable SP-FES, which exhibit an in-plane single-domain state, have dimensions less than 23 nm ($d/l_{\text{ex}} = 6.5$) and $\tau = (L/d) < 1$. Thus, the following simulations will concentrate on models within this parameter range.

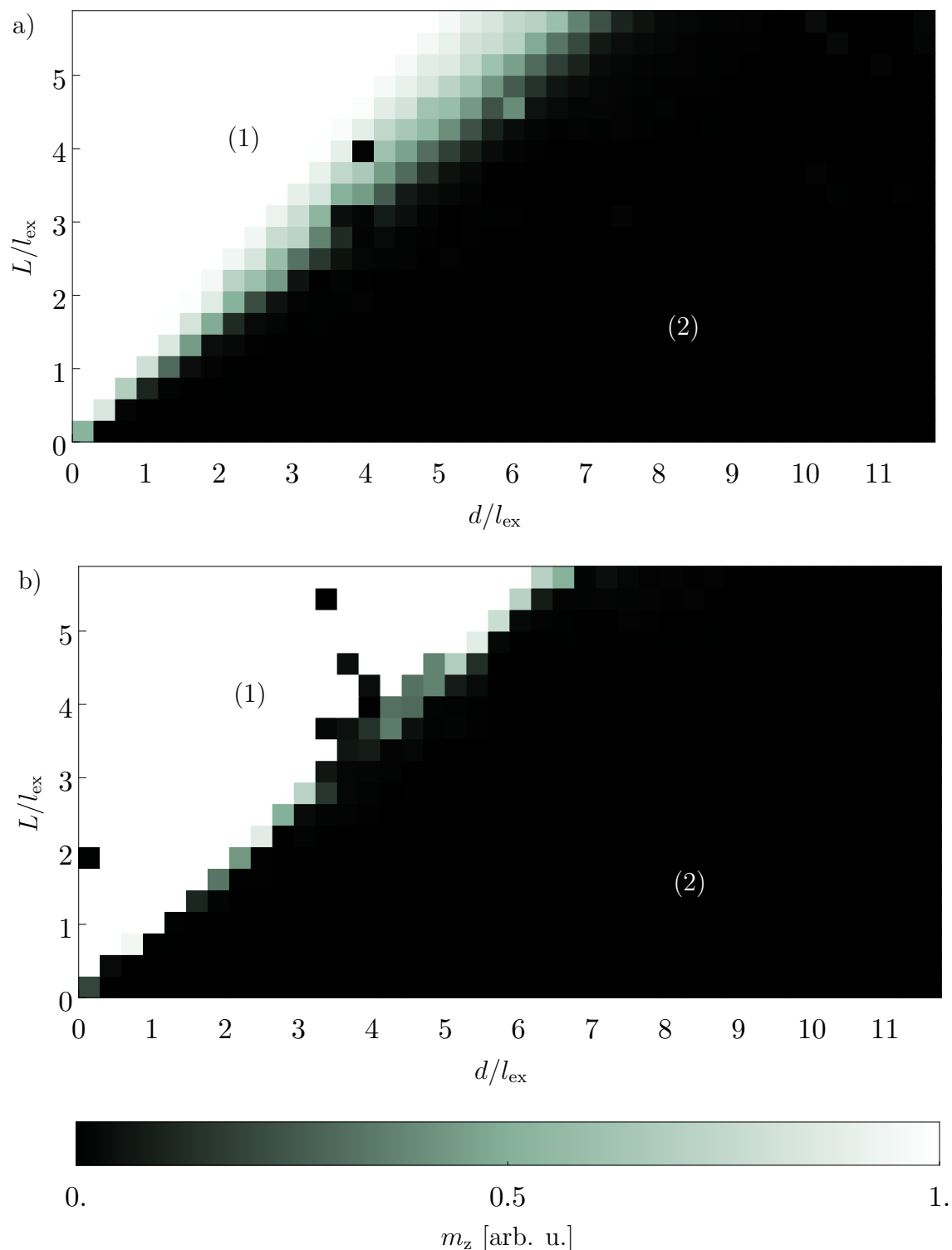


Figure 7.9: Phase diagram for a) single-crystalline and b) amorphous Fe_3O_4 simulation models as a function of their normalised dimensions d/l_{ex} and L/l_{ex} . The simulations can be separated into (1) out-of-plane states and (2) in-plane states. Compared to Fe there are no vortex closure states, but extensive spin canting when transitioning from ip to oop along the line at which $\tau = (L/d) \approx 1$.

7.2.3 Thermal stability and demagnetisation tensor

Another design point to consider when fabricating SP-FESs based on magnetic nano-structures is their magnetisation stability against thermal fluctuations. As mentioned in Section 2.3.2, nano-disks below a certain critical size can become superparamagnetic, which renders them useless for the applications as spin-polarised emitters as their magnetisation can randomly flip direction. Thus, the next step is to investigate the thermal stability of the nano-sized Fe and Fe₃O₄ nano-disks, which were previously found to have a single-domain state with \vec{M} lying in-plane.

Even though material parameters, such as the MCA, influence the threshold temperature at which the magnetisation direction becomes unstable, the main contribution for the nano-structures discussed here is determined by their shape. Therefore, the following numerical calculations of the demagnetisation energy E_D were done using

$$E_D = \frac{\mu_0}{2} M_S^2 N_z, \quad (7.2)$$

with the demagnetisation tensor, N_z , of an equivalent ellipsoid for a cylinder given by Ref. [256]

$$N_z = \frac{1}{1 - \tau_e^2} \left(1 - \frac{\tau_e \arccos(\tau_e)}{\sqrt{1 - \tau_e^2}} \right), \quad (7.3)$$

with

$$\tau_e = \frac{\pi}{8} \left(1 - \sqrt{1 + \frac{32\tau}{\pi^3} \left(1 + \log \frac{\tau^2}{16} \right)} \right). \quad (7.4)$$

Figure 7.10 a shows a polar plot of the magnitude of the demagnetisation energy for three different calculations, in which d is kept at 10 nm and L is set to be 9 nm, 5 nm and 1 nm, as shown in Figure 7.10 b - c, respectively. Here one can see, that if $d \sim L$ (blue plot) the structure has no real preferred direction as the shape is almost spherical. With increasing aspect ratio, the ip magnetisation becomes magnetically more favourable (orange plot with $d = 2L$) until it reaches its most stable state (here: green plot with $L = d/10$).

To function as a stable SP-FES, the energy barrier, which is defined as the energy difference between the two directions at which $\theta = 0$ and $\theta = \pi/2$, has to be higher than the thermal energy. Thus, a plot of the energy barrier over the cylinder diameter, ranging from 2 nm to 22 nm and in which $\tau < 1$, is shown in Figure 7.11 a and Figure 7.11 b for Fe and Fe₃O₄, respectively. The corresponding temperature is plotted on the right y -axis. Both plots demonstrate that the energy barrier increases exponentially with decreasing aspect ratio τ . The dotted orange line indicates the threshold at which the energy barrier is high enough for the magnetisation to have

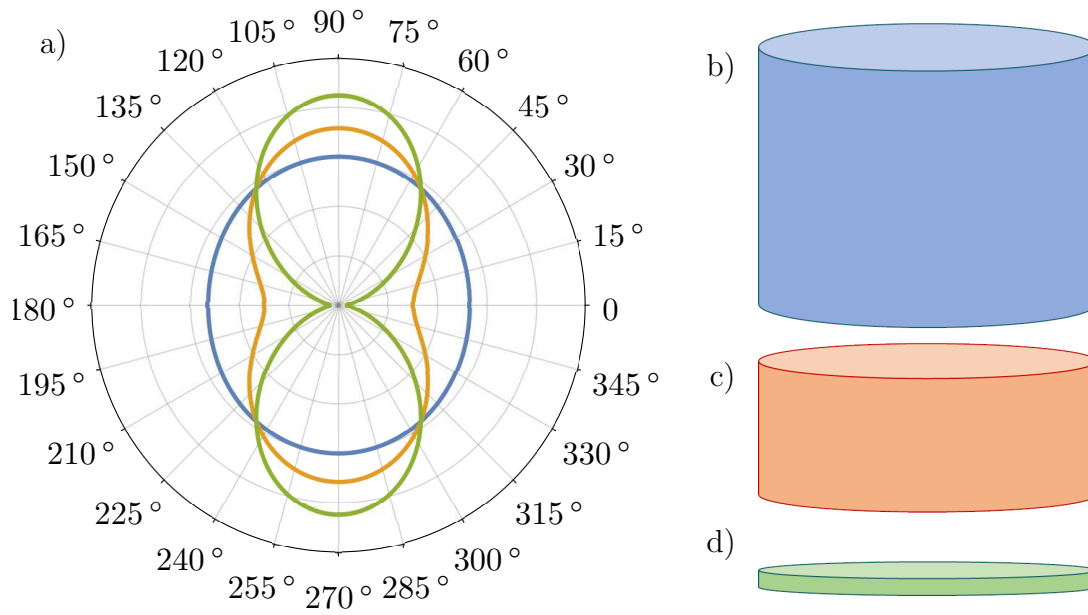


Figure 7.10: a) Polar diagram of the magnitude of the demagnetisation energy for three different circular nano disks with b) $d = 10$ nm, $L = 9$ nm, c) $d = 10$ nm, $L = 5$ nm and d) $d = 10$ nm, $L = 1$ nm.

a stable orientation at room temperature (~ 300 K). This would be the theoretical working condition for perfect field emitters without any heating. However, it was found both experimentally and theoretically that, depending on the current density, material, and dimensions of the nano-sized emitter extensive Joule heating can occur [257–259]. Thus, the red dotted line corresponds to a temperature of 1273 K, which is the melting point of Au and thus the highest operational temperature for the emitters described in Section 7.1. Experiments and simulations of nano-sized Cu wires and CNTs prove that depending on the previously mentioned parameters such high temperatures are realistically achievable during field emission.

The insets in both figures show an enlarged view of the temperature range up to 2000 K. Here, one can see that in the case of iron (Figure 7.11 a) only a disk with $d = 2$ nm and $L = 1$ nm would exhibit superparamagnetic behaviour at room temperature, while an elevated temperature of 1000°C would render all emitters with a diameter smaller than 4 nm unusable. In the case of magnetite, all cylinders with diameters below 7 nm exhibit superparamagnetic behaviour at room temperature or below 10 nm at 1000°C . Even structures with larger diameters experience an unstable magnetisation direction if the aspect ratio is too small. This is in good agreement with experimental values found for Fe_3O_4 nanoparticles, which are superparamagnetic for radii smaller than 10 nm [260]. This shows that magnetic nano-cylinders and nano-disks made from Fe are more stable against thermal fluctuations of \vec{M}

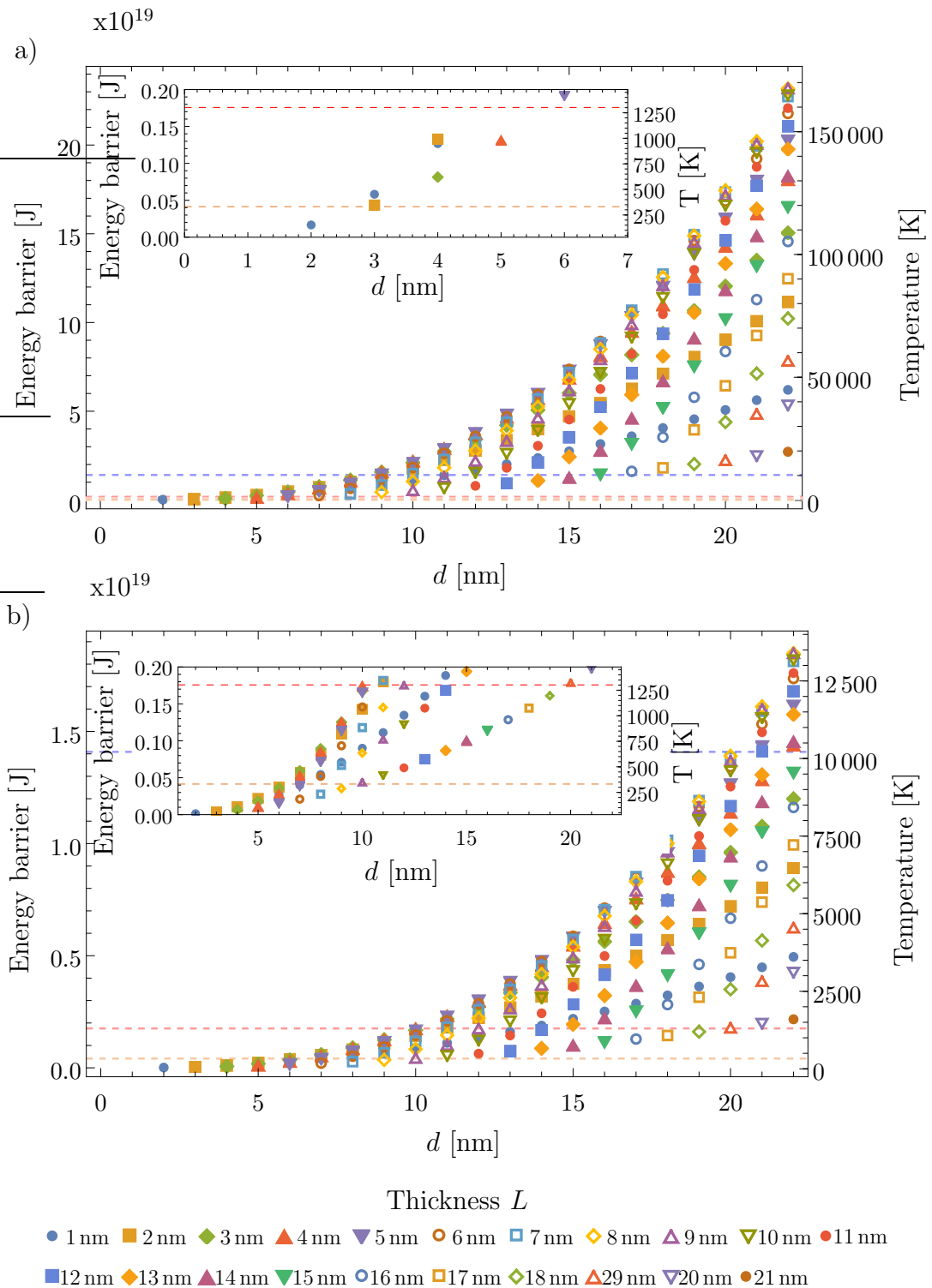


Figure 7.11: Dimensional-dependency of the threshold temperature for the onset of superparamagnetism in a) Fe and b) Fe_3O_4 nano-disks. The orange (red) dashed line indicates the 300 K (1273 K) threshold dimensions below which the magnetisation starts to fluctuate. The blue line represents the Néel relaxation time above which a structure has a stable magnetisation for one week.

compared to their Fe_3O_4 counterparts. This is expected as iron's saturation magnetisation is much larger than Fe_3O_4 's and hence it has a higher energy barrier.

Another parameter to investigate, when considering the feasibility of a SP-FES, is the Néel relaxation time, τ_N , which describes the average time for the magnetisation to flip between two orientations. The correlation between energy barrier and relaxation time is given by the Néel-Arrhenius equation

$$\tau_N = \tau_0 \exp\left(\frac{K_u V}{k_B T}\right), \quad (7.5)$$

with τ_0 being the ‘‘attempt time’’ taken to be 10^{-9} s and $K_u V$ being the energy barrier (V : volume; K_u : anisotropy energy) [261].

For spin-polarised field emission, the emitter should have a stable magnetisation direction for at least one week. Under the assumption of operating at room temperature without Joule heating, the energy barrier would need to be higher than 1.5×10^{-19} J to be stable for about seven days. This dependency is indicated by the blue lines in Figure 7.11 a and 7.11 b. Using this criterion, it can be seen that for Fe all combination of d and L with diameters larger than 17 nm and smaller diameters between 10 nm to 16 nm with low aspect ratios τ (disk-like structures), are stable against magnetisation flipping for more than seven days. In the case of Fe_3O_4 only larger diameters ($d < 20$ nm) with low τ have a sufficiently long Néel relaxation time to be viable spin-polarised field emission sources.

7.2.4 Current stability

One other potential problem of small systems with a weak magnetisation stability is a current-induced reduction in saturation magnetisation. The idea is that the electrons in the non-magnetic part of the emitter, such as the GaAs in Figure 7.1 and Figure 7.2, are unpolarised and thus have a random spin orientation. Upon applying an external field, these electrons will migrate into the FM layer, inside which they will collide with other electrons and scatter. Hence these unpolarised electrons will transfer their randomised torque which consequently might destroy or diminish the FM layer's magnetisation and subsequently its polarisation efficiency.

To test the influence of this effect, MuMax simulations were conducted in which a current of 1 mA is applied to a single-crystalline Fe model of $L = 3$ nm and $d = 9$ nm for 20 ns, with a current density of 10^{13} A/m². These simulations showed, that the effect of the unpolarised current interacting with the spin-polarised electrons of the ferromagnetic layer results in a maximum change of 0.7% and an average change of 0.003% between the spin orientations with and without an applied current, which is

negligibly small.

7.3 Conclusion

This chapter introduced a potential concept for point-like spin-polarised field emission sources and investigated several design aspects using micromagnetic simulations.

The SP-FES design is based on using a magnetic thin film deposited on micropillars which will subsequently be milled down to have a radius of only a few nanometres using focused-ion milling. A preliminary test of this ion milling process using a Zeiss X-beam FIB/SEM is shown in Figure 7.12 a). The figure shows a milled AFM tip, whose apex diameter was reduced to less than 50 nm and which now has a high aspect ratio. Figure 7.12 b) displays a matrix of fabricated nanopillars with sizes varying from 1 μm to 10 μm and a length of 10 μm , which should further be used to deposit the ferromagnetic layer on top and subsequent ion milling. The pillars were etched out of a GaAs substrate via reactive ion etching and were gold-coated afterwards.

The subsequently grown ferromagnetic thin film should act as a spin-polarising layer for the emitted electrons. To maximise its spin-polarising ability it should be in a single-domain state with ip magnetisation. Thus, to identify the most suitable parameters for this magnetic layer, MuMax simulations of cylindrical Fe and Fe₃O₄ models were conducted. The crystallinity, diameter and thickness of these models were varied and their magnetisation was investigated. The results for both single-

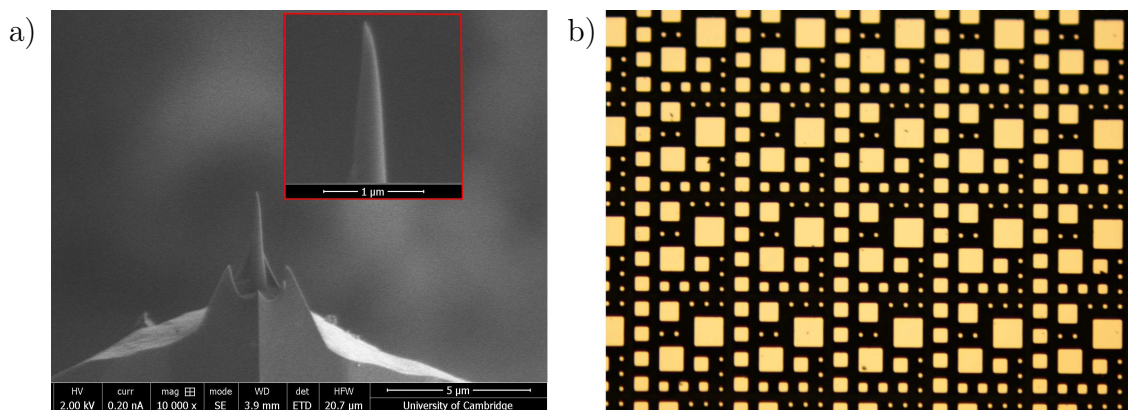


Figure 7.12: a) SEM image of an ion milled AFM tip, which now has a high aspect ratio and an apex diameter of less than 50 nm. b) Image of gold coated GaAs micropillars fabricated via reactive ion etching, seen from the top. The pillars sides range from 1 μm to 10 μm .

crystalline and amorphous Fe showed the existence of three phases in which the magnetisation was oriented in-plane ($L/l_{\text{ex}} < d/l_{\text{ex}}$), out-of-plane ($L/l_{\text{ex}} > d/l_{\text{ex}}$) and in a magnetic vortex structure for diameters much larger than the exchange length ($L/l_{\text{ex}} < d/l_{\text{ex}}$ and $d \gg l_{\text{ex}}$). Of these states, only the first would be feasible for further investigation. The same simulations for amorphous and single-crystalline Fe_3O_4 gave similar results with regards to its in-plane ($L/l_{\text{ex}} < d/l_{\text{ex}}$) and out-of-plane ($L/l_{\text{ex}} > d/l_{\text{ex}}$) states but did not exhibit magnetic vortices due to the materials much higher exchange stiffness constant compared to Fe. However, models with $L/l_{\text{ex}} \approx d/l_{\text{ex}}$ showed a high spin canting, which is disadvantageous for a high spin-polarisation.

Another design aspect was the emitter's magnetisation stability against temperature, current and over a prolonged period of time. Thus, calculations of the anisotropy-related energy barrier were presented to find the dimension's critical limits for superparamagnetism. It was shown that Fe, with its higher saturation magnetisation, exhibits stable ferromagnetism for smaller dimensions than Fe_3O_4 , which was only stable for models with diameters larger than 10 nm. Furthermore, to operate as a viable SP-FES the ferromagnetic layer should exhibit a stable magnetisation direction for at least one week. Calculations of the Neél relaxation time for Fe showed that most models with diameters larger than 10 nm are stable, especially if their aspect ratio is small. In the case of Fe_3O_4 only large nano-disks ($d > 20$ nm) with very low aspect ratios ($\tau \ll 1$) would have a relaxation time of more than seven days. Lastly, the influence of applying an unpolarised electric current on the models' magnetisation was found to be negligible (0.003%) for both materials.

In conclusion, these simulations have shown that Fe would be the most suitable material choice for such spin-polarised field emission sources as described in Section 7.1. Its lower exchange stiffness constant and higher saturation magnetisation lead to lower surface canting and a stable in-plane magnetisation at elevated temperatures and over a prolonged period of time even for models with small diameters. Consequently, the best parameters to fabricate reliable spin-polarised field emission sources is to use Fe nano-disks with diameters between 10 nm to 22 nm and low aspect ratios of $\tau \ll 1$.

8 | Summary and further work

In this chapter, the conclusions from the presented work and the main experimental and theoretical results are summarised. Also, some suggestions for the next steps and future experiments are given.

8.1 Summary

The presented work has been devoted to investigating several aspects to produce spin-polarised field emission from point-like nano-emitters. To achieve this result several tasks have been accomplished.

One objective of this work was to develop a novel simulation method to study electron field emission from different nano-sized structures. This computational technique should be capable of taking into account both the atomic- and macroscopic dimensions of an emitter. Thus, this dissertation has presented in Section 3.1 the computational development of such a multi-scale simulation method that allowed such demanding calculations to be performed. This technique is based on the combination of finite element based classical calculation of the electrical field distribution of the macroscopic model with density functional theory simulations, which account for the atomic structure of the system. For this purpose, the DFT program ONETEP was extended to allow the implementation of boundary condition matching between the two models. To obtain optimised results rigorous tests of several simulation parameters, such as energy cut-off and NGWF radii were performed. Once the method had been verified, the optimised parameters were used to study two different emission models, which are presented in Chapter 4.

The systems studied were a capped (5,5) CNT and a four-sided tungsten-pyramid, as both materials have been identified as having great field emission properties and having extensive industrial applications. For both structures material properties such as charge distribution, molecular orbitals, local density of states and the potential barrier shape with and without an applied field, have been examined. Moreover, a precise definition for the metallic surface was found, based on the distribution of

the conducting electrons around the atomic structure at the Fermi equipotential. Based on these simulations, connections between simulated properties and experimentally found effects such as emission patterns could be made. These results showed the multi-scale atomistic-continuum model to be an accurate and efficient computational tool, which can be used to explore how certain material properties affect the field emission performance.

Chapter 5 introduces and discusses the results obtained from three different ferromagnetic thin-film samples using a SPLEEM setup. These samples were 8 ML-Fe/Ag(001), 5 ML-Fe/W(110) and 1 MLAg/5 ML-Fe/W(110). They were first analysed in regard to their growth quality and magnetisation direction. By monitoring the intensity oscillations during sample growth, it was further possible to determine their onset thickness of ip magnetisation. In the case of Fe/Ag(001) ferromagnetism occurs after about 4 ML and the samples had an easy axis along the [100] direction, while for Fe/W(110) the magnetic contrast started to appear after 1.5 ML and the magnetisation was oriented along the $[1\bar{1}0]$ direction. Following this initial analysis energy loss scans were conducted by adjusting the bias of the MCP accordingly as to allow the study of the low energy electron regions. For all samples, three scans at $E_0 = 10$ eV, 15 eV and 20 eV were presented and their different features were discussed. Moreover, these scans were used to determine the energy-dependent SE peak position for the subsequent energy-selective secondary electron yield measurements. This novel technique is capable of scanning the energy- and spin-dependent electron yield for electrons of a certain energy over a large range of primary beam energies in a very fast time frame. This has the advantage of keeping the material clean and free from oxidation during the measurement. Utilising this spectroscopy technique, a material-independent decrease in electron yield and scattering asymmetry was found for increasing primary energies. This decrease in SE yield is unexpected and is in contrast to the theoretically and experimentally determined SE yield found for $E_0 > 100$ eV. These initial experiments indicated the new experimental technique's capabilities which might aid in the investigations of new phenomena.

Furthermore, energy-dependent reflectivity scans in conjunction with DFT simulations allowed to investigate the samples' unoccupied density of states above the Fermi level. These energy-dependent spin-asymmetry spectra also allowed to determine at which electron beam energy a maximum magnetic contrast would occur for the different samples. Analysing the threshold energy in the spectra also gave information about the material work function.

To analyse and quantify a field emitter's spin-polarisation, a multi-purpose UHV chamber with an attached Mott polarimeter was remodelled and improved. This pro-

cess was detailed in Chapter 6. The finished setup has shown to be capable of, *inter alia*, achieving a base pressure in the low 10^{-10} mbar, of conducting LEED and AES measurement and of sputter-annealing the sample. Furthermore, a versatile sample holder for field emission experiment was introduced and several design aspects, such as anode-cathode distance, varying applied electric field and aperture shapes have been investigated using COMSOL simulations. It was found that a “top-hat” shaped anode with a chamfered aperture at a distance of 1.5 cm from the emitting tip yields the best results. The numerical simulations of this design indicate an emittance in the range of 95% for voltages higher than 5 kV. Using an additional suppressor electrode increases the emitted electron count to about 100%. Moreover, the sample holder design was based on the implementation of standardised AFM tips, onto which the nano-sized emitters can be mounted, to allow for easy sample exchange and reproducible positioning within the assembly. The optimised sample holder assembly was fabricated and should be capable to yield field emitted electrons from a variety of nano-sized emitters, whose polarisation can be analysed using the Mott polarimeter.

Chapter 7 introduces two possible fabrication approaches for potential spin-polarised field emission sources. These emitters are based on spin-polarised emission from ultra-thin Fe and Fe₃O₄ nano-disks grown on conducting nano-pillars. For the purpose of this work, these disks should be in a single-domain state to maximise spin-polarised emission and to have an in-plane magnetisation. Hence, investigations into size-related effects on magnetic properties using micromagnetic simulations have been presented and discussed. In particular, the influence of the model’s dimensions and crystallinity on its magnetic anisotropy was shown for both materials and the structures’ superparamagnetic limits were calculated. It was found that emission tips based on Fe nano-disks with diameters larger than 9 nm and thicknesses between 10 nm to 20 nm are suitable candidates to be used as liable SP-FESs. Thus, these calculations allowed for the tailoring of the emitter’s magnetic behaviour regarding its thermal-stability and high spin-polarisation to achieve optimum working conditions.

8.2 Further work

Research continuing this work can be divided into two areas regarding the computational and experimental results in this dissertation.

To reduce the computational cost of simulating models with large numbers of atoms, a molecular mechanics program was employed to optimise the atomic posi-

tions prior to the DFT simulation. This approach could be explored in more detail by conducting further DFT geometry optimisations with pre-optimised fixed atomic positions. Combining the MM and DFT could aid to relax large structures in a more reasonable time. However, even more important when considering field emission is the continued development of the atomistic-continuum simulation method itself. As the simulations are currently limited to equilibrium states they are only capable of simulating the potential inside the material. However, to simulate field emission, one needs to go further as the tunnelling of electrons happens to be in the tunnelling region outside the surface. Hence, the next step in the investigation of field emission from multi-scale emitters would be to progress beyond the static calculations and to implement a dynamic time-dependent description of FE. This approach of using time-dependent DFT has been done using plane-wave programs such as VASP and for small structures in external, homogeneous fields [33, 262, 263]. However, these simulations do not take the macroscopic model into account and are limited to small models. Thus the next step would be to implement the multi-scale boundary-condition matching method into a time-dependent linear-scaling DFT method.

This work reported on the first test measurements carried out with the newly developed ESSEY mode for the SPLEEM. These initial measurements showed novel effects and features in magnetic materials which should be investigated further. For this purpose, the spin-polarisation of the emitted electrons should be measured using a Mott polarimeter. This would give insights into the scattering processes and the number of spin-flip events, which in turn might help to determine the ratio of true secondary electrons to inelastically scattered primary electrons. Furthermore, as some of the results found here were unexpected and some questions had to be left open further tests and measurement using the ESSEY mode should be conducted for higher primary energies and for other crystallographic directions. With regards to the energy-dependent reflectivity scans, it would be beneficial to conduct more precise DFT simulations taking the complete sample composition, thickness, and vacuum surface into account. This would give a more exact band structure and would take surface and interface effects into consideration. Furthermore, to analyse the work function and the energies of band onsets the primary beam energy should be varied in smaller increments to give more precise values. It would also be beneficial to conduct thickness-dependent measurements of several non-magnetic over-layers on a magnetic film to determine the thickness-dependent spin-damping.

A direct continuation of the experimental part of this thesis done in Cambridge would be the actual fabrication and subsequent experimental analysis of the spin-polarised field emission sources proposed in Chapter 7. Emitters based on this

approach should be able to produce spin-polarised currents and are inert to oxidation. Due to their size, they have the advantage of an increased magnitude of the local electric field at the tip apex, which results in the enhancement of the emission current compared to tips with larger radii under the same external field. In addition, the low density of states at the tip should make emitted electrons highly coherent and mono-energetic so that they might be used as an efficient low-energy electron point source. Another approach to producing spin-polarised emission currents is based on the use of CNTs which either have Fe adsorbates or which have Fe nano-particles encapsulated inside [235, 263, 264]. These two approaches could also be investigated prior to their fabrication using the multi-scale atomistic-continuum model developed during this thesis. The experimental analysis of such tips could be done by using the newly designed specialised sample holder and the Mott detector.

List of Acronyms

AE	Auger electron
AES	Auger electron spectroscopy
AFM	atomic-force-microscopy
BC	boundary conditions
bcc	body-centred cubic
BO	Born-Oppenheimer approximation
BSE	backscattered electron
CNT	carbon nanotube
CVD	chemical vapour deposition
DFT	density functional theory
DoS	density of states
EDFT	ensemble density functional theory
EELS	electron energy loss spectroscopy
ESSEY	energy-selective secondary electron yield
fcc	face-centred cubic
FE	field emission
FEM	finite element method
FES	field emission source
FIB	focused ion beam
FM	ferromagnet
FN	Fowler-Nordheim
FoV	field of view
FWHM	full width at half maximum
GGA	generalized gradient approximation
HOMO	highest occupied molecular orbital
IMFP	inelastic mean free path
IP	ion pump
ip	in-plane

KS	Kohn-Sham
LDA	local density approximation
LDoS	local density of states
LEED	low-energy electron diffraction
LEEM	low-energy electron microscopy
LUMO	lowest unoccupied molecular orbital
MBE	molecular beam epitaxy
MCA	magnetocrystalline anisotropy
MCP	multichannel-plate
ML	monolayer
MM	molecular mechanics
MOKE	magneto-optical Kerr effect
NGWF	non-orthogonal generalised Wannier function
NIMS	National Institute of Material Science
NoM	noble metal
ONETEP	Order-N Electronic Total Energy Package
oop	out-of-plane
PAW	projector augmented wave method
PBE	Perdew, Burke and Ernzerhof
PE	primary electron
RoI	region of interest
SE	secondary electron
SEM	scanning electron microscopy
SOC	spin-orbit coupling
SP	spin-polarised
SP-FES	spin-polarised field emission source
SPEEL	spin-polarised electron energy loss
SPEELS	spin-polarised electron energy loss spectroscopy
SPLEEM	spin-polarised low-energy electron microscopy
TMP	turbomolecular pump
UHV	ultra-high vacuum
XC	exchange and correlation

Bibliography

- [1] C. Kleint, *Prog. Surf. Sci.* **42**(1), 101 (1993).
- [2] D. T. Pierce, *Phys. Scr.* **38**(2), 291 (1988).
- [3] B. Inkson, in *Materials Characterization Using Nondestructive Evaluation (NDE) Methods* (Woodhead Publishing, 2016), pp. 17 – 43, ISBN 978-0-08-100040-3.
- [4] G. X. Guo, K. Tokunaga, E. Yin, F. C. Tsai, A. D. Brodie, and N. W. Parker, *J. Vac. Sci. Technol. B* **19**(3), 862 (2001).
- [5] L. R. Baylor, W. L. Gardner, X. Yang, R. J. Kasica, M. A. Guillorn, B. Blalock, H. Cui, D. K. Hensley, S. Islam, D. H. Lowndes, A. V. Melechko, V. I. Merkulov, *et al.*, *J. Vac. Sci. Technol. B* **22**(6), 3021 (2004).
- [6] S. H. Hsu, W. P. Kang, S. Raina, and M. Howell, in *28th International Vacuum Nanoelectronics Conference (IVNC)* (2015), pp. 184–185.
- [7] K. Subramanian, W. P. Kang, and J. L. Davidson, *Appl. Phys. Lett.* **93**(20), 203511 (2008).
- [8] Q. H. Wang, A. A. Setlur, J. M. Lauerhaas, J. Y. Dai, E. W. Seelig, and R. P. H. Chang, *Appl. Phys. Lett.* **72**(22), 2912 (1998).
- [9] A. A. Kuznetsov, S. B. Lee, M. Zhang, R. H. Baughman, and A. A. Zakhidov, *Carbon* **48**(1), 41 (2010).
- [10] M. T. Cole, M. Nakamoto, and W. I. Milne, in *Handbook of Digital Imaging* (American Cancer Society, 2015), pp. 1–28, ISBN 9781118798706.
- [11] A. J. Melmed, *J. Vac. Sci. Technol. B* **9**(2), 601 (1991).
- [12] T. L. Van Well, M. Redshaw, N. D. Gamage, and R. E. B. Kandegedara, *J. Vis. Exp.* **113**, 54030 (2016).

- [13] H. Lemke, T. Göddenhenrich, H. P. Bochem, U. Hartmann, and C. Heiden, *Rev. Sci. Instrum.* **61**(10), 2538 (1990).
- [14] A. V. Crewe, D. N. Eggenberger, J. Wall, and L. M. Welter, *Rev. Sci. Instrum.* **39**(4), 576 (1968).
- [15] H. Todokoro, N. Saitou, and S. Yamamoto, *Jpn. J. Appl. Phys.* **21**(10), 1513 (1982).
- [16] I.-S. Hwang, H.-S. Kuo, C.-C. Chang, and T. T. Tsong, *ECS Trans.* **25**(10), 3 (2019).
- [17] F. Houdellier, L. de Knoop, C. Gatel, A. Masseboeuf, S. Mamishin, Y. Taniguchi, M. Delmas, M. Monthieux, M. Hýtch, and E. Snoeck, *Ultramicroscopy* **151**, 107 (2015).
- [18] A. E. Vladár, Z. Radi, M. T. Postek, and D. C. Joy, *Scanning Microsc.* **28**(3), 133 (2006).
- [19] H.-W. Fink, *Phys. Scr.* **38**(2), 260 (1988).
- [20] A. Kyritsakis, G. C. Kokkorakis, J. P. Xanthakis, T. L. Kirk, and D. Pescia, *Appl. Phys. Lett.* **97**(2), 023104 (2010).
- [21] K. P. Liao, Y. Hu, T.-L. Lin, and Y.-C. Lan, *J. Vac. Sci. Technol. B* **25**(2), 484 (2007).
- [22] H. Zhang, J. Tang, J. Yuan, Y. Yamauchi, T. T. Suzuki, N. Shinya, K. Nakajima, and L.-C. Qin, *Nat. Nanotechnol.* **11**(3), 273 (2016).
- [23] H. Zhang, J. Tang, J. Yuan, and L.-C. Qin, *MRS Bulletin* **42**(7), 511–517 (2017).
- [24] N. Xu and S. E. Huq, *Mater. Sci. Eng. R Rep* **48**(2), 47 (2005).
- [25] V. N. Tondare, C. Balasubramanian, S. V. Shende, D. S. Joag, V. P. Godbole, S. V. Bhoraskar, and M. Bhadbhade, *Appl. Phys. Lett.* **80**(25), 4813 (2002).
- [26] D. Joag, D. Late, and U. Lanke, *Solid State Commun.* **130**(5), 305 (2004).
- [27] Q. H. Li, Q. Wan, Y. J. Chen, T. H. Wang, H. B. Jia, and D. P. Yu, *Appl. Phys. Lett.* **85**(4), 636 (2004).
- [28] P. Cutler, J. He, J. Miller, N. Miskovsky, B. Weiss, and T. Sullivan, *Prog. Surf. Sci.* **42**(1), 169 (1993).

- [29] G. N. Furse and D. V. Glazanov, *J. Vac. Sci. Technol. B* **16**(2), 910 (1998).
- [30] R. G. Forbes, *J. Appl. Phys.* **103**(11), 114911 (2008).
- [31] A. Kyritsakis and J. P. Xanthakis, *Proc. Math. Phys. Eng.* **471**(2174), 20140811 (2015).
- [32] Y. Sun, D. H. Shin, K. N. Yun, Y. M. Hwang, Y. Song, G. Leti, S.-G. Jeon, J.-I. Kim, Y. Saito, and C. J. Lee, *AIP Advances* **4**(7), 077110 (2014).
- [33] S. Han, M. H. Lee, and J. Ihm, *Phys. Rev. B* **65**, 085405 (2002).
- [34] B. Lepetit, *J. Appl. Phys.* **122**(21), 215105 (2017).
- [35] N. Egorov and E. Sheshin, in *Field Emission Electronics* (Springer International Publishing, Cham, 2017), pp. 295–367, ISBN 978-3-319-56561-3.
- [36] F. Giubileo, A. Di Bartolomeo, L. Iemmo, G. Luongo, and F. Urban, *Appl. Sci.* **8**(4), 526 (2018).
- [37] X. Wang, Q. Li, J. Xie, Z. Jin, J. Wang, Y. Li, K. Jiang, and S. Fan, *Nano Lett.* **9**(9), 3137 (2009).
- [38] N. Gupta, S. M. Gupta, and S. Sharma, *Carbon Lett.* pp. 1–29 (2019).
- [39] J.-M. Bonard, J.-P. Salvetat, T. Stöckli, L. Forro, and A. Chatelain, *Appl. Phys. A* **69**(3), 245 (1999).
- [40] N. De Jonge and J.-M. Bonard, *Philos. Trans. A Math. Phys. Eng. Sci.* **362**(1823), 2239 (2004).
- [41] S. Iacobucci, M. Fratini, A. Rizzo, F. Scarinci, Y. Zhang, M. Mann, C. Li, W. I. Milne, M. M. El Gomati, S. Lagomarsino, and G. Stefani, *Appl. Phys. Lett.* **100**(5), 053116 (2012).
- [42] V. Chouhan, T. Noguchi, and S. Kato, *J. Appl. Phys.* **119**(13), 134303 (2016).
- [43] T. Scheunemann, R. Feder, J. Henk, E. Bauer, T. Duden, H. Pinkvos, H. Poppa, and K. Wurm, *Solid State Commun.* **104**(12), 787 (1997).
- [44] M. S. Altman, *J. Condens. Matter Phys.* **22**(8), 084017 (2010).
- [45] Y. Wu, A. K. Schmid, M. S. Altman, X. Jin, and Z. Qiu, *PRL* **94**(2), 027201 (2005).

- [46] M. Altman, H. Pinkvos, J. Hurst, H. Poppa, G. Marx, and E. Bauer, MRS Online Proceedings Library **232** (1991).
- [47] G. Chen, A. Mascaraque, A. T. N'Diaye, and A. K. Schmid, Appl. Phys. Lett. **106**(24), 242404 (2015).
- [48] Q. Wu, R. Zdyb, E. Bauer, and M. S. Altman, Phys. Rev. B **87**, 104410 (2013).
- [49] C. Zhou, G. Chen, J. Xu, J. Liang, K. Liu, A. K. Schmid, and Y. Wu, Ultramicroscopy **200**, 132 (2019).
- [50] R. van Gastel, N. C. Bartelt, P. J. Feibelman, F. Léonard, and G. L. Kellogg, Phys. Rev. B **70**, 245413 (2004).
- [51] J. Kessler, *Polarized electrons*, vol. 1 (Springer Science & Business Media, 2013).
- [52] R. Feder, *Polarized electrons in surface physics*, vol. 1 (World Scientific, 1986).
- [53] X. Jin, B. Ozdol, M. Yamamoto, A. Mano, N. Yamamoto, and Y. Takeda, Appl. Phys. Lett. **105**(20), 203509 (2014).
- [54] Y. A. Mamaev, L. G. Gerchikov, Y. P. Yashin, D. A. Vasiliev, V. V. Kuzmichev, V. M. Ustinov, A. E. Zhukov, V. S. Mikhrin, and A. P. Vasiliev, Appl. Phys. Lett. **93**(8), 081114 (2008).
- [55] N. Yamamoto, X. Jin, A. Mano, Y. Nakagawa, T. Nakanishi, T. Ujihara, S. Okumi, M. Yamamoto, T. Konomi, Y. Takeda, T. Ohshima, T. Saka, *et al.*, AIP Conf. Proc. **1149**(1), 1052 (2009).
- [56] M. Kuwahara, T. Nakanishi, S. Okumi, M. Yamamoto, M. Miyamoto, N. Yamamoto, K. ichi Yasui, T. Morino, R. Sakai, K. Tamagaki, and K. Yamaguchi, Jpn. J. Appl. Phys. **45**(8A), 6245 (2006).
- [57] J. K. Bae, A. Galdi, L. Cultrera, F. Ikponmwen, J. Maxson, and I. Bazarov, J. Appl. Phys. **127**(12), 124901 (2020).
- [58] G. Busch, M. Campagna, and H. C. Siegmans, Phys. Rev. B **4**, 746 (1971).
- [59] R. Sizmann, Nucl. Instrum. Methods **132**, 523 (1976).
- [60] G. Chrobok, M. Hofmann, G. Regenfus, and R. Sizmann, Phys. Rev. B **15**, 429 (1977).

- [61] M. Landolt and M. Campagna, Phys. Rev. Lett. **38**, 663 (1977).
- [62] Y. Niu and M. Altman, Surf. Sci. **604**(11), 1055 (2010).
- [63] R. Bryl and M. S. Altman, J. Appl. Phys. **94**(7), 4670 (2003).
- [64] Y. R. Niu and M. S. Altman, Appl. Phys. Lett. **95**(20), 203113 (2009).
- [65] T. Irisawa, T. K. Yamada, and T. Mizoguchi, New J. Phys. **11**(11), 113031 (2009).
- [66] N. Müller, W. Eckstein, W. Heiland, and W. Zinn, Phys. Rev. Lett. **29**, 1651 (1972).
- [67] E. Kisker, G. Baum, A. H. Mahan, W. Raith, and K. Schröder, Phys. Rev. Lett. **36**, 982 (1976).
- [68] G. Chrobok and M. Hofmann, Phys. Lett. A **57**(3), 257 (1976).
- [69] G. Baum, E. Kisker, A. Mahan, W. Raith, and B. Reihl, Appl. Phys. **14**(2), 149 (1977).
- [70] S.-h. Phark, J. A. Fischer, M. Corbetta, D. Sander, and J. Kirschner, Appl. Phys. Lett. **103**(3), 032407 (2013).
- [71] M.-B. Martin, B. Dlubak, R. S. Weatherup, M. Piquemal-Banci, H. Yang, R. Blume, R. Schloegl, S. Collin, F. Petroff, S. Hofmann, J. Robertson, A. Anane, *et al.*, Appl. Phys. Lett. **107**(1), 012408 (2015).
- [72] M. Born and R. Oppenheimer, Ann. Phys. **389**(20), 457 (1927).
- [73] P. Hohenberg and W. Kohn, Phys. Rev. **136**, B864 (1964).
- [74] W. Kohn and L. J. Sham, Phys. Rev. **140**, A1133 (1965).
- [75] C.-K. Skylaris, P. D. Haynes, A. A. Mostofi, and M. C. Payne, J. Chem. Phys **122**(8), 084119 (2005).
- [76] J. P. Perdew and A. Zunger, Phys. Rev. B **23**, 5048 (1981).
- [77] J. C. Womack, N. Mardirossian, M. Head-Gordon, and C.-K. Skylaris, J. Chem. Phys **145**(20), 204114 (2016).
- [78] J. Dziedzic, Q. Hill, and C.-K. Skylaris, J. Chem. Phys **139**(21), 214103 (2013).
- [79] W. Kohn, Phys. Rev. Lett. **76**, 3168 (1996).

- [80] D. R. Bowler and T. Miyazaki, Rep. Prog. Phys **75**(3), 036503 (2012).
- [81] W. Kohn, Phys. Rev. **115**, 809 (1959).
- [82] J. D. Cloizeaux, Phys. Rev. **135**, A685 (1964).
- [83] S. Ismail-Beigi and T. A. Arias, Phys. Rev. Lett. **82**, 2127 (1999).
- [84] R. McWeeny, Rev. Mod. Phys. **32**, 335 (1960).
- [85] A. A. Mostofi, P. D. Haynes, C. K. Skylaris, and M. C. Payne, Mol. Simul. **33**(7), 551 (2007).
- [86] J. C. A. Prentice, J. Aarons, J. C. Womack, A. E. A. Allen, L. Andrinopoulos, L. Anton, R. A. Bell, A. Bhandari, G. A. Bramley, R. J. Charlton, R. J. Clements, D. J. Cole, *et al.*, J. Chem. Phys **152**(17), 174111 (2020).
- [87] C.-K. Skylaris, A. A. Mostofi, P. D. Haynes, O. Diéguez, and M. C. Payne, Phys. Rev. B **66**, 035119 (2002).
- [88] P. D. Haynes, C.-K. Skylaris, A. A. Mostofi, and M. C. Payne, J. Condens. Matter Phys. **20**(29), 294207 (2008).
- [89] C.-K. Skylaris, A. A. Mostofi, P. D. Haynes, O. Diéguez, and M. C. Payne, Phys. Rev. B **66**, 035119 (2002).
- [90] A. Aharoni *et al.*, *Introduction to the Theory of Ferromagnetism*, vol. 109 (Clarendon Press, 2000).
- [91] M. Getzlaff, *Fundamentals of magnetism* (Springer Science & Business Media, 2007).
- [92] R. O’Handley, *Modern Magnetic Materials: Principles and Applications* (Wiley, 1999).
- [93] S. Blundell, *Magnetism in Condensed Matter*, Oxford Master Series in Condensed Matter Physics (OUP Oxford, 2001).
- [94] C. A. F. Vaz, J. A. C. Bland, and G. Lauhoff, Rep. Prog. Phys **71**(5), 056501 (2008).
- [95] N. Khalid, J.-Y. Kim, A. Ionescu, T. Hussain, F. Oehler, T. Zhu, R. A. Oliver, I. Farrer, R. Ahmad, and C. H. W. Barnes, J. Appl. Phys. **123**(10), 103901 (2018).

- [96] C. M. Collins, R. J. Parmee, W. I. Milne, and M. T. Cole, *Adv. Sci.* **3**(5), 1500318 (2016).
- [97] T. Ebbesen, H. Lezec, H. Hiura, J. Bennett, H. Ghaemi, and T. Thio, *Nature* **382**(6586), 54 (1996).
- [98] J. N. Coleman, U. Khan, W. J. Blau, and Y. K. Gun'ko, *Carbon* **44**(9), 1624 (2006).
- [99] A. Krishnan, E. Dujardin, T. W. Ebbesen, P. N. Yianilos, and M. M. J. Treacy, *Phys. Rev. B* **58**, 14013 (1998).
- [100] M.-F. Yu, B. S. Files, S. Arepalli, and R. S. Ruoff, *Phys. Rev. Lett.* **84**, 5552 (2000).
- [101] D. G. Papageorgiou, Z. Li, M. Liu, I. A. Kinloch, and R. J. Young, *Nanoscale* **12**, 2228 (2020).
- [102] S. Berber, Y.-K. Kwon, and D. Tománek, *Phys. Rev. Lett.* **84**, 4613 (2000).
- [103] C. W. Chang, D. Okawa, H. Garcia, A. Majumdar, and A. Zettl, *Phys. Rev. Lett.* **99**, 045901 (2007).
- [104] W. Zhu, C. Bower, G. Kochanski, and S. Jin, *Diam. Relat. Mater.* **10**(9), 1709 (2001).
- [105] R. Heyrovská, arXiv (2008).
- [106] P. R. Bandaru, *J. Nanosci. Nanotechnol.* **7**(4-5), 1239 (2007).
- [107] Y. Matsuda, J. Tahir-Kheli, and W. A. Goddard, *J. Am. Chem. Soc.* **1**(19), 2946 (2010).
- [108] L. Liu, G. Han, H. Wang, and J. Wan, *Ad Hoc Networks* **55**, 50 (2017), ISSN 1570-8705.
- [109] L. B. Freund and S. Suresh, *Thin film materials: stress, defect formation and surface evolution* (Cambridge University Press, 2004).
- [110] A. P. Guimarães and A. P. Guimaraes, *Principles of nanomagnetism*, vol. 7 (Springer, 2009).
- [111] P. Pouloupoulos and K. Baberschke, *J. Condens. Matter Phys.* **11**(48), 9495 (1999).

- [112] K. Y. Guslienko, *J. Nanosci. Nanotechnol.* **8**(6), 2745 (2008).
- [113] K. N. Koo, A. F. Ismail, M. H. D. Othman, N. Bidin, and M. A. Rahman, *Mal. J. Fund. Appl. Sci.* **15**(1), 23 (2019).
- [114] PDE Solutions Inc: Flexpde 7 (<https://www.pdesolutions.com>).
- [115] QuantumATK version 2016, Synopsys QuantumATK (www.synopsys.com/silicon/quantumatk.html).
- [116] S. Smidstrup, T. Markussen, P. Vancaeyveld, J. Wellendorff, J. Schneider, T. Gunst, B. Verstichel, D. Stradi, P. A. Khomyakov, U. G. Vej-Hansen, M.-E. Lee, S. T. Chill, *et al.*, *J. Condens. Matter Phys.* **32**(1), 015901 (2019).
- [117] D. W. Brenner, O. A. Shenderova, J. A. Harrison, S. J. Stuart, B. Ni, and S. B. Sinnott, *J. Condens. Matter Phys.* **14**(4), 783 (2002).
- [118] J. P. Perdew and Y. Wang, *Phys. Rev. B* **45**(23), 13244 (1992).
- [119] P. E. Blöchl, *Phys. Rev. B* **50**(24), 17953 (1994).
- [120] N. Marzari, D. Vanderbilt, and M. C. Payne, *Phys. Rev. Lett.* **79**, 1337 (1997).
- [121] J. A. Venables, *Surface processes in epitaxial growth* (Cambridge University Press, 2000), p. 144–183.
- [122] J. Matthews, *Epitaxial growth part A* (Elsevier, 2012).
- [123] A. M. Ilyin, in *Microscopy Methods in Nanomaterials Characterization* (Elsevier, 2017), Micro and Nano Technologies, pp. 363 – 381, ISBN 978-0-323-46141-2.
- [124] D. Woodruff, in *Reference Module in Materials Science and Materials Engineering* (Elsevier, 2016), ISBN 978-0-12-803581-8.
- [125] N. microstructural characterization platform for advanced nanomaterials, *SPLEEM equipment* (accessed: 18.08.2020), URL <https://www.nims.go.jp/nmcp/eng/equipment10.html>.
- [126] M. Suzuki, M. Hashimoto, T. Yasue, T. Koshikawa, Y. Nakagawa, T. Konomi, A. Mano, N. Yamamoto, M. Kuwahara, M. Yamamoto, S. Okumi, T. Nakanishi, *et al.*, *Appl. Phys. Express* **3**(2), 026601 (2010).

- [127] L. Yu, W. Wan, T. Koshikawa, M. Li, X. Yang, C. Zheng, M. Suzuki, T. Yasue, X. Jin, Y. Takeda, R. Tromp, and W.-X. Tang, *Ultramicroscopy* **216**, 113017 (2020), ISSN 0304-3991.
- [128] X. Jin, A. Mano, F. Ichihashi, N. Yamamoto, and Y. Takeda, *Appl. Phys. Express* **6**(1), 015801 (2013).
- [129] N. Yamamoto, T. Nakanishi, A. Mano, Y. Nakagawa, S. Okumi, M. Yamamoto, T. Konomi, X. Jin, T. Ujihara, Y. Takeda, T. Ohshima, T. Saka, *et al.*, *J. Appl. Phys.* **103**(6), 064905 (2008).
- [130] T. Yasue, M. Suzuki, K. Tsuno, S. Goto, Y. Arai, and T. Koshikawa, *Rev. Sci. Instrum.* **85**(4), 043701 (2014).
- [131] N. Rougemaille and A. K. Schmid, *Eur. Phys. J. Appl. Phys.* **50**(2), 20101 (2010).
- [132] Y. Zhu, ed., *Spin-polarized low energy electron microscopy (SPLEEM)* (Springer US, Boston, MA, 2005), pp. 361–379, ISBN 978-0-387-23395-6.
- [133] Z. J. Ding, H. M. Li, R. Shimizu, and K. Goto, *J. Surf. Anal.* **15**(2), 186 (2008).
- [134] E. Bauer, *Surface Microscopy with Low Energy Electrons* (Springer New York, 2014).
- [135] R. Zdyb and E. Bauer, *Phys. Rev. Lett.* **88**, 166403 (2002).
- [136] S. N. Samarin, O. M. Artamonov, A. P. Baraban, M. Kostylev, P. Guagliardo, J. Berakdar, and J. F. Williams, *Phys. Rev. B* **94**, 155440 (2016).
- [137] R. Zdyb and E. Bauer, *J. Condens. Matter Phys.* **25**(27), 272201 (2013).
- [138] E. Bauer, *SPLEEM* (Springer Berlin Heidelberg, Berlin, Heidelberg, 2005), pp. 111–136, ISBN 978-3-540-26641-9.
- [139] T. J. Gay and F. B. Dunning, *Rev. Sci. Instrum.* **63**(2), 1635 (1992).
- [140] G. C. Burnett, T. J. Monroe, and F. B. Dunning, *Rev. Sci. Instrum.* **65**(6), 1893 (1994).
- [141] F. Dunning, *Nucl. Instrum. Methods Phys. Res. A: Accel. Spectrom. Detect. Assoc. Equip.* **347**(1), 152 (1994).

- [142] J. Sromicki, K. Bodek, D. Conti, S. Kistryn, J. Lang, S. Navert, O. Naviliat-Cuncic, E. Stephan, C. Sys, J. Zejma, W. Haeberli, E. Reichert, *et al.*, Phys. Rev. Lett. **82**, 57 (1999).
- [143] Z. Czyżewski, D. O. MacCallum, A. Romig, and D. C. Joy, J. Appl. Phys. **68**(7), 3066 (1990).
- [144] N. F. Mott and N. H. D. Bohr, Proc. Math. Phys. Eng. Sci. **124**(794), 425 (1929).
- [145] K. P. Kopper, *Electron Spin Polarimetry Studies of Evolving Magnetism at the Atomic Scale*, Ph.D. thesis, University of Cambridge (2007).
- [146] S. Masur, E. Linscott, and C. Edgcombe, J. Electron Spectrosc. Relat. Phenom. p. 146896 (2019).
- [147] C. Edgcombe, S. Masur, E. Linscott, J. Whaley-Baldwin, and C. Barnes, Ultramicroscopy **198**, 26 (2019).
- [148] F. Jollet, M. Torrent, and N. Holzwarth, Comput. Phys. Commun. **185**(4), 1246 (2014).
- [149] M. D. Segall, C. J. Pickard, R. Shah, and M. C. Payne, Mol. Phys. **89**(2), 571 (1996).
- [150] J. Gomez-Jeria, J. Chil. Chem. Soc. **54**, 482 (2009), ISSN 0717-9707.
- [151] L. Liu, C. S. Jayanthi, H. Guo, and S. Y. Wu, Phys. Rev. B **64**, 033414 (2001).
- [152] B. Gao, J. Jiang, Z. Wu, and Y. Luo, J. Chem. Phys **128**(8), 084707 (2008).
- [153] S. C. Lim, K. Lee, I. H. Lee, and Y. H. Lee, Nano **02**(02), 69 (2007).
- [154] C. J. Edgcombe and U. Valdrè, J. Microsc. **203**(2), 188 (2001).
- [155] J. P. Perdew, K. Burke, and M. Ernzerhof, Phys. Rev. Lett. **77**, 3865 (1996).
- [156] W. S. Su, T. C. Leung, and C. T. Chan, Phys. Rev. B **76**, 235413 (2007).
- [157] B. Shan and K. Cho, Phys. Rev. Lett. **94**, 236602 (2005).
- [158] J. Zhao, J. Han, and J. P. Lu, Phys. Rev. B **65**, 193401 (2002).
- [159] C.-W. Chen and M.-H. Lee, Nanotechnology **15**(5), 480 (2004).
- [160] Y.-N. Wen and J.-M. Zhang, Comput. Mater. Sci. **42**(2), 281 (2008).

- [161] N. D. M. Hine, J. Dziejczak, P. D. Haynes, and C.-K. Skylaris, *J. Chem. Phys.* **135**(20), 204103 (2011).
- [162] J. Wan, Y. L. Fan, D. W. Gong, S. G. Shen, and X. Q. Fan, *Model. Simul. Mater. Sci. Eng.* **7**(2), 189 (1999).
- [163] C. Chan and S. G. Louie, *Phys. Rev. B* **33**(4), 2861 (1986).
- [164] J. D. Gale, *J. Chem. Soc., Faraday Trans.* **93**, 629 (1997).
- [165] L. Swanson and L. Crouser, *Phys. Rev. Lett.* **16**(10), 389 (1966).
- [166] E. Plummer and J. Gadzuk, *Phys. Rev. Lett.* **25**(21), 1493 (1970).
- [167] Z. Ibrahim and M. Lee, *Prog. Surf. Sci.* **67**(1-8), 309 (2001).
- [168] E. W. Plummer and A. E. Bell, *J. Vac. Sci. Technol.* **9**(2), 583 (1972).
- [169] L. Swanson and G. Schwind, in *Advances in Imaging and Electron Physics* (Elsevier, 2009), vol. 159 of *Advances in Imaging and Electron Physics*, pp. 63 – 100.
- [170] N. W. Ashcroft and N. D. Mermin, *Solid State Physics* (Holt-Saunders, 1976).
- [171] R. J. Hicken, S. J. Gray, A. Ercole, C. Daboo, D. J. Freeland, E. Gu, E. Ahmad, and J. A. C. Bland, *Phys. Rev. B* **55**, 5898 (1997).
- [172] M. Canepa, S. Terreni, P. Cantini, A. Campora, and L. Mattera, *Phys. Rev. B* **56**, 4233 (1997).
- [173] D. Bürgler, C. Schmidt, D. Schaller, F. Meisinger, R. Hofer, and H.-J. Güntherodt, *Phys. Rev. B* **56**(7), 4149 (1997).
- [174] M. Stampanoni, A. Vaterlaus, M. Aeschlimann, and F. Meier, *Phys. Rev. Lett.* **59**, 2483 (1987).
- [175] Z. Q. Qiu, J. Pearson, and S. D. Bader, *Phys. Rev. Lett.* **70**, 1006 (1993).
- [176] D. M. Schaller, D. E. Bürgler, C. M. Schmidt, F. Meisinger, and H.-J. Güntherodt, *Phys. Rev. B* **59**, 14516 (1999).
- [177] C. Klein, R. Ramchal, M. Farle, and A. K. Schmid, *Surf. Interface Anal.* **38**(12-13), 1550 (2006).
- [178] H. Noro, R. Persaud, and J. A. Venables, *Surf. Sci.* **357-358**, 879 (1996).

- [179] S. Suto, K.-D. Tsuei, E. W. Plummer, and E. Burstein, *Phys. Rev. Lett.* **63**, 2590 (1989).
- [180] T. Komesu, G. D. Waddill, and J. G. Tobin, *J. Condens. Matter Phys.* **18**(39), 8829 (2006).
- [181] J. Kirschner, D. Rebenstorff, and H. Ibach, *Phys. Rev. Lett.* **53**, 698 (1984).
- [182] J. Kirschner, *Phys. Rev. Lett.* **55**, 973 (1985).
- [183] J. Leuker, H. Ortjohann, R. Zimny, and H. Winter, *Surf. Sci.* **388**, 262 (1997).
- [184] M. Busch, M. Gruyters, and H. Winter, *Surf. Sci.* **600**(19), 4598 (2006), ISSN 0039-6028.
- [185] O. Wells, in *Encyclopedia of Materials: Science and Technology* (Elsevier, Oxford, 2001), pp. 8265–8269, ISBN 978-0-08-043152-9.
- [186] G. N. Derry, M. E. Kern, and E. H. Worth, *J. Vac. Sci. Technol. A* **33**(6), 060801 (2015).
- [187] S. J. Clark, M. D. Segall, C. J. Pickard, P. J. Hasnip, M. I. J. Probert, K. Refson, and M. C. Payne, *Z. Kristallogr. Cryst. Mater.* **220**(5-6), 567 (2005).
- [188] D. M. Ceperley and B. J. Alder, *Phys. Rev. Lett.* **45**, 566 (1980).
- [189] E. Bauer, *Rep. Prog. Phys* **57**(9), 895 (1994).
- [190] A. J. Dekker, *Secondary Electron Emission* (Macmillan Education UK, London, 1981), pp. 418–445, ISBN 978-1-349-00784-4.
- [191] Y. Zhu, *Modern techniques for characterizing magnetic materials* (Springer Science & Business Media, 2005).
- [192] O. Y. Ridzel, V. Astašauskas, and W. S. Werner, *J. Electron Spectros. Relat. Phenom.* **241**, 146824 (2020).
- [193] X. Sun, Z. J. Ding, and Y. Yamauchi, *Surf. Interface Anal.* **38**(4), 668 (2006).
- [194] O. Paul, M. Taborelli, and M. Landolt, *Surf. Sci.* **211-212**, 724 (1989).
- [195] S. F. Mao, X. Sun, X. W. Fang, B. Da, and Z. J. Ding, *Surf. Interface Anal.* **44**(6), 703 (2012).
- [196] K. von Bergmann, M. Bode, and R. Wiesendanger, *Phys. Rev. B* **70**, 174455 (2004).

- [197] S. F. Huang, R. S. Chang, T. C. Leung, and C. T. Chan, *Phys. Rev. B* **72**, 075433 (2005).
- [198] O. Fruchart, P. O. Jubert, M. Eleoui, F. Cheynis, B. Borca, P. David, V. Santonacci, A. Liénard, M. Hasegawa, and C. Meyer, *J. Condens. Matter Phys.* **19**(5), 053001 (2007).
- [199] N. Rougemaille and A. K. Schmid, *J. Appl. Phys.* **99**(8), 08S502 (2006).
- [200] U. Gradmann and G. Waller, *Surf. Sci.* **116**(3), 539 (1982).
- [201] J. Graf, C. Jozwiak, A. K. Schmid, Z. Hussain, and A. Lanzara, *Phys. Rev. B* **71**, 144429 (2005).
- [202] K. Wagner, N. Weber, H. Elmers, and U. Gradmann, *J. Magn. Magn. Mater.* **167**(1), 21 (1997).
- [203] R. Zdyb and E. Bauer, *Surf. Rev. Lett.* **09**(03n04), 1485 (2002).
- [204] J. A. Venables, *Phys. A: Stat. Mech. Appl.* **239**(1), 35 (1997).
- [205] T. Furukawa and K. Koike, *Surf. Sci.* **425**(2), 180 (1999).
- [206] M. S. Chung and T. E. Everhart, *J. Appl. Phys.* **45**(2), 707 (1974).
- [207] P. Moras, B. Bihlmayer, E. Vescovo, P. M. Sheverdyaeva, M. Papagno, L. Ferrari, and L. Carbone, *J. Condens. Matter Phys.* **29**(49), 495806 (2017).
- [208] Y. J. Chen, M. H. Kuo, and C. S. Shern, *Appl. Phys. Lett.* **93**(1), 012503 (2008).
- [209] H. Seiler, *J. Appl. Phys.* **54**(11), R1 (1983).
- [210] E. Bauer, *J. Electron Spectros. Relat. Phenom.* (2019).
- [211] D. P. Woodruff, *Modern techniques of surface science* (Cambridge University Press, 2016).
- [212] Autodesk®; Inventor® Professional 2018 (<https://www.autodesk.co.uk/products>).
- [213] COMSOL®5.4; COMSOL Multiphysics Reference Manual (www.comsol.com).
- [214] P. Zhang, S. B. Fairchild, T. C. Back, and Y. Luo, *AIP Advances* **7**(12), 125203 (2017).
- [215] D. S. D. Gunn and S. J. Jenkins, *Phys. Rev. B* **83**, 115403 (2011).

- [216] S. J. Jenkins, Q. Ge, and D. A. King, *Phys. Rev. B* **64**, 012413 (2001).
- [217] M. B. Knickelbein, *J. Chem. Phys.* **116**(22), 9703 (2002).
- [218] K. P. Kopper, D. Küpper, R. Reeve, T. Mitrelias, D. S. D. Gunn, and S. J. Jenkins, *Phys. Rev. B* **80**, 052406 (2009).
- [219] K. P. Kopper, D. Küpper, R. Reeve, T. Mitrelias, and J. A. C. Bland, *J. Appl. Phys.* **103**(7), 07C904 (2008).
- [220] R. M. Reeve, S.-L. Chin, A. Ionescu, and C. H. W. Barnes, *Phys. Rev. B* **84**, 184431 (2011).
- [221] S.-L. Chin, A. Ionescu, R. M. Reeve, J. Cheng, and C. H. Barnes, *Surf. Sci.* **608**, 282 (2013).
- [222] S. Lyon, in *Shreir's Corrosion* (Elsevier, Oxford, 2010), pp. 2205 – 2223, ISBN 978-0-444-52787-5.
- [223] A. Alekhin, I. Razdolski, M. Berritta, D. Bürstel, V. Temnov, D. Diesing, U. Bovensiepen, G. Woltersdorf, P. M. Oppeneer, and A. Melnikov, *J. Condens. Matter Phys.* **31**(12), 124002 (2019).
- [224] A. Alekhin, I. Razdolski, N. Ilin, J. P. Meyburg, D. Diesing, V. Roddatis, I. Rungger, M. Stamenova, S. Sanvito, U. Bovensiepen, and A. Melnikov, *Phys. Rev. Lett.* **119**, 017202 (2017).
- [225] J. Bass and W. P. Pratt, *J. Condens. Matter Phys.* **19**(18), 183201 (2007).
- [226] M. Isasa, E. Villamor, L. E. Hueso, M. Gradhand, and F. Casanova, *Phys. Rev. B* **91**, 024402 (2015).
- [227] A. Marczyńska, J. Skoryna, M. Lewandowski, and L. Smardz, *Acta Phys. Pol. A.* **127**(2) (2015).
- [228] M. K. Miller, K. F. Russell, K. Thompson, R. Alvis, and D. J. Larson, *Microsc. Microanal.* **13**(6), 428–436 (2007).
- [229] J. Hu, Y. Ji, Y. Shi, F. Hui, H. Duan, and M. Lanza, *Ann. J. Mater. Sci. Eng.* **1**, 16 (2014).
- [230] Y. S. Dedkov, M. Fonin, and C. Laubschat, *Appl. Phys. Lett.* **92**(5), 052506 (2008).

- [231] Y. S. Dedkov, M. Fonin, U. Rüdiger, and C. Laubschat, *Appl. Phys. Lett.* **93**(2), 022509 (2008).
- [232] B. Dlubak, M.-B. Martin, R. S. Weatherup, H. Yang, C. Deranlot, R. Blume, R. Schloegl, A. Fert, A. Anane, S. Hofmann, P. Seneor, and J. Robertson, *ACS Nano* **6**(12), 10930 (2012).
- [233] N. Rougemaille, A. T. N'Diaye, J. Coraux, C. Vo-Van, O. Fruchart, and A. K. Schmid, *Appl. Phys. Lett.* **101**(14), 142403 (2012).
- [234] F. Hui, S. Chen, X. Liang, B. Yuan, X. Jing, Y. Shi, and M. Lanza, *Crystals* **7**(9), 269 (2017).
- [235] Q. Liu, R. Zou, Y. Bando, D. Golberg, and J. Hu, *Prog. Mater. Sci.* **70**, 1 (2015).
- [236] A. Vansteenkiste and B. Van de Wiele, *J. Magn. Magn. Mater.* **323**(21), 2585 (2011).
- [237] C. Kittel, *Rev. Mod. Phys.* **21**(4), 541 (1949).
- [238] M. J. Donahue and D. G. Porter, *OOMMF User's Guide*, Version 1.0; <http://math.nist.gov/oommf/> (1999).
- [239] D. J. Dunlop and Ö. Özdemir, *Rock magnetism: fundamentals and frontiers*, vol. 3 (Cambridge University Press, 2001).
- [240] C. Graham, *Phys. Rev.* **112**(4), 1117 (1958).
- [241] S. M. Suturin, A. M. Korovin, S. V. Gastev, M. P. Volkov, A. A. Sitnikova, D. A. Kirilenko, M. Tabuchi, and N. S. Sokolov, *Phys. Rev. Mater.* **2**, 073403 (2018).
- [242] Y. S. Dedkov, U. Rüdiger, and G. Güntherodt, *Phys. Rev. B* **65**, 064417 (2002).
- [243] M. Fonin, Y. S. Dedkov, R. Pentcheva, U. Rüdiger, and G. Güntherodt, *J. Condens. Matter Phys.* **20**(14), 142201 (2008).
- [244] H.-T. Jeng and G. Y. Guo, *Phys. Rev. B* **65**, 094429 (2002).
- [245] A. Pratt, M. Kurahashi, X. Sun, D. Gilks, and Y. Yamauchi, *Phys. Rev. B* **85**, 180409 (2012).

- [246] H.-C. Wu, S. K. Arora, O. N. Mryasov, and I. V. Shvets, *Appl. Phys. Lett.* **92**(18), 182502 (2008).
- [247] L. R. Bickford, *Phys. Rev.* **78**, 449 (1950).
- [248] P. Li, C. Xia, Z. Zhu, Y. Wen, Q. Zhang, H. N. Alshareef, and X.-X. Zhang, *Adv. Funct. Mater.* **26**(31), 5679 (2016).
- [249] D. Ortega, E. Vélez-Fort, D. A. García, R. García, R. Litrán, C. Barrera-Solano, M. Ramírez-del Solar, and M. Domínguez, *Philos. Trans. A Math. Phys. Eng. Sci.* **368**(1927), 4407 (2010).
- [250] M. Goiriena-Goikoetxea, K. Y. Guslienko, M. Rouco, I. Orue, E. Berganza, M. Jaafar, A. Asenjo, M. L. Fernández-Gubieda, L. Fernández Barquín, and A. García-Arribas, *Nanoscale* **9**, 11269 (2017).
- [251] S.-H. Chung, R. D. McMichael, D. T. Pierce, and J. Unguris, *Phys. Rev. B* **81**, 024410 (2010).
- [252] G. S. Abo, Y. Hong, J. Park, J. Lee, W. Lee, and B. Choi, *IEEE Trans. Magn.* **49**(8), 4937 (2013).
- [253] D. L. Leslie-Pelecky and R. D. Rieke, *Chem. Mater.* **8**(8), 1770 (1996).
- [254] D. S. Negi, H. Sharona, U. Bhat, S. Palchoudhury, A. Gupta, and R. Datta, *Phys. Rev. B* **95**, 174444 (2017).
- [255] K. L. Krycka, J. A. Borchers, R. A. Booth, Y. Ijiri, K. Hasz, J. J. Rhyne, and S. A. Majetich, *Phys. Rev. Lett.* **113**, 147203 (2014).
- [256] M. Beleggia, M. D. Graef, and Y. T. Millev, *J. Phys. D Appl. Phys.* **39**(5), 891 (2006).
- [257] K. Eimre, S. Parviainen, A. Aabloo, F. Djurabekova, and V. Zadin, *J. Appl. Phys.* **118**(3), 033303 (2015).
- [258] A. Kyritsakis and F. Djurabekova, *Comput. Mater. Sci.* **128**, 15 (2017).
- [259] P. Vincent, S. T. Purcell, C. Journet, and V. T. Binh, *Phys. Rev. B* **66**, 075406 (2002).
- [260] A. S. Teja and P.-Y. Koh, *Prog. Cryst. Growth Charact.* **55**(1), 22 (2009).
- [261] P. C. Fannin and S. W. Charles, *J. Phys. D Appl. Phys.* **27**(2), 185 (1994).

- [262] K. Tada and K. Watanabe, Phys. Rev. Lett. **88**, 127601 (2002).
- [263] J. A. Driscoll, B. Cook, S. Bubin, and K. Varga, J. Appl. Phys. **110**(2), 024304 (2011).
- [264] X. Zou, G. Zhou, J. Li, B. Yan, J. Wu, B.-L. Gu, and W. Duan, Appl. Phys. Lett. **94**(19), 193106 (2009).